Etude par couplage de méthodes spectroscopiques et électrochimiques des facteurs responsables de la stabilité de couches d'oxydes sur des alliages contenant du chrome et du molybdène

Zuocheng Wang

▶ **To cite this version:**

Zuocheng Wang. Etude par couplage de méthodes spectroscopiques et électrochimiques des facteurs responsables de la stabilité de couches d'oxydes sur des alliages contenant du chrome et du molybdène. Autre. Université Paris sciences et lettres, 2019. Français. NNT : 2019PSLEC036 . tel-03204168

HAL Id: tel-03204168
https://pastel.hal.science/tel-03204168

Submitted on 21 Apr 2021

HAL is a multi-disciplinary open access archive for the deposit and dissemination of scientific research documents, whether they are published or not. The documents may come from teaching and research institutions in France or abroad, or from public or private research centers.

L'archive ouverte pluridisciplinaire **HAL**, est destinée au dépôt et à la diffusion de documents scientifiques de niveau recherche, publiés ou non, émanant des établissements d'enseignement et de recherche français ou étrangers, des laboratoires publics ou privés.

PSL UNIVERSITÉ PARIS

THÈSE DE DOCTORAT
DE L'UNIVERSITÉ PSL

Préparée à Chimie ParisTech

Key factors for the stability of the oxide film on alloys containing chromium and molybdenum studied by combining spectroscopic methods and electrochemical methods

Soutenue par
Zuocheng WANG
Le 6 décembre 2019

Ecole doctorale n° 388
Chimie physique et chimie analytique de Paris centre

Spécialité
Chimie Physique

Composition du jury :

M. Philippe REFAIT Professeur, Université de La Rochelle	*Président*
M. Bernard NORMAND Professeur, INSA Lyon	*Rapporteur*
M. John F. WATTS Professeur, Université de Surrey	*Rapporteur*
Mme Sannakaisa VIRTANEN Professeur, Université d'Erlangen	*Examinateur*
Mme Marjorie OLIVIER Professeur, Université de Mons	*Examinateur*
M. Vincent, MAURICE Directeur de recherche, CNRS, ENSCP	*Examinateur*
M. Philippe MARCUS Directeur de recherche, CNRS, ENSCP	*Directeur de thèse*

Chimie Paris ParisTech | PSL

Acknowledgements

This thesis work was done at Institut de Recherche de Chimie Paris (IRCP), in the team Physico-Chimie des Surfaces (PCS).

First and foremost, I would like to express my deepest sense of gratitude to my supervisors, Philippe Marcus and Vincent Maurice, for accepting me as a PhD student in your group, for your precise and valuable comments on the thesis manuscript, for your guidance, support, experience and inspiration.

Moreover, I would like to express my sincere regards to the jury members, Bernard Normand, John F. Watts, Sannakaisa Virtanen, Marie-George Olivier and Philippe Refait for devoting their precious time to the review of my thesis manuscript and for their scientific evaluation.

Futhermore I would like to thanks Sandrine Zanna, Frédéric Wiame, Antoine Seyeux, Francesco Di-Franco and Lorena H. Klein, for your guidance, sharing your knowledge of surface analysis, inspiring discussions and collaborations.

I would like also thanks my co-authors, Eirini-Maria Paschalidou for the important helps to this work.

My sincere thanks to Jolanta Światowska and Dimitri Mercier for helping me to solve experimental issues.

The secretaries, Anne Tan for your efficient helps with the administrative matters.

All the present and former members in Laboratoire de Physico-Chimie des Surfaces at Institut de Recherche de Chimie Paris, CNRS-Chimie ParisTech, for sharing the good times and happy hours in the lab.

Table of contents

General introduction

Stainless steels are iron-based alloys which have a minimum chromium weight of 10.5%. They are well known and largely used in our daily life and in industrial applications since they combine excellent mechanical properties with superior corrosion resistance. The key for their high corrosion resistance is an ultra-thin but protective surface oxide film, usually called the passive film, forming a barrier efficiently isolating the metallic substrate from the environment. This passive film consists of iron and chromium oxide/hydroxide species and must be enriched in chromium to provide efficient passivity in the most aggressive environments. This oxide film formed in air is usually stable and protective in ordinary environment. However in more severe situations like in acidic solutions and in the presence of aggressive ions such as chlorides, the film may become unstable leading to passivity breakdown and to the initiation of localized corrosion phenomena if passivity does not self-repair properly. Although the passivity of stainless steels and its breakdown has been the subject of numerous corrosion science studies, the details of the physicochemical alterations of the surface oxide film induced by the transition from native oxide-covered surface state to passive state in aggressive aqueous medium and the role of the presence of chlorides in the environment on these alterations remain to be investigated with modern surface analytical techniques combined to electrochemical analysis.

The objective of this work was to apply such a strategy in order to understand how an acidic chemical environment influences the surface oxide film providing passivity to 316L stainless steel, and in particular the mechanisms of Cr and Mo enrichments that are key aspects of the passivity of Mo-bearing austenitic stainless steels. The role of chlorides added in the electrolyte on the alterations of the passive state at a stage preceding the initiation of localized corrosion was also studied as well as how these alterations are impacted by pre-passivation of the surface in a chloride-free electrolyte.

This manuscript contains five chapters. Chapter I is a bibliographic study of the state of the art. In this chapter, the history and the different types of stainless steels are presented. Then the

electrochemical aspects of the passivity of stainless steels as well as the thickness, composition and structure of passive films are resumed. After that the different types of corrosion are introduced before concluding and contextualizing the objective of this work.

Chapter II presents the different techniques applied in this work. Surface spectroscopic techniques include X-ray Photoelectron Spectroscopy (XPS) and Time-of-Flight Secondary Ion Mass Spectrometry (ToF-SIMS). They were used to analyze the composition, stratified structure and thickness of the oxide films. Electrochemical techniques such as Linear Scan Voltametry (LSV), potentiostatic polarisation, Electrochemical Impedance Spectroscopy (EIS) and Photo-Current Spectroscopy (PCS) were used to characterize the electrochemical aspects of passivity as well as the electronic properties of the surface oxides. Atomic Force Microscopy (AFM) was used in complement for topographic analysis.

Chapter III reports the study of the properties of the native oxide layer formed on a polycrystalline austenitic 316L SS surface in air and the modifications brought by electrochemical passivation in acid solution. ToF-SIMS and XPS surface analysis were used to characterize the layered structure, thickness and composition of the oxide film and their modifications. PCS, applied *in situ* and combined with electrochemical analysis, was used to obtain direct information on the electronic properties of the thin photo-conducting surface films. LSV and EIS were applied to evidence the modifications of the corrosion resistance.

Chapter IV focuses on the mechanisms by which the Cr and Mo enrichments in the native surface oxide film are modified when exposing a polycrystalline austenitic 316L SS to an acid aqueous solution. ToF-SIMS elemental depth profile analysis and XPS compositional surface analysis were applied to interrogate the modifications induced by immersion without and with application of anodic polarization in the passive domain. An experimental protocol avoiding contact to ambient air of the samples during transfer from liquid environment for electrochemical treatment to the different UHV platforms for surface analysis was adopted, enabling us to highlight the key effect of immersion under open circuit conditions on the Cr and Mo enrichments.

Chapter V addresses the alterations of the surface oxide films brought by electrochemical passivation in Cl-containing sulfuric acid solutions. Potentiodynamic and potentiostatic polarization measurements were used to define the electrochemical conditions best suited to alter the passive state without initiating localized corrosion (i.e metastable pitting) at the micrometer scale. ToF-SIMS and XPS were applied to characterize the layered structure,

thickness and composition of the passive film and the entry of chlorides. Surface morphology was studied by AFM.

The three chapters presenting the results of this work, Chapters III, IV, and V, are in form of articles published or to be published in scientific journals.

The main conclusions of this thesis are given in the final section together with the perspectives opened by the present study.

A summary of this work in French language is presented in Annex.

Chapter I

State of the art and objectives of the thesis

I.1. Introduction to stainless steels

I.1.1. General introduction

Stainless steels are iron-based alloys which have a minimum chromium weight of 10.5% and maximum carbon weight of 1.2%. The word ‘stainless’ means ‘resistant to corrosion’ and indicates the higher corrosion resistance of this type of steel compared to other steels. The key to the high corrosion resistance is the presence of an ultrathin (several nanometers) but continuous and protective surface film, the passive film, mixing iron and chromium (hydr)oxides and strongly enriched in chromium. Some other elements (nickel, molybdenum, niobium, titanium or others) can be added to stainless steels to improve their properties, thus creating the huge family of stainless steel combining excellent mechanical properties and high corrosion resistance. This advantage of stainless steel opens a large application domain. In our daily life, many objects such as kitchen ustensils and office tools are made of stainless steel. In the industrial world, stainless steels are widely used in several domains such as the chemical industry and the energy industry for example. The increasing demand for stainless steel led to an exponential increase of the world production, from 1 million tons yearly in 1950s to 50.7 millions tons in 2018 [1].

Compared to the history of iron and steel which go back to the Iron Age, the history of stainless steel is still very young. In his book “*History of Stainless Steel*” [2], Harold M. Cobb pointed out in 1797 that french chemist Louis Nicolas Vauquelin discovered chromium oxide and first isolates chromium metal from chromium oxide. After one quarter century, in 1821, Pierre Berthier observed that iron alloyed with chromium was more resistant to acid than without chromium. Then, different stainless steel such as high chromium steel, low carbon ferrochromium have been discovered but there were no systematic classification of stainless steel. In 1904, Léon Guillet, Albert Portevin and Walter Giesen published series of research and first classified the different stainless steels according to their crystallographic structure.

From this moment stainless steels were classified in three different types: ferritic, martensitic and austenitic stainless steels [2].

I.1.2. Types of stainless steels

a. Ferritic stainless steels

Ferritic stainless steels have ferrite (body-centered cubic, bcc, crystalline structure) as their main phase. The quantity of chromium is often between 11 and 18 wt%. They have a yield strength generally higher than austenitic stainless steels, but are less resistant to corrosion and are more fragile at low temperatures. Several operations can improve the corrosion resistance of this type of stainless steel. Increasing the chromium content can increase the corrosion resistance. Adding other elements has a similar effect. For example, the addition of molybdenum improves the corrosion resistance of ferritic stainless steel. Thus this type of stainless steel is interesting for applications where moderate corrosion resistance is required because of its lower cost, especially thanks to the low nickel content. The different grades of ferritic stainless steel and their applications are presented in **Figure I-1**

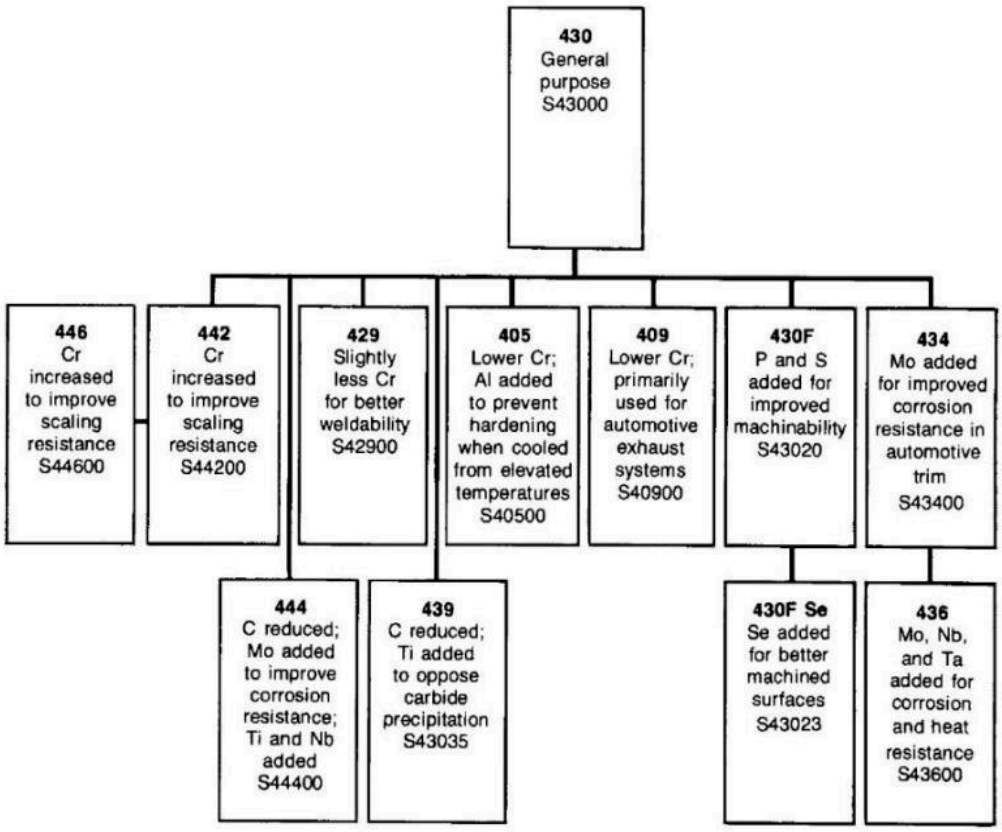

Figure I-1 Different grades and applications of ferritic stainless steel

b. Martensitic stainless steels

Martensitic stainless steels contain the martensite phase, which is a metastable tetragonal crystallographic structure due to the presence of carbon atoms in the interstitial sites. This type of stainless steels is made by a rapid cooling (quenching) where the carbon can not diffuse to the intergranular boundaries. The quantity of carbon influences the ratio of martensite, the higher carbon content increasing the martensite ratio. The specificity of martensitic stainless steel is its high hardness thanks to the presence of the martensite structure. But this phase decreases the corrosion resistance and makes the material brittle. So this type of stainless steel is used for applications where hardness is required, such as cutting, bearing, grinding etc. The different grades of martensitic stainless steel and their applications are presented in **Figure I-2**.

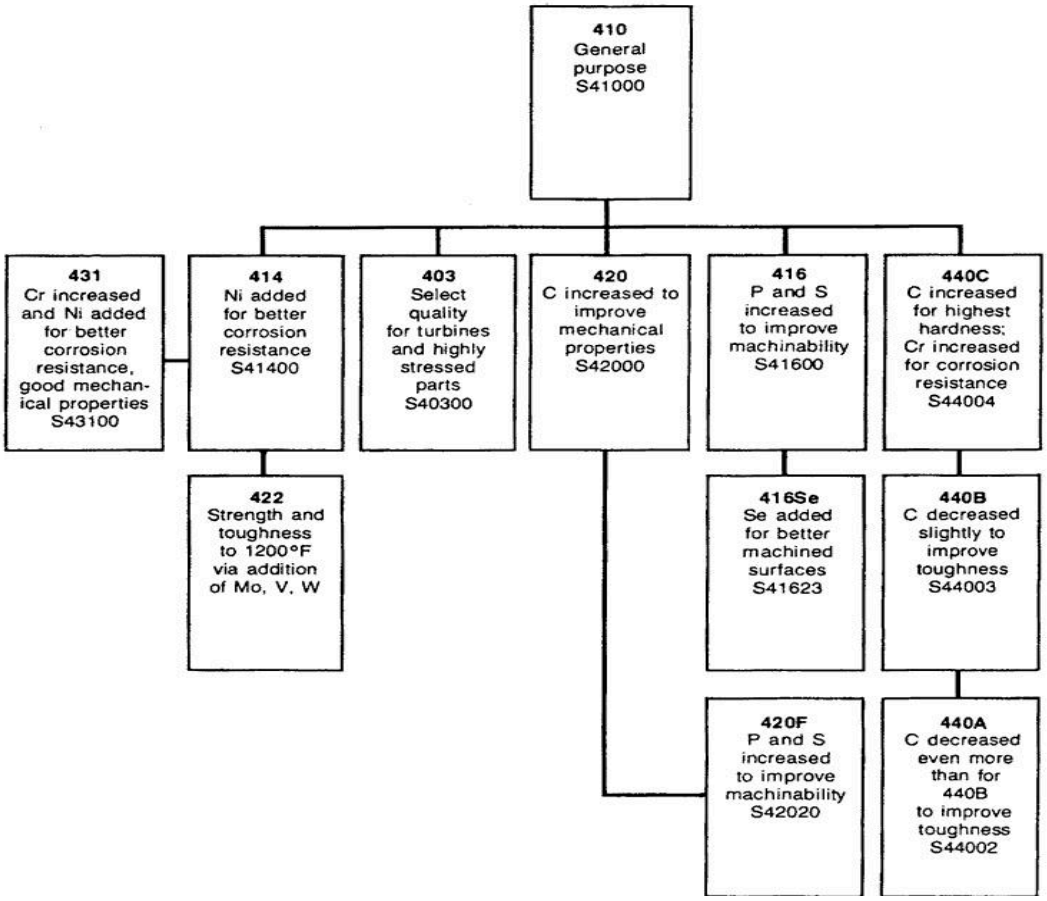

Figure I-2 Different grades and applications of martensitic stainless steel

c. Austenitic stainless steels

Austenitic stainless steels have austenite (face-centered cubic, fcc) crystalline structure as their primary phase. The content in chromium is generally between 16 and 18 wt% and that in nickel between 8 and 10 wt%. The addition of nickel keeps the austenitic structure stable but increases the cost. This type of stainless steel combines good corrosion resistance in many environments with good mechanical properties, in particular ductility. The excellent combination gives them a large application domain and makes them the most commonly used in our daily life. Thus the production of austenitic stainless steel is higher than that of other types of stainless steels since they represent more than half of the total stainless steel production. The different grades of austenitic stainless steel and their applications are presented in **Figure I-3**.

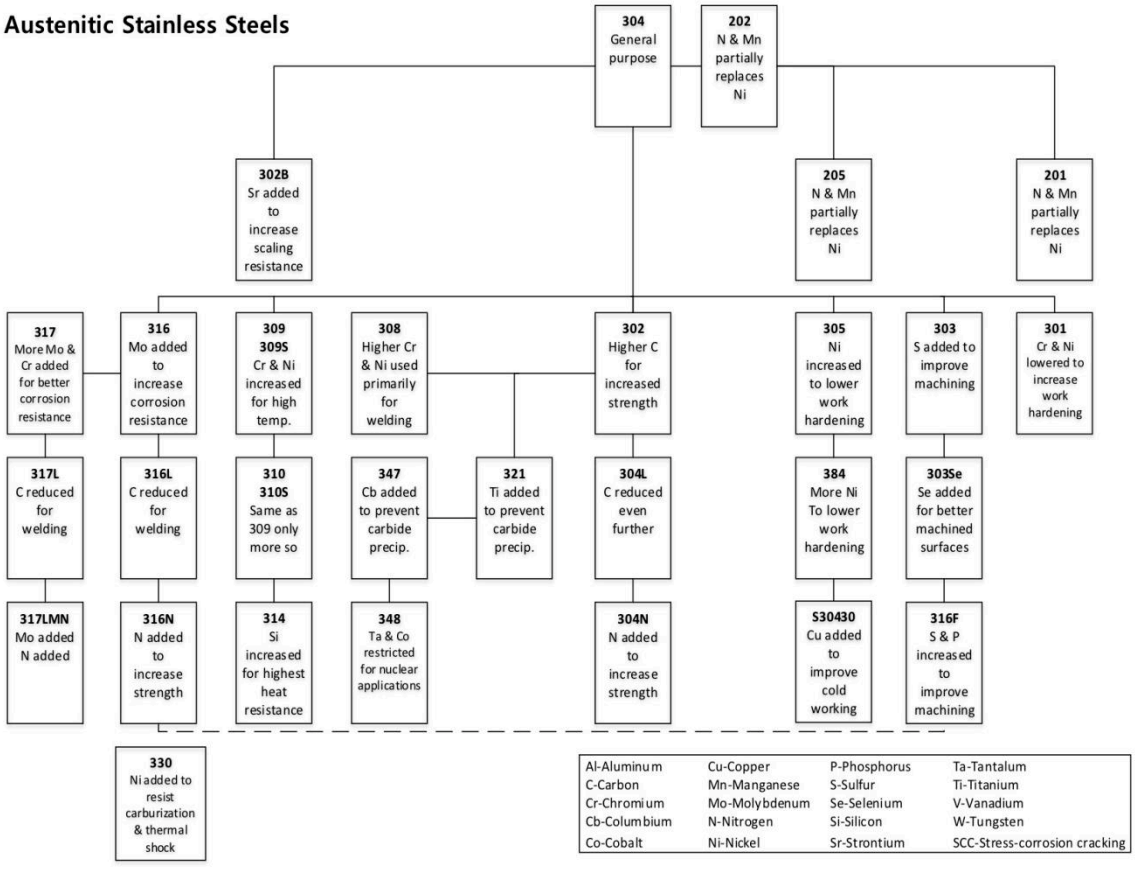

Figure I-3 Different grades and applications of austenitic stainless steel

I.2. Passivity of stainless steel

In 1908, Philip Monnartz studied the effect of the carbon content on the corrosion resistance of high chromium steel and showed that the passivity phenomenon is the key factor of the stainlessness of the stainless steel. In 1911, he studied the resistance of iron chromium alloy in

acid solution [3]. It was in this paper that the term "*passivity*" has been used and described as dependent on oxidizing conditions, and that passivity is responsible for the great increase in corrosion resistance. It was also in this paper that the quantity of 12 wt% chromium was pointed out as necessary to maintain the stainlessness of stainless steel.

The passive film formed on stainless steel, which is the key to passivity, has been widely studied since then and until now. In the following, the mechanism of passivation and the formation of passive film will be presented first and then the properties of the passive film.

I.2.1. Passivation mechanism

Passivation is often produced in a humid atmosphere or in aqueous media, at moderate temperatures. The oxidation mechanisms at high temperatures are different and will not be discussed here. Figure I-4 present a schematic view of the formation of the passive film on stainless steel [4].

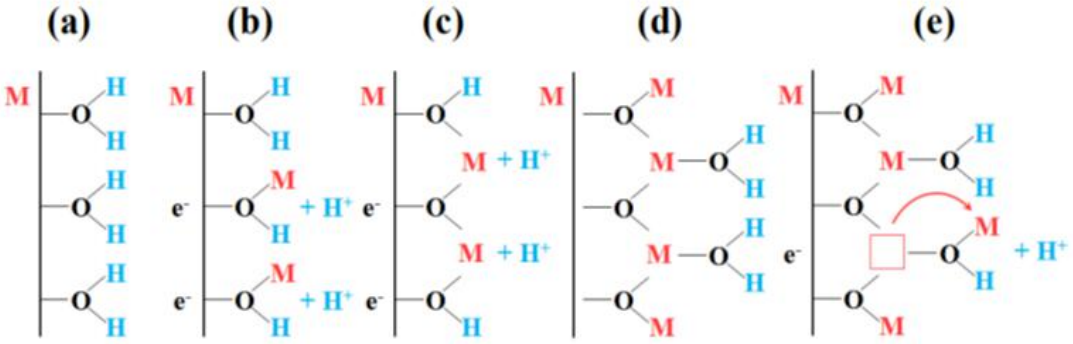

Figure I-4 Formation of the passive film on stainless steel [4]

There are five steps of formation of the passive film:

a) adsorption of H_2O on the metal surface,

b) deprotonation and migration of metal cations from the metal,

c) further deprotonation and bridging between neighboring oxide sites,

d) adsorption of H_2O on the oxide surface,

e) deprotonation and migration of a metal cation in the oxide which creates a vacancy for migration of metal cations from the metal.

Several steps of this process can be expressed by chemical equations. Steps a and b can be expressed as:

$$M + H_2O \rightarrow MOH + H^+ + e^- \qquad \text{eq. I-1}$$

Steps from b to c can be expressed as:

$$MOH \rightarrow MO + H^+ + e^- \qquad \text{eq. I-2}$$

Once the step c is completed, the formation of a single layer of oxide on the surface is completed. The growth of the passive film can be seen as a repetition of eq. I-1 and eq I-2. So the global equation of passivation can be expressed as

$$M + H_2O \rightarrow MO + 2H^+ + 2e^- \qquad \text{eq. I-3}$$

For stainless steel, the metal M is principally Fe and Cr.

The growth of oxide layers is a complex process combining the transport of species at the metal/oxide interface, across the oxide and at the oxide/electrolyte interface. Different models have been proposed to describe the growth of oxide layers on the surface of metals and alloys, for example, the Cabrera-Mott model [5], the Fehlner-Mott model [6], the point defect model (PDM) of Macdonald [7], the general model proposed by Seyeux and Marcus [8][9].

I.2.2. Electrochemical aspects of passivity on stainless steels

Electrochemical analysis is widely used to study the reactivity and especially the corrosion resistance of alloys. In this part, we present electrochemical results obtained on Fe-Cr, Fe-Cr-Mo, Fe-Cr-Ni and Fe-Cr-Ni-Mo alloys to illustrate the influence of addition elements on the passivity of stainless steels.

a. Fe-Cr alloys

Potentiodynamic polarization is a method widely used for characterizing the electrochemical properties and passivity. Figure I-5 presents typical potentiodynamic polarization curves obtained on Fe-Cr alloys [10].

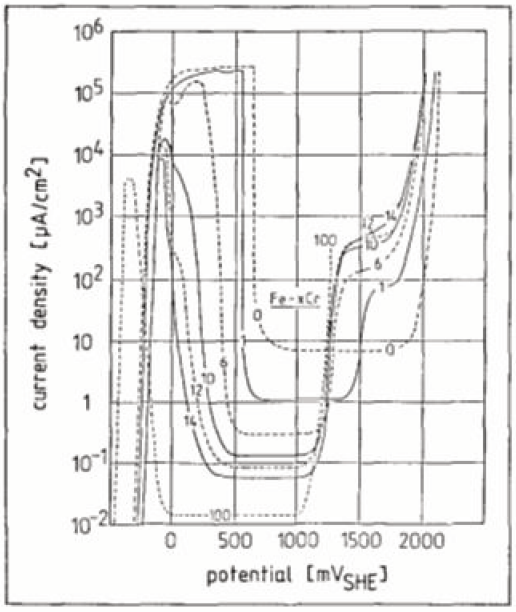

Figure I-5 Potentiodynamic polarization curves of Fe-xCr alloys in 0.5 M H_2SO_4 [10]

As seen in Figure I-5 presenting the anodic parts corresponding to the oxidative corrosion reactions, the curves start at the corrosion potential with a steep increase of current associated with the anodic dissolution of the alloy. Then the current reaches a peak of activation which represents the start of passivation. Then the decrease of current is associated with the formation of the passive film that slows down dissolution by several orders of magnitude. The plateau of residual currents corresponds to the passive domain. At higher potential, the re-increase of the current marks the entry in the transpassive region where the passive film is unstable. Many authors reported the similar polarization curves for stainless steels, see e.g. [11][12][13][14][15][16][17].

Such curves allow comparing the corrosion resistance of different alloys. For example, in Figure I-5, the Fe-Cr alloys with a higher chromium content have lower passivation potentials and passive currents. This confirms that the increasing addition of Cr improves the passivity of the Fe-Cr alloy.

Potentiostatic polarization is another technique often used to compare the electrochemical properties of different alloys. Figure I-6 shows the potentiostatic polarization curves of Fe-Cr alloys with different ratio of chromium. Several studies have reported the same type of potentiostatic polarization curves, see e.g. [13][18][19].

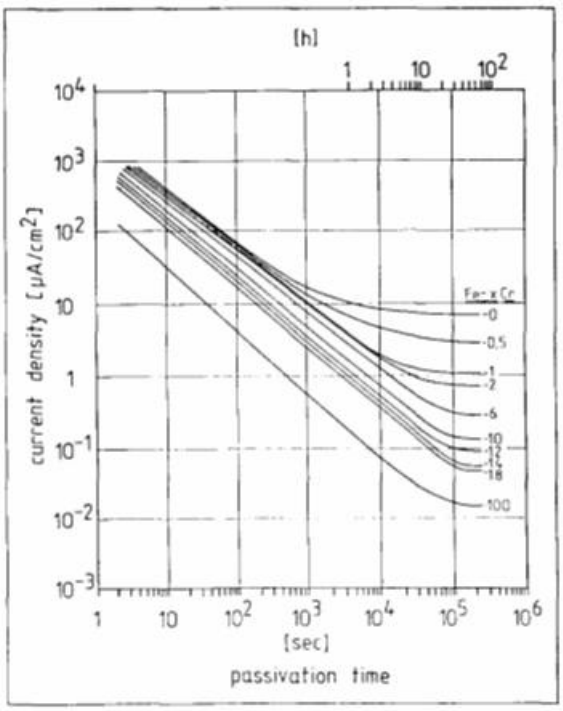

Figure I-6 Potentiostatic polarization curves of the Fe-Cr alloys in 0.5M H_2SO_4 [10]

In Figure I-6, the passivation current decreases with time due to formation of an increasingly protective passive film until reaching steady state. With chromium increase, the passivation current decreases showing improved passivity properties. This also confirms the improved corrosion resistance of Fe-Cr alloy obtained with higher chromium content.

These electrochemical studies clearly show that chromium has a positive effect on the corrosion resistance of Fe-Cr alloys.

b. Fe-Cr-Mo alloy

Starting from an Fe-Cr alloy, the addition of other elements can modify the property of passivity, which can be characterized also by electrochemical analysis. Molybdenum is one of the addition elements that improves the corrosion resistance of stainless steel, as shown by the potentiodynamic polarization curves presented in Figure I-7 [20].

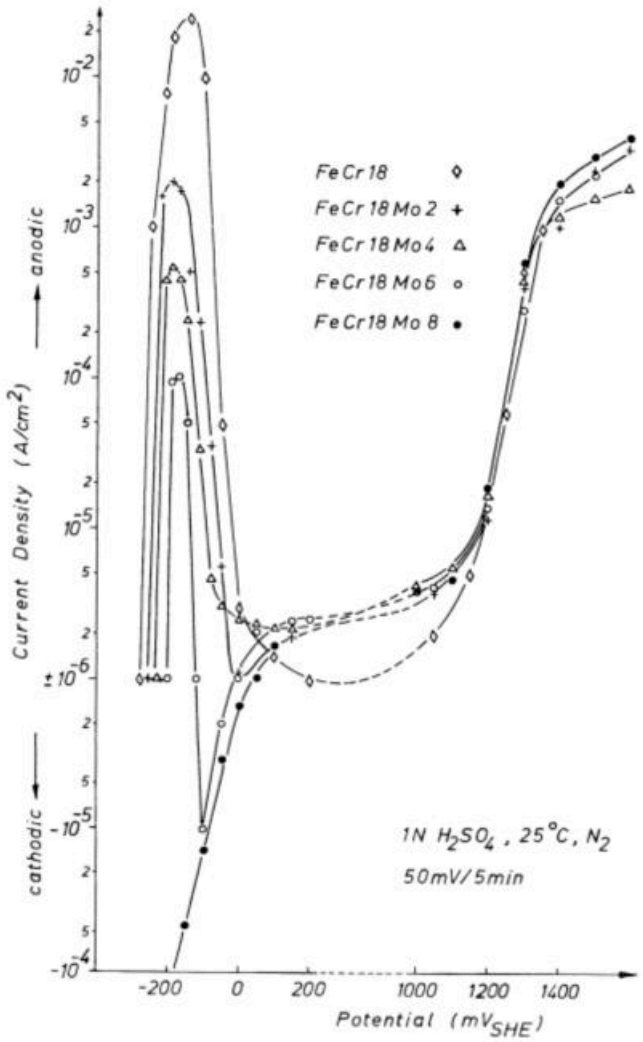

Figure I-7 Potentiodynamic polarization for Fe-18Cr-xMo alloys in 0.5 M H_2SO_4 [20]

It can be seen that, with the same Cr content, a higher Mo ratio increases the corrosion potential and decreases the passivation potential and current. It also broadens the passive region and shrinks the active region. Thus Mo facilitates the passivation process. No effect is observed on the transpassive potential. These effects have also been observed in other studies, see e.g. [11][12][21][22][23]. For a high Mo content of at 8%, there is no more an activation peak, as also observed in other studies [25][24].

Potentiostatic polarization curves showing the effect of Mo addition in Fe-Cr alloys are presented in Figure I-8 [18].

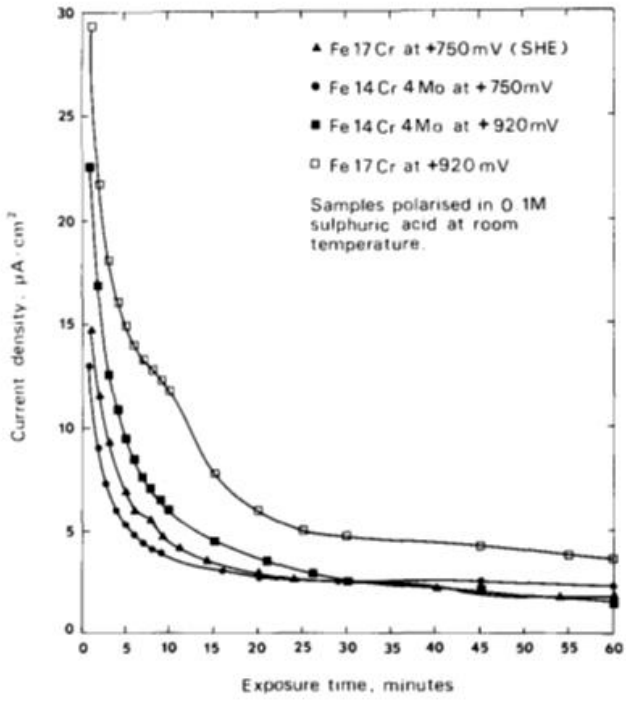

Figure I-8 Potentiostatic polarization curves for Fe-Cr alloy and Fe-Cr-Mo alloys in 0.1 M H_2SO_4 [18]

It is clearly seen that the decrease of the passivation current is faster with the addition of Mo in the Fe-Cr alloy, especially at +920 mV/SHE, which confirms that Mo promotes the passivation process. Other studies confirm this observation [22].

c. Fe-Cr-Ni alloy

Beside molybdenum, nickel is also an element often added into Fe-Cr alloys not only to stabilize the austenitic structure but also to improve the corrosion resistance. The influence of Ni addition is exemplified in Figure I-9 [19].

Compared to curve 1 for the Fe-17Cr alloy Figure I-9 (a), curve 3 for the Fe-Cr-Ni alloy (304 SS) exhibits a much higher corrosion potential, a lower active current and a lower passive current. No remarkable difference of the transpassive potential is observed. Compare to curve 2 for the Fe-15Cr-4Mo alloy, curve 1 and 3 show the same effects, evidencing that the addition of Ni has the similar effect as the addition of Mo but is much more efficient.

This is confirmed by the polarization curves in Figure I-9 (b) that also show that the Fe-18.5Cr-9.6Ni alloy has the lowest passivation current compared to the Fe-17Cr and Fe-15Cr-4Mo alloys.

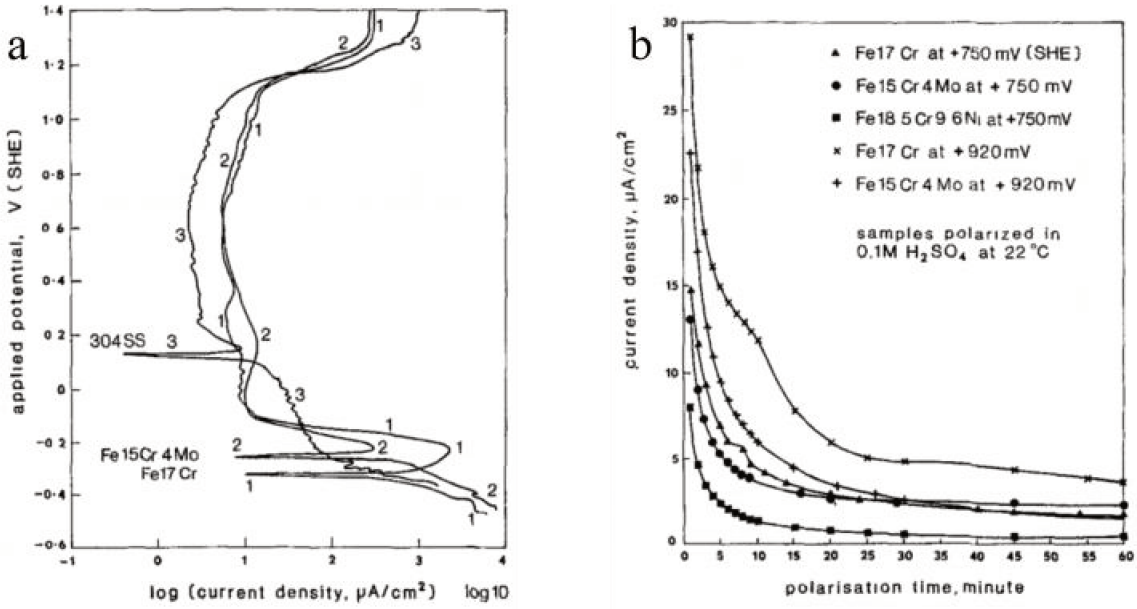

Figure I-9 Potentiodynamic (a) and Potentiostatic (b) polarization curves for Fe-Cr, Fe-Cr-Mo and Fe-Cr-Ni alloys in 0.1 M H_2SO_4 [19]

d. Fe-Cr-Ni-Mo alloy

Both Ni and Mo have a beneficial effect on the corrosion resistance of stainless steel. The combination of these two addition elements, such as in the commonly used 316 stainless steel, provides superior corrosion resistance. This is shown in Figure I-10 that compares potentiodynamic polarization curves obtained in 1 N HCl for Fe-20Cr-25Ni-xMo alloys with x ranging from 0 to 5. The increase of Mo increases the corrosion potential and decreases the passivation potential and passivation current, like observed for Fe-Cr-Mo alloys. The increase of Mo ratio also broadens remarkably the passive region. Not only the addition of Mo facilitates the passivation process in the quite aggressive Cl-containing solution but it also improves the resistance to the breakdown of passivity and initiation of localized corrosion. Several studies confirmed this conclusion, see e.g. [25][26][27][28][29].

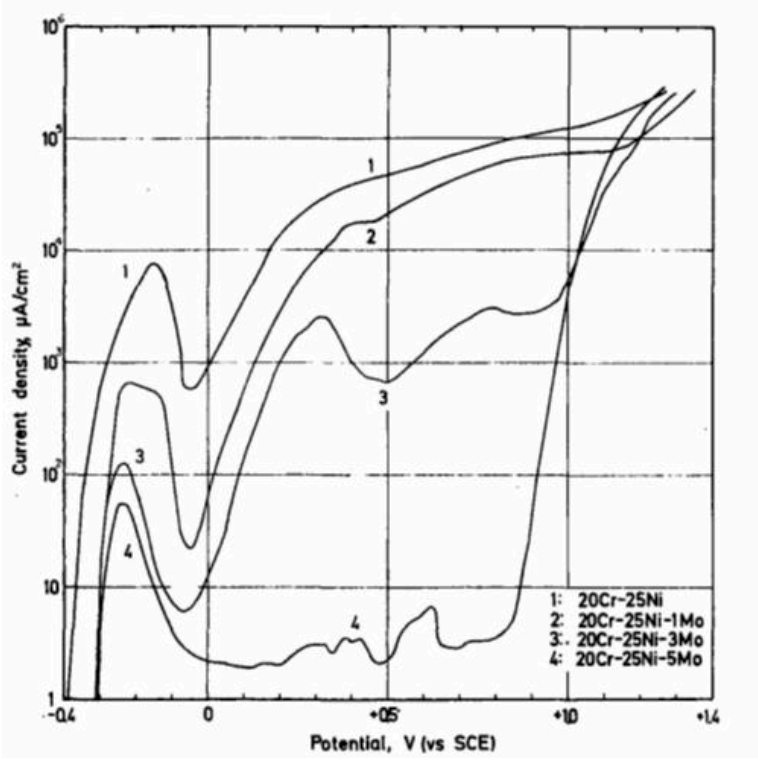

Figure I-10 Potentiodynamic polarization curves of Fe-Cr-Ni and Fe-Cr-Ni-Mo alloys in 1 N HCl [11]

I.2.3. Composition and duplex structure of passive films on stainless steels

As we know, the properties of the passive film and thus the corrosion resistance of passivable metals and alloys are governed by their composition and structure. Several surface analytical techniques can be applied to seek this information. X-ray Photoelectron Spectroscopy (XPS) and Auger Electron Spectroscopy (AES) can be used to measure the surface composition, and XPS to identify the surface chemical species and quantify their concentrations. Among other techniques, Time of Flight Secondary Ion Mass Spectrometry (ToF-SIMS) is quite powerfull to seek the variations of the elemental composition with depth and the eventual stratification of the chemical structure of the surface oxide. Scanning Tunnelling Microscopy (STM) and Atomic Force Microscopy (AFM) provide topographic information of the topmost surface at the nanometer scale and atomic scale in the most favorable cases. These methods are often used in combination with electrochemical analysis.

In the following, the composition and structure of passive films obtained from surface analysis are presented.

a. Fe-Cr alloy

For binary Fe-Cr alloys, even though there are only two principal elements, the composition of the passive film may not be simple.

XPS result shows that chromium is present in the trivalent valence state Cr(III) but the formed species would depend on the treatment of the surface. Several studies reported a $CrO_x(OH)_{3-2x}\cdot nH_2O$ composition after electrochemical polarization in acidic solution [21][22][30], with x and n depending on the sample composition and polarization conditions. Marcus and Olefjord reported that chromium hydroxide would become the principal Cr^{3+} species after electrochemical polarization in acidic solution [27]. After electrochemical polarization at a potential higher than the transpassive potential, chromium is in the hexavalent state Cr(VI) [10].

For iron, some authors reported both the divalent Fe(II) and trivalent Fe(III) states to be present at the same time [10][14][15][21][22][27][30][31], but others observed only iron as Fe^{3+} [17][32]. The valence state of iron would depend on the electrochemical polarization conditions, the Fe(III) state being only detected after a very long passivation time (> 24 h) [14][15].

The structure of the film is not simple either. A duplex structure has been proposed with an inner region mixing Fe(III) and Cr(III) oxides and enriched in chromium and an outer region of Cr(III) hydroxide [17]. Other studies also reported a duplex structure but with an inner region also mixing Fe(III) and Cr(III) oxides and enriched in chromium but with the outer region consisting of iron oxide instead of chromium hydroxide [33]. The main difference lies in the outer region of the film and might arise from the different passivation conditions. The work of Maurice et al [17] was performed in acidic solution (0.5 M H_2SO_4) where iron oxide preferentially dissolves and that of Hakiki et al [33] in a buffer solution (0.05 M H_3BO_3 + 0.075 M $Na_2B_4O_7\cdot 10\ H_2O$) where iron oxide is more stable.

The thickness of the film is reported in the range 1-3 nm in acidic solution, but several parameters have an influence. Castle and Qiu reported that, in acidic solution, a higher polarization potential and a longer passivation time induces a higher thickness [18][34]. In alkaline solution, the passive film is often thicker than in acidic solution, because dissolution has less impact in alkaline solution [35].

b. Fe-Cr-Mo alloy

The addition of Mo in a ferritic Fe-Cr alloy has two main effects on the passive film: it impacts the Cr content and Mo is present in the film.

Several studies reported that the main component of the passive film on Fe-Cr-Mo alloys remains chromium (hydr)oxide, but the addition of Mo would promote the Cr enrichment in the passive film [18][19][23][34]. According to Marcus and Olefjord, the addition of Mo has no significant influence on the Cr enrichment [27]. The presence of Mo in the passive film has been confirmed by many authors but there are different points of view. Some authors reported that Mo is enriched in the passive film after passivation in acidic solution [23] [36]. Other studies reported no enrichment [37].

Molybdenum is present in different valence states. Many studies reported the hexavalent state Mo(VI) [11][23][27][26][29][38][39][40][41][42], but the presence of the Mo(II) [29], Mo(III) [26], Mo(IV) [26][27][38] and Mo(V) [27][40] valence states has also been reported.

The presence of Mo does not modify the duplex structure of the passive film [27][43]. Also, Mo does not influence signicantly the thickness of the passive film [27][37][40].

c. Fe-Cr-Ni alloy

The presence of Ni in austenitic Fe-Cr-Ni stainless steels has very little influence on the passive film.

The composition of the passive film is similar to that on Fe-Cr alloys, and also enriched in chromium (hydr)oxides. Some authors reported that there is no Ni oxide present in the passive film [23][24][44][45]. Other researchers observed the presence of Ni oxide in the passive film but only at trace level [19][46]. Hashimoto et al explain that this is due to Ni being less reactive than Fe and Cr it is more difficult to oxidize Ni than Fe and Cr [40], which is in agreement with thermodynamic predictions based on the standard Gibbs energies of oxide formation ($\Delta_f G_m°(Cr_2O_3(s))$=-1058.1 kJ·mol^{-1}, $\Delta_f G_m°(Fe_2O_3(s))$=-714.0 kJ·mol^{-1}, $\Delta_f G_m°(NiO(s))$=-211.7 kJ·mol^{-1}).

The duplex structure of the passive film of Fe-Cr-Ni alloys is also unchanged compared to that on Fe-Cr alloys. However, the addition of Ni impacts the composition of the modified alloy region underneath the passive film. Many authors agree that Ni is enriched in this modified alloy region film [10][19][23][24][44][45]. In the work of Castle and Qiu, the Ni enrichment was not detected after 1 hour of passivation but becomes detectable after a

passivation time of 69 hours. The Ni enrichment is the result of the selective oxidation of Fe and Cr for the growth of the passive film.

The thickness of the passive film is also in the range of 1-3 nm [17][24]. with no significant influence of the addition of Ni in the alloy.

d. Fe-Cr-Ni-Mo alloy

Fe-Cr-Ni-Mo alloys can be considered as a combination of the Fe-Cr-Mo and Fe-Cr-Ni alloys. The main components of the passive film remain Cr oxide and Fe (hydr)oxides.

With Mo present in the austenitic Fe-Cr-Ni alloy, the passive film also includes Mo oxide like on the Fe-Cr-Mo alloy. The main valence state is Mo(VI) [23][24][26][39][41][42]. Some studies reported that Mo(VI) is present as MoO_4^{2-} [52], but others reported Mo(VI) present as MoO_3 [47][48]. According to Pardo et al [47][48], Mo(IV) can be found for passivation in acidic solution, but the presence of Mo(VI) is independent of the pH of the solution. Ni oxide is only present in trace quantity in the passive film when detected, like for Fe-Cr-Ni alloys [23][41][42][49]. The enrichment of Ni in the modified alloy region underneath the passive film has also been reported for Fe-Cr-Ni-Mo alloys [23][24].

The duplex structure of the passive film is similar to that on Fe-Cr-Mo alloys. Researchers agree that the inner part is enriched in Cr(III) oxide [23][24][41][42][49][50][53][54]. The outer part is a mix of iron and chromium (hydr)oxides depending on the conditions of passivation [23][24][41][42][54]. Some studies reported that Mo is principally in the outer part of the passive film [24][47][48][52][54]. The duplex model proposed by Maurice et al for a model single crystal Fe-17Cr-14.5Ni-2.3Mo (100) surface is presented in FigureI-11 [54]. According to their work, the inner layer essentially consists of Cr(III) oxide and the outer layer of Fe(III) (hydr)oxide. Mo would be in the inner layer of the native oxide film formed in air and Mo would become enriched in the outer layer of the film after passivation in sulfuric acid.

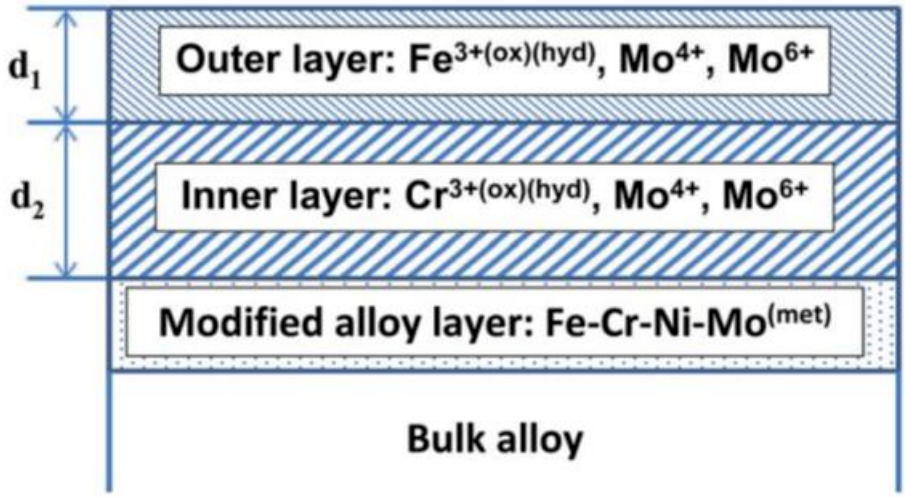

Figure I-11 Model of duplex structure proposed for the passive film on single crystal Fe-17Cr-14.5Ni-2.3Mo (100) surface [54]

The thickness of the passive film on Fe-Cr-Ni-Mo alloys is also in the range 1-3 nm [41][42][54], showing no impact of the presence of Mo and Ni.

I.3. Corrosion of stainless steel

Passive films on stainless steels are in principal compact and protective and form a physical barrier isolating the substrate from the environment. In case of local breakdown, generated by a mechanical event, for example a scratch, or due to local chemical instability, the passive film has, in general, the ability to reform through a process called repassivation. Nevertheless, in most aggressive environments, the stability of the passive film and its ability to self-repair may be compromised, which may result in localized corrosion processes.

I.3.1. Mechanism of corrosion

Here we concentrate on aqueous corrosion. Other types of corrosion such as high temperature corrosion will not be discussed. Corrosion reactions are redox reactions which contain anodic and cathodic counterparts. In aqueous corrosion, the anodic reactions imply the metal which is the principal element giving electrons and gets oxidized to produce metallic cations. The reaction can be expressed as:

$$M \rightarrow M^{n+} + ne^{-} \qquad \text{eq.I-4}$$

The metallic cation formed by eq. I-4 becomes a corrosion product via different reactions such as:

$$M^{n+} + nH_2O \rightarrow M^{n+}(H_2O)_n \quad \text{eq. I-5}$$

$$M^{n+} + \frac{n}{2}H_2O \rightarrow MO_{\frac{n}{2}} + nH^+ \quad \text{eq. I-6}$$

$$M^{n+} + nH_2O \rightarrow M(OH)_n + nH^+ \quad \text{eq. I-7}$$

As we can see from these equations, the corrosion product can be a complex, an oxide or a hydroxide depending on the environment.

At free potential, i.e. in the absence of applied polarization, these anodic processes of oxidation require that the electrons that are produced are consumed by a cathodic reaction. Any oxidant present in solution can be reduced. Typical examples of cathodic reactions are the reduction of dissolved oxygen and reduction of H^+/H_2O:

$$O_2 + 2H_2O + 4e^- \rightarrow 4OH^- \quad \text{eq. I-8}$$

$$O_2 + 4H^+ + 4e^- \rightarrow 2H_2O \quad \text{eq. I-9}$$

$$2H^+ + 2e^- \rightarrow H_2 \quad \text{eq. I-10}$$

Eq. I-8 is the reaction in neutral or basic environment, eq. I-9 and eq. I-10 are reactions in acidic environment where eq. I-9 is the reaction in presence of oxygen and eq. I-10 the reaction in the absence of oxygen.

I.3.2. The different types of corrosion

In the real world, different types of corrosion such as general corrosion and localized corrosion can take place depending on material and environmental conditions. These different types of corrosion are presented in the following.

a. General corrosion

General corrosion is a uniform degradation of the material by dissolution at any point of the surface, as opposed to other forms of corrosion that are localized. In this case, anodic and cathodic sites are very close and randomly distributed on the surface. This phenomenon is translated on a macroscopic scale by a loss of thickness in function of time, which corresponds to the rate of corrosion. The unit of the corrosion rate can be expressed as mm/year. For stainless steels, this type of corrosion can happen in very extreme environments

like very acidic environment where the passive film is not stable. General corrosion can be detected by measuring the time evolution of the thickness of the material.

b. Galvanic corrosion

Galvanic corrosion occurs when two metals with different activity are in electric contact in an electrolyte. It is typical of the functioning of an electrochemical battery. In this case, most of the active metal will be attacked (anode) while the less active metal will be protected (cathode). Galvanic corrosion is aggravated if the area of the cathode surpasses by far the area of the anode. This type of corrosion can be avoided by many methods such as decreasing the area of the cathode. This type of corrosion can be used voluntarily to protect a metal (the cathode) by sacrificing with an active anode. Galvanic corrosion happens often on duplex stainless steels due to the galvanic coupling between two phases which leads to the preferential dissolution of one phase. This type of corrosion depends on the potential applied, the composition of the medium and the composition of each phase. Single phase stainless steels are less sensitive to galvanic corrosion.

c. Stress corrosion cracking

Stress corrosion cracking is an extremely dangerous type of corrosion. It happens in corrosive environment on a material subject to tensile forces, either residual or directly applied. It is characterized by the appearance of cracks propagating perpendicular to stress, along grain boundaries (intergranular cracking) or through grains (transgranular cracking) [55]. Austenitic stainless steels are sensitive to this type of corrosion due to their face-centered cubic structure that favors planar deformation and can generate local stress concentrations.

d. Crevice corrosion

Cavernous corrosion occurs in confined areas. These confined spaces are generally called crevices, where exchanges of component with the outside environment is limited. In particular, the dissolved oxygen content decreases over time, resulting in differential aeration between the crevice (anode) and the outside environment (cathode) which is also called a concentration cell. Moreover, the concentration of cations increases in the cavern, and their hydrolysis leads to severe acidification of the medium. If the pH falls below the pH of depassivation, a mechanism similar to generalized corrosion takes place in the cavern. Moreover, to respect the electroneutrality, anions such as chloride ions migrate within the cavern, which may further generate pitting corrosion. To prevent this form of corrosion, the design of the parts

must be optimized so as to avoid caverns. Also regular flushing of the equipment is also possible to allow a renewal of the environment.

e. Intergranular corrosion

On stainless steels, intergranular corrosion is most often related to chromium carbides or secondary phases precipitated at the grain boundaries. The formation of chromium precipitates locally depletes chromium in the surrounding alloy matrix, which favors passivity breakdown and poisons repassivation in this region. Intergranular corrosion can be interpreted as a galvanic coupling between the precipitates (cathode) and the zone depleted in chromium (anode). This type of corrosion happens in very oxidative environment or at high potentials . Decreasing the carbon content is a good method to avoid this type of corrosion. Examples in industry is the 304L and 316L SS grades in which the carbon quantity is lower than in 304 and 316 SS grades.

f. Pitting corrosion

Pitting corrosion is a form of localized corrosion that usually occurs in neutral media in the presence of aggressive ions such as halogen ions or sulfur species. Localized corrosion by pitting is a major problem that can be encountered in metals and alloys protected by a passive layer. Indeed, this mode of corrosion starts at a very small scale (atomic or nanometric) at which the attack remains invisible, and then develops until it appears at the microscopic and macroscopic scale. It then becomes extremely difficult to fight against pit propagation.

ⅰ） Pitting initiation mechanism

Three main mechanisms have been proposed for passivity breakdown induced by the interaction with aggressive ions such as chlorides. They focus on passive film penetration by the chlorides, chloride adsorption, or film breaking and poisoning of self-repair by chlorides [56]. The schematic view of these three mechanisms is presented in Figure I-12.

The first step of this mechanism is the adsorption of chloride ions on the surface of the passive layer. This surface is covered by a hydroxyl layer so the adsorption of the chloride ions occurs by replacing the adsorbed OH. This requires the concentration of chlorides in the solution to be sufficiently high, that the adsorbed chlorides are more stable than the adsorbed OH and that the replacement kinetics be fast enough[57].

The penetration mechanism for pit initiation (Figure I-12a) involves the transport of the aggressive anions through the passive film to the metal/oxide interface where aggressive dissolution is promoted. Some authors reported the observation of chloride ions in the passive film during the passivation in electrolyte with chloride [29][58]. These observation support the penetration mechanism. But other authors did not find any evidence of chlorides in passive films [59][60].

The adsorption mechanism (Figure I-12b) is based on the notion of competitive adsorption of chloride ions and oxygen. Strehblow reported the presence of chloride during passivation enhanced the transfer of cations from the oxide to the electrolyte even without the formation of pit corrosion. This phenomena would make the film thinner [60]. When thinning occurs locally because of some local adsorbed species, the local electric field strength will increase, which may eventually lead to complete breakdown and the formation of a pit nucleus. But other studies reported that there was no difference in oxide thickness on Fe samples prepassivated in borate solution and then galvanostatically anodized at 5 $\mu A/cm^2$ in solutions with or without Cl^- [59].

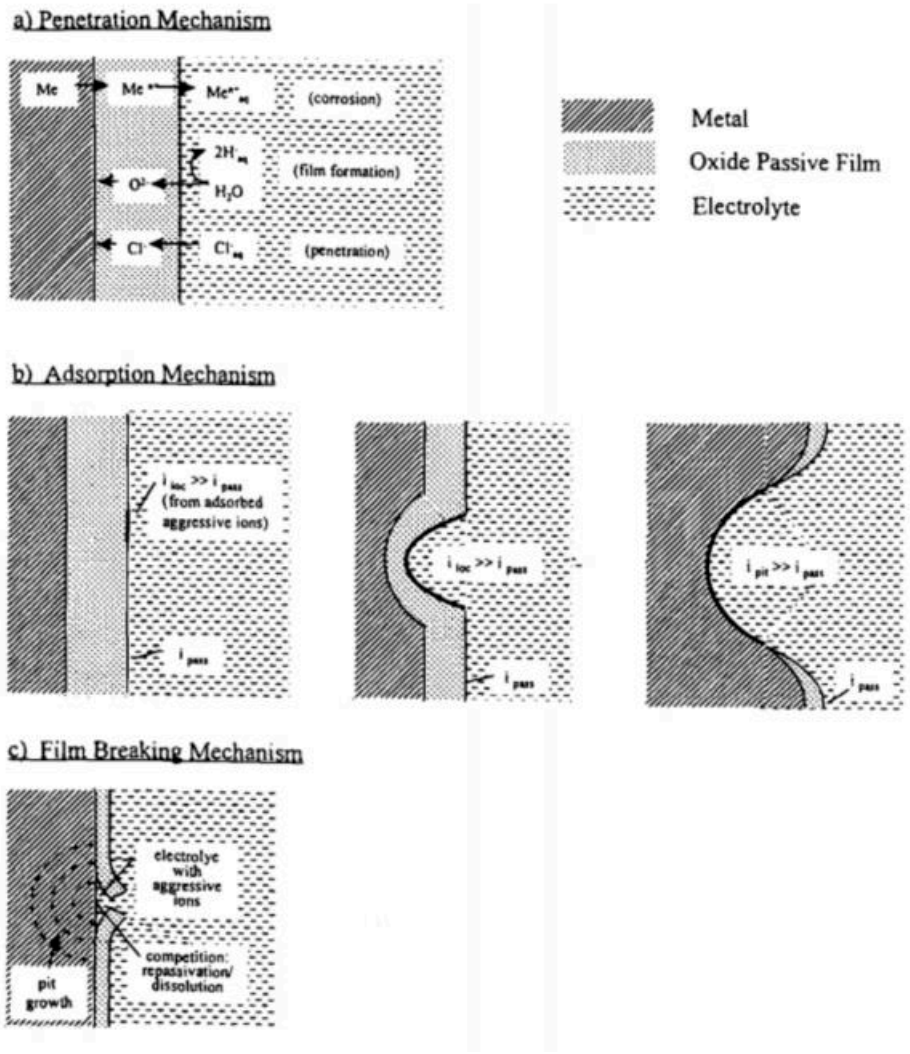

Figure I-12 Schematic view of three mechanism of pitting corrosion [56]

The film-breaking mechanism (Figure I-12c) considers that the thin passive film is in a continual state of breakdown and repair. The breakdown of the passive film might be due mechanic stress or attack of aggressive ions by one of the mechanisms mentioned above. The breakdown can be repaired by repassivation of the surface. This phenomena can be detected by electrochemical measurements since associated with a special type of current transient presented in Figure I-13 [61]. The current transient starts with a slow increase of current corresponding to the breakdown of the passive film and the creation of the pit nucleus; a sudden shut down of current follows corresponding to the self-repair of the passive film. The pits formed with this type of current transient are called metastable pits. Many authors confirmed this observation [62][64][65][66].

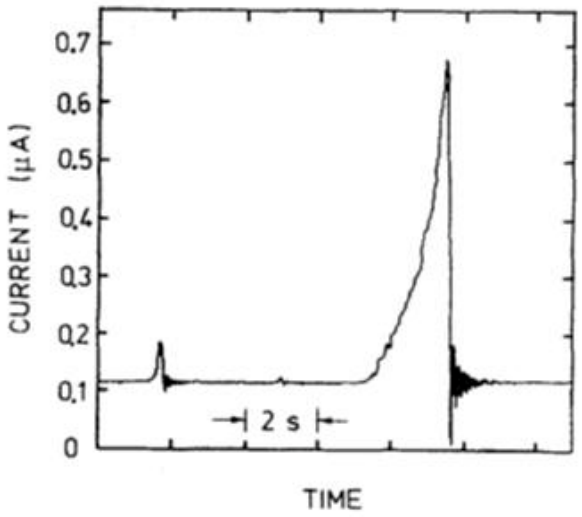

Figure I-13 Typical current transients for metastable pitting corrosion [61]

ii) Parameters influencing the pitting corrosion

Many parameters influence the process of pitting corrosion. These parameters can be classified in two groups associated to the material or to the environment.

Marcus has discussed the influence on pitting corrosion of different addition elements in the alloy [67]. Two categories of alloying elements that promote the passivation process has been distinguished (Figure I-14). On the one hand, the passivation promoters are characterized by a high heat (enthalpy) of oxygen adsorption combined with a relatively low metal-metal bond strength. Thus the metal bonds can break easily and nucleation and growth the passive film is favored. Examples of passivation promoters are chromium, aluminum and titanium. On the other hand, moderators or blockers of dissolution are characterized by a high heat (enthalpy) of oxygen adsorption and a relatively high metal-metal bond strength. Thanks to their high oxygen adsorption heat, these elements may also participate in the passivation and be incorporated in the passive film. Examples of moderators or dissolving blockers are molybdenum, niobium, tantalum and tungsten. The moderators, especially molybdenum, improve the pitting corrosion resistance. Some studies reported an effect of blocker of dissolution [7][11][23][26][28][29][34][38][47][48][68], and some studies, sometimes the same, reported an effect of (re)passivation promoter [21][23][39][41][28][47][48][68][69].

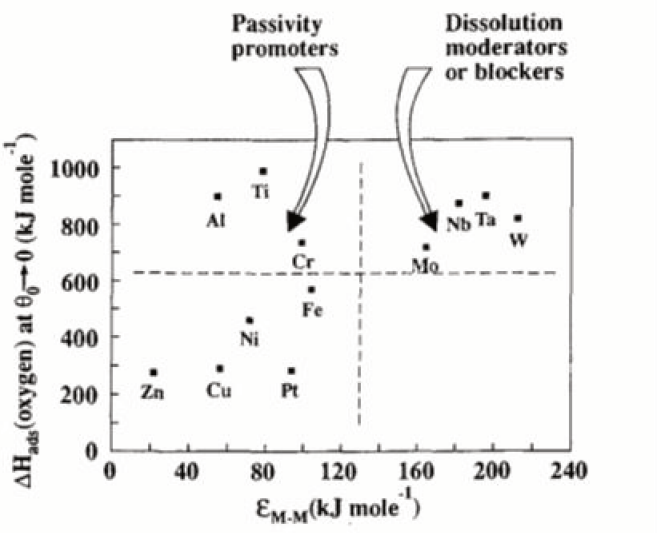

Figure I-14 Passivity promoters and dissolution moderators according to the synergy between the heat of adsorption of oxygen and the ease in the disruption of metal-metal bond [67]

Besides surface composition, another property influencing pitting corrosion is the surface roughness. Some studies conclude that decreasing the roughness increases the resistance to pitting corrosion [70][71][72].

The environment also influences the pitting corrosion. It is well known that increasing the concentration of aggressive ions such as chloride will favor the pitting corrosion, recent observations still prove this observation [73][74]. Besides chlorides, the presence of other ions such as sulfur ions may favor pitting corrosion [75], while some other ions such as molybdates and tungstates can behave as an inhibitor and mitigate pitting corrosion [76]. Other parameters of the environment such as temperature also influence pitting corrosion, a higher temperature increasing the possibility to create a pit [65].

g. Other types of corrosion

There are also other types of corrosion. Corrosion-cavitation is due to the implosion of gas bubbles on the surface in a fluid flowing at high speed and subjected to pressure variations. These implosions can destroy the passive film. Corrosion-erosion is linked to the movement of a more or less corrosive fluid that tears mechanically the passive film. Bio-corrosion is influence by the presence of microorganism that can destabilize the passive film.

I.4. Objectives of the thesis

In the first part of this chapter, the basic knowledge about the passivity and the properties of the passive film on stainless steel has been introduced. The electrochemical aspects show that the addition of different elements such as Ni and Mo improve remarkably the corrosion resistance. Then the composition and duplex structure of passive films obtained in acid or alkaline aqueous solutions have been presented. Most studies show that the passive film formed in acid solution provides good corrosion resistance. But as we know, stainless steel surfaces are already covered in air by a so-called native oxide film. In most studies, a cathodic reduction treatment is applied in order to remove this air-formed native oxide however without proper characterization of the surface state after pretreatment, so that the passive film is produced starting from a surface state possibly reproducible but not well-defined. The alterations brought by well-controlled electrochemical passivation to an air-formed native oxide are rarely discussed in passivation studies, although the pre-passive state formed by the native oxide-covered surface may largely influence the properties of the passive film.

The first objective of this thesis was to study in details the transition from native oxide-covered surface state to passive surface state on 316L stainless steel, and in particular the mechanisms of Cr and Mo enrichments that are key aspects of the passivity of Mo-bearing austenitic stainless steels. The results obtained on this part of the work are presented in chapter III and chapter IV.

In the second part of the present chapter, the different types of corrosion of stainless steels were introduced with a focus on the initiation of localized corrosion by pitting. Many studies addressed metastable pitting considering it as the initiation stage of pitting corrosion. But the metastable pits formed in these studies are most often of micrometric scale dimensions, which can be considered as far beyond passivity breakdown. On stainless steels, only electrochemical studies have been done on metastable pitting at nanometric scale, which can be considered as closer to the real initiation stage of localized corrosion by pitting [62][63]. However, to our knowledge, none of the studies applied surface analytical techniques to characterize the chloride-induced alterations of the passive state at this initial stage of pitting corrosion.

The second objective of this thesis was thus to study how chlorides added in the electrolyte alter the passive state at a stage preceding metastable pitting at the micrometer scale and how these alterations can be impacted by pre-passivation of the surface in a chloride-free electrolyte. The results obtained on this part of the work are presented in chapter V.

In order to reach these objectives, surface analysis using spectroscopic methods such as XPS, ToF-SIMS and Photo-Current Spectroscopy (PCS) were applied in combination with electrochemical analysis.

.

Reference

1. ISSF Stainless Steel in Figures http://www.worldstainless.org/Files/issf/non-image-files/PDF/ISSF_Stainless_Steel_in_Figures_2019_English_public_version.pdf
2. H. M. Cobb, The history of stainless steel, ASM International (2010)
3. P. Monnartz, Iron-chromium alloys with special consideration of resistance to acids, Metallurgie 8 (1911) 161–176.
4. B. Baroux, Le phénomène de passivité, in La corrosion des métaux – Passivité et corrosion localisée, Collection : Technique et Ingénierie, Dunod, Paris (2014) 119–138.
5. N. Cabrera, N. F. Mott, Theory of the oxidation of metals, Reports on Progress in Physics 12 (1948) 163–184.
6. F.P. Fehlner, N.F. Mott, Low-temperature oxidation, Oxid Met. 2 (1970) 59–99. doi:10.1007/BF00603582.
7. D.D. Macdonald, The Point Defect Model for the Passive State, J. Electrochem. Soc. 139 (1992) 3434–3449. doi:10.1149/1.2069096.
8. A. Seyeux, V. Maurice, P. Marcus, Oxide Film Growth Kinetics on Metals and Alloys I. Physical Model, J. Electrochem. Soc. 160 (2013) C189–C196. doi:10.1149/2.036306jes.
9. K. Leistner, C. Toulemonde, B. Diawara, A. Seyeux, P. Marcus, Oxide Film Growth Kinetics on Metals and Alloys II. Numerical Simulation of Transient Behavior, J. Electrochem. Soc. 160 (2013) C197–C205. doi:10.1149/2.037306jes.
10. R. Kirchheim, B. Heine, H. Fischmeister, S. Hofmann, H. Knote, U. Stolz, The passivity of iron-chromium alloys, Corrosion Science. 29 (1989) 899–917. doi:10.1016/0010-938X(89)90060-7.
11. K. Sugimoto, Y. Sawada, The role of molybdenum additions to austenitic stainless steels in the inhibition of pitting in acid chloride solutions, Corrosion Science. 17 (1977) 425–445. doi:10.1016/0010-938X(77)90032-4.
12. P. Marcus, M. Moscatelli, The Role of Alloyed Molybdenum in the Dissolution and the Passivation of Nickel-Molybdenum Alloys in the Presence of Adsorbed Sulfur, J. Electrochem. Soc. 136 (1989) 1634–1637. doi:10.1149/1.2096984.
13. S. Mischler, A. Vogel, H.J. Mathieu, D. Landolt, The chemical composition of the passive film on Fe-24Cr and Fe-24Cr-11Mo studied by AES, XPS and SIMS, Corrosion Science. 32 (1991) 925–944. doi:10.1016/0010-938X(91)90013-F.
14. W.P. Yang, D. Costa, P. Marcus, Chemical Composition, Chemical States, and Resistance to Localized Corrosion of Passive Films on an Fe-17%Cr Alloy, J. Electrochem. Soc. 141 (1994) 111–116. doi:10.1149/1.2054669.
15. W.P. Yang, D. Costa, P. Marcus, Resistance to Pitting and Chemical Composition of Passive Films of a Fe-17%Cr Alloy in Chloride-Containing Acid Solution, J. Electrochem. Soc. 141 (1994) 2669–2676. doi:10.1149/1.2059166.

16. S. Haupt, H.-H. Strehblow, A combined surface analytical and electrochemical study of the formation of passive layers on FeCr alloys in 0.5 M H2SO4, Corrosion Science. 37 (1995) 43–54. doi:10.1016/0010-938X(94)00104-E.

17. V. Maurice, W.P. Yang, P. Marcus, XPS and STM Study of Passive Films Formed on Fe-22Cr(110) Single-Crystal Surfaces, J. Electrochem. Soc. 143 (1996) 1182–1200. doi:10.1149/1.1836616.

18. J.E. Castle, J.H. Qiu, A co-ordinated study of the passivation of alloy steels by plasma source mass spectrometry and x-ray photoelectron spectroscopy—1. characterization of the passive film, Corrosion Science. 29 (1989) 591–603. doi:10.1016/0010-938X(89)90010-3.

19. J.E. Castle, J.H. Qiu, The Application of ICP-MS and XPS to Studies of Ion Selectivity during Passivation of Stainless Steels, J. Electrochem. Soc. 137 (1990) 2031–2038. doi:10.1149/1.2086860.

20. M.B.Rockel, The Effect of Molybdenum on the Corrosion Behavior of Iron-Chromium Alloys, CORROSION. 29 (1973) 393–396. doi:10.5006/0010-9312-29.10.393.

21. K. Hashimoto, K. Asami, K. Teramoto, An X-ray photo-electron spectroscopic study on the role of molybdenum in increasing the corrosion resistance of ferritic stainless steels in HC1, Corrosion Science. 19 (1979) 3–14. doi:10.1016/0010-938X(79)90003-9.

22. K. Hashimoto, K. Asami, An X-ray photo-electron spectroscopic study of the passivity of ferritic 19Cr stainless steels in 1 NHCl, Corrosion Science. 19 (1979) 251–260. doi:10.1016/0010-938X(79)90010-6.

23. I. Olefjord, The passive state of stainless steels, Materials Science and Engineering. 42 (1980) 161–171. doi:10.1016/0025-5416(80)90025-7.

24. E. De Vito, P. Marcus, XPS study of passive films formed on molybdenum-implanted austenitic stainless steels, Surf. Interface Anal. 19 (1992) 403–408. doi:10.1002/sia.740190175.

25. M. Bojinov, G. Fabricius, T. Laitinen, K. Mäkelä, T. Saario, G. Sundholm, Influence of molybdenum on the conduction mechanism in passive films on iron–chromium alloys in sulphuric acid solution, Electrochimica Acta. 46 (2001) 1339–1358. doi:10.1016/S0013-4686(00)00713-1.

26. C.R. Clayton, Y.C. Lu, A Bipolar Model of the Passivity of Stainless Steel: The Role of Mo Addition, J. Electrochem. Soc. 133 (1986) 2465–2473. doi:10.1149/1.2108451.

27. P. Marcus, I. Olefjord, A Round Robin on combined electrochemical and AES/ESCA characterization of the passive films on Fe-Cr and Fe-Cr-Mo alloys, Corrosion Science. 28 (1988) 589–602. doi:10.1016/0010-938X(88)90026-1.

28. R. f. a Jargelius-Pettersson, Electrochemical investigation of the influence of nitrogen alloying on pitting corrosion of austenitic stainless steels, Corrosion Science. 41 (1999) 1639–1664. doi:10.1016/S0010-938X(99)00013-X.

29. L. Wegrelius, F. Falkenberg, I. Olefjord, Passivation of Stainless Steels in Hydrochloric Acid, J. Electrochem. Soc. 146 (1999) 1397–1406. doi:10.1149/1.1391777.

30. K. Asami, K. Hashimoto, S. Shimodaira, An XPS study of the passivity of a series of iron—chromium alloys in sulphuric acid, Corrosion Science. 18 (1978) 151–160. doi:10.1016/S0010-938X(78)80085-7.

31. P. Keller, H.-H. Strehblow, XPS investigations of electrochemically formed passive layers on Fe/Cr-alloys in 0.5 M H2SO4, Corrosion Science. 46 (2004) 1939–1952. doi:10.1016/j.corsci.2004.01.007.

32. C. Calinski, H.-H. Strehblow, ISS Depth Profiles of the Passive Layer on Fe/Cr Alloys, J. Electrochem. Soc. 136 (1989) 1328–1331. doi:10.1149/1.2096915.

33. N.B. Hakiki, S. Boudin, B. Rondot, M. Da Cunha Belo, The electronic structure of passive films formed on stainless steels, Corrosion Science. 37 (1995) 1809–1822. doi:10.1016/0010-938X(95)00084-W.

34. J.E. Castle, J.H. Qiu, A co-ordinated study of the passivation of alloy steels by plasma source mass spectrometry and x-ray photoelectron spectroscopy—II. growth kinetics of the passive film, Corrosion Science. 29 (1989) 605–616. doi:10.1016/0010-938X(89)90011-5.

35. C.-O.A. Olsson, D. Landolt, Passive films on stainless steels—chemistry, structure and growth, Electrochimica Acta. 48 (2003) 1093–1104. doi:10.1016/S0013-4686(02)00841-1.

36. C. Leygraf, G. Hultquist, I. Olefjord, B.-O. Elfström, V.M. Knyazheva, A.V. Plaskeyev, Ya.M. Kolotyrkin, Selective dissolution and surface enrichment of alloy components of passivated Fe18Cr and Fe18Cr3Mo single crystals, Corrosion Science. 19 (1979) 343–357. doi:10.1016/0010-938X(79)90026-X.

37. A.E. Yaniv, J.B. Lumsden, R.W. Staehle, The Composition of Passive Films on Ferritic Stainless Steels, J. Electrochem. Soc. 124 (1977) 490–496. doi:10.1149/1.2133335.

38. M.-W. Tan, E. Akiyama, A. Kawashima, K. Asami, K. Hashimoto, The effect of air exposure on the corrosion behavior of amorphous Fe-8Cr-Mo-13P-7C alloys in 1 M HCl, Corrosion Science. 37 (1995) 1289–1301. doi:10.1016/0010-938X(95)00035-I.

39. W. Yang, R.-C. Ni, H.-Z. Hua, A. Pourbaix, The behavior of chromium and molybdenum in the propagation process of localized corrosion of steels, Corrosion Science. 24 (1984) 691–707. doi:10.1016/0010-938X(84)90059-3.

40. K. Hashimoto, K. Asami, A. Kawashima, H. Habazaki, E. Akiyama, The role of corrosion-resistant alloying elements in passivity, Corrosion Science. 49 (2007) 42–52. doi:10.1016/j.corsci.2006.05.003.

41. I. Olefjord, B. Brox, U. Jelvestam, Surface Composition of Stainless Steels during Anodic Dissolution and Passivation Studied by ESCA, J. Electrochem. Soc. 132 (1985) 2854–2861. doi:10.1149/1.2113683.

42. I. Olefjord, B.-O. Elfstrom, The Composition of the Surface during Passivation of Stainless Steels, CORROSION. 38 (1982) 46–52. doi:10.5006/1.3577318.

43. F.D. Franco, A. Seyeux, S. Zanna, V. Maurice, P. Marcus, Effect of High Temperature Oxidation Process on Corrosion Resistance of Bright Annealed Ferritic Stainless Steel, J. Electrochem. Soc. 164 (2017) C869–C880. doi:10.1149/2.1851713jes.

44. L. Ma, F. Wiame, V. Maurice, P. Marcus, New insight on early oxidation stages of austenitic stainless steel from in situ XPS analysis on single-crystalline Fe–18Cr–13Ni, Corrosion Science. 140 (2018) 205–216. doi:10.1016/j.corsci.2018.06.001.

45. V. Maurice, W.P. Yang, P. Marcus, X‐Ray Photoelectron Spectroscopy and Scanning Tunneling Microscopy Study of Passive Films Formed on (100) Fe‐18Cr‐13Ni Single‐Crystal Surfaces, J. Electrochem. Soc. 145 (1998) 909–920. doi:10.1149/1.1838366.

46. A.R. Brooks, C.R. Clayton, K. Doss, Y.C. Lu, On the Role of Cr in the Passivity of Stainless Steel, J. Electrochem. Soc. 133 (1986) 2459–2464. doi:10.1149/1.2108450.

47. A. Pardo, M.C. Merino, A.E. Coy, F. Viejo, R. Arrabal, E. Matykina, Effect of Mo and Mn additions on the corrosion behaviour of AISI 304 and 316 stainless steels in H2SO4, Corrosion Science. 50 (2008) 780–794. doi:10.1016/j.corsci.2007.11.004.

48. A. Pardo, M.C. Merino, A.E. Coy, F. Viejo, R. Arrabal, E. Matykina, Pitting corrosion behaviour of austenitic stainless steels – combining effects of Mn and Mo additions, Corrosion Science. 50 (2008) 1796–1806. doi:10.1016/j.corsci.2008.04.005.

49. J. B. Lumsden and R. W. Staehle Application of Auger Electron Spectroscopy to the Determination of the Composition of Passive Films on Type 316 SS Scripta Metallurgica, 6, 1205-1208 (1972)

50. I. Olefjord, L. Wegrelius, Surface analysis of passive state, Corrosion Science. 31 (1990) 89–98. doi:10.1016/0010-938X(90)90095-M.

51. G. M. Bulman and A. C. C. Tseung An Ellipsometric Study of Passive Film Growth on Stainless Steel Corrosion Science, 13, 531-544 (1973)

52. Y.C. Lu, C.R. Clayton, Evidence for a Bipolar Mechanism of Passivity in Mo Bearing Stainless Steels, J. Electrochem. Soc. 132 (1985) 2517–2518. doi:10.1149/1.2113614.

53. N.E. Hakiki, M.D.C. Belo, A.M.P. Simões, M.G.S. Ferreira, Semiconducting Properties of Passive Films Formed on Stainless Steels Influence of the Alloying Elements, J. Electrochem. Soc. 145 (1998) 3821–3829. doi:10.1149/1.1838880.

54. V. Maurice, H. Peng, L.H. Klein, A. Seyeux, S. Zanna, P. Marcus, Effects of molybdenum on the composition and nanoscale morphology of passivated austenitic stainless steel surfaces, Faraday Discuss. 180 (2015) 151–170. doi:10.1039/C4FD00231H.

55. P. Kritzer, Corrosion in high-temperature and supercritical water and aqueous solutions: a review, The Journal of Supercritical Fluids. 29 (2004) 1–29. doi:10.1016/S0896-8446(03)00031-7.

56. G.S. Frankel, Pitting Corrosion of Metals A Review of the Critical Factors, J. Electrochem. Soc. 145 (1998) 2186–2198. doi:10.1149/1.1838615.

57. P. Marcus, V. Maurice, H.-H. Strehblow, Localized corrosion (pitting): A model of passivity breakdown including the role of the oxide layer nanostructure, Corrosion Science. 50 (2008) 2698–2704. doi:10.1016/j.corsci.2008.06.047.

58. P. Marcus, J.-M. Herbelin, The entry of chloride ions into passive films on nickel studied by spectroscopic (ESCA) and nuclear (36Cl radiotracer) methods, Corrosion Science. 34 (1993) 1123–1145. doi:10.1016/0010-938X(93)90293-P.

59. J.A. Bardwell, B. MacDougall, G.I. Sproule, Use of SIMS to Investigate the Induction Stage in the Pitting of Iron, J. Electrochem. Soc. 136 (1989) 1331–1336. doi:10.1149/1.2096916.

60. Strehblow, H.-H. Strehblow, in Corrosion Mechanisms in Theory and Practice, P. Marcus and J. Oudar, Editors, p. 201, Marcel Dekker, Inc., New York (1995)., (1995).

61. G.S. Frankel, L. Stockert, F. Hunkeler, H. Boehni, Metastable Pitting of Stainless Steel, CORROSION. 43 (1987) 429–436. doi:10.5006/1.3583880.

62. G.T. Burstein, P.C. Pistorius, S.P. Mattin, The nucleation and growth of corrosion pits on stainless steel, Corrosion Science. 35 (1993) 57–62. doi:10.1016/0010-938X(93)90133-2.

63. G.T. Burstein, S.P. Mattin, Nucleation of corrosion pits on stainless steel, Philosophical Magazine Letters. 66 (1992) 127 – 131. doi:10.1080/09500839208229274.

64. H. Böhni, T. Suter, A. Schreyer, Micro- and nanotechniques to study localized corrosion, Electrochimica Acta. 40 (1995) 1361–1368. doi:10.1016/0013-4686(95)00072-M.

65. N.J. Laycock, M.H. Moayed, R.C. Newman, Metastable Pitting and the Critical Pitting Temperature, J. Electrochem. Soc. 145 (1998) 2622–2628. doi:10.1149/1.1838691.

66. W. Tian, N. Du, S. Li, S. Chen, Q. Wu, Metastable pitting corrosion of 304 stainless steel in 3.5% NaCl solution, Corrosion Science. 85 (2014) 372–379. doi:10.1016/j.corsci.2014.04.033.

67. P. Marcus, On some fundamental factors in the effect of alloying elements on passivation of alloys, Corrosion Science. 36 (1994) 2155–2158. doi:10.1016/0010-938X(94)90013-2.

68. G.O. Ilevbare, G.T. Burstein, The role of alloyed molybdenum in the inhibition of pitting corrosion in stainless steels, Corrosion Science. 43 (2001) 485–513. doi:10.1016/S0010-938X(00)00086-X.

69. R. Goetz, D. Landolt, The influence of chromium content and potential on the surface composition of Fe-Cr-Mo alloys studied by AES, Electrochimica Acta. 29 (1984) 667–676. doi:10.1016/0013-4686(84)87126-1.

70. K. Sasaki, G.T. Burstein, The generation of surface roughness during slurry erosion-corrosion and its effect on the pitting potential, Corrosion Science. 38 (1996) 2111–2120. doi:10.1016/S0010-938X(96)00066-2.

71. T. Hong, M. Nagumo, Effect of surface roughness on early stages of pitting corrosion of Type 301 stainless steel, Corrosion Science. 39 (1997) 1665–1672. doi:10.1016/S0010-938X(97)00072-3.

72. M.H. Moayed, N.J. Laycock, R.C. Newman, Dependence of the Critical Pitting Temperature on surface roughness, Corrosion Science. 45 (2003) 1203–1216. doi:10.1016/S0010-938X(02)00215-9.

73. G. Meng, Y. Li, Y. Shao, T. Zhang, Y. Wang, F. Wang, Effect of Cl− on the Properties of the Passive Films Formed on 316L Stainless Steel in Acidic Solution, Journal of Materials Science & Technology. 30 (2014) 253–258. doi:10.1016/j.jmst.2013.07.010.

74. M. Ghahari, D. Krouse, N. Laycock, T. Rayment, C. Padovani, M. Stampanoni, F. Marone, R. Mokso, A.J. Davenport, Synchrotron X-ray radiography studies of pitting corrosion of stainless steel: Extraction of pit propagation parameters, Corrosion Science. 100 (2015) 23–35. doi:10.1016/j.corsci.2015.06.023.

75. J. Stewart, D.E. Williams, The initiation of pitting corrosion on austenitic stainless steel: on the role and importance of sulphide inclusions, Corrosion Science. 33 (1992) 457–474. doi:10.1016/0010-938X(92)90074-D.

76. C.R. Alentejano, I.V. Aoki, Localized corrosion inhibition of 304 stainless steel in pure water by oxyanions tungstate and molybdate, Electrochimica Acta. 49 (2004) 2779–2785. doi:10.1016/j.electacta.2004.01.039.a

Chapter II

Characterization techniques and experimental conditions

In this chapter, the electrochemical and surface characterization techniques used in this work are presented as well as the experimental conditions. Electrochemistry was used to characterize the passivation properties of 316L austenitic stainless steel and to control the transition from native oxide-covered surface state to electrochemically passivated surface state. The composition and bilayer structure of the surface oxide films were analyzed by XPS and ToF-SIMS. AFM was used for surface morphology characterization and determination of the conditions of metastable pitting corrosion at the nanometric scale. PCS was used for characterizing the electronic properties of the oxide films. Sample composition and surface preparation are also presented in details in this chapter.

II.1. Electrochemical setup

Several electrochemical methods have been used in this work. Potentiodynamic polarization by Linear Scan Voltametry (LSV) was used to define the electrochemical response as a function of applied potential and thus to determine corrosion potential, active and passive regions and transpassivity domain. Potentiostatic polarization was used to produce a well-defined passivated surface state and to control passivity breakdown and metastable pitting corrosion.

A three-electrodes system was used. Figure II-1 shows the electrochemical cell connected to the potentiostat. This cell is a closed vessel containing the electrolyte with apertures for:

- the Working Electrode (WE), which is the 316L SS sample. The sample is in a sample holder enabling electrical contact with the potentiostat. The sealing between sample and electrolyte is insured by a viton O-ring. The area exposed to the electrolyte is 0.5 cm^2.

- the Reference Electrode (RE), which is a Saturate Calomel Electrode (SCE). The potential of SCE is +248 mV vs Normal Hydrogen Electrode (NHE) at 25 °C. The RE is connected via a salt bridge filled with the electrolyte. The reason is to avoid chloride contamination which might come from the RE.

- the Counter electrode (CE), which is a spiral wire made of gold. The counter electrode is often made of noble metal like gold or platinum in order to avoid reaction between counter electrode and electrolyte.

- the degassing tube allowing to bubble argon gas in order to minimize to the content of dissolved oxygen. The electrolyte was bubbled for 30 min before the electrochemical measurement with the tube in the solution to exhaust dissolved oxygen. Then the tube was pulled out of the electrolyte and kept over the liquid level to avoid oxygen reentry into the cell.

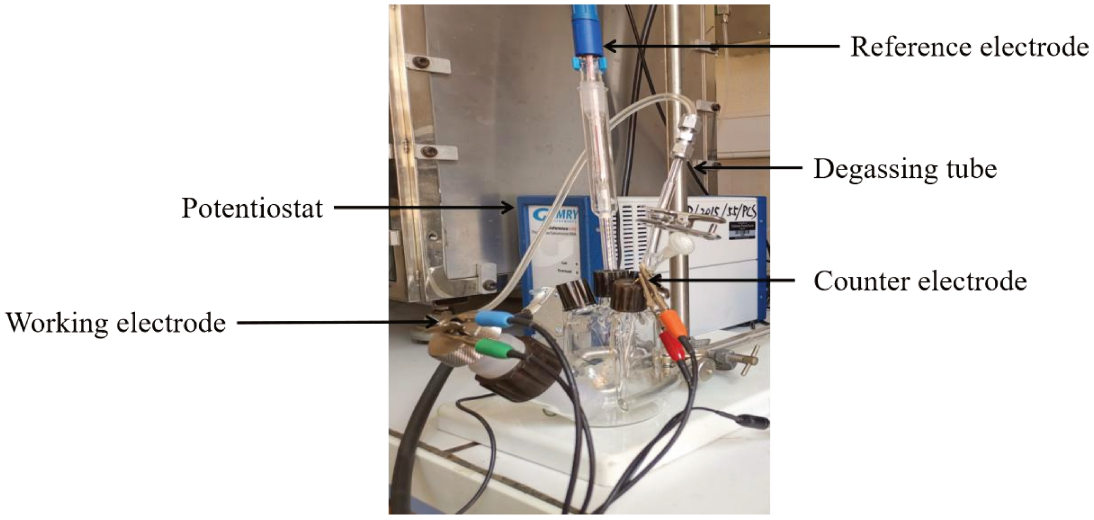

Figure II-1 electrochemical setup with the 3-electrode cell connected to the potentiostat

The potentiostat used in this work is a Gamry Reference 600 potentiostat (Gamry, USA). Details on the experimental conditions for the electrochemical analysis by LSV as well as for the potentiostatic passivation treatments are given in Chapters III, IV and V.

II.2. X-ray Photoelectron Spectroscopy (XPS)

X-ray photoelectron spectroscopy (XPS), also called ESCA (Electron Spectroscopy for Chemical Analysis), is a surface analysis technique that allows a chemical analysis on a depth

less than or equal to about 10 nm. This nondestructive method can detect quantitatively the chemical environment and chemical composition. Varying the take-off angle of the measured photoelectrons gives the possibility to retrieve information on the stratification of the extreme surface over a depth of less than 10 nm. This technique is sensitive to almost all chemical elements except hydrogen and helium. The detection limit is about 0.5 to 1 atomic percent. These capabilities are perfectly adapted for the analysis of ultrathin oxide films and metal or alloy surfaces including on stainless steel [1]-[6].

II.2.1. Principle

The principle of XPS is based on the photoelectric effect that describes the ejection of electrons from a surface when photons impinge upon it. This process is called photoemission. Figure II-2 presents a schematic view of the photoemission process.

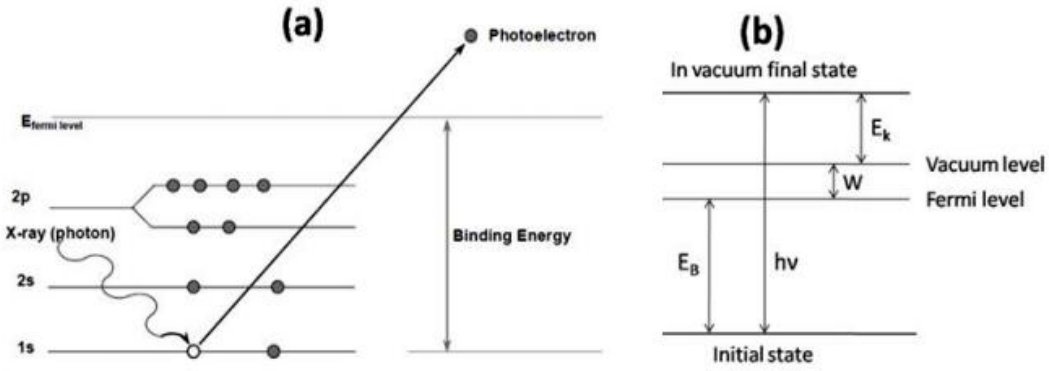

Figure II-2 Schematic view of photoemission [7]

From Figure II-2 b, energy conservation can be written as :

$$h\nu = E_B + E_k + W \qquad \text{eq. II-1}$$

where

hν is the photon energy with h the Planck constant (6.62 x 10^{-34} Js) and ν the frequency (Hz) of the radiation. hν is a known value fixed by the X-Ray source (1486.6 eV for Al-Kα and 1253.6 eV for Mg-Kα) .

E_B is the binding energy of the photoelectron with respect to Fermi level. It is characteristic of the chemical element and its chemical environment.

E_k is the kinetic energy of the photoelectron ejected from the sample with respect to the vacuum level. Its value is measured by the hemispherical analyzer.

W is the spectrometer work function. It represents the minimum energy required to remove an electron from the solid. Its value can be determined using reference sample, e.g. with the Au $4f_{7/2}$ component of a pure gold sample.

In XPS, the emission of a photoelectron leads to a hole in the electronic orbital or origin, that can be filled by an electron from a higher level. This phenomenon is accompanied by an excess of energy dissipated by de-excitation, either by the emission of photons (X-ray fluorescence), or by the emission of an electron located on a higher electronic level (Auger electron). Auger electrons are characterized by specific kinetic energies independent of the energy of the incident X-ray radiation. They are also characteristic of the emitting chemical element.

II.2.2. Spectrum decomposition and quantitative calculations

A XPS spectrum records the number of photoelectrons as a function of binding energy. Generally there are two types of spectrum, one type is the low resolution survey which is recorded from 0 eV to 1200 eV binding energy with a high pass energy (100 eV) of the analyzer and a large step size (1 eV). This type of spectrum is used to identify the chemical nature of the elements present on the surface of the sample. Another type of spectrum is the high resolution core level spectrum which is recorded for a small and specific binding energy region corresponding to a selected core level of the elements. The pass energy for this type of spectrum is lower (20 eV) and the step size is also smaller (0.1 eV). The high resolution spectrum is used to identify the chemical information like oxidation state and chemical environment of the element. Quantitative analysis is based on this type of spectrum.

The core level spectrum may contains several components, each oxidation state having a contribution to the signal. In order to distinguish each component, decomposition of the spectrum is very important for XPS analysis. In this work the XPS data processing is performed with CasaXPS software.

Before starting the decomposition, it is necessary to subtract the continuous background,

which is observable all over the energy field. Two phenomena contribute to the continuous background. First, before reaching the surface of the sample, a number of photoelectrons will be influenced by inelastic collisions, which will decrease their kinetic energy. Second, when an electron passes near a nucleus, it will be accelerated and this can cause the emission of a photon (Bremmstrahlung radiation). The subtraction of the continuous background noise was carried out using the iterative method of Shirley [8].

Once the background is subtracted, it is possible to fit the experimental spectrum using peak components. There are several parameters defining a peak: the Binding Energy (BE), the Full width at half maximum (FWHM) and the lineshape. The Lorentzian Asymmetric lineshape is used for metallic components. The lineshape is a function called LA (α, β, m), where α, β are two parameters influencing the spread of the tail of the Lorentzian curve resulting in steeper edges to the lineshape and m is the parameter defining the width of the Gaussian [9]. The function of the lineshape is set by fitting a pure 316L SS metallic surface, the spectra and lineshape functions of Fe, Cr, Ni, Mo are presented in Figure II-3.

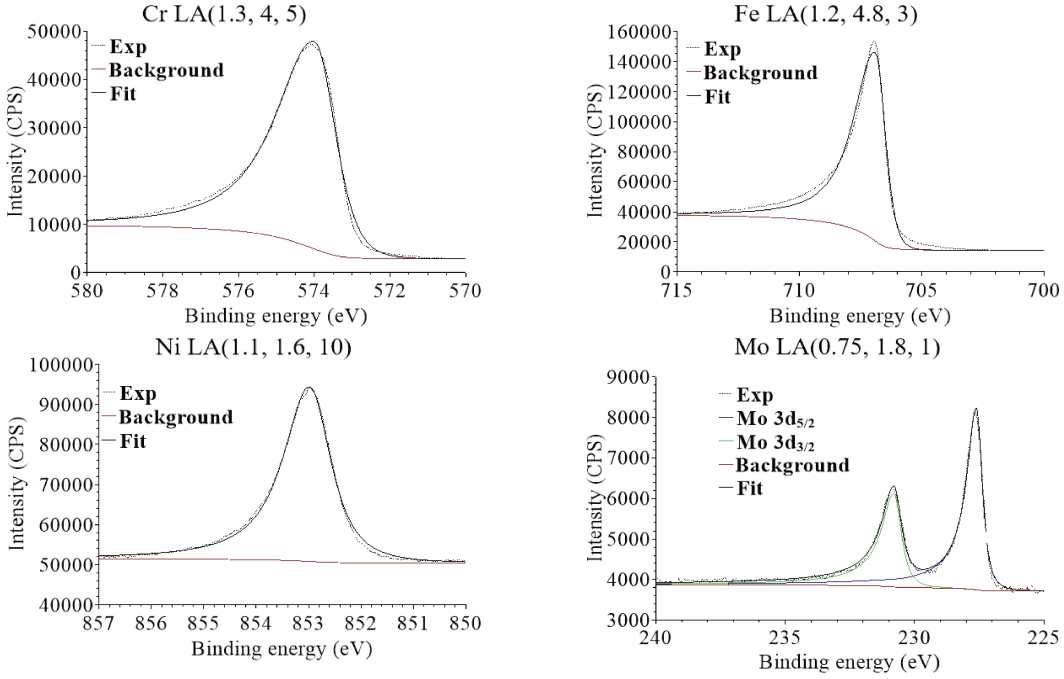

Figure II-3 Lineshape of metallic components for the Cr $2p_{3/2}$, Fe $2p_{3/2}$, Ni $2p_{3/2}$, Mo 3d core levels

For the non-metallic elements like C, O, S, Cl and components like the oxide/hydroxide of

metal, the peaks are symmetric. So the Gaussian/Lorentzian lineshape is a function GL (χ). where χ represent the percentage of Lorentzian, in our case χ is set as 30, meaning that the ratio of G/L is 70/30 [8].

In this work, five peaks were used to decompose the Cr(III) oxidized state, as proposed previously [10]. We also fitted a pure Cr oxide reference sample prepared in the XPS spectrometer. This pure Cr oxide sample was prepared with a pure Cr metallic sample. First the sample was introduced in the Ultra-High-Vacuum (UHV) chamber and sputtered with Ar ions to remove the air formed Cr oxide. Then, it was oxidized by exposure to gaseous oxygen at high temperature in order to produce an oxide film thick enough to avoid the observation of metallic peak due to complete attenuation of the photoelectrons by the surface oxide. The series of five peaks fit very well the experimental spectrum (Figure II-4).

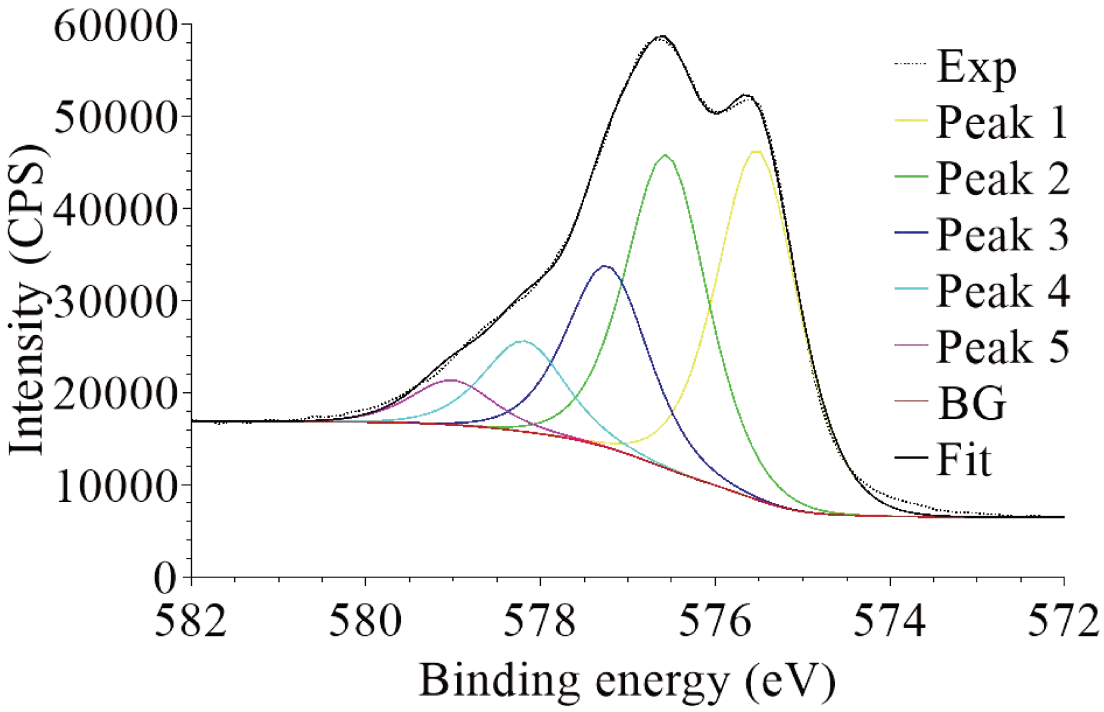

Figure II-4 Fit of Cr_2O_3 with a series of five peaks as proposed in Reference [10]

Fitting parameters of these 5 peaks are presented in Table II-1, this fit defines the binding energy , the FWHM and the intensity ratio of peaks 2-5 compared to peak 1. These parameters will be used in the following decomposition in chapter III, IV, and V.

Table II-1 Fitting parametes for pure Cr_2O_3 prepared in UHV

Peak	Binding energy (±0.1eV)	FWHM (±0.1eV)	Intensity (%)
Peak 1	575.5	1.1	35.5
Peak 2	576.5 (Peak 1 + 1.0)	1.1	30.4 (86% of peak 1)
Peak 3	577.3 (Peak 1 + 1.8)	1.1	19.7 (55% of peak 1)
Peak 4	578.3 (Peak 1 + 2.8)	1.1	8.9 (25% of peak 1)
Peak 5	578.7 (Peak 1 + 3.2)	1.1	5.5 (16% of peak 1)

Once the decomposition of the spectra is done, it is possible to process the measured intensities using a layered oxide film model in order to calculate the thickness and composition of the oxide film and the composition of the metal underneath the surface oxide for stainless steel. Maurice et al. have used a bilayer structure model of the oxide film for the calculation [11]. In our case, we also constructed a bilayer structure model based on the information retrieved from the ToF-SIMS analysis.

An example of bilayer model is presented in Figure II-5.

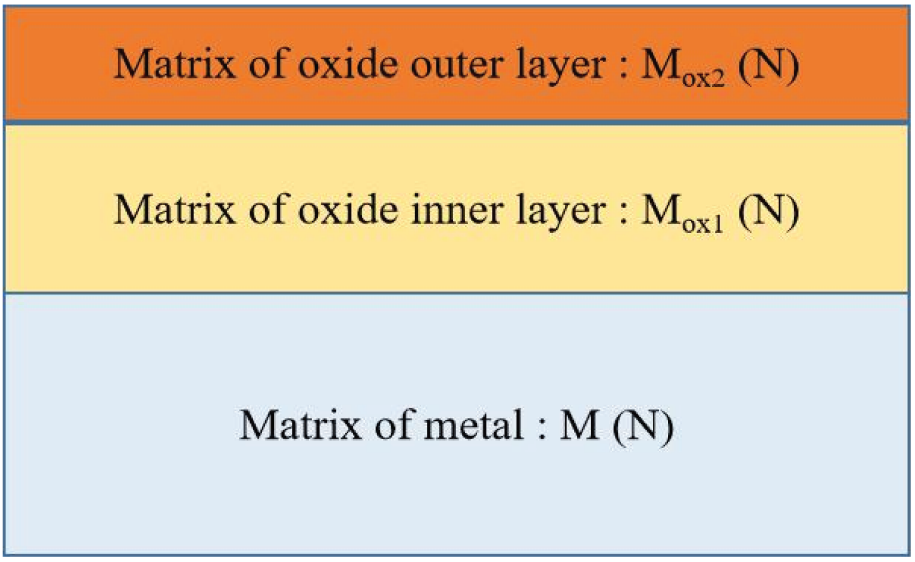

Figure II-5 Example of bilayer model of an oxide film of homogeneous thickness covering a metallic surface

Based on this model, the intensity of element N in the matrix of metal M can be expressed as:

$$I_N^M = k \cdot A(\beta) \cdot F \cdot T(E_k) \cdot \lambda_N^M \cdot D_N^M \cdot \sigma_N \cdot \exp\left(\frac{-d_{ox1}}{\lambda_N^{M_{ox1}} \cdot \sin(\beta)}\right) \cdot \exp\left(\frac{-d_{ox2}}{\lambda_N^{M_{ox2}} \cdot \sin(\beta)}\right) \cdot \sin(\beta) \quad \text{eq. II-2}$$

Where

k is the constant dependent of the spectrometer but not of the element.

A(β) is the analyzed area of the sample dependent of angle β

β is the take-off angle between the surface of the sample and the direction in which the photoelectrons are analyzed.

F is the photoelectron flux

$T(E_k)$ is the transmission factor of the analyzer. It depends on the kinetic energy of the analyzed electron

λ is the inelastic mean free path of the analyzed photoelectrons of element N in matrix M

D is the density of the element N in matrix M

σ is the photoionization cross section of element N for a given core level

d is the thickness of the oxide matrix

The intensity of element N in the matrix of the oxide inner layer M_{ox1} can be expressed as:

$$I_N^{M_{ox1}} = k \cdot A(\beta) \cdot F \cdot T(E_k) \cdot \lambda_N^{M_{ox1}} \cdot D_N^{M_{ox1}} \cdot \sigma_N \cdot \exp\left(\frac{-d_{ox2}}{\lambda_N^{M_{ox2}} \cdot \sin(\beta)}\right) \cdot \left[1 - \exp\left(\frac{-d_{ox1}}{\lambda_N^{M_{ox1}} \cdot \sin(\beta)}\right)\right] \cdot \sin(\beta)$$

eq. II-3

The thickness of the inner layer can be expressed as:

$$d_{ox1} = \lambda_N^{M_{ox1}} \cdot \sin(\beta) \cdot \ln\left(1 + \frac{D_N^M}{D_N^{M_{ox1}}} \frac{\lambda_N^M}{\lambda_N^{M_{ox1}}} \frac{I_N^{M_{ox1}}}{I_N^M}\right) \quad \text{eq. II-4}$$

The intensity of element N in the matrix of the oxide outer layer M_{ox2} can be expressed as:

$$I_N^{M_{ox2}} = k \cdot A(\beta) \cdot F \cdot T(E_k) \cdot \lambda_N^{M_{ox2}} \cdot D_N^{M_{ox2}} \cdot \sigma_N \cdot [1 - \exp(\frac{-d_{ox2}}{\lambda_N^{M_{ox2}} \cdot \sin(\beta)})] \cdot \sin(\beta)$$ eq. II-5

The thickness of the outer layer can be expressed as:

$$d_{ox2} = \lambda_N^{M_{ox2}} \cdot \sin(\beta) \cdot \ln(1 + \frac{D_N^M}{D_N^{M_{ox2}}} \frac{\lambda_N^M}{\lambda_N^{M_{ox2}}} \frac{I_N^{M_{ox2}}}{I_N^M}) \cdot \exp(\frac{-d_{ox1}}{\lambda_N^{M_{ox2}} \cdot \sin(\beta)})$$ eq. II-6

The calculation of composition and thickness are based on these equations.

II.2.3. Instrument and conditions

The instrument used in this work is a Thermo Electron ESCALAB 250 spectrometer (Figure II-6) operating at about 10^{-9} mbar. The X-ray source was an AlK_α monochromatized radiation ($h\nu$ = 1486.6 eV). Survey spectra were recorded with a pass energy of 100 eV at a step size of 1 eV. High resolution spectra of the core level regions were recorded with a pass energy of 20 eV at a step size of 0.1 eV. The take-off angles of the analyzed photoelectrons were 40° and/or 90°. Further details on the conditions of measurement are given in Chapters III, IV and V.

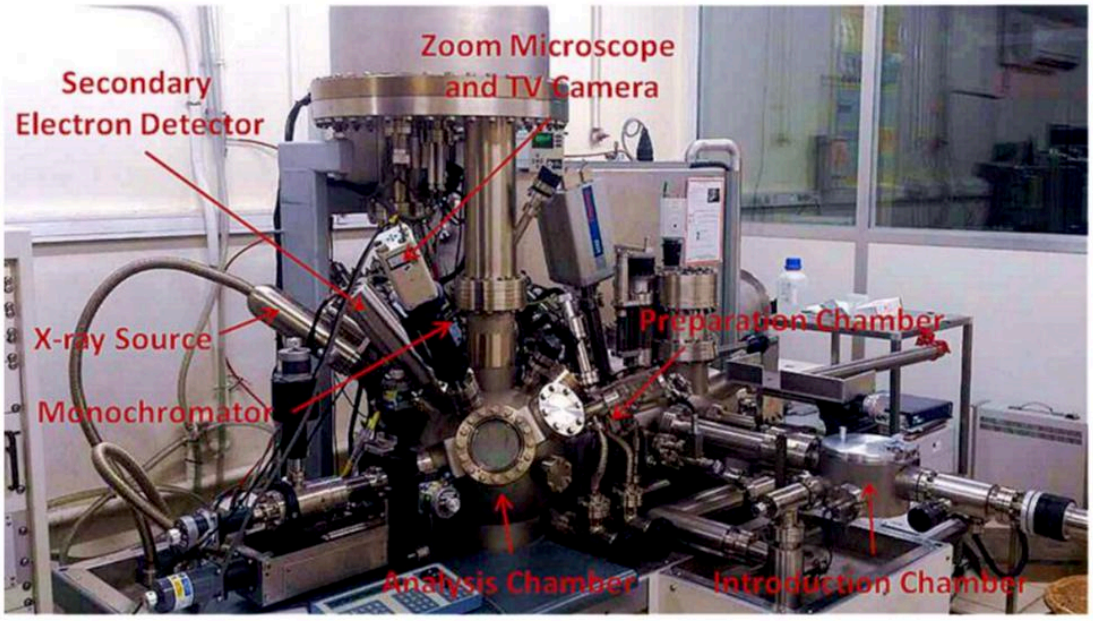

Figure II-6 Photo of the Thermo Electron ESCALAB 250 XPS spectrometer

II.3. Time-of-Flight Secondary Ion Mass Spectrometry (ToF-SIMS)

Time-of-Flight Secondary Ion Mass Spectrometry (ToF-SIMS) is a lightly sensitive surface analytical technique well established for industrial and research applications [2][3][5][12]-[14]. ToF-SIMS is an acronym for the combination of the analytical technique Secondary Ion Mass Spectrometry with Time-of-Flight mass analysis. The technique provides detailed elemental and molecular information about the surface, thin layers, interfaces of the sample, and gives a full three-dimensional analysis. Moreover, the most interesting capabilities of this spectrometry are the high sensitivity (part per billion), detection of isotope and the detection of hydrogen.

II.3.1. Principle

ToF-SIMS uses a focused beam of ions (typically Bi^+) that is pulsed on a material surface with a kinetic energy of a few keV, resulting in a collision cascade inside the material and the emission of various secondary particles, such as electrons, neutral species, atoms and molecules from the surface. The ions, which are the species of interest analyzed in a ToF-SIMS measurement are emitted from the first 2-3 monolayers and are characteristic of the surface composition. In ToF-SIMS spectrometry, a static scheme is maintained. Under such conditions, a nearly non-perturbated surface is probed during each primary beam pulse. Figure II-7 shows a schematic view of this principle.

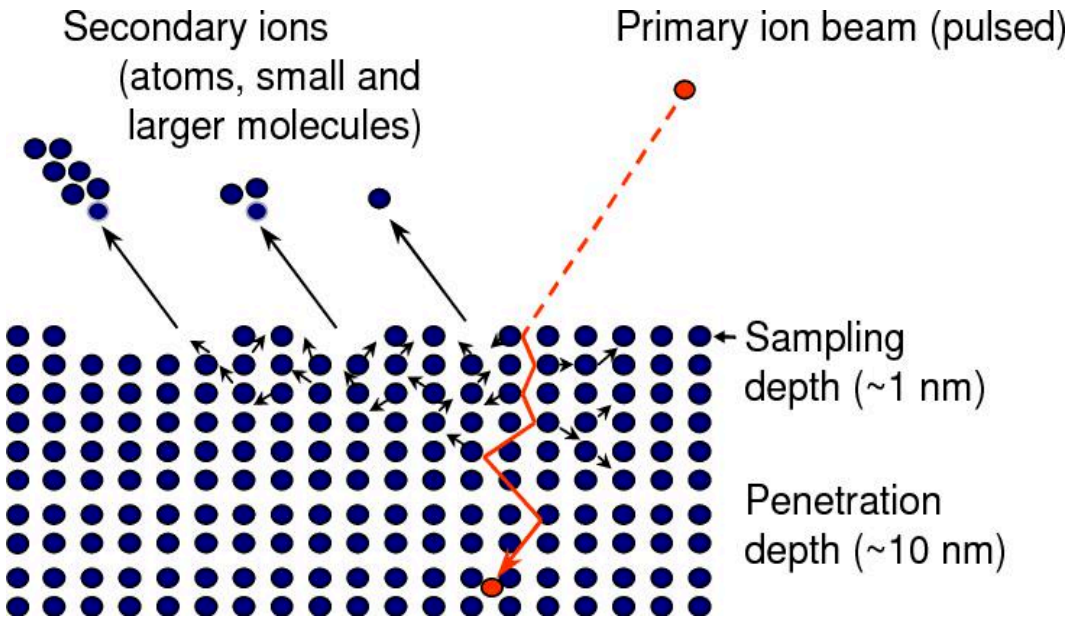

Figure II-7 Schematics of the principle of SIMS [15]

The secondary ions, produced during the collision, are accelerated under an electric field (U) and enter the ToF analyzer.

Based on this principle, the kinetic energy of the secondary ions can be expressed as:

$$E_k = q \cdot U = \frac{1}{2} \cdot m \cdot v^2 \qquad \text{eq.II-7}$$

Where

q is the charge of the secondary ion,

U is the acceleration tension,

m is the mass of the secondary ion,

v is the speed of secondary ion

Thus, as soon as the secondary ions enter the analyzer, they fly a path of length L in vacuum (collision-free space) with a velocity equal to:

$$v = \sqrt{\frac{2 \cdot q \cdot U}{m}} \qquad \text{eq. II-8}$$

The measured time of flight (t) is linked to the mass of the ions according to the relation :

$$t = \frac{L}{v} = L \cdot \sqrt{\frac{m}{2 \cdot q \cdot U}} \qquad \text{eq. II-9}$$

For a given charge, lighter ions travel faster through the analyzer, and ions are sorted according to their mass/charge ratio.

ToF-SIMS allows different analytical modes. In this work, we used the depth profiling. In this mode, two ion beams are used (dual beam mode): a primary ion beam for analysis (Bi^+) and an ion beam for erosion (Cs^+). The successive use of each beam allows to make a ToF-SIMS analysis at the bottom of a crater eroded during the sputtering phase of the measurement. Thus, one obtains a complete mass spectrum at each sputtering time step and one can build depth elemental composition profiles that represent the intensity of each secondary ion as a function of the sputtering time.

II.3.2. Instrument and conditions

In this work, a ToF-SIMS 5 spectrometer (Ion ToF–Munster, Germany) has been used for ToF-SIMS analysis, Figure II-8 presents a photo of the spectrometer. It is operated at about 10^{-9} mbar. The depth profile analysis interlaces topmost surface analysis in static SIMS conditions using a pulsed 25 keV Bi^+ primary ion source delivering 1.2 pA current over a 100 × 100 μm^2 area with sputtering using a 1 keV Cs^+ sputter beam giving a 32 nA target current over a 300 × 300 μm^2 area. Analysis was centered inside the eroded crater to avoid edge effects. The profiles are recorded with negative secondary ions that have higher yield for oxide matrices than for metallic matrices. The Ion-Spec software is used for data acquisition and processing.

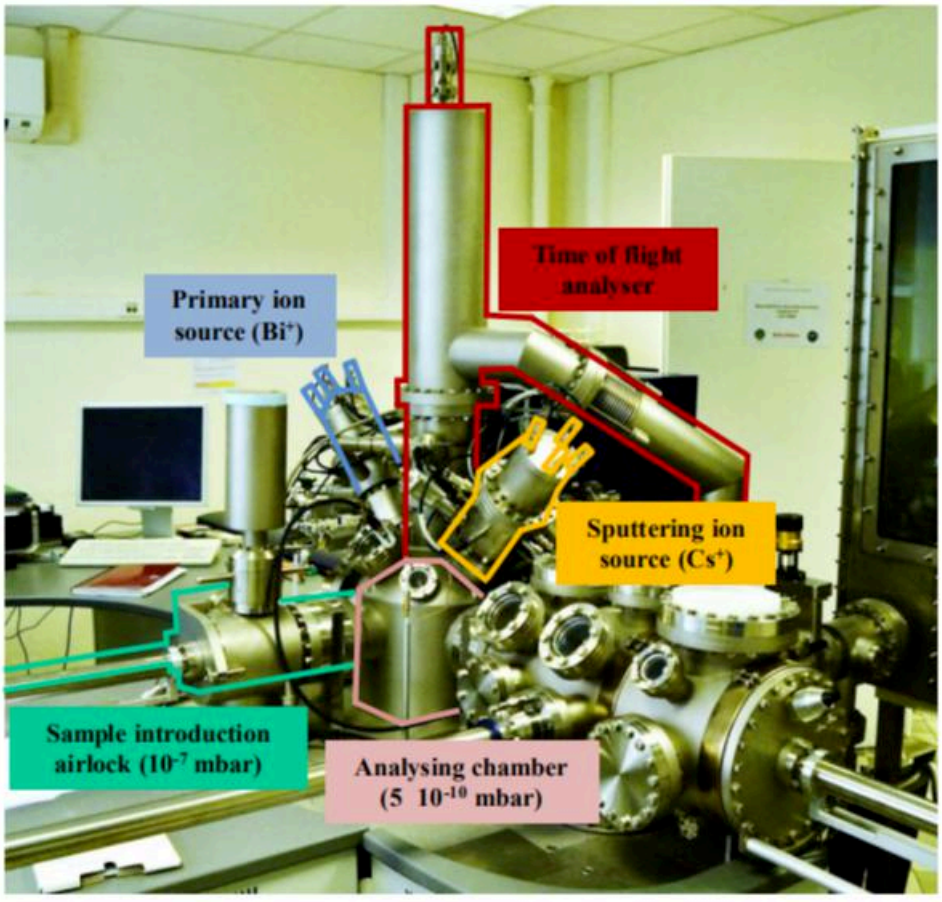

Figure II-8 Photo of the ToF-SIMS 5 spectrometer

II.4. Atomic Force Microscopy (AFM)

Atomic Force Microscopy (AFM) is a technique that provides a mapping of the topology of

the surface of a sample with a vertical resolution that can be less than one nanometer. Unlike Scanning Tunneling Microscopy (STM), it does not require an electrically conductive sample. All types of samples can be analyzed with AFM, including insulating samples. This advantage gives AFM a large application [16][17].

II.4.1. Principle

The AFM is based upon the principle of sensing the forces between a sharp tip and the surface to be investigated. The forces are measured by measuring the deflection of a very small cantilever. The deflection is produced in the cantilever as a result of the interaction of the tip with the sample resulting from attractive/repulsive forces. The deflection of the cantilever is measured by the movement of the reflection point of a laser beam on a photodetector. Figure II-9 present a schematic diagram of the AFM working principle.

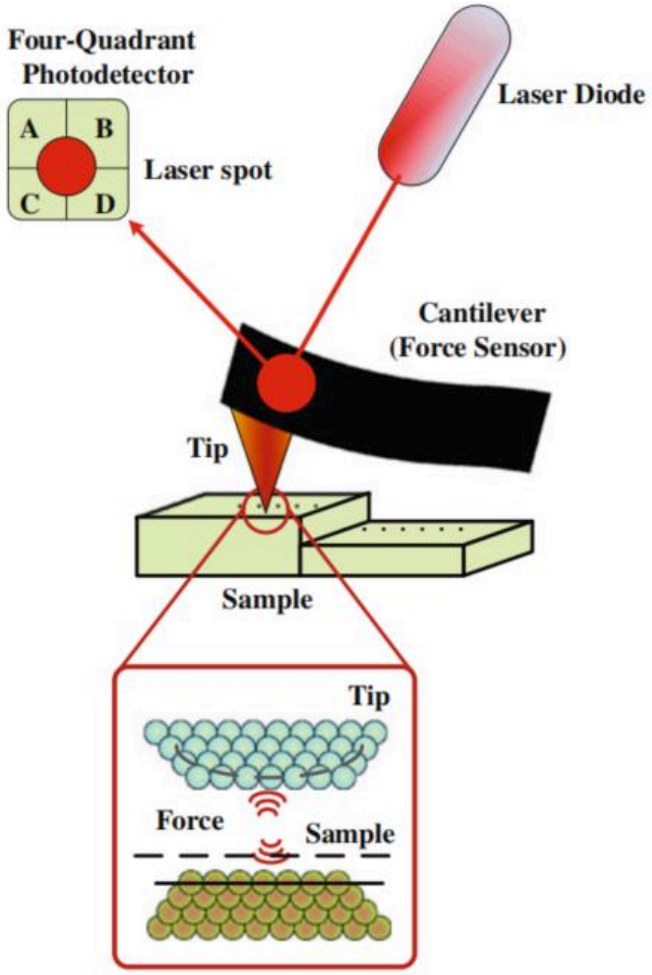

Figure II-9 Diagram of the AFM working principle

II.4.2. Operation modes

AFM can be operated in different modes depending of the application. These different modes can be classified into three types based on the interaction forces. The interaction forces depend on the distance between the surface and the tip, Figure II-10 presents the relation of interactive forces with the distance separating probe from sample.

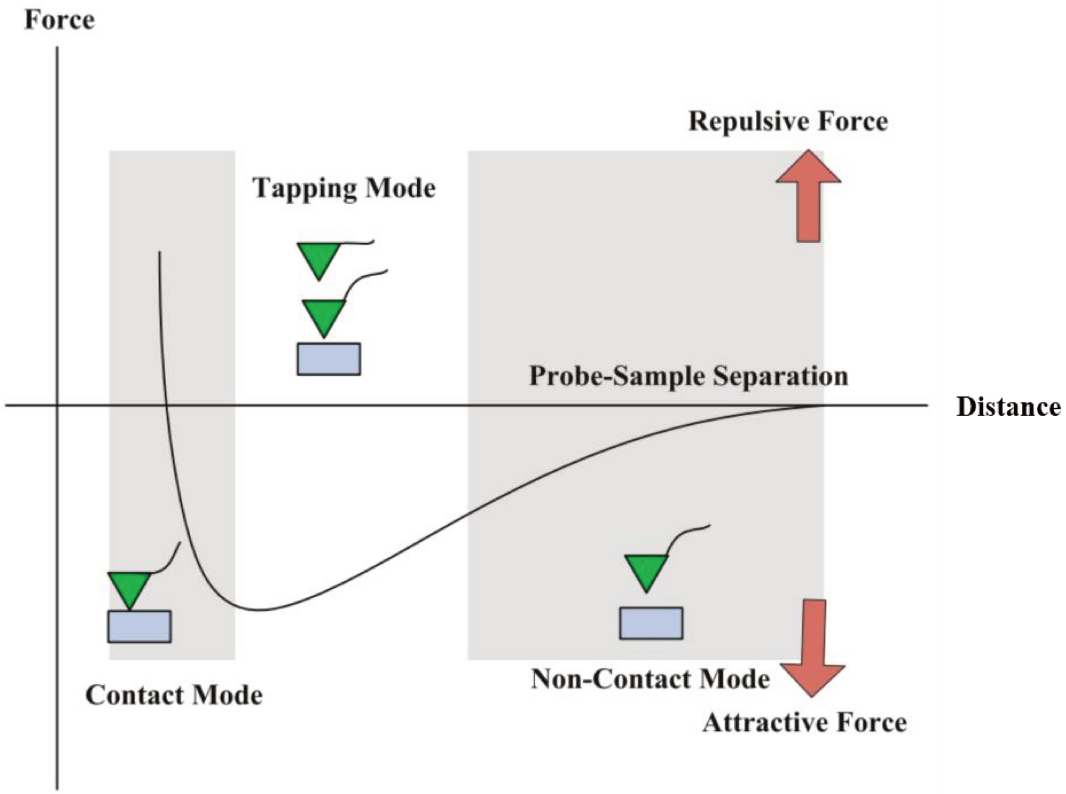

Figure II-10 Plot of force as a function of probe-sample distance [18]

As we can see in this figure, there are three regimes associated with three different modes called “contact mode”, “tapping mode” and “non-contact mode”.

In contact mode, the tip and the surface of the sample are in soft physical contact. Here the repulsive force between the sample and the probe are measured. The resolution of this mode is excellent, but the constant contact between the tip and the sample can deteriorate the tip as well as the sample.

In tapping mode, the cantilever oscillates at a frequency close to its resonance frequency and the tip is punctually in contact with the surface of the sample, resulting in modifications of the

amplitude, phase and resonance frequency of the cantilever. This is an intermediate mode between the contact mode and the non-contact mode which reduces the deterioration of tip and sample. The resolution of this mode is not as good as for the contact mode but higher than for the non contact mode. The relatively high resolution and low deterioration of tip and sample makes this mode the most used.

In non-contact mode, the cantilever oscillates at a frequency close to its resonance frequency without touching the surface of the sample. Here the attractive force between the sample and the probe are measured. The resolution of this mode is lower than the contact mode but there are no deterioration of the tip and sample.

II.4.3. Instrument and conditions

In this work, AFM images were obtained with a Nano-Observer AFM microscope (CSI instruments) shown in Figure II-11. The tapping mode was used. The probe is a silicon probe called Model FORT from AppNano. The frequency f of the cantilever is 50-70 kHz and the stiffness factor k is 1-5 N/m. The nominal tip radius is inferior to 10 nm. AFM images were acquired in the topography mode and analyzed with the software Gwyddion.

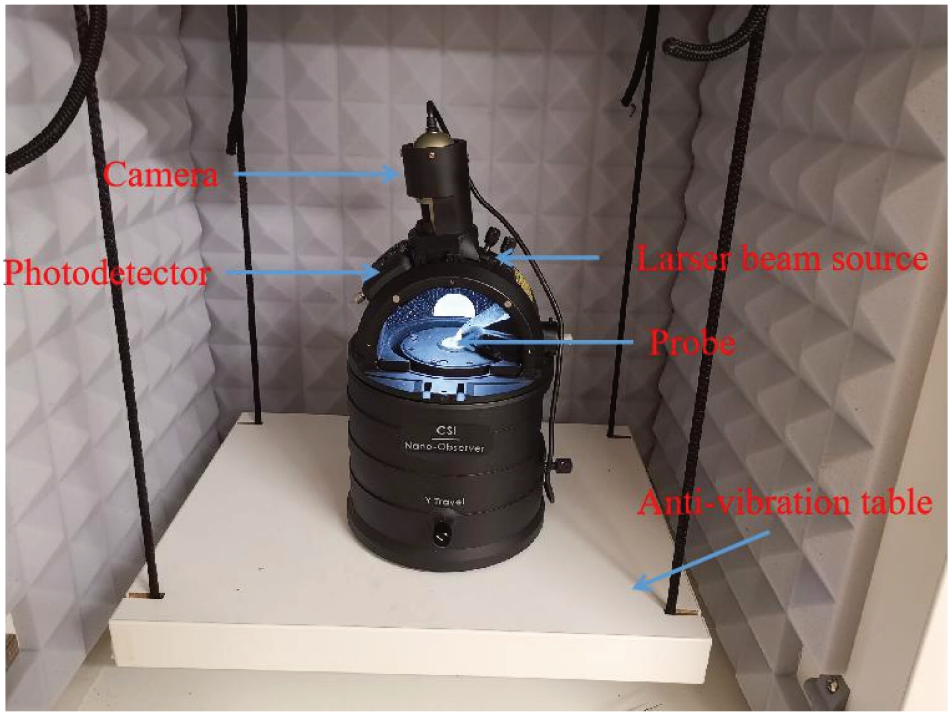

Figure II-11 Nano-Observer AFM microscope used in this work

II.5. Photo-Current Spectroscopy (PCS)

Photocurrent spectroscopy is a very powerful technique for characterizing *in-situ* the solid-state electronic properties of semiconducting and insulating materials. It is able to provide detailed information on characteristic energy levels of oxide film/electrolyte junctions such as the band gap value (E_g), the flat band potential (U_{fb}) and conductor type. These details help us to identify the composition and the structure of the thin passive films. Also it is possible to study the mechanism of charge transfer (electrons and ions) at the metal/corrosion layer/electrolyte interface. There are several advantages of PCS analysis. This technique can be applied to large area on the microscopic region of the surface with a high sensitivity. Also it is a non destructive surface analysis technique. All these advantages enables a large application especially for solar energy conversion and microelectronics [12][19]-[22].

II.5.1. Principle

The principle of photocurrent spectroscopy is also based on the photoemission phenomena as in XPS. But here the photoelectron are not analyzed directly but in the form of photocurrent by applying a potential. In the case of a thin oxide film on a metal or alloy surface (e.g. stainless steel), the relation between optical band gap (E_g) and photocurrent intensity (I_{ph}) can be expressed as [20]

$$I_{ph} \cdot h\nu = const.(h\nu - E_g)^{n/2} \qquad \text{eq. II-10}$$

Where

hν is the energy of photon, with h the Planck constant (6.62 x 10^{-34} Js) and ν the frequency (Hz) of the radiation.

n is a value which depends on the transition state between valence band (VB) and conduction band (CB). For a direct transition n = 1, for a direct forbidden n = 3 and, in our case, for an indirect transition n = 4.

Based on the value of the band gap, it is possible to correlate the composition of the film by the following equations [19]

$$E_g = 2.17(\chi_{av} - \chi_O)^2 - 2.71 \quad \text{eq. II-11}$$

$$E_g = 1.35(\chi_{av} - \chi_O)^2 - 1.49 \quad \text{eq. II-12}$$

Eq. II-11 is for a sp metal oxide and eq. II-12 is for a d metal oxide.

χ_O is the oxygen electronegativity and χ_{av} is the average electronegativity of the metal partners in the oxides expressed as:

$$\chi_{av} = \frac{m\chi_M + n\chi_N}{m+n} \quad \text{eq. II-13}$$

where χ_M and χ_N are the electronegativity of the metal partners and the m and n are their ratio.

Using these equations, it is possible to estimate the band gap value based on the composition of the oxide film measured by XPS.

II.5.2. Instrument and conditions

A Zennium electrochemical workstation (ZAHNER, Germany) operated with the Thales software was used (Figure II-12). The measurements were performed in 0.1 M $Na_2B_4O_7$ electrolyte (di-Sodium tetraborate , pH ~9.5) prepared from pure chemicals (R.P.NORMAPUR®) and Millipore® water using a standard 3-electrode cell with a Pt spiral as the counter electrode and an Ag/AgCl (in 3.5 M KCl) electrode as reference electrode. The photocurrent spectra were recorded in the wavelength range from 310 to 700 nm (correspond to 1.7 eV to 4 eV) with the Zahner Zennium CIMPS system (TLS-03) at a 3.16 Hz frequency.

As we can see there is also a potentiostat in this workstation so there are also several electrochemical analysis like Linear Sweep Voltammetry (LSV) and Electrochemical Impedance Spectroscopy (EIS) that can be performed with this instrument. The electrochemical impedance spectra were generated by applying a sinusoidal signal of 10 mV amplitude over the frequency range 0.1 Hz–100 kHz. The spectra were analyzed with the Zview software.

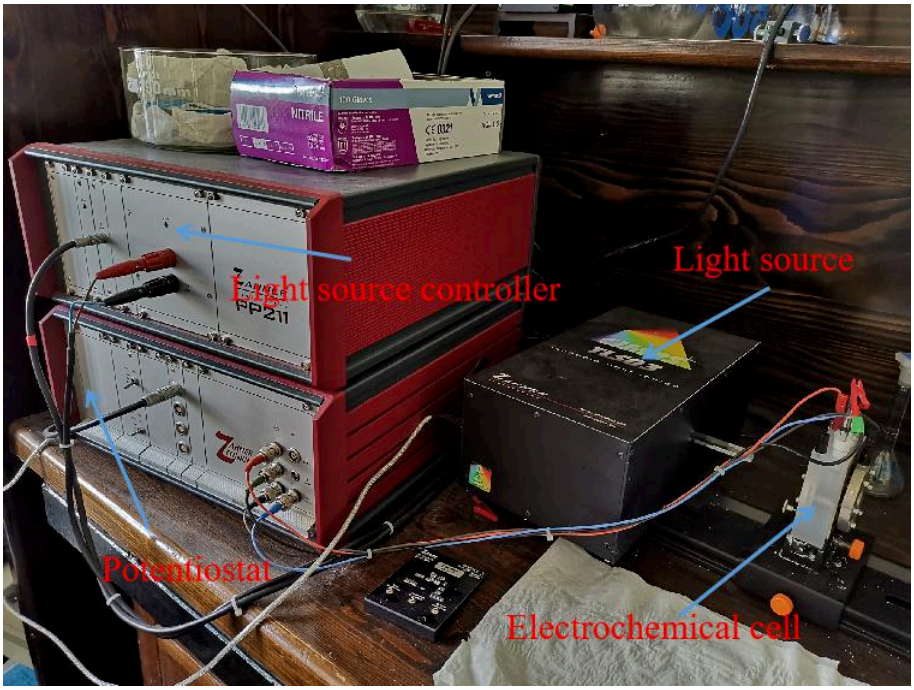

Figure II-12 Zennium electrochemical workstation

II.6. Sample and surface preparation

Square-shaped 316L stainless steel samples were used in this work. The composition is detailed in Table II-1

	Fe	Cr	Ni	Mo	C	Mn	P	S	Si	N
wt%	Balance	19	13	2.70	≤0.03	≤2	≤0.04	≤0.03	≤0.75	≤0.10
at%	Balance	20	12	1.56	≤0.14	≤2	≤0.07	≤0.05	≤1.49	≤0.40

Table II-1 Composition of 316L SS samples used in this work

Surface preparation was performed by mechanical polishing first with emery paper of successive 1200 and 2400 grades and then with diamond suspensions of successive 6, 3, 1 and 0.25 µm grades. Cleaning and rinsing was performed after each polishing step in successive ultrasonicated baths of acetone, ethanol and Millipore® water (resistivity > 18 MΩ cm). Filtered compressed air was used for drying.

Reference

1. J.E. Castle, C.R. Clayton, The use of x-ray photo-electron spectroscopy analyses of passive layers on stainless steel, Corrosion Science. 17 (1977) 7–26. doi:10.1016/0010-938X(77)90036-1.

2. E. Gardin, S. Zanna, A. Seyeux, A. Allion-Maurer, P. Marcus, Comparative study of the surface oxide films on lean duplex and corresponding single phase stainless steels by XPS and ToF-SIMS, Corrosion Science. 143 (2018) 403–413. doi:10.1016/j.corsci.2018.08.009.

3. E. Gardin, S. Zanna, A. Seyeux, A. Allion-Maurer, P. Marcus, XPS and ToF-SIMS characterization of the surface oxides on lean duplex stainless steel – Global and local approaches, Corrosion Science. 155 (2019) 121–133. doi:10.1016/j.corsci.2019.04.039.

4. L. Ma, F. Wiame, V. Maurice, P. Marcus, New insight on early oxidation stages of austenitic stainless steel from in situ XPS analysis on single-crystalline Fe–18Cr–13Ni, Corrosion Science. 140 (2018) 205–216. doi:10.1016/j.corsci.2018.06.001.

5. S. Tardio, M.-L. Abel, R.H. Carr, J.E. Castle, J.F. Watts, Comparative study of the native oxide on 316L stainless steel by XPS and ToF-SIMS, Journal of Vacuum Science & Technology A. 33 (2015) 05E122. doi:10.1116/1.4927319.

6. E.D. Vito, P. Marcus, XPS study of passive films formed on molybdenum-implanted austenitic stainless steels, Surface and Interface Analysis. 19 (1992) 403–408. doi:10.1002/sia.740190175.

7. E. Paterson, R. Swaffield, Clay Mineralogy: Spectroscopic and Chemical Determinative Methods, Springer Netherlands, 1994

8. Peak Fitting in XPS http://www.casaxps.com/help_manual/manual_updates/peak_fitting_in_xps.pdf

9. LA line shape http://www.casaxps.com/help_manual/manual_updates/LA_Lineshape.pdf

10. M.C. Biesinger, B.P. Payne, A.P. Grosvenor, L.W.M. Lau, A.R. Gerson, R.St.C. Smart, Resolving surface chemical states in XPS analysis of first row transition metals, oxides and hydroxides: Cr, Mn, Fe, Co and Ni, Applied Surface Science. 257 (2011) 2717–2730. doi:10.1016/j.apsusc.2010.10.051.

11. V. Maurice, H. Peng, L.H. Klein, A. Seyeux, S. Zanna, P. Marcus, Effects of molybdenum on the composition and nanoscale morphology of passivated austenitic stainless steel surfaces, Faraday Discuss. 180 (2015) 151–170. doi:10.1039/C4FD00231H.

12. F.D. Franco, A. Seyeux, S. Zanna, V. Maurice, P. Marcus, Effect of High Temperature Oxidation Process on Corrosion Resistance of Bright Annealed Ferritic Stainless Steel, J. Electrochem. Soc. 164 (2017) C869–C880. doi:10.1149/2.1851713jes.

13. A. Mazenc, A. Galtayries, A. Seyeux, P. Marcus, S. Leclercq, ToF-SIMS study of the behavior of thermally oxidized films formed on nickel-based 690 alloy in high-temperature water, Surf. Interface Anal. 45 (2013) 583–586. doi:10.1002/sia.5060.

14. X. Wu, S. Voyshnis, A. Seyeux, Y. Chumlyakov, P. Marcus, ToF-SIMS study of oxide films thermally grown on nickel-base alloys, Corrosion Science. 141 (2018) 175–181. doi:10.1016/j.corsci.2018.06.043.

15. H. Kangas, M. Kleen, Surface chemical and morphological properties of mechanical pulp fines, Nordic Pulp & Paper Research Journal. 19 (2004) 191–199. doi:10.3183/npprj-2004-19-02-p191-199.

16. T. Massoud, V. Maurice, L.H. Klein, A. Seyeux, P. Marcus, Nanostructure and local properties of oxide layers grown on stainless steel in simulated pressurized water reactor environment, Corrosion Science. 84 (2014) 198–203. doi:10.1016/j.corsci.2014.03.030.

17. V. Maurice, T. Nakamura, L.H. Klein, P. Marcus, 1 Initial stages of the localized corrosion by pitting of passivated nickel surfaces studied by STM and AFM, (n.d.).

18. S.K. Das, H.R. Pota, I.R. Petersen, Intelligent Tracking Control System for Fast Image Scanning of Atomic Force Microscopes, in: A.T. Azar, S. Vaidyanathan (Eds.), Chaos Modeling and Control Systems Design, Springer International Publishing, Cham, 2015: pp. 351–391. doi:10.1007/978-3-319-13132-0_14.

19. F. Di Franco, M. Santamaria, G. Massaro, F. Di Quarto, Photoelectrochemical monitoring of rouging and de-rouging on AISI 316L, Corrosion Science. 116 (2017) 74–87. doi:10.1016/j.corsci.2016.12.016.

20. A. Di Paola, F. Di Quarto, C. Sunseri, A photoelectrochemical characterization of passive films on stainless steels, Corrosion Science. 26 (1986) 935–948. doi:10.1016/0010-938X(86)90084-3.

21. A. Di Paola, D. Shukla, U. Stimming, Photoelectrochemical study of passive films on stainless steel in neutral solutions, Electrochimica Acta. 36 (1991) 345–352. doi:10.1016/0013-4686(91)85260-E.

22. H. Jang, C. Park, H. Kwon, Photoelectrochemical study of the growth of the passive film formed on Fe-20Cr-15Ni in a pH 8.5 buffer solution, Met. Mater. Int. 16 (2010) 247–252. doi:10.1007/s12540-010-0413-0.

Chapter III

Passivation-induced physicochemical alterations of the native surface oxide film on 316L austenitic stainless steel

This chapter reproduces the final preprint of an original article published in the Journal of The Electrochemical Society with the reference:
Z. Wang, F.D. Franco, A. Seyeux, S. Zanna, V. Maurice, P. Marcus, Passivation-induced physicochemical alterations of the native surface oxide film on 316L austenitic stainless steel, J. Electrochem. Soc. 166 (2019) C3376-C3388, doi: 10.1149/2.0321911jes

Abstract

Time of Flight Secondary Ion Mass Spectroscopy, X-Ray Photoelectron Spectroscopy, *in situ* Photo-Current Spectroscopy and electrochemical analysis were combined to characterize the physicochemical alterations induced by electrochemical passivation of the surface oxide film providing corrosion resistance to 316L stainless steel. The as-prepared surface is covered by a ~2 nm thick, mixed (Cr(III)-Fe(III)) and bi-layered hydroxylated oxide. The inner layer is highly enriched in Cr(III) and the outer layer less so. Molybdenum is concentrated, mostly as Mo(VI), in the outer layer. Nickel is only present at trace level. These inner and outer layers have band gap values of 3.0 and 2.6-2.7 eV, respectively, and the oxide film would behave as an insulator. Electrochemical passivation in sulfuric acid solution causes the preferential dissolution of Fe(III) resulting in the thickness decrease of the outer layer and its increased enrichment in Cr(III) and Mo(IV-VI). The further Cr(III) enrichment of the inner layer causes loss of photoactivity and improved corrosion protection with the anodic shift of the corrosion potential and the increase of the polarization resistance by a factor of ~4. Aging in the passive state promotes the Cr enrichment in the inner barrier layer of the passive film.

III.1. Introduction

Stainless steels (SS) are widely used thanks to their excellent mechanical properties and corrosion resistance. Surface analytical studies, including X-Ray Photoelectron Spectroscopy (XPS), performed on ferritic Fe-Cr(-Mo) [1]-[19] and austenitic Fe-Cr-Ni(-Mo) [20]-[40] SS substrates have shown that a continuous and protective surface oxide/hydroxide layer, the

passive film, markedly enriched in Cr(III) and only a few nanometers thick when formed at ambient temperature, provides the corrosion resistance. The Cr enrichment in the passive film, which is the key factor for the corrosion resistance, is strong in acid aqueous environment because of the competitive dissolution of the iron and chromium oxide species and comparatively small dissolution rate of Cr(III) oxide. In alkaline aqueous solutions, the lower solubility of Fe(II)/Fe(III) oxides mitigates the Cr enrichment. For Ni-bearing SS, there is no or very little Ni(II) in the passive films and the metallic alloy region underneath the oxide is enriched with Ni(0) [20][21][22][27][28][29][30]. Mo-bearing SS, including austenitic AISI 316L, have better corrosion resistance in chloride-containing environments, where passive film breakdown can be followed by the initiation of localized corrosion by pitting. Mo(IV) or Mo(VI) oxide species enter the passive film composition at a few at% level without markedly altering the thickness [10][21][22][27][30][32][35]. Molybdenum has been proposed to mitigate passive film breakdown or to promote passive film repair.

The Cr(III) enrichment may not be homogeneous in the passive film, as suggested by recent studies performed at the nanometer scale [27][41], and the heterogeneities may cause the local failure of the corrosion resistance and of the initiation of localized corrosion [42]. These heterogeneities of Cr enrichment would find their origin in the mechanisms of pre-passivation leading to the initial formation, most often in air, of the native oxide and in the subsequent modifications of the oxide film induced by immersion in solution. The better understanding of the mechanisms governing the Cr enrichment requires to thoroughly investigate both the initial stages of oxidation leading to pre-passivation of the SS surface [43] and the modifications brought by electrochemical passivation of the native oxide-covered SS surface.

Here we report on the properties of the native oxide layer formed on a polycrystalline austenitic 316L SS surface in air and modified by electrochemical passivation in acid solution. Time-of-Flight Secondary Ion Mass Spectroscopy (ToF-SIMS) and XPS surface analysis were used to characterize the layered structure, thickness and composition of the oxide film and their modifications. Photocurrent Spectroscopy (PCS), applied *in situ* and combined with electrochemical analysis [44][45][46][47], was used to obtain direct information on the electronic properties of the thin photo-conducting surface films. Linear Scan Voltammetry and Electrochemical Impedance Spectroscopy were applied to discuss the corrosion resistance.

III.2. Experimental

Polycrystalline AISI 316L austenitic SS samples were used. The bulk wt% composition of the main alloying elements was Fe–19Cr–13Ni–2.7Mo (Fe–20Cr–12Ni–1.6Mo at%). Surface preparation was performed by mechanical polishing first with emery paper of successive 1200 and 2400 grades and then with diamond suspensions of successive 6, 3, 1 and 0.25 μm grades. Cleaning and rinsing was performed after each polishing step in successive ultrasonicated baths of acetone, ethanol and Millipore® water (resistivity > 18 MΩ cm). Filtered compressed air was used for drying. The R_a roughness of the as-polished surfaces was 2.4 nm measured by AFM on 10 × 10 μm^2 areas. The native oxide film was analyzed after short time (5-10 min) exposure in ambient air after surface preparation. The passive oxide film was formed by electrochemical passivation in a 3-electrode cell. The potential was stepped from open circuit value (U_{OC} = -0.23 V vs SCE) to U_{Pass} = 0.3 V vs SCE and maintained to this value for 1 or 20 hours. The selected value corresponded to the minimum of passive current in 0.05 M H_2SO_4 aqueous solution as determined from polarization curves (see Chapter V). The electrolyte was prepared from ultrapure chemicals (VWR®) and Millipore® water. No cathodic pre-treatment was performed in order to avoid any reduction-induced alteration of the initial native oxide film prior to passivation. The R_a roughness of the passivated surfaces was 2.1 nm measured by AFM on 10 × 10 μm^2 areas.

Depth profile elemental analysis of the oxide-covered surfaces was performed using a ToF-SIMS 5 spectrometer (Ion ToF – Munster, Germany) operated at about 10^{-9} mbar. The depth profile analysis interlaced topmost surface analysis in static SIMS conditions using a pulsed 25 keV Bi^+ primary ion source delivering 1.2 pA current over a 100 × 100 μm^2 area with sputtering using a 1 keV Cs^+ sputter beam giving a 32 nA target current over a 300 × 300 μm^2 area. Analysis was centered inside the eroded crater to avoid edge effects. The profiles were recorded with negative secondary ions that have higher yield for oxide matrices than for metallic matrices. The Ion-Spec software was used for data acquisition and processing.

Surface chemical analysis was performed by XPS with a Thermo Electron ESCALAB 250 spectrometer operating at about 10^{-9} mbar. The X-ray source was an AlK_α monochromatized radiation (hν = 1486.6 eV). Survey spectra were recorded with a pass energy of 100 eV at a step size of 1 eV. High resolution spectra of the Fe 2p, Cr 2p, Ni 2p, Mo 3d, O 1s, and C 1s core level regions were recorded with a pass energy of 20 eV at a step size of 0.1 eV. The take-off angles of the analyzed photoelectrons were 40° and 90°. The binding energies (BE) were calibrated by setting the C 1s signal corresponding to olefinic bonds ($–CH_2–CH_2–$) at 285.0 eV. Reconstruction of the spectra (curve fitting) was performed with CasaXPS, using a

Shirley type background. Asymmetry was taken into account for the metallic components (Cr^0, Fe^0, Mo^0, Ni^0) by using the peak shape of LA(α, β, m) [48]. Lorentzian/Gaussian (70%/30%) peak shapes and a broader envelope was used to account for the multiplet splitting of the oxide components (Cr^{III}, Fe^{III}, Mo^{IV}, Mo^{VI}) [48][49].

Photoelectrochemical and electrochemical analysis was performed using a Zennium electrochemical workstation (ZAHNER, Germany) operated with the Thales software. The measurements were performed in 0.1 M $Na_2B_4O_7$ electrolyte (di-Sodium tetraborate , pH ~9.5) prepared from pure chemicals (R.P.NORMAPUR®) and Millipore® water using a standard 3-electrode cell with a Pt spiral as the counter electrode and an Ag/AgCl (in 3.5 M KCl) electrode as reference electrode. This buffer solution was selected in order to provide stability to the oxide films during measurements and thus to minimize their alteration. The photocurrent spectra were recorded in the wavelength range from 310 to 700 nm with the Zahner Zennium CIMPS system (TLS-03) at a 3.16 Hz frequency. The electrochemical impedance spectra were generated by applying a sinusoidal signal of 10 mV amplitude over the frequency range 0.1 Hz–100 kHz. The spectra were analyzed with the Zview software.

III.3. Results and discussion

III.3.1.Surface analysis

III.3.1.1. Native oxide film

The ToF-SIMS negative ion depth profiles of the 316L stainless steel sample covered by the native oxide film are shown in Figure III-1. In Figure III-1a, the intensity profiles of secondary ions characteristic for the oxide film ($^{18}O^-$, $^{18}OH^-$, CrO_2^-, FeO_2^-, NiO_2^- and MoO_2^-) and the substrate (Cr_2^-, Fe_2^- and Ni_2^-) are plotted in logarithmic scale versus sputtering time. As proposed previously [50], the profile of the Ni_2^- ions is used to define the position of the "modified alloy" region between the oxide film and the metallic bulk substrate regions, where Ni is found enriched as observed previously on austenitic and duplex stainless steels [20]-[22][27]-[30][50]. This region is measured from 20 to 48 s of sputtering time, meaning that the oxide film region is from 0 to 20 s and the metallic substrate region after 48 s. The sputtering rate can be estimated to 0.1 nm s^{-1} based on the thickness of the oxide film of 2 nm determined by XPS as discussed below. In the surface oxide region, the most predominant profiles of the oxidized metals are those of the CrO_2^-, FeO_2^- and to a lesser extent MoO_2^- ions

while that of the NiO_2^- ions has much lower intensity, suggesting that only traces of oxidized nickel are present in the native oxide film as supported by the XPS analysis discussed below and in agreement with previous data [20]-[22][27]-[30].

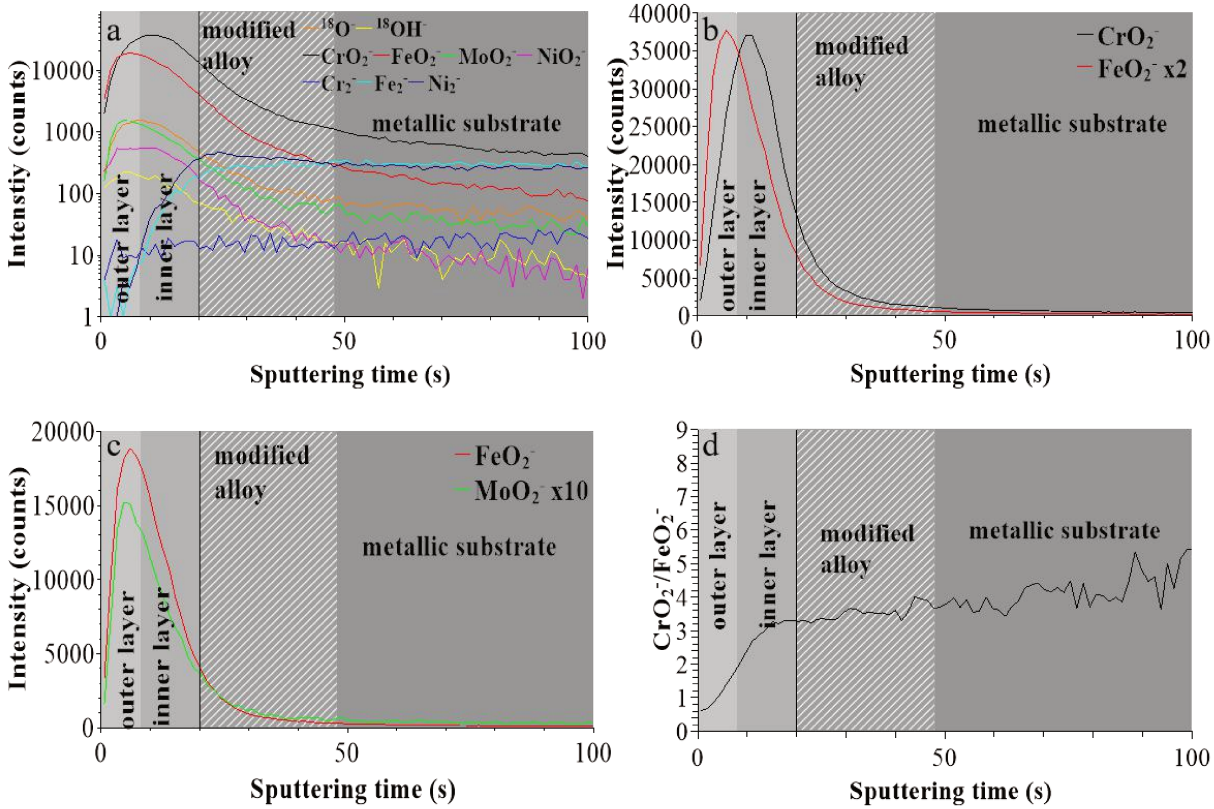

Figure III-1 ToF-SIMS depth profiles for the native oxide film on 316L SS: (a) $^{18}O^-$, $^{18}OH^-$, CrO_2^-, FeO_2^-, NiO_2^-, MoO_2^-, Cr_2^-, Fe_2^- and Ni_2^- secondary ions, (b) CrO_2^- and FeO_2^- secondary ions, (c) FeO_2^- and MoO_2^- secondary ions, (d) CrO_2^-/ FeO_2^- intensity ratio.

Figure III-1b and Figure III-1c compare the profiles of the secondary ions that are characteristic for the oxide species predominantly present in the surface film. Figure III-1b shows that the profiles of FeO_2^- and CrO_2^- ions peak at different positions, at 6 and 10 s, respectively. This is consistent with the native oxide film having a bilayer structure with iron and chromium oxides more concentrated in the outer and inner layers, respectively, as previously reported for oxide films on stainless steels [7][17][27][29][46]. The interface between outer and inner layer can be positioned at 8 s which is the median sputtering time position of the two intensity maxima. In Figure III-1c, the FeO_2^- and MoO_2^- ions profiles peak at the same position (6 s), showing very similar in-depth distributions of the iron and molybdenum oxide species concentrated in the outer layer of the oxide film. In order to confirm the partition of the concentration of the two major elements in the oxide film, the

intensity ratio of the CrO_2^- to FeO_2^- ions has been plotted *vs* sputtering time in Figure III-1d. According to this graph, the Cr/Fe ratio in the oxide increases in the outer part of the film. In the inner layer of the oxide film, the Cr/Fe ratio increases until 15 s and then becomes constant.

Figure III-2 shows the angle-resolved XPS Cr $2p_{3/2}$, Fe $2p_{3/2}$, Mo 3d, Ni $2p_{3/2}$ and O 1s core level spectra recorded at 90 and 40° take-off angles.

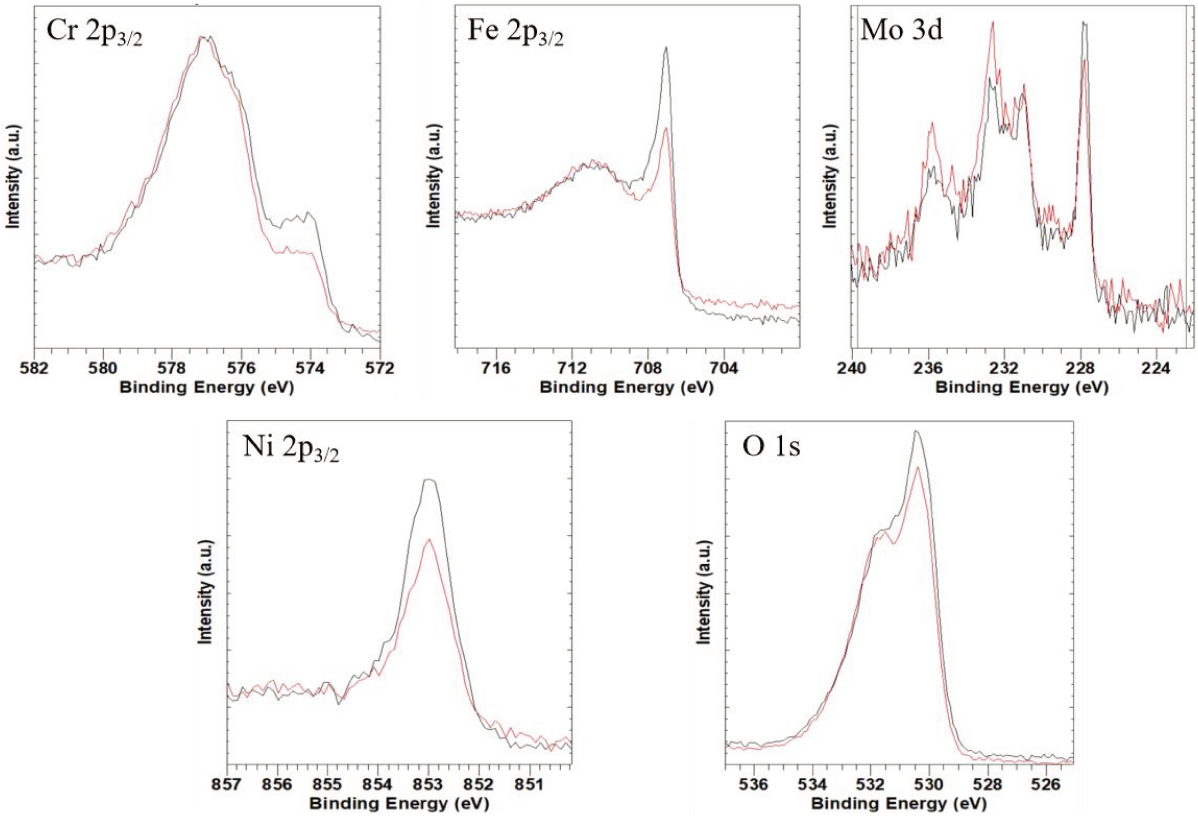

Figure III-2 Angle-resolved XPS core level spectra recorded at 40° (red line) and 90° (black line) take-off angle for the native oxide film on 316L SS: (a) Cr $2p_{3/2}$, (b) Fe $2p_{3/2}$, (c) Mo $3d_{5/2\text{-}3/2}$, (d) Ni $2p_{3/2}$ and (e) O 1s regions. The spectra were normalized in intensity at background level.

For the Cr $2p_{3/2}$, Fe $2p_{3/2}$ and Mo 3d core levels, the intensity ratio of the oxide peaks at higher BE (see below) to the metal peaks at lower BE (see below) increases with decreasing take-off angles, confirming that the oxide film lies above the metallic alloy substrate. The Ni $2p_{3/2}$ core level spectra show no oxide peaks at higher BE and an intensity decrease at lower take-off angle of the metal peaks. This is because Ni, only present in the metallic alloy, is increasingly attenuated by the surface oxide film. For the O 1s core level, the intensity ratio of the higher BE peak associated to OH^- ligands (see below) to the lower BE peak associated to O^{2-} ligands

(see below) is slightly higher at 90° than at 40°. This indicates some stratification in the depth distribution of the oxide/hydroxide ligands according to the bilayer structure of the oxide film with the hydroxide species more concentrated in the outer layer and the oxide species in the inner layer. This stratification was repeatedly observed and more marked in the passive films.

Figure III-3 shows the reconstruction of the XPS Cr $2p_{3/2}$, Fe $2p_{3/2}$, Mo 3d and O 1s core level spectra for the native oxide-covered sample. The BE values, Full Widths at Half-Maximum (FWHM) values and relative intensities of the component peaks obtained by curve fitting are compiled in Table III-1.

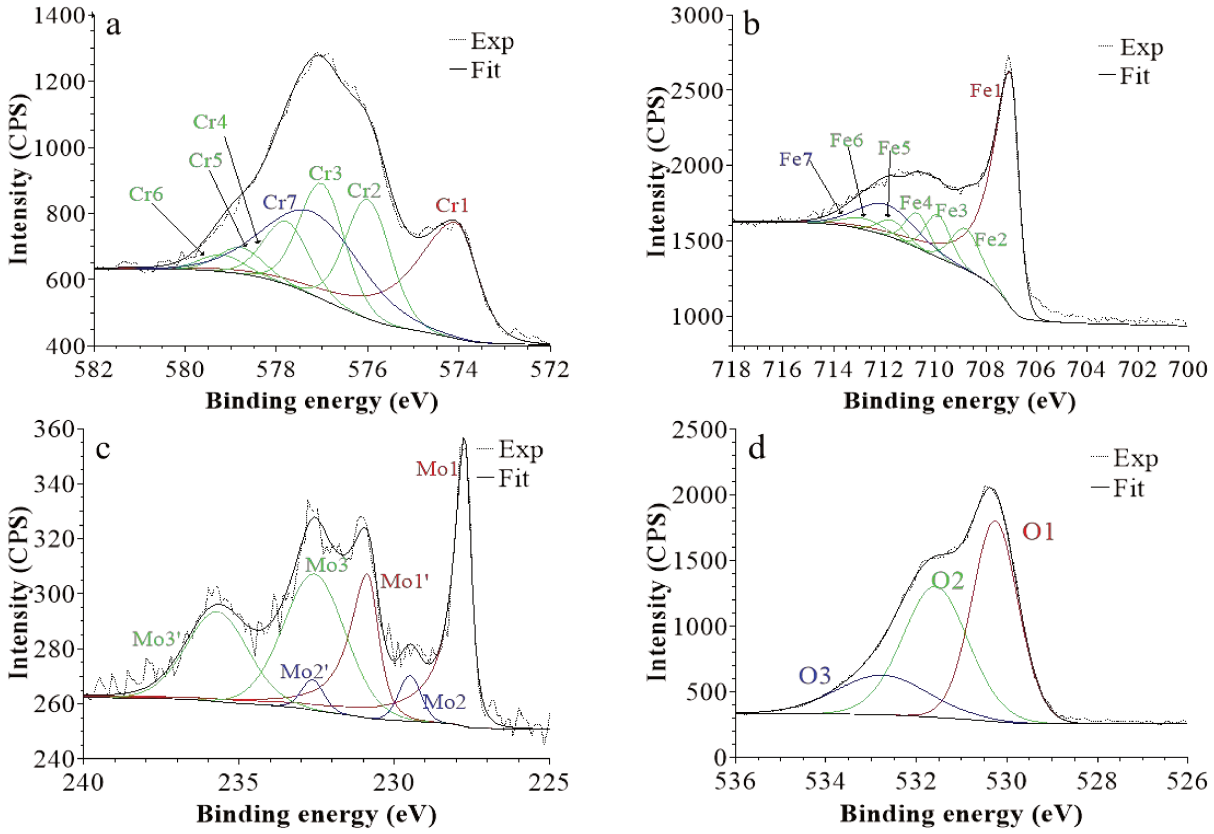

Figure III-3 XPS core level spectra and their reconstruction for the native oxide film on 316L SS: (a) Cr $2p_{3/2}$, (b) Fe $2p_{3/2}$, (c) Mo $3d_{5/2-3/2}$ and (d) O 1s regions (take-off angle: 90°).

The Cr $2p_{3/2}$ spectrum (Figure III-3a) was reconstructed using one peak (Cr1) at 574.1 eV, assigned to metallic Cr^0 in the substrate and a series of five peaks (Cr2-Cr6), assigned to Cr^{III} oxide in the surface oxide layer, as proposed previously [48][49]. It was verified that such a series of five peaks could fit the spectrum for an anhydrous thermal Cr oxide film grown by exposing a Cr substrate to gaseous oxygen in the XPS preparation chamber. In the present case, one additional peak (Cr7) at 577.2 eV, assigned to Cr^{III} hydroxide in the oxide film [2][16][20], was necessary to optimize the fit with the experimental envelope. Given the

lower relative intensity of this Cr7 component, it was deliberately chosen to use a single but wider peak rather than a series of five narrower peaks as done for the oxide component. No additional Cr^{VI} component at a BE of 579.5 eV [48] was needed.

Table III-1 BE, FWHM and relative intensity values of the peak components used for reconstruction of the XPS spectra on polycrystalline 316L SS after formation in ambient air of the native oxide film and after passivation at 0.3 V/SCE in 0.05 M H_2SO_4.

			Native oxide film			Passive oxide film 1 h			Passive oxide film 20 h		
Core level	Peak	Assignment	BE (±0.1 eV)	FWHM (±0.1 eV)	Intensity (%)	BE (±0.1 eV)	FWHM (±0.1 eV)	Intensity (%)	BE (±0.1 eV)	FWHM (±0.1 eV)	Intensity (%)
Fe $2p_{3/2}$	Fe1	Fe metallic	707.0	0.8	55.1	707.0	0.8	63.3	707.0	0.8	63.8
	Fe2	Fe^{III} oxide	708.8	1.3	8.9	708.8	1.2	8.2	708.9	1.2	8.5
	Fe3	Fe^{III} oxide	709.9	1.1	8.0	709.8	1.1	7.4	709.9	1.1	7.6
	Fe4	Fe^{III} oxide	710.7	1.1	6.3	710.7	1.1	5.7	710.8	1.1	5.9
	Fe5	Fe^{III} oxide	711.7	1.3	3.6	711.7	1.3	3.3	711.8	1.3	3.4
	Fe6	Fe^{III} oxide	712.8	2.0	3.6	712.8	2.0	3.3	712.9	2	3.4
	Fe7	Fe^{III} hydroxide	711.9	2.7	14.5	711.9	2.7	8.8	711.9	2.7	7.5
Cr $2p_{3/2}$	Cr1	Cr metallic	574.1	1.1	26.4	574.1	1.1	24.5	574.0	1.1	21.2
	Cr2	Cr^{III} oxide	576.0	1.2	17.8	576.2	1.4	17.4	576.1	1.3	19.0
	Cr3	Cr^{III} oxide	577.0	1.2	17.2	577.2	1.4	16.9	577.1	1.3	18.4
	Cr4	Cr^{III} oxide	577.8	1.2	9.4	578..0	1.4	9.2	577.9	1.3	10.1
	Cr5	Cr^{III} oxide	578.8	1.2	39	579.0	1.4	3.8	578.9	1.3	4.2
	Cr6	Cr^{III} oxide	579.2	1.2	2.5	579.4	1.4	2.4	579.3	1.3	2.6
	Cr7	Cr^{III} hydroxide	577.2	2.5	22.8	577.2	2.5	25.8	577.2	2.5	24.4
Mo $3d_{5/2}$	Mo1	Mo metallic	227.7	0.5	28.4	227.8	0.5	28.6	227.7	0.5	27.4
	Mo2	Mo^{IV} oxide	229.5	0.8	3.4	229.6	0.9	4.6	229.5	0.9	3.6
	Mo3	Mo^{VI} oxide	232.6	2.3	28.4	232.7	2.5	27.1	232.6	2.5	29.3
Mo $3d_{3/2}$	Mo1’	Mo metallic	230.9	0.8	18.8	230.9	0.9	18.8	230.8	0.8	18.1
	Mo2’	Mo^{IV} oxide	232.6	0.8	2.3	232.7	0.9	3.1	232.7	0.9	2.4
	Mo3’	Mo^{VI} oxide	235.7	2.3	18.8	235.8	2.5	17.9	235.6	2.5	19.3
Ni $2p_{3/2}$	Ni	Ni metallic	852.9	0.9	100	852.9	0.9	100	852.8	0.9	100
O 1s	O1	O^{2-}	530.3	1.2	43.1	530.3	1.2	33.7	530.3	1.2	40.5
	O2	OH^-	531.6	1.7	39.9	531.8	1.7	39.5	531.7	1.8	44.2
	O3	H_2O	532.8	2.4	17	532.7	2.5	26.9	532.8	2.5	15.3

Similarly, in the Fe $2p_{3/2}$ spectrum (Figure III-3b), the peak at 706.8 eV (Fe1) relates to metallic Fe^0 in the substrate and the series of five peaks (Fe2-Fe6) to Fe^{III} in the surface oxide layer [7][23][34][48][51][52]. The additional peak needed at 711.9 eV (Fe7) is assigned to

Fe^{III} hydroxide in the oxide film. No series of five peaks associated to Fe^{II} in the surface oxide layer was needed for reconstruction [48].

In the Mo $3d_{5/2-3/2}$ core level spectrum (Figure III-3c), the 5/2-3/2 doublet (Mo1/Mo1') of the metallic Mo^0 component is positioned at 227.5-230.6 eV [7][36]. The 5/2-3/2 doublets at 229.5-232.6 eV (Mo2/Mo2') and 232.6-235.7 eV (Mo3/Mo3') are assigned to Mo^{IV} and Mo^{VI} in the surface oxide layer, respectively [22][27][31][33][36][53]. The intensity ratio of the Mo^{VI} to Mo^{IV} doublets is ~8, indicating that Mo^{VI} species are mostly present.

The O 1s spectrum (Figure III-3d) was reconstructed with three components at 530.3 (O1), 531.6 (O2) and 532.9 (O3) eV assigned to the oxide (O^{2-}), hydroxide (OH^-) and water (H_2O) ligands in the oxide film [11][34]. The broader O3 component may be explained by surface contamination by species including double bonded oxygen. The OH^-/O^{2-} intensity ratio is 0.9 for the native oxide.

The Ni $2p_{3/2}$ spectrum (Figure III-2e) could be reconstructed with a single peak at 852.9 eV BE corresponding to metallic Ni^0 in the substrate [24], evidencing that the Ni oxide species, measured in the oxide film region by ToF-SIMS, were at trace level below the detection limit of XPS (~0.5 at%).

Based on the partition of the oxide film evidenced by the ToF-SIMS data and the depth distribution of the oxygen ligands measured by angle-resolved XPS, a bilayer model was built for quantitative processing of the XPS measured intensities [27]. The model, shown in Figure III-4, assumes a mixed chromium-iron oxide inner layer, neglecting any molybdenum content, and a mixed iron-chromium-molybdenum oxide/hydroxide outer layer.

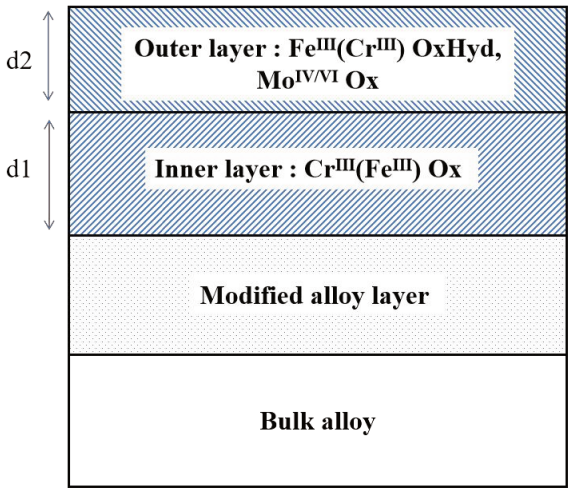

Figure III-4 Model of duplex oxide film on modified alloy substrate used for calculating thickness and composition from the XPS data

The equivalent thickness and composition of the outer and inner layers and the composition of the alloy underneath were calculated from the intensities of the oxidized and metallic components used for reconstruction: Cr2-Cr6 assigned to inner layer and Cr7 assigned to outer layer, Fe2-Fe4 assigned to inner layer and Fe5-Fe7 assigned to outer layer, Mo2-Mo3 assigned to outer layer, and Cr1, Fe1, Mo1 and Ni1 all assigned to modified alloy substrate. A classical model of intensity attenuation by continuous layers was used. The results are presented in Table III-2.

Table III-2 Thickness and composition of the native and passive oxide films on polycrystalline 316L SS as calculated form the XPS data based on the model in Figure III-4

		Global film	**Outer layer**	**Inner layer**	**Modified alloy**
Native film	d (nm)	2	0.8	1.2	/
	[Fe] (at%)	39	41	36	52
	[Cr] (at%)	55	44	64	18
	[Ni] (at%)	/	/	/	28
	[Mo](at%)	6	15	/	3
	Ratio Cr/Fe	1.4	1.1	1.8	/
Passive film 1h	d (nm)	1.9	0.7	1.2	/
	[Fe] (at%)	26	26	26	51
	[Cr] (at%)	67	56	74	20
	[Ni] (at%)	/	/	/	26
	[Mo](at%)	7	18	/	4
	Ratio Cr/Fe	2.6	2.2	2.8	/
Passive film 20h	d (nm)	1.9	0.6	1.3	/
	[Fe] (at%)	26	32	23	53
	[Cr] (at%)	68	49	77	16
	[Ni] (at%)	/	/	/	28
	[Mo](at%)	6	19	/	2
	Ratio Cr/Fe	2.6	1.5	3.3	/

The total thickness is found to be 2 nm, slightly larger than that (1.7 nm calculated using a similar model) reported for the native oxide film formed in air on a Fe–17Cr–14.5Ni–2.3Mo (wt%) single-crystalline surface prepared by mechanical polishing, electropolishing and high temperature annealing in reducing hydrogen atmosphere [27]. This difference might be due, at least partially, to the different surface preparation and the remaining presence of a cold-worked layer on the polycristalline mechanically polished surface. In the present case, the

thicknesses of the outer and inner layers of the surface oxide are 0.8 and 1.2 nm, respectively. Their ratio of 2/3 is in agreement with the value of ~8/12 obtained from sputtering time in the ToF-SIMS depth profiles, not far from the 41/59 value found on the single-crystalline surface [27].

The overall composition of the oxide film, obtained by weighting the cation concentration value of each element by the fractional thickness of the inner and outer layers, as well as the composition of the modified alloy beneath the oxide film are also shown in Table III-2. Chromium is found markedly enriched with Cr^{III} ions representing 55% of the metal cations in the film and slightly depleted (18 at% instead of 20 at% in the bulk alloy) in the modified alloy underneath the oxide film. The overall Cr/Fe ratio in the oxide film is 1.4 vs. 0.3 in the modified alloy. This ratio is found higher in the inner layer than in the outer layer of the oxide film, reproducing the trend evidenced by the ToF-SIMS depth profiles. Nickel, not found in measurable amount in the oxide film, is enriched in the alloy underneath the oxide film (28 at% instead of 12 at% in the bulk alloy), also in agreement with the ToF-SIMS depth profiles. These enrichments are quite similar to the results for the single-crystalline surface [27]. Concerning molybdenum, it is found enriched in the native oxide film (6 at% of $Mo^{IV/VI}$ instead of 1.6 at% of Mo^0 in the bulk alloy), more significantly than on the single-crystalline surface (2 at%) but also enriched in the alloy underneath the oxide film (3 at%), in contrast to the absence of enrichment found on the single-crystalline surface (1.5 at%), possibly also owing to the different surface preparation and/or microstructure effects.

III.3.1.2. Passive films

The ToF-SIMS negative ion depth profiles for the 316L stainless steel samples passivated in 0.05 M H_2SO_4(aq) are shown in Figure III-5 (1 h) and Figure III-6 (20 h). In the surface oxide regions, the most predominant profiles of the oxidized metallic elements remain those of the CrO_2^-, FeO_2^- and to a lesser extent MoO_2^- ions for both passive films (Figure III-5a and Figure III-6a). Like for the native oxide film, the NiO_2^- ions have much lower intensity. Using the Ni_2^- ions profiles and the same criterion as for the native oxide-covered sample, the metallic substrate regions are positioned at 49 s for both passive films. The oxide film is from 0 to 19 s for the 1 h passive film and from 0 to 20 s for the 20 h passive film, suggesting no marked variation of the overall thickness compared to the native oxide film. For both passive films, the modified alloy region is enriched in Ni as shown by the peaks (attenuated in

logarithmic scale) observed in the Ni2- ions profiles at the beginning of this region. This enrichment is confirmed by XPS (Table III-1)..

For the 1 h passivated sample, the profiles of the FeO_2^- and CrO_2^- secondary ions and FeO_2^- and MoO_2^- secondary ions are compared in Figure III-5b and Figure III-5c, respectively, using the same intensity scales as in Figure III-1. The FeO_2^- and CrO_2^- profiles also peak at different positions, 5 and 10 s, respectively, showing a bilayer structure also for the passive film with Fe and Cr oxides more concentrated in the outer and inner layers, respectively. By using the same method, we assign the outer/inner layer interface at 7 s. The FeO_2^- and MoO_2^- profiles both peak at 5 s and superimpose at longer sputtering time (Figure III-5c). The partition of the passive film is confirmed in Figure III-5d presenting the variation of the intensity ratio of CrO_2^- to FeO_2^- ions. The tendency of the curve is the same as for the native oxide film but with a higher Cr/Fe ratio, meaning that the passive oxide film has a higher chromium enrichment both in the outer and inner layers.

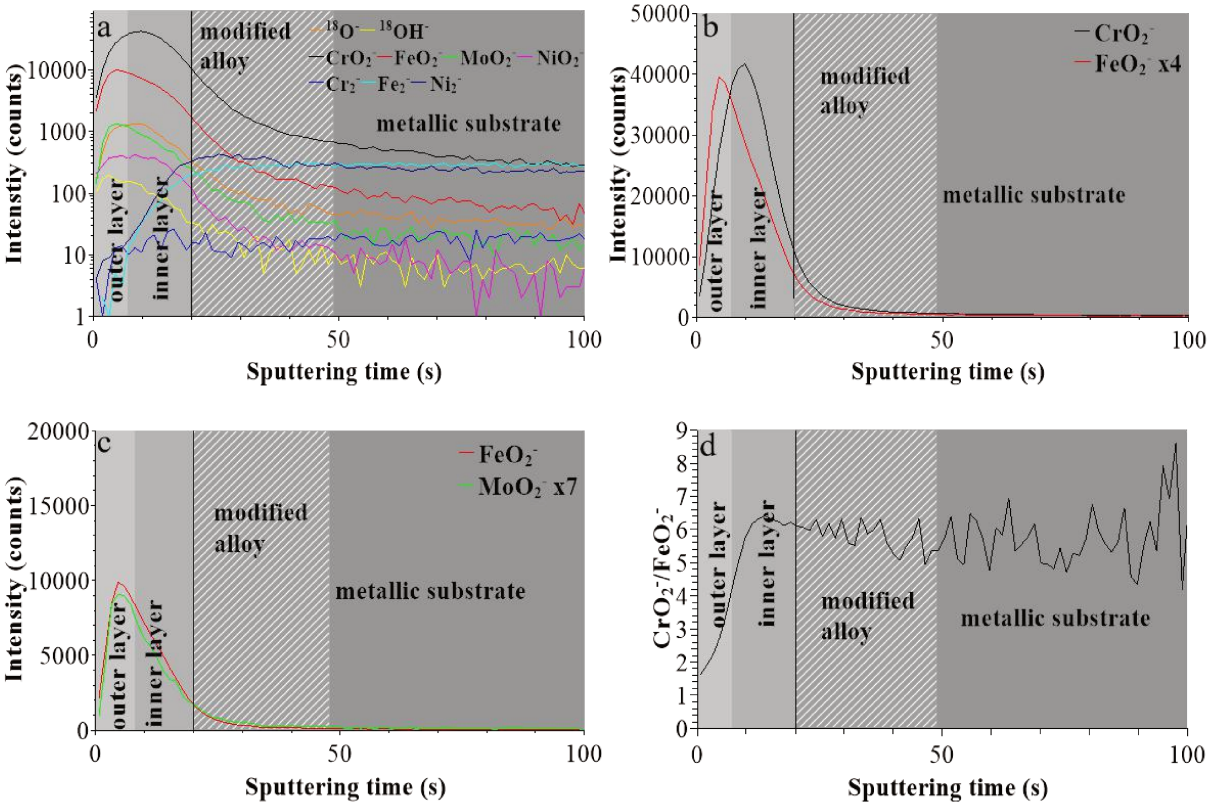

Figure III-5 ToF-SIMS depth profiles for 316L stainless steel passivated in 0.05 M H_2SO_4 at U_E= 0.3 V/SCE for 1 h : (a) $^{18}O^-$, $^{18}OH^-$, CrO_2^-, FeO_2^-, NiO_2^-, MoO_2^-, Cr_2^-, Fe_2^- and Ni_2^- secondary ions, (b) CrO_2^- and FeO_2^- secondary ions, (c) FeO_2^- and MoO_2^- secondary ions, (d) CrO_2^-/ FeO_2^- intensity ratio.

For the 20 h passivated sample, the FeO_2^- and CrO_2^- profiles, shown in Figure III-6b, also peak at different positions, 5 and 8 s, confirming the bilayer structure for the 20 h passive film with Fe and Cr oxides more concentrated in the outer and inner layers, respectively (interface is placed at 6 s). The FeO_2^- and MoO_2^- profiles both peak at 5 s and superimpose at longer sputtering time (Figure III-6c). The partition of the passive film is confirmed in Figure III-6d presenting the variation of the intensity ratio of CrO_2^- to FeO_2^- ions. The Cr/Fe ratio is slightly higher than that for the 1 h passive film, suggesting further Cr enrichment under the effect of aging in the passive state.

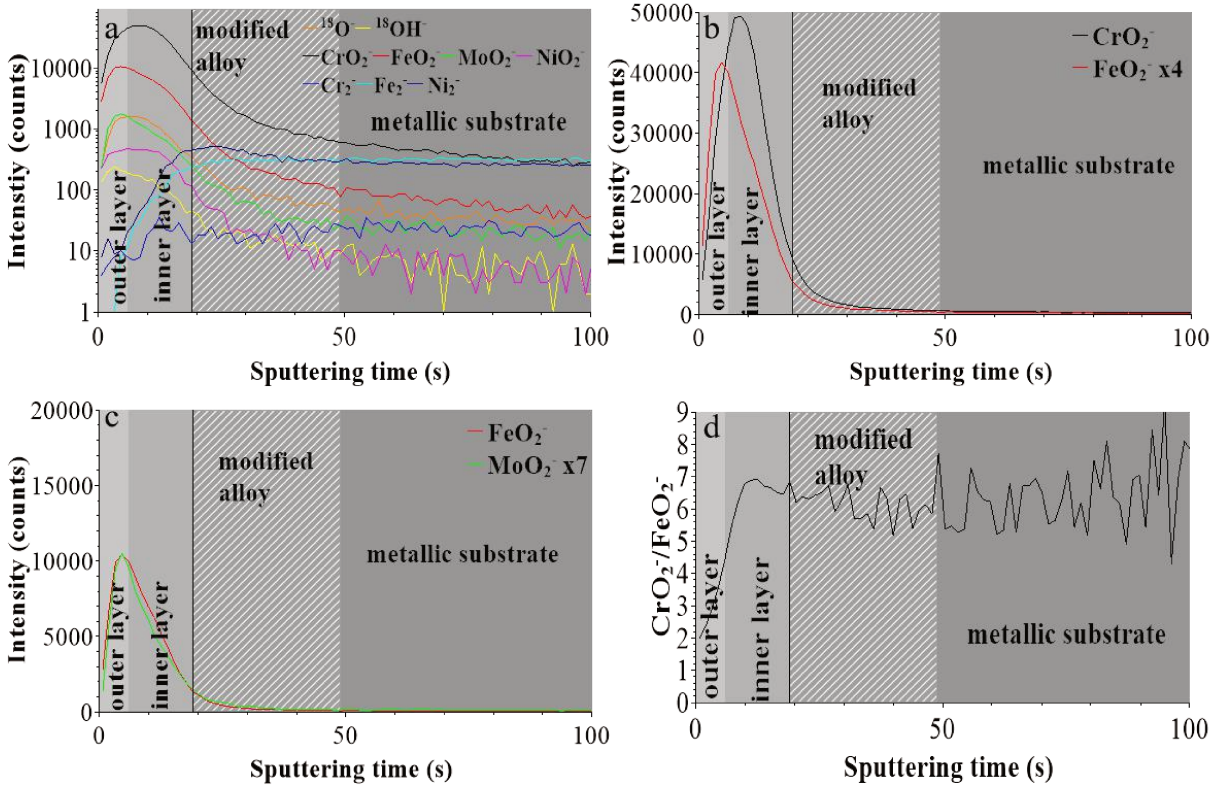

Figure III-6 ToF-SIMS depth profiles for 316L stainless steel passivated in 0.05 M H_2SO_4 at U_E= 0.3 V/SCE for 20 h : (a) $^{18}O^-$, $^{18}OH^-$, CrO_2^-, FeO_2^-, NiO_2^-, MoO_2^-, Cr_2^-, Fe_2^- and Ni_2^- secondary ions, (b) CrO_2^- and FeO_2^- secondary ions, (c) FeO_2^- and MoO_2^- secondary ions, (d) CrO_2^-/ FeO_2^- intensity ratio.

Figure III-7 compares the ToF-SIMS data for native oxide-covered and passivated samples. As expected under identical analytical conditions of the same substrate in all samples, the intensity of the Fe_2^- ions is the same in the metallic substrate region beyond 50 s (Figure III-7a). This means that no normalization is necessary to compare the profiles of the three samples. The shift towards shorter sputtering time of the increase in intensity of the Fe_2^- ions reflects the decrease in thickness of the surface oxide film; it is is noticeable for the 20 h

passive film only. The Cr content in the inner layer is higher on the two passivated samples, indicating increased Cr oxide enrichment after electrochemical passivation and a promoting effect of aging (Figure III-7b). In the outer layer, the Fe content is slightly decreased (Figure III-7c), indicating that preferential iron oxide dissolution in acid solution is the cause of the increasing Cr enrichment. A small increase of Mo oxide content in the outer layer is suggested after 20 h passivation but not confirmed after 1 h (Figure III-7d).

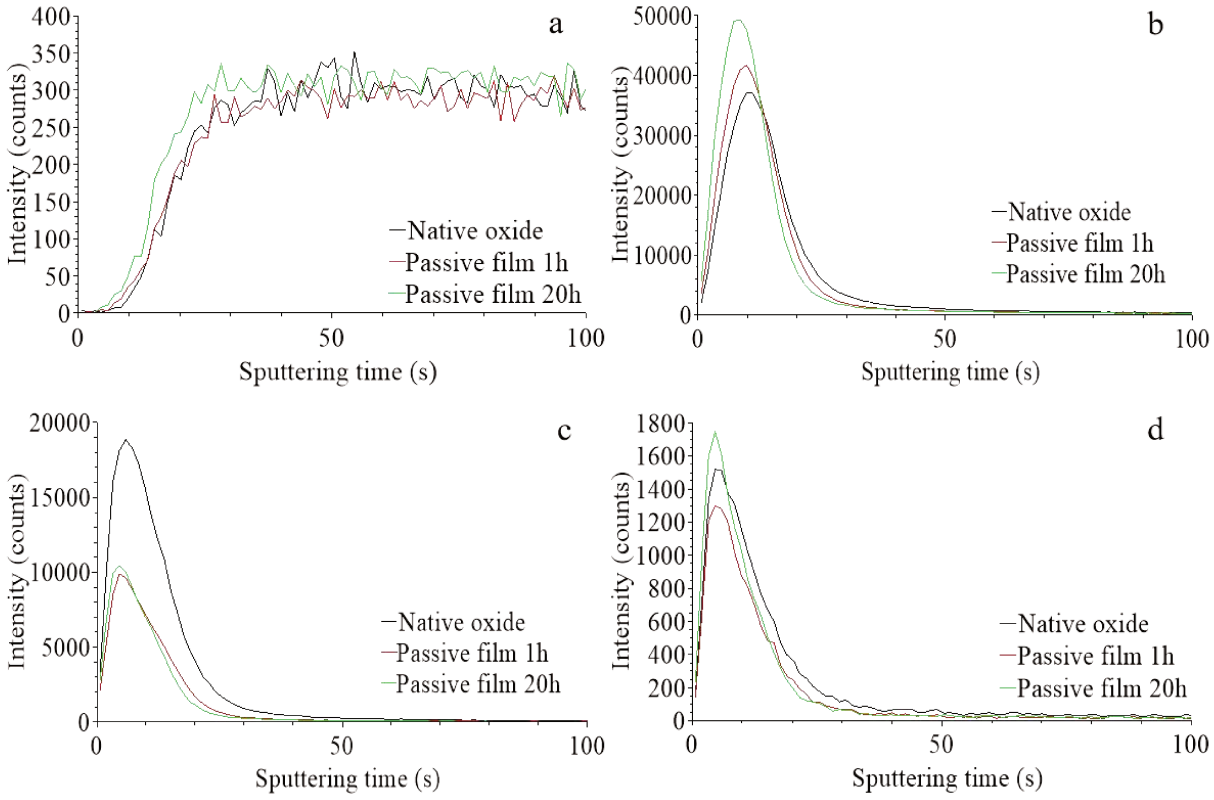

Figure III-7 Comparison of ToF-SIMS depth profiles for the native and passive oxide films: (a) Fe_2^- secondary ions, (b) CrO_2^- secondary ions, (c) FeO_2^- secondary ions, (d) MoO_2^- secondary ions

The XPS spectra recorded for the 1 h passivated sample are similar to those for the native oxide-covered sample (Figure III-8). The fitting results are also presented in Table III-1. The Cr $2p_{3/2}$ components associated to metallic Cr^0 in the substrate (Cr1), Cr^{III} oxide (Cr2-Cr6) and Cr^{III} hydroxide (Cr7) in the passive film are observed at 574.1 eV, 576.2-579.4 eV and 577.2 eV respectively (Figure III-8a) [13][16][33][48][49]. The Fe $2p_{3/2}$ components associated to metallic Fe^0 in the substrate (Fe1), Fe^{III} oxide (Fe2-Fe6) and Fe^{III} hydroxide (Fe7) in the passive film are observed at 707 eV, 708.8-712.8 eV and 711.9 eV respectively (Figure III-8b) [7][22][23][34][48][51][52]. The Mo $3d_{5/2-3/2}$ doublet components associated to metallic Mo^0

in the substrate and Mo^{IV} and Mo^{VI} in the passive film are observed at 227.8-230.9 eV, 229.6-232.7 eV and 232.7-235.8 eV, respectively (Figure III-8c) [31][33][36][53]. Since passivation was performed in sulfuric acid, a S 2s peak at 232.9 eV had to be considered. The presence of sulfate was confirmed by the S 2p spectrum (signal at 168.9 eV, see Chapter V). The intensity ratio of the Mo^{VI} to Mo^{IV} doublets is ~6. The three O 1s components assigned to the oxide (O^{2-}), hydroxide (OH^-) and water (H_2O) ligands in the oxide film are observed at 530.3, 531.8 and 532.7 eV, respectively (Figure III-8d) [11][34]. The intensity ratio of OH^-/O^{2-} is 1.2 for the 1 h passivated sample, higher than for the native oxide-covered sample (0.9). It was confirmed by comparing the C 1s spectra that the increase of this component is not related to a higher carbonate contamination on the passivated sample, so that it can be concluded that the passive film is indeed more hydroxylated than the native oxide film as expected after formation in the aqueous solution.

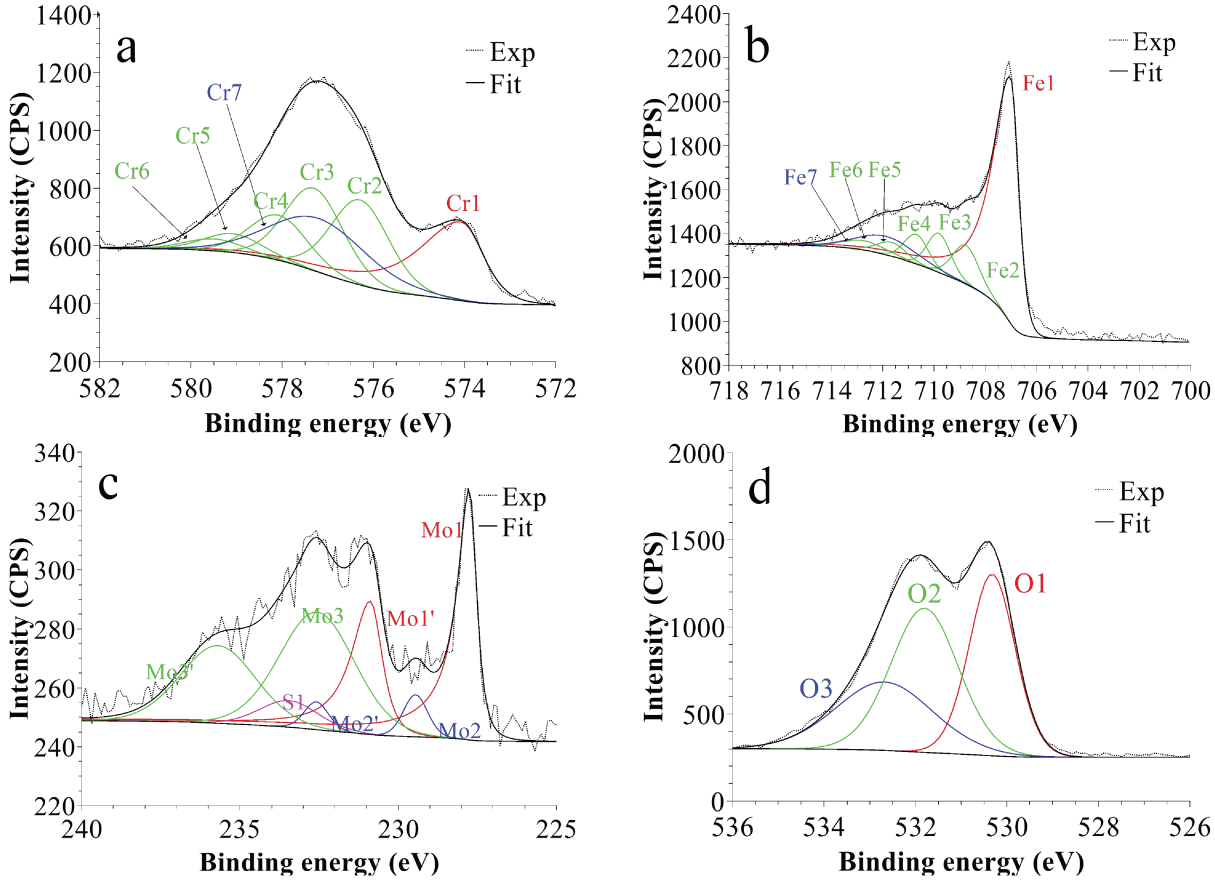

Figure III-8 XPS core level spectra and their reconstruction for 316L SS passivated in 0.05 M H_2SO_4 at U_E= 0.3 V/SCE for 1 h: (a) Cr $2p_{3/2,}$ (b) Fe $2p_{3/2,}$ (c) Mo $3d_{5/2-3/2}$ and (d) O 1s regions (take-off angle: 90°).

Figure III-9 shows the XPS spectra for the 20 h passivated sample. The fitting results are presented in Table III-1. The BE positions and FWHM values of component peaks are identical within ±0.1 eV to those for the 1 h passive and native oxide films. Only slight changes of the relative intensities are observed. Noteworthy is the slight decrease of the OH^-/O^{2-} intensity ratio to 1.1, indicating that dehydroxylation of the passive film is promoted by aging in the passive state in agreement with previous studies [2][20][27].

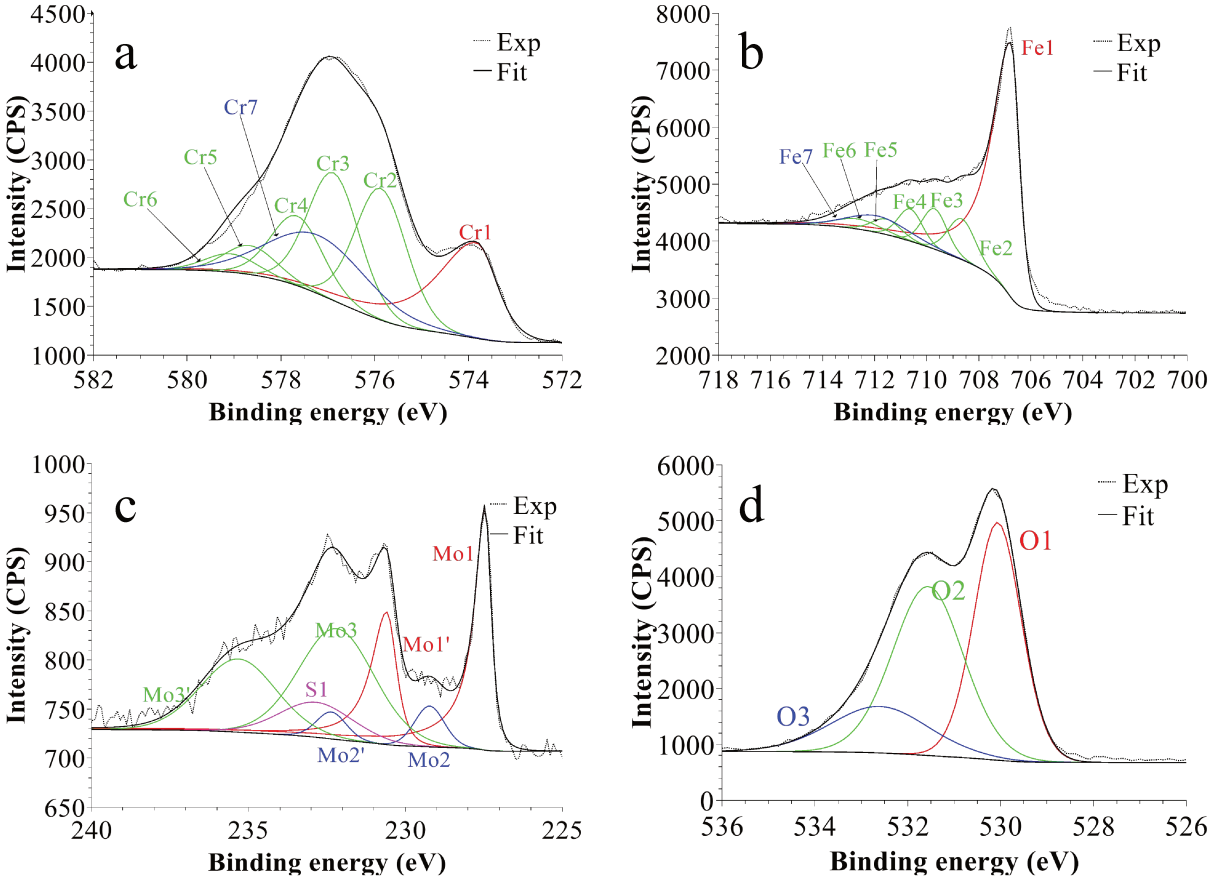

Figure III-9 XPS core level spectra and their reconstruction for 316L SS passivated in 0.05 M H_2SO_4 at U_E= 0.3 V/SCE for 20 h: (a) Cr $2p_{3/2,}$ (b) Fe $2p_{3/2,}$ (c) Mo $3d_{5/2\text{-}3/2}$ and (d) O 1s regions (take-off angle: 90°).

Using the same model of the bilayer structure (Figure III-4), thickness and composition of the 1 h and 20 h passive films were calculated (Table III-2). Compared with the native oxide film, the slight decrease of the thickness suggested by ToF-SIMS is confirmed and concentrated in the outer layer. We calculate values of 0.7 nm for 1 h and 0.6 nm for 20 h passivation instead of 0.8 nm for the native oxide. The composition of outer layer is calculated as 26%Fe^{III}-56%Cr^{III}-18%$Mo^{IV/VI}$ for 1 h and 32%Fe^{III}-49%Cr^{III}-19%$Mo^{IV/VI}$ for 20 h passivation instead

of 41%Fe^{III}-44%Cr^{III}-15%$Mo^{IV/VI}$ for the native oxide, confirming chromium and molybdenum enrichment after passivation. The inner layer composition is 26%Fe^{III}-74%Cr^{III} for 1 h and 23%Fe^{III}-77%Cr^{III} for 20 h passivation instead of 36% Fe^{III}-64% Cr^{III} for the native oxide. It reproduces the increased balance in favor of chromium also observed by ToF-SIMS (Figure III-5d and Figure III-6d) and reflected by the increase of the Cr/Fe ratio calculated from the XPS data (Table III-2). The global composition of the film also reflects the increase of the chromium enrichment induced by passivation. The Cr^{III} concentration increases to 67% in the oxide film after 1 h passivation versus 55% in the native oxide but remains constant after 20 h passivation (68%). The passivation-induced $Mo^{IV/VI}$ enrichment of the oxide film outer layer is not marked when considering the global composition of the oxide. The alloy underneath the oxide film is found still markedly enriched in nickel and only slightly in molybdenum after passivation. The slight chromium depletion observed underneath the native oxide seems vanished after 1 h passivation and would reappear after longer passivation.

These modifications of the oxide film composition are consistent with the preferential iron oxide dissolution induced by passivation in acid solution [16][27][30][32][37]. Comparing with the results reported for the single-crystalline surface [27], the differences observed in the present case are the absence of variation of thickness of the inner layer of the oxide film after passivation whereas an increase was observed on the single-crystalline surface. The decrease in chromium depletion in the alloy underneath the film observed after 1 h passivation was also observed on the single-crystalline surface. The effect of aging in the passive state is to increase the Cr enrichment in the inner layer of the oxide film, considered as the barrier layer, but not in the outer layer, considered as an exchange layer with the electrolyte. It confirms previous findings on Mo-free austenitic [20] and ferritic [2][12] SS. Concerning molybdenum, its enrichment in the outer layer as well as its overall concentration in the oxide film do not seem to be promoted by aging in the passive state, nor its enrichment in the modified alloy underneath the passive film. The confinement of MoIV/VI enrichment in the outer layer of the passive film is in agreement with previous works in the presence of molybdates [22][30][32]. It is supportive of the bipolar model developed to explain how molybdenum would mitigate passive film breakdown [34]-[36].

III.3.2. Photoelectrochemical characterization

III.3.2.1. Native oxide

The photoelectrochemical study was conducted in 0.1 M $Na_2B_4O_7$ electrolyte (pH ~ 9.5) at open circuit potential U_{OC} = -0.07 V vs Ag/AgCl and at slightly higher potential (U_E = 0.2 V vs Ag/AgCl in order to minimize the changes in the oxide film composition induced by anodic polarization. Figure III-10a shows the photocurrent spectrum recorded at U_{OC} on the native oxide film. The decrease of the photocurrent efficiency to noise level with increasing wavelength (decreasing energy) is consistent with the presence of a surface oxide film with an optical band gap at the interface between electrolyte and metal substrate. It is possible to estimate a band gap value using eq. III-1, valid for an indirect optical transition and photon energies close to the band gap value [54]:

$$(Q_{ph}\, h\nu)^n \propto (h\nu - Eg) \qquad \text{eq.III-1}$$

where hν is the photon energy and E_g is the optical band gap (or mobility gap for amorphous materials); n is assumed to be 0.5 for non-direct optical transitions [54][55]. The photocurrent yield Q_{ph} is assumed to be proportional to the light absorption coefficient. It is defined as:

$$Q_{ph} = \frac{I_{ph}}{e\phi_0(1-R)} \qquad \text{eq.III-2}$$

where I_{ph} is the collected photocurrent and e the electron charge. The incident photon flux on the interface Φ_0 is corrected for the reflection at the metal/oxide/electrolyte interface with R being the total reflectivity of the junction.

The inset of Figure III-10a shows the $(Q_{ph}\cdot h\nu)^{0.5}$ vs hν plot. Two linear regions are evidenced. From the line fitting of the high energy region, one estimates an optical band gap close to 3.0 eV by extrapolating the $(Q_{ph}h\nu)^{0.5}$ value to the noise level set at 1×10^{-3} a.u.. Using the same procedure, a band gap close to 2.7 eV is estimated from the line fitting of the low energy region.

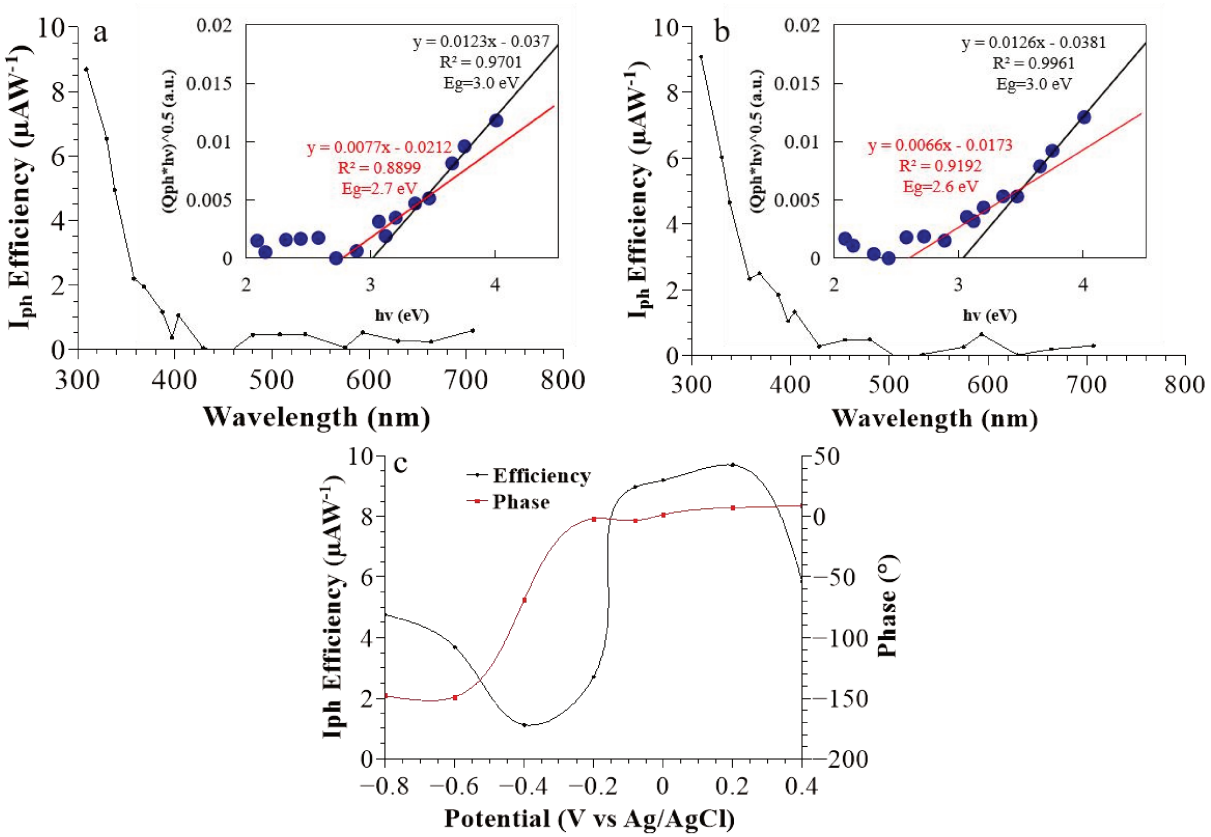

Figure III-10 PCS analysis in 0.1 M $Na_2B_4O_7$ of the native oxide film on 316L SS: (a,b) photocurrent spectra and $(Q_{ph}h\nu)^{0.5}$ vs $h\nu$ plots (insets) at (a) U_{OCP} = - 0.07 V vs Ag/AgCl and (b) at U_E= 0.2 V vs Ag/AgCl; (c) photocurrent and phase vs applied potential for λ = 309 nm.

Figure III-10b shows the photocurrent spectrum recorded at U_E = 0.2 V vs Ag/AgCl for the same native oxide sample. No marked difference is observed between the two spectra. Also in this case, the $(Q_{ph}\cdot h\nu)^{0.5}$ vs hν plot evidences two linear regions (see inset of Figure III-10b), with band gap values estimated to 3.0 eV and 2.6 eV from the high and low energy regions, respectively, in agreement with the values determined at open circuit potential. Thus, anodic polarization at 0.2 V vs Ag/AgCl does not induce marked alterations of the passive film, as suggested by the absence of variation of the band gap values. The partition in two linear regions of the $(Q_{ph}\cdot h\nu)^{0.5}$ vs hν plots can be associated with the bilayer structure of the oxide film evidenced by ToF-SIMS and confirmed by XPS, owing to the different chemical composition of the outer and inner layers. A two-region partition of the photocurrent spectra was also found for thermal oxide films formed on bright-annealed ferritic stainless steel [46], and on passive films formed on austenitic stainless after immersion in high pressurized water [45] and after electrochemically-induced rouging [47]. A bilayer structure of the surface oxide

films with outer and inner layers of different chemical composition and associated to different band gap values was also formed in these cases.

The plots of the photocurrent efficiency and phase recorded versus applied potential at a wavelength of 309 nm are shown in Figure III-10c. The marked drop of the photocurrent at $U_E \geq$ 0.2 V vs Ag/AgCl can be the result of the very high electric field modifying the surface oxide film in this potential range. At lower applied potentials, the photocurrent variation is inversed when shifting in the cathodic direction. The photocurrent first decreases between 0.2 and -0.4 V, as typical for anodic photocurrent, and then increases between -0.4 and -0.8 V as typical for cathodic photocurrent. The variation of the photocurrent phase shows a transition centered at about -0.4 V, from about 10° in the anodic region to about -150° in the cathodic region. This behavior characterizes an insulating material, for which depending on the applied potential with respect to the flat band potential and thus on the direction of the electric field both anodic and cathodic photocurrents can be measured [47]. Since for insulating layers the flat band potential can be assumed to be close to the inversion photocurrent potential, we can estimate the flat band potential of the native oxide film formed on 316L SS to be about -0.4 V vs Ag/AgCl at pH ~9.5. This value is in agreement with the value reported for passive films grown on pure chromium [55]. Due to the very low thickness of the oxide film, we cannot exclude that the cathodic photocurrent arises from electron photoemission processes [45]. In this case the oxide would behave as a thin n-type semiconductor.

In order to confirm the sign of the generated photocurrent, current vs time plots were recorded at different U_E values under constant wavelength while manually chopping the irradiation (Figure III-11). The generated photocurrent changes from anodic to none when the applied potential changes from 0.1 to -0.4 V vs Ag/AgCl. The drop to zero at U_E= -0.4 V is consistent with the data reported in Figure 7c and the determination of the flat band potential. The cathodic current expected at lower applied potential cannot be detected because the background current is too high.

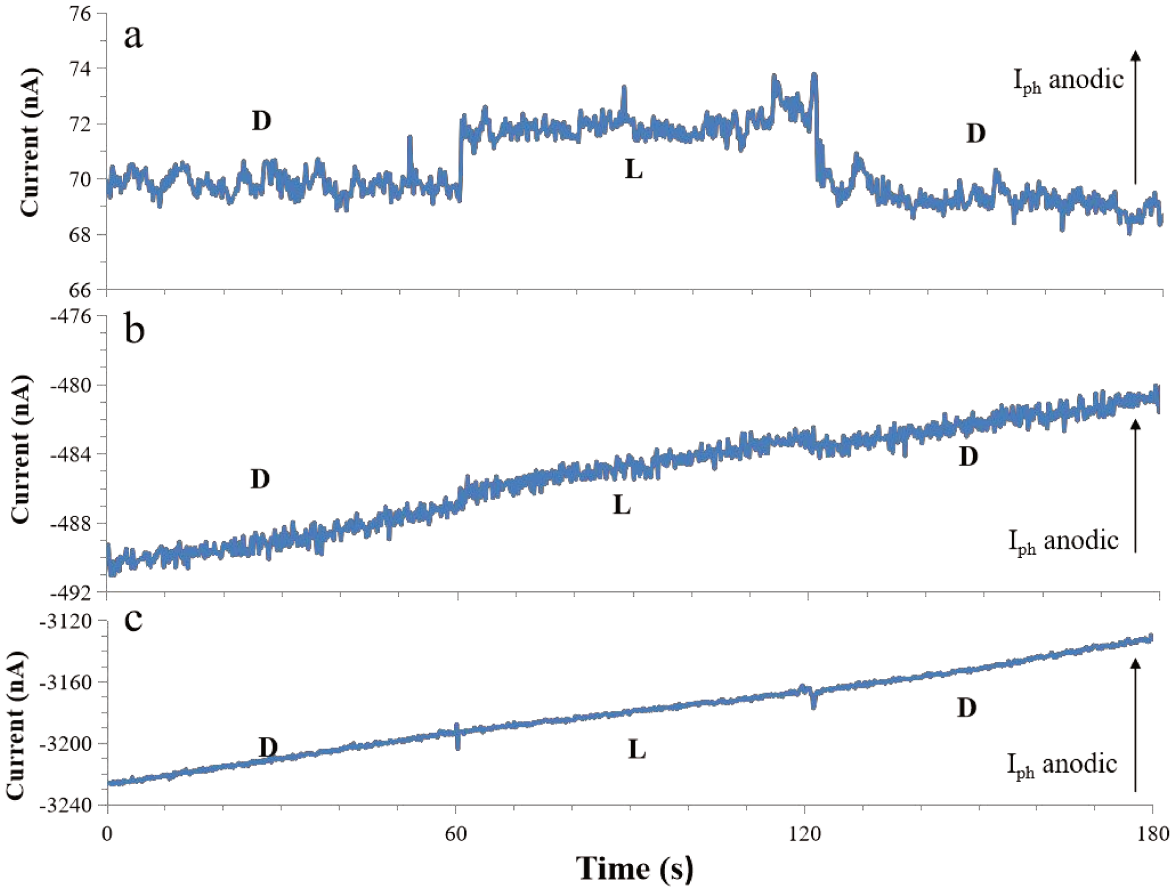

Figure III-11 Photocurrent vs time as measured in 0.1 M $Na_2B_4O_7$ under polarization without (D) and with (L) illumination (λ=309 nm) on the native oxide-covered 316L SS sample: (a) U_E= 0.1 V vs Ag/AgCl. b) U_E= -0.2 V vs Ag/AgCl c) U_E= -0.4 V vs Ag/AgCl.

III.3.2.2. Passive films

The photocurrent spectra for the austenitic stainless steel samples passivated in 0.05 M H_2SO_4 at U_{Pass}= 0.3 V/SCE are presented in Figure III-12. They were obtained in 0.1 M $Na_2B_4O_7$ at U_E = 0.2 V vs Ag/AgCl and can thus be directly compared to that for the native oxide film. For both passivated samples, the photocurrent efficiency is lower than for the native oxide-covered sample mostly at low wavelength (high energy), meaning that the passive films are less photoactive in this region associated with the inner layer of the oxide films. The low measured photocurrents prevent a reliable determination of the band gap as made for the native oxide film.

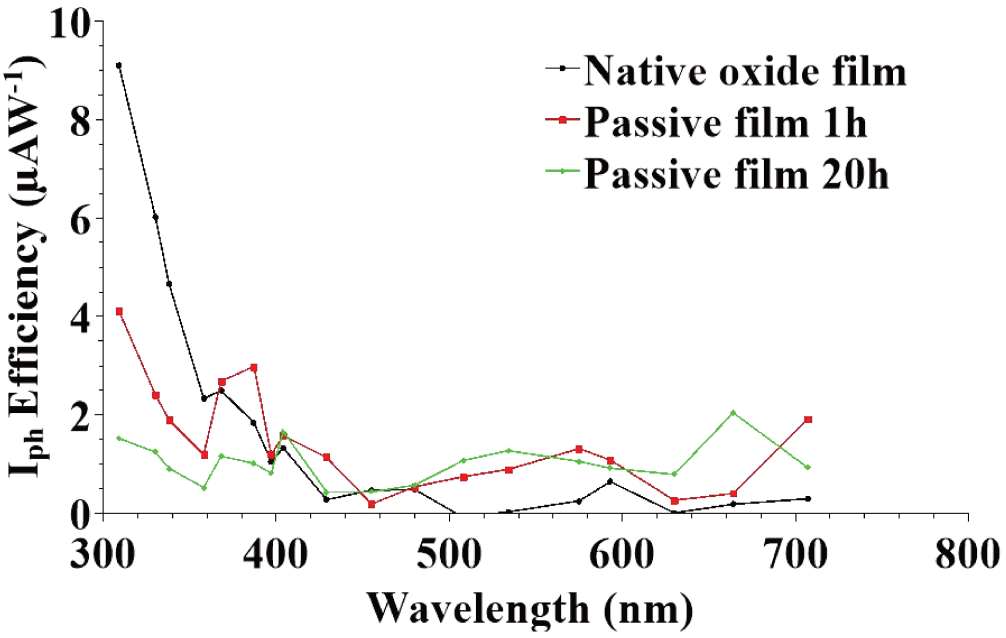

Figure III-12 PCS analysis in 0.1 M $Na_2B_4O_7$ for 316L stainless steel passivated in 0.05 M H_2SO_4 at U_E= 0.3 V/SCE for 1 h and 20 h and comparison with the native oxide-covered sample.

According to the XPS and ToF-SIMS results, the main passivation-induced alterations of the oxide film are (i) slight decrease in thickness, (ii) higher hydroxylation of the oxide matrix, (iii) Mo enrichment and (iv) Cr enrichment. The slight decrease in thickness affects the outer layer as a result of preferential iron oxide dissolution induced by passivation. Hydroxylation is also mostly concentrated in the outer layer as shown by the angle-resolved XPS data (Figure III-2e). As for the Mo enrichment, it increases in the outer layer as discussed above. In contrast, the Cr enrichment increases in both layers after passivation as discussed and it may be at the origin of the loss of photo-activity observed after passivation. Besides, its slight increase with passivation time is also in agreement with increase loss of photo-activity after 20 h passivation.

III.3.2.3. Modeling

In order to get a more precise estimate of the optical band gap and photo-generated carriers transport properties of the two in-series layers of the oxide films, we have applied a model previously proposed to simulate the photoelectrochemical behavior of bilayered films [56][57]. According to this model, the collected photocurrent can be calculated as the sum of

the contributions coming from each layer for the bilayered structure. The following equation is used for interpolating the experimental data:

$$(Q \cdot h\nu)^{1/2} = \left[\left(T_{out} G_{out} + e^{-\alpha_{out} D_{out}} \times T_{inn} G_{inn}\right) h\nu\right]^{1/2} \quad \text{eq.III-3}$$

In this equation, the subscripts "inn" and "out" refer to the inner and outer layers, respectively, G and T to the generation and transport term in each layer, respectively, α_{out} to the absorption coefficient of photon by the outer layer, and D_{out} to the thickness of the outer layer. The photon flux impinging the inner layer surface is assumed to be $\Phi_0 e^{-\alpha_{out} D_{out}}$.

The expressions for the G and T terms are [57]:

$$G = \eta_g \left[1 - \exp(-\alpha D)\right] \quad \text{eq.III-4}$$

and

$$T = \frac{\mu\tau F}{D}\left[1 - \exp\left(-\frac{D}{\mu\tau F}\right)\right] \quad \text{eq.III-5}$$

where η_g (λ, F) is the generation efficiency, lower than 1 as result of geminate recombination effects in disordered materials at low electrode potentials with respect to the flat band potential [58]. α is the absorption coefficient at the given wavelength, D the total film thickness ($D = D_{out} + D_{inn}$) and F the electric field inside the film. μ and τ are the mobility and lifetime of the photogenerated carriers (holes, h, and electrons, e), respecting the following equation:

$$\mu\tau = \mu_e\tau_e + \mu_h\tau_h \quad \text{eq.III-6}$$

In order to take into account possible multiple reflection effects at the metal/oxide interface, an average value of the total reflectivity, R, of the electrolyte/surface oxide film/metal junction has been estimated under the hypothesis of a single absorbing layer on an absorbing substrate [59]. The refractive indexes relating to water [60], the composition of surface oxide [61]and stainless steel [62]were used.

Figure III-13 presents the experimental $(Q \cdot h\nu)^{0.5}$ vs hν plots and their fit according to eq. III-4 for the native oxide film. The D_{out} and D_{inn} values obtained by XPS have been used. The fitted values of α, in the range 10^5 - 10^3 cm^{-1} for the Fe-rich outer layer and 10^4 - 10^2 cm^{-1} for the Cr-rich inner layer are in quite good agreement with the values usually reported for iron and chromium oxides [63][64]. Table III-3 presents the other fitting parameters. For the native

oxide film, the band gap of the inner layer is 3.3 eV and the band gap of the outer layer is 2.4 eV. These two values are in reasonable good agreement with those obtained by linear fitting of the $(Q_{ph} \cdot h\nu)^{0.5}$ vs hν plots (Figure III-10). For the passive films, no fits of the experimental curves could be achieved due to the weak measured photo currents (Figure III-12).

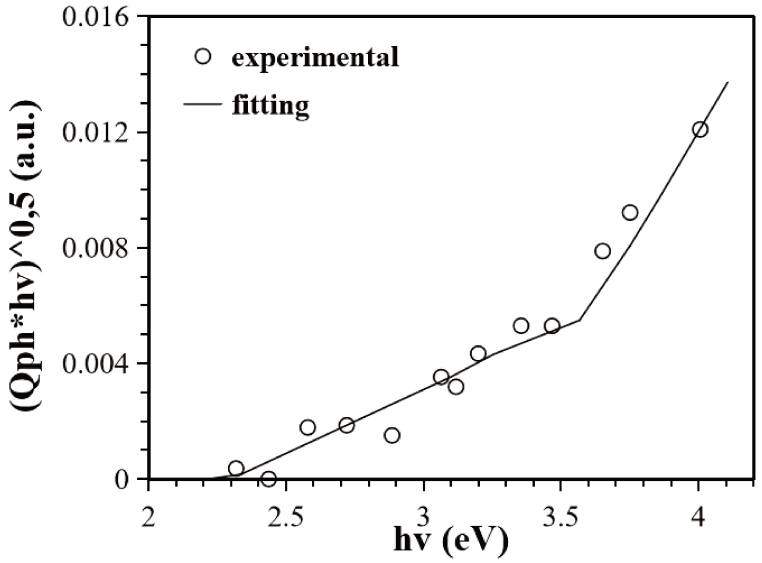

Figure III-13 Fit (continuous line), according to eq. (3), of the experimental $(Qh\nu)^{1/2}$ vs hν plots (points) for the native oxide film

Table III-3 Best fit parameters for fitting, according to eq. III-3 the photo current plots in Figure III-10

Sample	$(\mu\tau)_{inn}$ ($cm^2\ V^{-1}$)	$E_{g\ inn}$ (eV)	$(\mu\tau)_{outer}$ ($cm^2\ V^{-1}$)	$E_{g\ outer}$ (eV)
Native oxide film	3.0×10^{-18}	3.3	4.0×10^{-17}	2.4

According to previous works [64][65][66], the bandgap value of mixed oxides AaBbOo depends on the electronegativity of the oxide. For d-metal oxides, the relationship is the following:

$$Eg - \Delta Eam\ (eV) = 1.35\ (\chi av - \chi O)^2 - 1.49 \qquad \text{eq.III-7}$$

where χO is the oxygen electronegativity (3.5 in the Pauling scale) and χav an average electronegativity parameter defined as the arithmetic mean between the electronegativity of the metal partners in the oxides, i.e.:

$$\chi_{av} = \frac{a}{a+b}\chi_A + \frac{b}{a+b}\chi_B \qquad \text{eq.III-8}$$

ΔEam = 0 for crystalline oxides, whilst increasing values are expected (up to around 0.5 eV) if the lattice disorder affects the density of states distribution both near the valence and conduction band edges [58].

In our case, we can develop eq.III-9 based on eq.III-8:

$$\chi_{av} = \frac{a}{a+b+c}\chi_A + \frac{b}{a+b+c}\chi_B + \frac{c}{a+b+c}\chi_c \qquad \text{eq.III-9}$$

For the native oxide film the composition of the outer and inner layers are taken as 41%Fe-44%Cr-15%Mo and 36%Fe-64%Cr, respectively, from the XPS data (Table III-2). We assume χFe^{3+} = 1.9 ± 0.05, χCr^{3+} = 1.6 ± 0.05 and χMo^{6+} = 1.65 ± 0.05. Using eq. III-7 and eq. III-9 we can calculate the theoretical values of the band gaps and, considering the electronegativity uncertainty, obtain values of 2.7 ± 0.3 eV and 2.8 ± 0.3 eV for the outer and inner layers, respectively (considering ΔE_{am} is 0 eV). These values are in reasonable good agreement with the values obtained by the modeling of the experimental data of Figure III-10. For the passive films, the theoretical values of the band gaps can also be calculated from the composition of the layers determined by surface analysis. Considering the compositions of 26%Fe-56%Cr-18%Mo and 23%Fe-77%Cr for the outer and inner layers of the 1 h passive film, we obtain values of 2.9 ± 0.3 eV and 3.0 ± 0.3 eV, respectively, reflecting the effect of the increased Cr enrichment on the expected band gap values. For the 20 h passive film, the expected respective values would also be 2.9 ± 0.3 eV and 3.0 ± 0.3 eV.

III.4. Electrochemical characterization

Figure III-14a compares the polarization curves recorded in 0.1 M $Na_2B_4O_7$ electrolyte (pH ~9.5) at 1 mV s^{-1} for the native oxide-covered and 1 h pre-passivated samples. On both samples, no active-passive transition is observed in agreement with the presence of Cr-enriched surface oxides films. The passivity region is stable up to 0.4 V vs Ag/AgCl, suggesting that transpassivity associated with Cr(VI) oxide formation and dissolution is not reached in these conditions. The curves confirm that anodic polarization in 0.1 M $Na_2B_4O_7$ does not modify markedly the passive film composition, as supported by the photoelectrochemical characterizations performed at 0.2 V. The PCS data recorded at 0.4 V (Figure III-10c) suggest however some modifications of the native oxide film. The corrosion potential is shifted toward the anodic direction for the pre-passivated sample and the passive current density is lower, meaning that the passive oxide film produced by polarization in acid

solution offers better corrosion protection than the native oxide film in agreement with the enhanced Cr-enrichment measured by surface analysis.

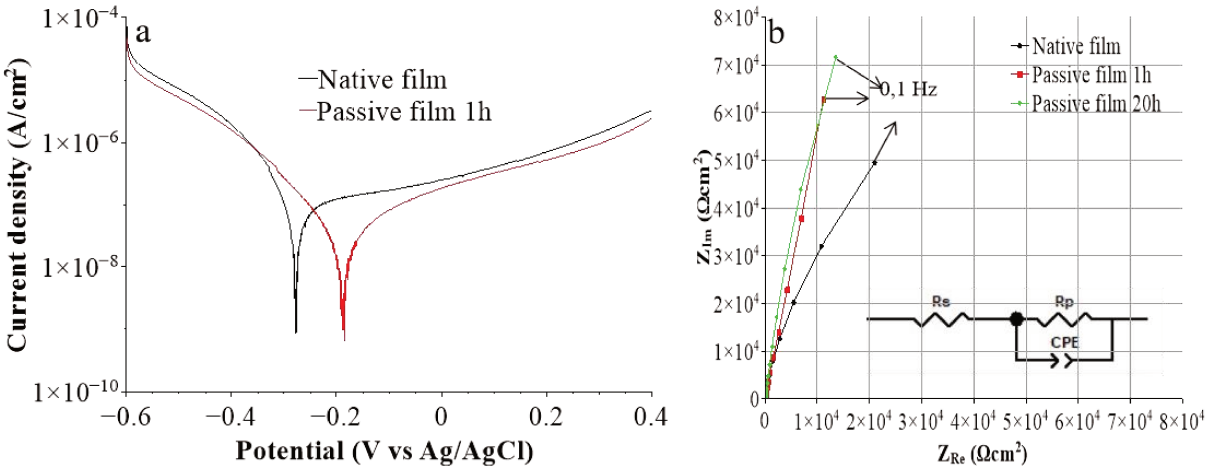

Figure III-14 Comparative electrochemical analysis of native oxide-covered and pre-passivated 316L SS: (a) polarization curves recorded in 0.1 M $Na_2B_4O_7$ (pH 9.5) at 1 mV s^{-1} scan rate; (b) EIS spectra (Nyquist plots) recorded in 0.1 M $Na_2B_4O_7$ (pH 9.5) at 0 V vs Ag/AgCl. The inset shows the equivalent circuit used for fitting the data.

The potential U_E = 0 V vs Ag/AgCl was selected to record electrochemical impedance spectra based on the polarization curves. Figure III-14b presents the EIS data in Nyquist representation. A portion of a deformed semicircle describes the dependence of the imaginary vs real components of the impedance [67]. This has been discussed as related to the influence of the frequency on the overall surface oxide capacitance caused by gap states for amorphous or strongly disordered thin oxide layers [58] and by surface states and adsorption phenomena [47]. The simplified equivalent circuit shown in the inset was used to fit the EIS data. It introduces a constant phase element to model the frequency-dependent equivalent capacitance and to calculate the polarization resistance R_P as a rough estimate of the corrosion resistance. The values of best fit parameters are compiled in Table III-4. The polarization resistance increases for the pre-passivated samples whereas the other parameters remain essentially unchanged. This means that despite the passivation-induced slight thickness decrease of the surface oxide film, evidenced by surface analysis, the corrosion resistance is higher than for the native oxide-covered sample film in agreement electrochemical polarization measurements. This confirms the effect associated with the enhanced Cr-enrichment of the surface oxide measured by surface analysis. No effect of aging in the passive state is detected on the polarization resistance.

Table III-4 Best fit parameters of the EIS spectra shown in Figure III-14b

Sample	R_s ($\Omega \cdot cm^2$)	R_P ($\Omega \cdot cm^2$)	Q ($S \cdot s^n cm^{-2}$)	n
Native oxide film	47.2	$1.8\ 10^5$	$2.5\ 10^{-5}$	0.92
Passive film 1 h	46.4	$8.3\ 10^5$	$2.2\ 10^{-5}$	0.92
Passive film 20 h	43.4	$8.3\ 10^5$	$2.2\ 10^{-5}$	0.92

III.5. Conclusion

ToF-SIMS, XPS, PCS and electrochemical measurements were combined in order to study the physicochemical alterations induced by electrochemical passivation of the surface oxide film providing corrosion resistance to 316L austenitic stainless steel. The native oxide film formed on the mechanically polished SS surface is ~2 nm thick and consists of a mixed Cr(III)-Fe(III) oxide hydroxylated in its outer part. It has a bilayer structure highly enriched in Cr(III) in the inner layer and less so in the outer layer. Molybdenum is concentrated, mostly as Mo(VI), in the outer layer and nickel is below the XPS detection limit. Photocurrent spectroscopy performed *in situ* in a borate buffer solution at and near open circuit potential confirmed the bilayer structure. The band gaps of the inner and outer layers are 3.0 eV and 2.6-2.7 eV, respectively, in agreement with the variation of the chromium enrichment. According to the PCS data, the oxide film would behave as an insulator with an inversion potential of ~ - 0.4 V vs. Ag/AgCl at pH ~ 9.5.

Electrochemical passivation in sulfuric acid solution causes the Cr(III) enrichment to increase in both layers of the oxide film and the Mo(IV-VI) enrichment to increase in the outer layer, owing to the preferential dissolution of Fe(III) in the electrolyte also reflected by the slight decrease of thickness of the outer layer of the oxide film. The decrease of the photoactivity measured *in situ* prevented a reliable experimental determination of the band gaps of the inner and outer layers after passivation but values of 3.0 and 2.9 eV, respectively, were calculated from the composition of the layers measured by XPS. Electrochemical passivation and the related enrichment in chromium of the oxide film improves the corrosion resistance as evidenced by the anodic shift of the corrosion potential and the increase of the polarization resistance observed on the pre-passivated surface by linear sweep voltammetry and impedance spectroscopy. Aging in the passive state promotes the Cr enrichment in the inner barrier layer of the passive film, however with no detectable effects on the polarization resistance. It also promotes dehydroxylation, thereby counter-acting the hydroxylation increase induced by passivation in aqueous electrolyte.

Acknowledgements

This project has received funding from the European Research Council (ERC) under the European Union's Horizon 2020 research and innovation program (ERC Advanced Grant no. 741123). Région Île-de-France is acknowledged for partial funding of the ToF-SIMS equipment.

References

1. P. Schmuki, From Bacon to barriers: a review on the passivity of metals and alloys, J Solid State Electrochem. 6 (2002) 145–164. doi:10.1007/s100080100219.

2. V. Maurice, W.P. Yang, P. Marcus, XPS and STM Study of Passive Films Formed on Fe-22Cr(110) Single-Crystal Surfaces, J. Electrochem. Soc. 143 (1996) 1182–1200. doi:10.1149/1.1836616.

3. M. Seo, N. Sato, Differential composition profiles in depth of thin anodic oxide films on iron-chromium alloy, Surface Science. 86 (1979) 601–609. doi:10.1016/0039-6028(79)90440-0.

4. G. Hultquist, M. Seo, T. Leitner, C. Leygraf, N. Sato, The dissolution behaviour of iron, chromium, molybdenum and copper from pure metals and from ferritic stainless steels, Corrosion Science. 27 (1987) 937–946. doi:10.1016/0010-938X(87)90060-6.

5. D.F. Mitchell, M.J. Graham, Comparison of Auger and SIMS analysis of a thin passive oxide film on iron—25% chromium, Surface and Interface Analysis. 10 (1987) 259–261. doi:10.1002/sia.740100507.

6. S. Mischler, H.J. Mathieu, D. Landolt, Investigation of a passive film on an iron chromium alloy by AES and XPS, Surf. Interface Anal. 11 (1988) 182–188. doi:10.1002/sia.740110403.

7. P. Marcus, I. Olefjord, A Round Robin on combined electrochemical and AES/ESCA characterization of the passive films on Fe-Cr and Fe-Cr-Mo alloys, Corrosion Science. 28 (1988) 589–602. doi:10.1016/0010-938X(88)90026-1.

8. C. Calinski, H.-H. Strehblow, ISS Depth Profiles of the Passive Layer on Fe/Cr Alloys, J. Electrochem. Soc. 136 (1989) 1328–1331. doi:10.1149/1.2096915.

9. R. Kirchheim, B. Heine, H. Fischmeister, S. Hofmann, H. Knote, U. Stolz, The passivity of iron-chromium alloys, Corrosion Science. 29 (1989) 899–917. doi:10.1016/0010-938X(89)90060-7.

10. J.E. Castle, J.H. Qiu, A co-ordinated study of the passivation of alloy steels by plasma source mass spectrometry and x-ray photoelectron spectroscopy—1. characterization of the passive film, Corrosion Science. 29 (1989) 591–603. doi:10.1016/0010-938X(89)90010-3.

11. J.E. Castle, J.H. Qiu, A co-ordinated study of the passivation of alloy steels by plasma source mass spectrometry and x-ray photoelectron spectroscopy—II. growth kinetics of the passive film, Corrosion Science. 29 (1989) 605–616. doi:10.1016/0010-938X(89)90011-5.

12. W.P. Yang, D. Costa, P. Marcus, Resistance to Pitting and Chemical Composition of Passive Films of a Fe-17%Cr Alloy in Chloride-Containing Acid Solution, J. Electrochem. Soc. 141 (1994) 2669–2676. doi:10.1149/1.2059166.

13. S. Haupt, H.-H. Strehblow, A combined surface analytical and electrochemical study of the formation of passive layers on FeCr alloys in 0.5 M H2SO4, Corrosion Science. 37 (1995) 43–54. doi:10.1016/0010-938X(94)00104-E.

14. L.J. Oblonsky, M.P. Ryan, H.S. Isaacs, In Situ Determination of the Composition of Surface Films Formed on Fe-Cr Alloys, J. Electrochem. Soc. 145 (1998) 1922–1932. doi:10.1149/1.1838577.

15. D. Hamm, K. Ogle, C.-O.A. Olsson, S. Weber, D. Landolt, Passivation of Fe–Cr alloys studied with ICP-AES and EQCM, Corrosion Science. 44 (2002) 1443–1456. doi:10.1016/S0010-938X(01)00147-0.

16. P. Keller, H.-H. Strehblow, XPS investigations of electrochemically formed passive layers on Fe/Cr-alloys in 0.5 M H2SO4, Corrosion Science. 46 (2004) 1939–1952. doi:10.1016/j.corsci.2004.01.007.

17. S. Mischler, A. Vogel, H.J. Mathieu, D. Landolt, The chemical composition of the passive film on Fe-24Cr and Fe-24Cr-11Mo studied by AES, XPS and SIMS, Corrosion Science. 32 (1991) 925–944. doi:10.1016/0010-938X(91)90013-F.

18. K. Hashimoto, K. Asami, K. Teramoto, An X-ray photo-electron spectroscopic study on the role of molybdenum in increasing the corrosion resistance of ferritic stainless steels in HC1, Corrosion Science. 19 (1979) 3–14. doi:10.1016/0010-938X(79)90003-9.

19. M.-W. Tan, E. Akiyama, A. Kawashima, K. Asami, K. Hashimoto, The effect of air exposure on the corrosion behavior of amorphous Fe-8Cr-Mo-13P-7C alloys in 1 M HCl, Corrosion Science. 37 (1995) 1289–1301. doi:10.1016/0010-938X(95)00035-I.

20. V. Maurice, W.P. Yang, P. Marcus, X-Ray Photoelectron Spectroscopy and Scanning Tunneling Microscopy Study of Passive Films Formed on (100) Fe-18Cr-13Ni Single-Crystal Surfaces, J. Electrochem. Soc. 145 (1998) 909–920. doi:10.1149/1.1838366.

21. I. Olefjord, B.-O. Elfstrom, The Composition of the Surface during Passivation of Stainless Steels, CORROSION. 38 (1982) 46–52. doi:10.5006/1.3577318.

22. E. De Vito, P. Marcus, XPS study of passive films formed on molybdenum-implanted austenitic stainless steels, Surf. Interface Anal. 19 (1992) 403–408. doi:10.1002/sia.740190175.

23. E. McCafferty, M.K. Bernett, J.S. Murday, An XPS study of passive film formation on iron in chromate solutions, Corrosion Science. 28 (1988) 559–576. doi:10.1016/0010-938X(88)90024-8.

24. P. Marcus, J.M. Grimal, The anodic dissolution and passivation of NiCrFe alloys studied by ESCA, Corrosion Science. 33 (1992) 805–814. doi:10.1016/0010-938X(92)90113-H.

25. M. Bojinov, G. Fabricius, T. Laitinen, K. Mäkelä, T. Saario, G. Sundholm, Influence of molybdenum on the conduction mechanism in passive films on iron–chromium alloys in sulphuric acid solution, Electrochimica Acta. 46 (2001) 1339–1358. doi:10.1016/S0013-4686(00)00713-1.

26. T. Yamamoto, K. Fushimi, M. Seo, S. Tsuri, T. Adachi, H. Habazaki, Depassivation–repassivation behavior of type-312L stainless steel in NaCl solution investigated by the micro-indentation, Corrosion Science. 51 (2009) 1545–1553. doi:10.1016/j.corsci.2008.11.020.

27. V. Maurice, H. Peng, L.H. Klein, A. Seyeux, S. Zanna, P. Marcus, Effects of molybdenum on the composition and nanoscale morphology of passivated austenitic stainless steel surfaces, Faraday Discuss. 180 (2015) 151–170. doi:10.1039/C4FD00231H.

28. K. Sugimoto, Y. Sawada, The role of molybdenum additions to austenitic stainless steels in the inhibition of pitting in acid chloride solutions, Corrosion Science. 17 (1977) 425–445. doi:10.1016/0010-938X(77)90032-4.

29. H. Ogawa, H. Omata, I. Itoh, H. Okada, Auger Electron Spectroscopic and Electrochemical Analysis of the Effect of Alloying Elements on the Passivation Behavior of Stainless Steels, CORROSION. 34 (1978) 52–60. doi:10.5006/0010-9312-34.2.52.

30. I. Olefjord, The passive state of stainless steels, Materials Science and Engineering. 42 (1980) 161–171. doi:10.1016/0025-5416(80)90025-7.

31. W. Yang, R.-C. Ni, H.-Z. Hua, A. Pourbaix, The behavior of chromium and molybdenum in the propagation process of localized corrosion of steels, Corrosion Science. 24 (1984) 691–707. doi:10.1016/0010-938X(84)90059-3.

32. I. Olefjord, B. Brox, U. Jelvestam, Surface Composition of Stainless Steels during Anodic Dissolution and Passivation Studied by ESCA, J. Electrochem. Soc. 132 (1985) 2854–2861. doi:10.1149/1.2113683.

33. A.R. Brooks, C.R. Clayton, K. Doss, Y.C. Lu, On the Role of Cr in the Passivity of Stainless Steel, J. Electrochem. Soc. 133 (1986) 2459–2464. doi:10.1149/1.2108450.

34. C.R. Clayton, Y.C. Lu, A Bipolar Model of the Passivity of Stainless Steel: The Role of Mo Addition, J. Electrochem. Soc. 133 (1986) 2465–2473. doi:10.1149/1.2108451.

35. Y.C. Lu, C.R. Clayton, A.R. Brooks, A bipolar model of the passivity of stainless steels—II. The influence of aqueous molybdate, Corrosion Science. 29 (1989) 863–880. doi:10.1016/0010-938X(89)90058-9.

36. C.R. Clayton, Y.C. Lu, A bipolar model of the passivity of stainless steels—III. The mechanism of MoO_4^{2-} formation and incorporation, Corrosion Science. 29 (1989) 881–898. doi:10.1016/0010-938X(89)90059-0.

37. I. Olefjord, L. Wegrelius, Surface analysis of passive state, Corrosion Science. 31 (1990) 89–98. doi:10.1016/0010-938X(90)90095-M.

38. H. Habazaki, A. Kawashima, K. Asami, K. Hashimoto, The corrosion behavior of amorphous Fe-Cr-Mo-P-C and Fe-Cr-W-P-C alloys in 6 M HCl solution, Corrosion Science. 33 (1992) 225–236. doi:10.1016/0010-938X(92)90147-U.

39. D.D. Macdonald, The Point Defect Model for the Passive State, J. Electrochem. Soc. 139 (1992) 3434–3449. doi:10.1149/1.2069096.

40. A. Elbiache, P. Marcus, The role of molybdenum in the dissolution and the passivation of stainless steels with adsorbed sulphur, Corrosion Science. 33 (1992) 261–269. doi:10.1016/0010-938X(92)90150-2.

41. T. Massoud, V. Maurice, L.H. Klein, A. Seyeux, P. Marcus, Nanostructure and local properties of oxide layers grown on stainless steel in simulated pressurized water reactor environment, Corrosion Science. 84 (2014) 198–203. doi:10.1016/j.corsci.2014.03.030.

42. V. Maurice, P. Marcus, Current developments of nanoscale insight into corrosion protection by passive oxide films, Current Opinion in Solid State and Materials Science. 22 (2018) 156–167. doi:10.1016/j.cossms.2018.05.004.

43. L. Ma, F. Wiame, V. Maurice, P. Marcus, New insight on early oxidation stages of austenitic stainless steel from in situ XPS analysis on single-crystalline Fe–18Cr–13Ni, Corrosion Science. 140 (2018) 205–216. doi:10.1016/j.corsci.2018.06.001.

44. A. Zaffora, F. Di Franco, M. Santamaria, H. Habazaki, F. Di Quarto, The influence of composition on band gap and dielectric constant of anodic Al-Ta mixed oxides, Electrochimica Acta. 180 (2015) 666–678. doi:10.1016/j.electacta.2015.08.068.

45. M. Santamaria, F.D. Franco, F.D. Quarto, M. Pisarek, S. Zanna, P. Marcus, Photoelectrochemical and XPS characterisation of oxide layers on 316L stainless steel grown in high-temperature water, J Solid State Electrochem. 19 (2015) 3511–3519. doi:10.1007/s10008-015-2849-0.

46. F.D. Franco, A. Seyeux, S. Zanna, V. Maurice, P. Marcus, Effect of High Temperature Oxidation Process on Corrosion Resistance of Bright Annealed Ferritic Stainless Steel, J. Electrochem. Soc. 164 (2017) C869–C880. doi:10.1149/2.1851713jes.

47. M. Santamaria, F. Di Quarto, H. Habazaki, Influences of structure and composition on the photoelectrochemical behaviour of anodic films on Zr and Zr–20at.%Ti, Electrochimica Acta. 53 (2008) 2272–2280. doi:10.1016/j.electacta.2007.09.046.

48. M.C. Biesinger, B.P. Payne, A.P. Grosvenor, L.W.M. Lau, A.R. Gerson, R.S.C. Smart, Resolving surface chemical states in XPS analysis of first row transition metals, oxides and hydroxides: Cr, Mn, Fe, Co and Ni, Applied Surface Science. 257 (2011) 2717–2730. doi:10.1016/j.apsusc.2010.10.051.

49. B.P. Payne, M.C. Biesinger, N.S. McIntyre, X-ray photoelectron spectroscopy studies of reactions on chromium metal and chromium oxide surfaces, Journal of Electron Spectroscopy and Related Phenomena. 184 (2011) 29–37. doi:10.1016/j.elspec.2010.12.001.

50. E. Gardin, S. Zanna, A. Seyeux, A. Allion-Maurer, P. Marcus, Comparative study of the surface oxide films on lean duplex and corresponding single phase stainless steels by XPS and ToF-SIMS, Corrosion Science. 143 (2018) 403–413. doi:10.1016/j.corsci.2018.08.009.

51. T. Yamashita, P. Hayes, Analysis of XPS spectra of Fe2+ and Fe3+ ions in oxide materials, Applied Surface Science. 254 (2008) 2441–2449. doi:10.1016/j.apsusc.2007.09.063.

52. V. Di Castro, S. Ciampi, XPS study of the growth and reactivity of FeMnO thin films, Surface Science. 331–333 (1995) 294–299. doi:10.1016/0039-6028(95)00190-5.

53. B. Brox, I. Olefjord, ESCA Studies of MoO2 and MoO3, Surf. Interface Anal. 13 (1988) 3–6. doi:10.1002/sia.740130103.

54. F. Di Quarto, F. La Mantia, M. Santamaria, In: Pyun SI, Jomg-Won L (eds) Modern Aspects of Electrochemistry No. 46 Progress in Corrosion Science and Engeneering I. Springer, New York, (2009), (n.d.).

55. C. Sunseri, S. Piazza, F.D. Quarto, Photocurrent Spectroscopic Investigations of Passive Films on Chromium, J. Electrochem. Soc. 137 (1990) 2411–2417. doi:10.1149/1.2086952.

56. S. Piazza, C. Sunseri, F.D. Quarto, A Simple Model for the Photoelectrochemical Behavior of Corrosion Layers with Variable Hydration Degree, CORROSION. 58 (2002) 436–447. doi:10.5006/1.3277634.

57. A. Zaffora, M. Santamaria, F.D. Franco, H. Habazaki, F.D. Quarto, Photoelectrochemical evidence of inhomogeneous composition at nm length scale of anodic films on valve metals alloys, Electrochimica Acta. 201 (2016) 333–339. doi:10.1016/j.electacta.2015.12.157.

58. F. Di Quarto, F. La Mantia, and M. Santamaria, In: Pyun SI, Jomg-Won L (eds) Modern Aspects of Electrochemistry No. 46 Progress in Corrosion Science and Engeneering I, Springer, New York, (2009)

59. A. Zaffora, M. Santamaria, F.D. Franco, H. Habazaki, F.D. Quarto, Photoelectrochemical evidence of nitrogen incorporation during anodizing sputtering – deposited Al–Ta alloys, Physical Chemistry Chemical Physics. 18 (2016) 351–360. doi:10.1039/C5CP04347F.

60. CRC Handbook of Chemistry and Physics, in: D.R. Lide (Ed.), 90th Edition, CRC Press/Taylor and Francis, Boca Raton, FL, (2010)., n.d.

61. H. Xu, L. Wang, D. Sun, H. Yu, The passive oxide films growth on 316L stainless steel in borate buffer solution measured by real-time spectroscopic ellipsometry, Applied Surface Science. 351 (2015) 367–373. doi:10.1016/j.apsusc.2015.05.165.

62. S. Adachi, The Handbook on Optical Constants of Metals, World Scientific, (2012)., n.d.

63. B. Karlsson, C.G. Ribbing, Optical constants and spectral selectivity of stainless steel and its oxides, Journal of Applied Physics. 53 (1982) 6340–6346. doi:10.1063/1.331503.

64. F. Di Quarto, C. Sunseri, S. Piazza, M.C. Romano, Semiempirical Correlation between Optical Band Gap Values of Oxides and the Difference of Electronegativity of the Elements. Its Importance for a Quantitative Use of Photocurrent Spectroscopy in Corrosion Studies, J. Phys. Chem. B. 101 (1997) 2519–2525. doi:10.1021/jp970046n.

65. F.D. Franco, G. Zampardi, M. Santamaria, F.D. Quarto, H. Habazaki, Characterization of the Solid State Properties of Anodic Oxides on Magnetron Sputtered Ta, Nb and Ta-Nb Alloys, J. Electrochem. Soc. 159 (2011) C33–C39. doi:10.1149/2.031201jes.

66. M. Santamaria, F. Di Franco, F. Di Quarto, P. Skeldon, G.E. Thompson, Tailoring of the Solid State Properties of Al–Nb Mixed Oxides: A Photoelectrochemical Study, J. Phys. Chem. C. 117 (2013) 4201–4210. doi:10.1021/jp312008m.

67. A. Alaoui Mouayd, M.E. Orazem, E.M.M. Sutter, B. Tribollet, A. Koltsov, Contribution of electrochemical dissolution during pickling of low carbon steel in acidic solutions, Corrosion Science. 82 (2014) 362–368. doi:10.1016/j.corsci.2014.01.036.

Chapter IV

Mechanisms of Cr and Mo enrichments in the passive oxide film on 316L austenitic stainless steel

This chapter reproduces the final preprint of an original article published in Frontiers Materials, section Environmental Materials with the reference:
Z. Wang, E.-M. Paschalidou, A. Seyeux, S. Zanna, V. Maurice, P. Marcus, Mechanisms of Cr and Mo enrichments in the passive oxide film on 316L austenitic stainless steel, Front. Mater. 6 (2019) 232. doi:10.3389/fmats.2019.00232.

Abstract

An approach preventing contact to ambient air during transfer from liquid environment for electrochemical treatment to UHV environment for surface analysis by X-Ray Photoelectron Spectroscopy and Time-of-Flight Secondary Ion Mass Spectrometry was applied to study the mechanisms of Cr and Mo enrichments in the passive oxide film formed on 316L austenitic stainless steel. Starting from the air-formed native oxide-covered surface, exposures were conducted in aqueous sulfuric acid solution first at open circuit potential and then under anodic polarization in the passive range. At open circuit potential the thickness of the bi-layered oxide film was observed to decrease and the enrichments of both Cr(III) and Mo, mostly Mo(VI), to markedly increase as well as the film hydroxylation. This is due to preferential dissolution of the Fe(III) oxide/hydroxide, not compensated by oxide growth in the absence of an electric field established by anodic polarization. Anodic polarization in the passive domain causes the bi-layered structure of the oxide film to re-grow by oxidation of iron, chromium and molybdenum, without impacting the Cr enrichment and only slightly mitigating the Mo enrichment. De-hydroxylation of the inner layer is also promoted upon anodic polarization. These results show that the treatment of the surface oxide film in acid solution at open circuit potential enhances Cr and Mo enrichments and promotes hydroxylation. Passivation by anodic polarization allows dehydroxylation, yielding more Cr oxide, without markedly affecting the Mo enrichment, also beneficial for the corrosion resistance.

IV.1. Introduction

Stainless steels (SS) are important technological materials of widespread application that combine excellent mechanical and corrosion properties. The high corrosion resistance is provided by the passive film, a surface oxide/hydroxide layer that is continuous and protective and does not exceed a few nanometers in thickness when formed at ambient temperature, as observed on Fe-Cr ferritic [1]-[19] and Fe-Cr-Ni austenitic [20]-[40] stainless steels. The markedly Cr(III)-enriched composition of the passive film is a key factor for the corrosion

resistance. In aqueous environments, it results from the competitive oxidation of iron and chromium with faster dissolution of Fe(II)/Fe(III) compared to Cr(III) species, especially in acid solutions [16].

On Fe-Cr-Ni austenitic stainless steels, the passive films contain no or very little Ni(II) species and the metallic alloy region underneath the oxide is enriched in nickel [20]-[27]. SS grades alloyed with a few at% Mo better resist localized corrosion by pitting in chloride-containing environments. Their passive films are slightly enriched in Mo(IV) or Mo(VI) species with no alterations of the thickness [10][21][22][24][35][37]. It has been proposed that the presence of molybdenum would mitigate the breakdown of the passive film preceding the initiation of localized corrosion [10][11][19][21][25][28][30][33]-[36][39] or promote the passive film repair after breakdown [18][21][29]-[31].

More recently, it has been reported that the Cr(III) enrichment in the passive film may not be homogeneous at the nanometer scale [27][41] and that the heterogeneities of the Cr local distribution may be responsible for the passive film breakdown leading to the local failure of the corrosion resistance [42]. The mechanisms of formation of the passive film include a pre-passivation stage during which a native oxide film is formed, most often in ambient air, and a subsequent stage where the native oxide film is altered, once exposed to the aqueous environment, to become the passive film. Hence, a thorough investigation of the Cr(III) enrichment mechanisms is necessary to develop the comprehensive knowledge on how to improve the resistance to local failure of passivity. It must address the initial stages of oxidation leading to pre-passivation of the SS surface [43][44] as well as the alterations of the native oxide film brought by immersion in the aqueous environment and by electrochemical anodic polarization in the passive range [45] (Chapter III).

In the present study, we addressed the mechanisms by which the Cr and Mo enrichments in the native surface oxide film are modified when exposing a polycrystalline austenitic 316L SS to an acid aqueous solution. Time-of-Flight Secondary Ion Mass Spectroscopy (ToF-SIMS) elemental depth profile analysis and X-ray Photoelectron Spectroscopy (XPS) compositional surface analysis were applied to interrogate the modifications induced by immersion without and with application of anodic polarization in the passive domain. An experimental protocol avoiding contact to ambient air of the samples during transfer from liquid environment for electrochemical treatment to the different UHV platforms for surface analysis was adopted, enabling us to highlight the key effect of immersion under open circuit conditions on the Cr and Mo enrichments

IV.2. Experimental

Polycrystalline 316L austenitic SS samples of bulk composition Fe–19Cr–13Ni–2.7Mo (wt%) (Fe–20Cr–12Ni–1.6Mo at%) were used. The surfaces were prepared by mechanical polishing first with emery paper of successive 1200 and 2400 grades and then with diamond suspensions of successive 6, 3, 1 and 0.25 μm grades. Ultrasonicated baths of acetone, ethanol and Millipore® water (resistivity > 18 MΩ cm) were successively used for cleaning and rinsing after each polishing step. Filtered compressed air was used for drying.

Similarly to approaches developed in the past for surface analytical studies of passivity [21][46][47], the experimental protocol was designed to avoid ambient air exposure of the electrochemically-treated samples. The samples, as received from surface preparation, were introduced in an Ar-filled (ΔP = ~200 Pa) glove box (Jacomex, France) equipped with a 3-electrode electrochemical cell for electrochemical treatment. The 3-electrode electrochemical cell was controlled by a Gamry 600 potentiostat. It included a Pt grid as counter electrode and saturated calomel reference electrode. The area (0.5 cm^2) of the working electrode was delimited by a Viton O-ring. The electrolyte was a 0.05 M H_2SO_4 aqueous solution prepared from ultrapure chemicals (VWR®) and Millipore® water and bubbled with argon prior to introduction in the glove box. Oxygen and water vapor concentrations in the glove box evolved from < 250 ppm and < 1000 ppm after introduction of the electrolyte to < 55 ppm and < 200 ppm after performing the electrochemical treatments, respectively.

The samples, covered by the native oxide film formed in air, were first stored under Ar atmosphere, then immersed at open circuit potential ($-0.26 \leq U_{OCP} \leq -0.22$ V/SCE) for 30 min and then passivated by a potential step to U_{Pass} = 0.5 V/SCE for 30 min. The selected U_{Pass} value corresponded to the minimum of passive current measured by linear sweep voltammetry (Figure IV-1). No cathodic pre-treatment was performed in order to avoid any reduction-induced alteration of the initial native oxide film exposed at U_{OCP}. After electrochemical treatment, the samples were emerged from the electrolyte at free potential, rinsed with Millipore® water and dried with argon. They were then installed under argon in containers that were air tight sealed for transfer to surface analysis by XPS and ToF-SIMS.

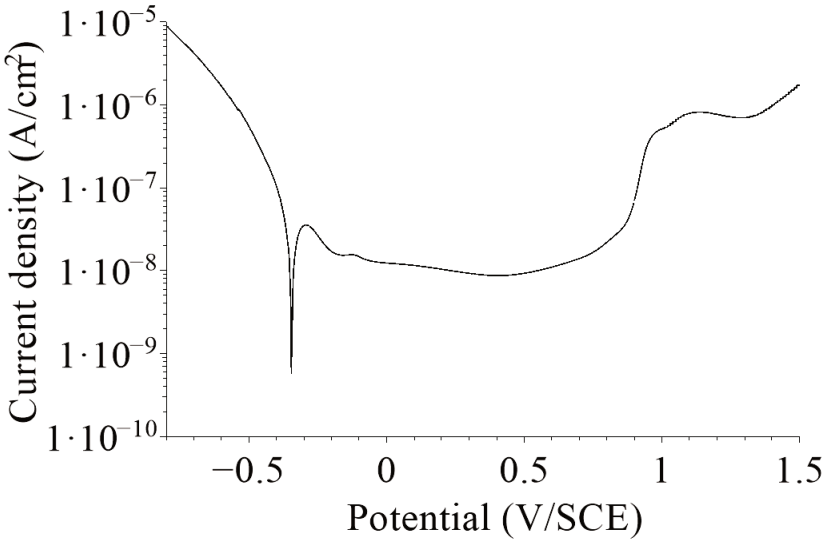

Figure IV-1 Polarization curve for the native oxide-covered 316L SS sample recorded in 0.05 M H_2SO_4 in the Ar-filled glove box after initial stabilization at open circuit potential for 30 min (dU/dt = 5 mV/s).

The air tight sealed containers with the samples under Ar atmosphere were transferred from the glove box used for electrochemical treatment to two separate Ar-filled glove boxes, one attached to the XPS spectrometer and the other attached to the ToF-SIMS spectrometer. In these glove boxes, the air tight sealed containers were opened under argon (ΔP = ~30 Pa, [O_2] < 5 ppm, [H_2O] < 1 ppm) and the samples mounted on the UHV holders for direct transfer to UHV. The three samples selected for comparative analysis were: (i) the initial native oxide-covered sample, as received from surface preparation and exposed to Ar atmosphere of the glove boxes, (ii) the sample treated at U_{OCP} and (iii) the sample treated at U_{Pass}. For each sample, XPS analysis was performed prior to ToF-SIMS depth profile analysis because of the locally destructive nature of SIMS. The air tight sealed containers were used for transfer between the XPS and ToF-SIMS platforms.

XPS analysis was performed with a Thermo Electron ESCALAB 250 spectrometer (VG Scientific, United Kingdom) operating at about 10^{-9} mbar. The X-ray source was an AlK_α monochromatized radiation (hν = 1486.6 eV). Survey spectra were recorded with a pass energy of 100 eV at a step size of 1 eV. High resolution spectra of the Fe 2p, Cr 2p, Ni 2p, Mo 3d, O 1s, S 2p and C 1s core level regions were recorded with a pass energy of 20 eV at a step size of 0.1 eV. The take-off angle of the analyzed photoelectrons was 90°. The binding energies (BE) were calibrated by setting the C 1s signal corresponding to olefinic bonds (–CH_2–CH_2–) at 285.0 eV. Spectral reconstruction was performed by curve fitting with the

CasaXPS software. Shirley type background subtraction and Lorentzian/Gaussian (70%/30%) peak shapes were used. Asymmetry of the peaks was taken into account for the metallic components (Cr^0, Fe^0, Mo^0, Ni^0). Symmetric but broader peak envelopes were used to account for the multiplet splitting of the oxide components (Cr^{3+}, Fe^{3+}, $Mo^{4+/6+}$).

A ToF-SIMS 5 spectrometer (Ion ToF – Munster, Germany) operated at about 10^{-9} mbar was used for depth profile elemental analysis. The analysis interlaced topmost surface analysis in static SIMS conditions using a pulsed 25 keV Bi^+ primary ion source delivering 1.2 pA current over a 100 × 100 μm^2 area with sputtering using a 1 keV Cs^+ sputter beam giving a 32 nA target current over a 600 × 600 μm^2 area (300 × 300 μm^2 for the sample treated at U_{pass}). Analysis was centered inside the eroded crater to avoid edge effects. The profiles were recorded with negative secondary ions which have higher yield for oxide matrices than for metallic matrices. The Ion-Spec software was used for data acquisition and processing.

IV. 3. Results and discussion

IV. 3. 1. Bi-layered chemical structure of the surface oxide films

Figure IV-2 presents the ToF-SIMS analysis of the elemental in-depth distribution for the native oxide-covered sample. In Figure IV-2a, the intensities of selected secondary ions characteristic of the oxide film ($^{18}O^-$, CrO_2^-, FeO_2^-, NiO_2^- and MoO_2^-) and substrate (Cr_2^-, Fe_2^- and Ni_2^-) are plotted in logarithmic scale versus sputtering time. The position of the "modified alloy" region between the oxide film and metallic bulk substrate regions, where Ni is found enriched in agreement with previous studies on austenitic stainless steels [20]-[27] (also see Chapter III), was defined using the Ni_2^- ions intensity profile and placed between 70 and 130 s of sputtering. In the oxide film region, the most intense profile of the alloying elements are those of the CrO_2^- and FeO_2^- ions followed by the MoO_2^- ions. The NiO_2^- ions are the least intense.

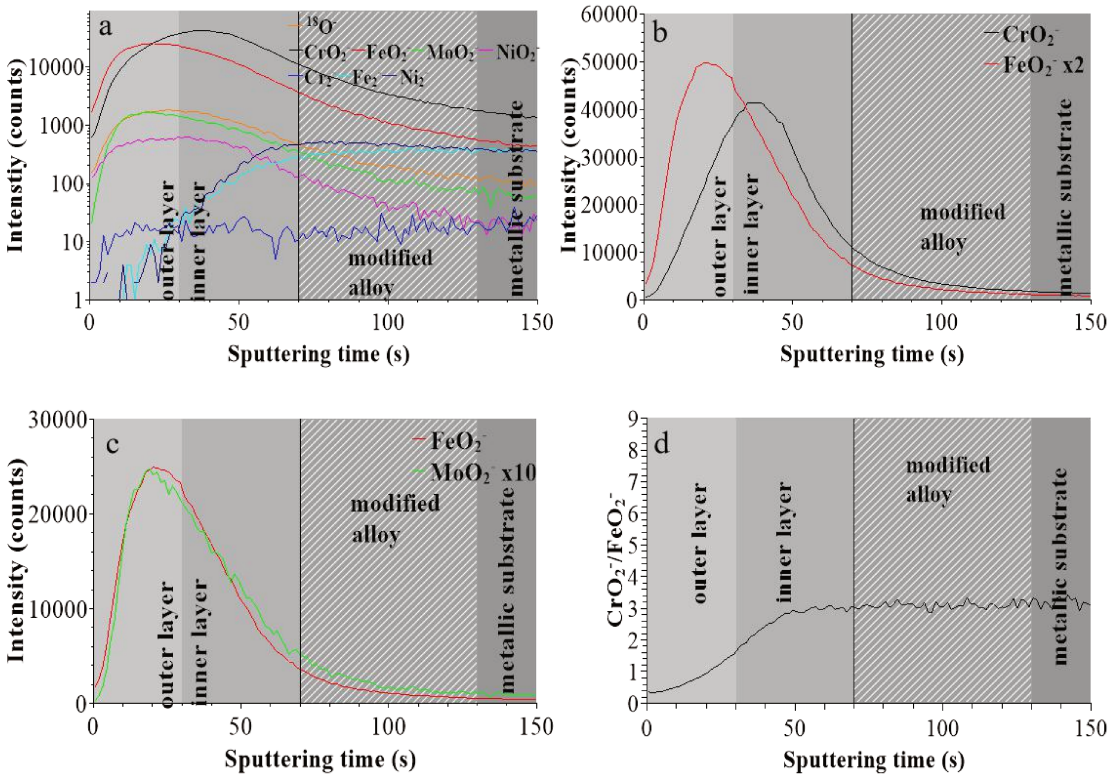

Figure IV-2 ToF-SIMS depth profiles for the native oxide film on 316L SS: (a) $^{18}O^-$, CrO_2^-, FeO_2^-, NiO_2^-, MoO_2^-, Cr_2^-, Fe_2^- and Ni_2^- secondary ions, (b) CrO_2^- and FeO_2^- secondary ions, (c) FeO_2^- and MoO_2^- secondary ions, (d) CrO_2^-/ FeO_2^- intensity ratio.

Figure IV-2b shows that the FeO_2^- and CrO_2^- ions profiles peak at different positions, at 20 and 40 s, respectively. This is consistent with the native oxide film having a bilayer structure with iron and chromium oxides more concentrated in the outer and inner layers, respectively, as in Chapter III and commonly reported for oxide films on stainless steels [7][17][27]. The interface between outer and inner layer was positioned at 30 s which is the median sputtering position between the two intensity maxima. Figure IV-2c shows that the MoO_2^- ions profile peaks at the same position as the FeO_2^- profile, meaning that Fe oxide and Mo oxide are concentrated in the outer layer and confirming previous data for native oxide film on 316L SS. Figure IV-2d shows that, starting from the extreme surface, the CrO_2^-/FeO_2^- intensity ratio continuously increases in the outer and inner parts of the oxide film before reaching saturation in the inner layer.

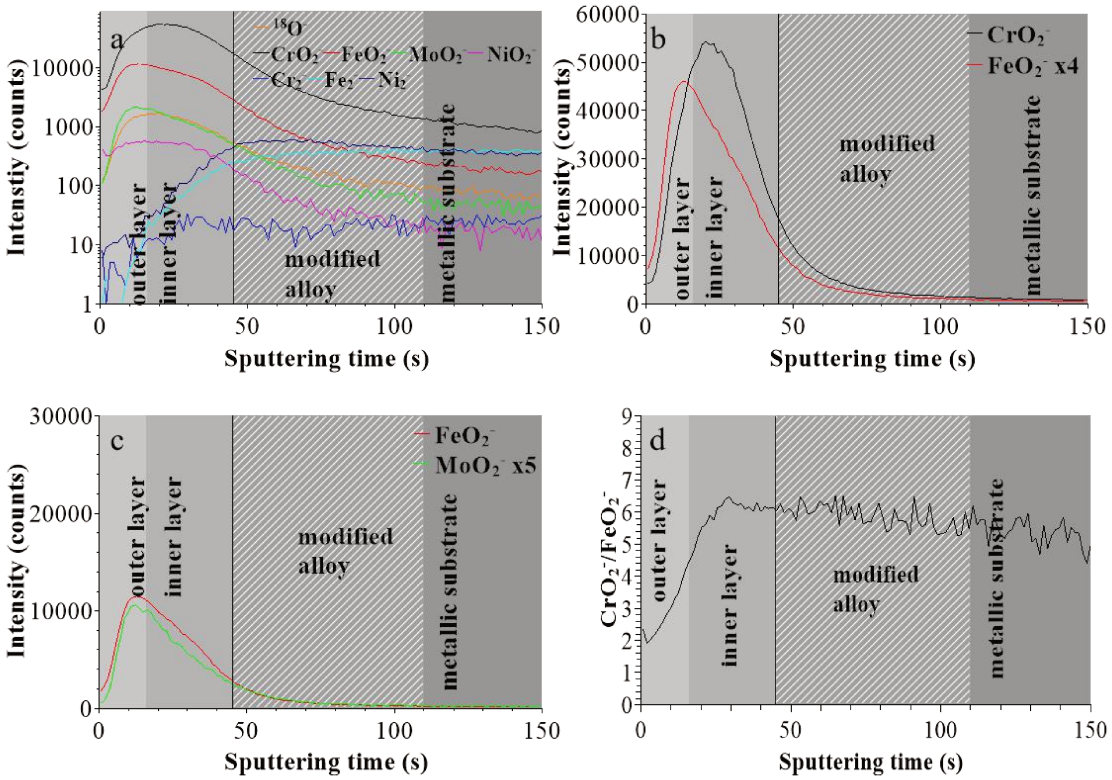

Figure IV-3 ToF-SIMS depth profiles for 316L SS immersed in 0.05 M H_2SO_4 at U_{OCP} for 30 min : (a) $^{18}O^-$, CrO_2^-, FeO_2^-, NiO_2^-, MoO_2^-, Cr_2^-, Fe_2^- and Ni_2^- secondary ions, (b) CrO_2^- and FeO_2^- secondary ions, (c) FeO_2^- and MoO_2^- secondary ions, (d) CrO_2^-/FeO_2^- intensity ratio.

For the sample treated at U_{OCP} (Figure IV-3), the "modified alloy" region was positioned between 45 to 110 s using the same method, suggesting a significant thickness decrease of the oxide film. The FeO_2^- and CrO_2^- intensity maxima are at 12 and 20 s of sputtering, respectively, with the median position at 16 s for the interface between outer and inner layers of the oxide film (Figure IV-3b). Compared to the native oxide film, the outer layer is much thinner (16 instead of 30 s) and the inner layer less altered (33 instead of 40 s) after treatment at U_{OCP}. The maxima of the MoO_2^- and FeO_2^- ions profiles are still observed at the same sputtering time in the outer layer, however with a marked decrease in intensity for the FeO_2^- ions compared to the MoO_2^- ions suggesting the marked preferential loss of iron oxide (Figure IV-3c). Consistently, the profiles of the CrO_2^-/FeO_2^- intensity ratio (Figure IV-3d), still increasing from extreme surface to inner part in the oxide film region, is overall higher (~6 vs. ~3 at saturation in the inner layer), suggesting an increase of the Cr enrichment of the oxide film due to iron oxide dissolution induced by immersion in sulfuric acid at open circuit potential.

For the sample treated at U_{PASS} (Figure IV-4), the "modified alloy" region is observed between 18 and 36 s using the same positioning method. However, due to the smaller sputtered area during analysis (300 × 300 µm^2 instead of 600 × 600 µm^2), the sputtering rate was ~4 times higher in this experiment. After correction, this "modified alloy" region is between 72 and 144 s, which is similar to that of the native oxide-covered sample (70-130 s). Figure IV-4b and c shows that the bilayer structure persists after passivation with molybdenum concentrated in the outer layer. The interface between outer and inner layer was positioned at 28 s (after correction of the sputtering rate), meaning that the thickness of passive film is quite similar to that of the native oxide film and larger than after treatment at U_{OCP}. The CrO_2^-/FeO_2^- intensity ratio (Figure IV-4d) shows a similar increasing profile than for the other two samples and reaches the value of ~6 at saturation in the inner layer, like for the film after treatment at U_{OCP} and suggesting similar enrichment in Cr in the inner layer of the passive film.

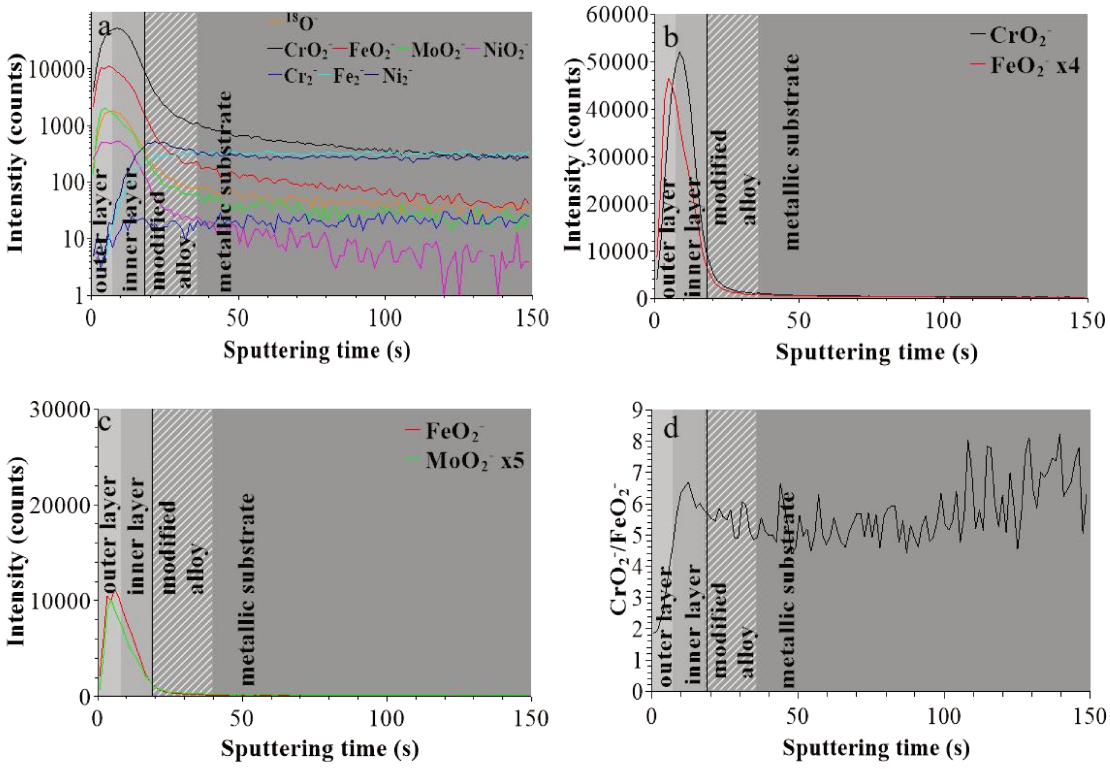

Figure IV-4 ToF-SIMS depth profiles for 316L SS passivated in 0.05 M H_2SO_4 at U_{PASS} = 0.5 V/SCE for 30 min : (a) $^{18}O^-$, CrO_2^-, FeO_2^-, NiO_2^-, MoO_2^-, Cr_2^-, Fe_2^- and Ni_2^- secondary ions, (b) CrO_2^- and FeO_2^- secondary ions, (c) FeO_2^- and MoO_2^- secondary ions, (d) CrO_2^-/FeO_2^- intensity ratio.

These data confirm that the in-depth chemical structure of the surface oxide films formed on 316L SS is bi-layered. This duplex structure is already formed in the initial native oxide film formed in air and persists after treatment at U_{OCP} and U_{Pass}. The observed changes are the positions of the interfaces, reflecting the thickness variations of the oxide films, and the intensity ratios of the secondary ions characteristic of the oxidized alloying elements present in the films and reflecting the variations of the Cr and Mo enrichments induced by immersion in sulfuric acid and anodic passivation. The XPS data presented hereafter allow us to quantitatively discuss these electrochemically induced thickness and compositional changes.

IV. 3. 2. Thickness and composition of the surface oxide films

The XPS Cr $2p_{3/2}$, Fe $2p_{3/2}$, Mo 3d and O 1s core level spectra recorded for the native oxide-covered sample are shown in Figure IV-5 and those measured after treatment at U_{OCP} and U_{Pass} in Figure IV-6 and Figure IV-7, respectively. Table IV-1 compiles the values of the binding energies (BE), full widths at half maximum (FWHM) and relative intensities of the component peaks used for reconstruction of the experimental curves by curve fitting. It also includes the measured Ni 2p3/2, S 2s and S 2p peak components.

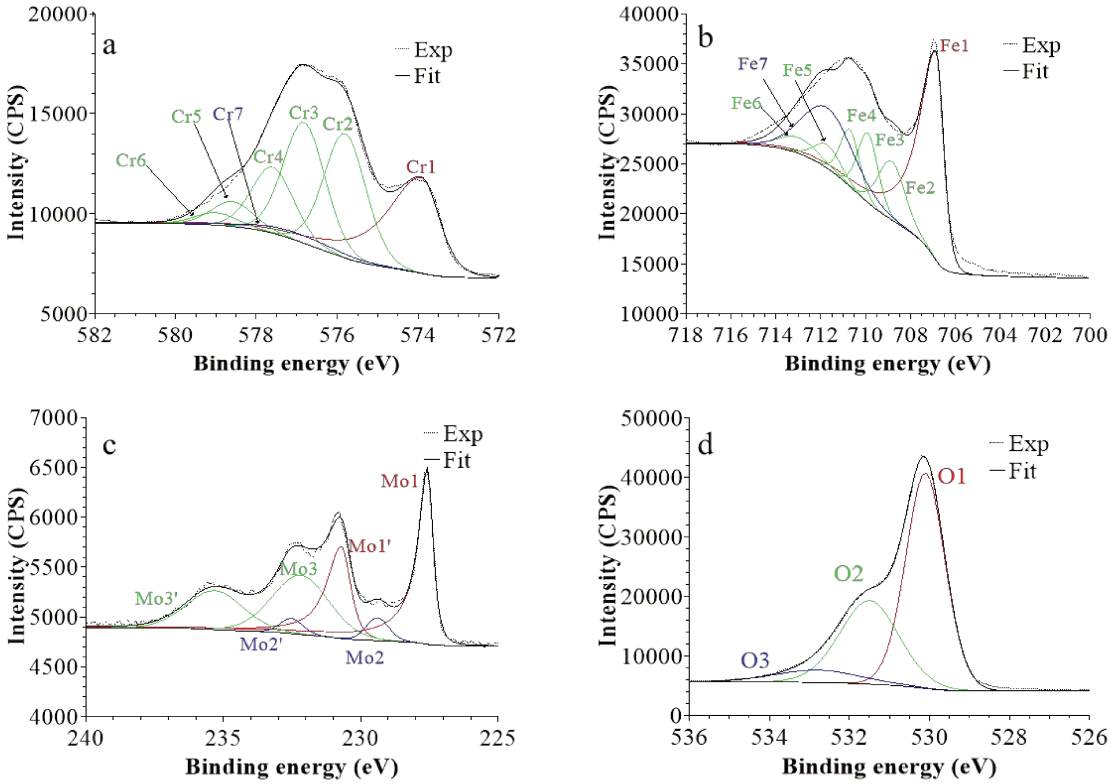

Figure IV-5 XPS core level spectra and their reconstruction for the native oxide film on 316L SS: (a) Cr $2p_{3/2}$, (b) Fe $2p_{3/2}$, (c) Mo $3d_{5/2\text{-}3/2}$ and (d) O 1s regions (take-off angle: 90°).

Following the previously proposed procedure (Chapter III) [46]-[49], the Fe $2p3_{/2}$ spectra were fitted with seven peaks, as exemplified in Figure IV-5 and detailed in Table IV-1. The first peak (Fe1) corresponds to metallic Fe^0 in the substrate. The next five peaks (Fe2-Fe6) form a series at fixed BE intervals, FWHMs and relative intensities and correspond to Fe^{III} oxide in the surface oxide layers. The additional peak (Fe7), needed at higher BE to optimize the fit, corresponds to Fe^{III} hydroxide also in the oxide films. No series of five peaks, at lower BEs and associated to Fe^{II} oxide [48], was needed for reconstruction. After treatment at U_{OCP} (Figure IV-6, Table IV-1), the Fe^{III} to Fe^0 intensity ratio markedly decreases, reflecting the loss of oxidized iron in the surface oxide film in agreement with the ToF-SIMS data. Within the range of ±0.1 eV allowed for fitting, one observes no significant changes of the BE and FWHM values of the metallic and oxidized iron components. After treatment at U_{Pass} (Figure IV-7, Table IV-1), the Fe^{III} to Fe^0 intensity ratio increases, indicating re-oxidation of iron. The BE and FWHM values remain unchanged.

Consistently, and also as proposed before (Chapter III) [48][50], seven peaks were also used for reconstructing the Cr 2p spectra (see e.g. Figure IV-5, Table IV-1). The first one (Cr1) is associated to metallic Cr^0 in the substrate, the next five peaks (Cr2-Cr6), also forming a well-defined series, to Cr^{III} oxide in the surface oxide layers, and the additional peak (Cr7) to Cr^{III} hydroxide in the oxide film. No Cr^{VI} peak expected at a BE of ~579.5 eV [48] was needed for curve fitting. After treatment at U_{OCP} (Figure IV-6, Table IV-1), the Cr^{III}(ox) to Cr^0 intensity ratio slightly decreases but the Cr^{III}(hyd) to Cr^0 intensity ratio markedly increases, indicating significant hydroxylation of chromium in the surface oxide. After treatment at U_{Pass} (Figure IV-7, Table IV-1), the Cr^{III}(ox) to Cr^0 intensity ratio increases markedly but the Cr^{III}(hyd) to Cr^0 intensity ratio only slightly, indicating re-oxidation and dehydroxylation of chromium. BE and FWHM values show no significant variations after treatment at U_{OCP} and U_{Pass}.

Table IV-1. BE, FWHM and relative intensity values of the components measured by XPS on polycrystalline 316L SS after formation in ambient air of the native oxide film, after immersion for 30 min at OCP in 0.05 M H_2SO_4, and after passivation for 30 min at 0.5 V/SCE in 0.05 M H_2SO_4.

			Native oxide film			OCP oxide film			Passive oxide film		
Core level	Peak	Assignment	BE (±0.1 eV)	FWHM (±0.1 eV)	Intensity (%)	BE (±0.1 eV)	FWHM (±0.1 eV)	Intensity (%)	BE (±0.1 eV)	FWHM (±0.1 eV)	Intensity (%)
Fe 2p3/2	Fe1	Fe^0 (met)	706.9	0.8	42.4	706.8	0.8	71.0	706.9	0.8	59.6
	Fe2	Fe^{III} (ox)	708.8	1.4	10.7	708.7	1.2	7.2	708.8	1.2	8.8
	Fe3	Fe^{III} (ox)	709.9	1.1	9.6	709.7	1.1	6.5	709.8	1.1	7.9
	Fe4	Fe^{III} (ox)	710.7	1.0	7.5	710.7	1.1	5.0	710.7	1.1	6.2
	Fe5	Fe^{III} (ox)	711.7	1.4	4.3	711.7	1.3	2.9	711.7	1.3	3.5
	Fe6	Fe^{III} (ox)	713.0	2.1	4.3	712.8	1.9	2.9	712.8	2.1	3.5
	Fe7	Fe^{III} (hyd)	711.8	2.7	21.3	711.9	2.7	4.5	711.9	2.7	10.5
Cr 2p3/2	Cr1	Cr^0 (met)	574.1	1.1	28.1	574.0	1.1	28.3	574.0	1.1	19.5
	Cr2	Cr^{III} (ox)	576.0	1.3	24.6	576.2	1.4	14.2	576.1	1.5	19.2
	Cr3	Cr^{III} (ox)	577.0	1.3	23.9	577.2	1.4	13.8	577.1	1.5	18.6
	Cr4	Cr^{III} (ox)	577.8	1.3	13.0	578.0	1.4	7.5	577.9	1.5	10.1
	Cr5	Cr^{III} (ox)	578.8	1.3	4.9	579.0	1.4	3.1	578.9	1.5	4.2
	Cr6	Cr^{III} (ox)	579.2	1.3	2.5	579.4	1.4	2.0	579.3	1.5	2.7
	Cr7	Cr^{III} (hyd)	577.2	2.5	3.1	577.2	2.5	31.1	577.2	2.5	25.7
Ni 2p3/2	Ni1	Ni^0 (met)	852.8	1.0	100	852.7	1.0	100	852.8	1.0	100
Mo 3d5/2	Mo1	Mo^0 (met)	227.6	0.5	32.2	227.5	0.5	31.3	227.6	0.5	26.1
	Mo2	Mo^{IV} (ox)	229.4	1.0	3.8	229.3	1.1	3.6	229.3	1.1	4.1
	Mo3	Mo^{VI} (ox)	232.2	2.3	24.3	232.3	2.5	25.4	232.2	2.3	30.2
Mo 3d3/2	Mo1’	Mo^0 (met)	230.7	0.8	21.2	230.7	0.8	20.6	230.7	0.8	17.2
	Mo2’	Mo^{IV} (ox)	232.6	1.0	2.5	232.4	1.1	2.4	232.4	1.1	2.7
	Mo3’	Mo^{VI} (ox)	235.3	2.3	16.0	235.4	2.5	16.7	235.3	2.5	19.9
O 1s	O1	O^{2-}	530.1	1.2	58.6	530.2	1.2	29.4	530.3	1.2	38.1
	O2	OH^-	531.5	1.7	34.1	531.7	1.7	50.7	531.7	1.8	47.3
	O3	H_2O	532.8	2.5	7.3	532.8	2.5	19.9	532.8	2.5	14.7
S 2s	S1	SO_4^{2-}	--	--	--	233.0	1.5	100	232.9	1.6	100
S 2p3/2	S2	SO_4^{2-}	--	--	--	168.9	1.2	64.34	168.8	1.3	66.90
S 2p1/2	S3	SO_4^{2-}	--	--	--	170.1	1.2	35.66	170.1	1.3	33.10

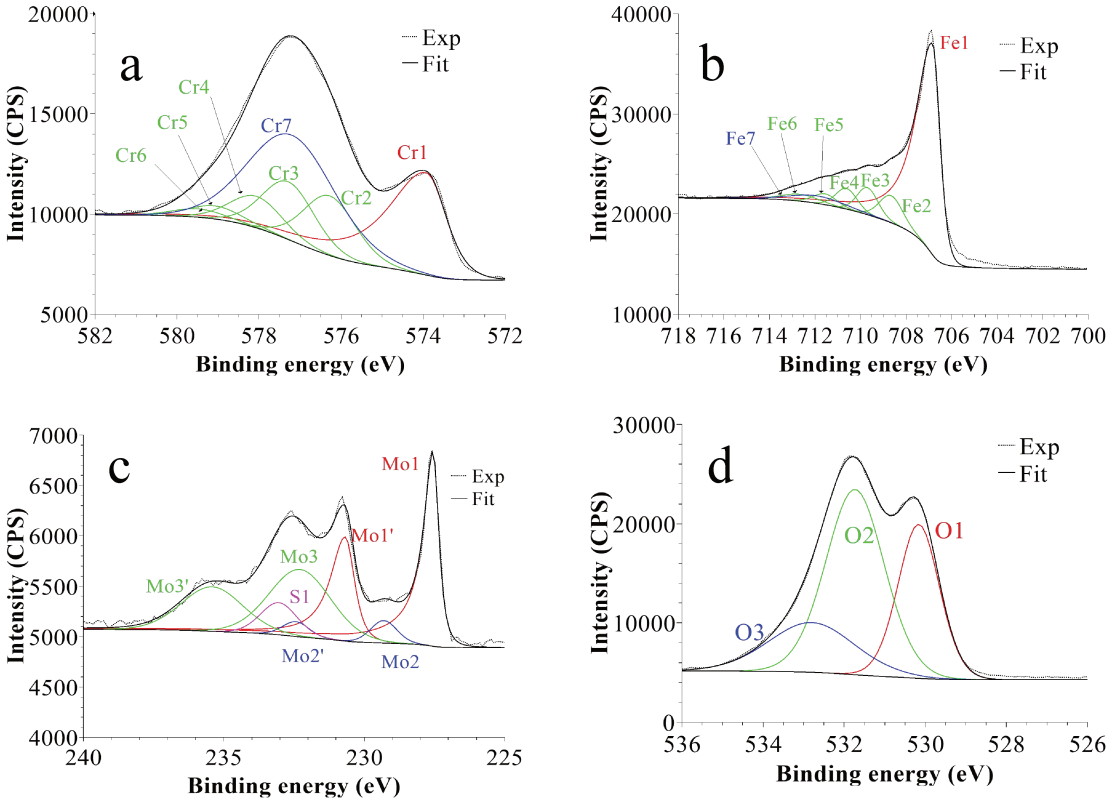

Figure IV-6 XPS core level spectra and their reconstruction for 316L SS immersed in 0.05 M H_2SO_4 at U_{OCP} for 30 min: (a) Cr $2p_{3/2,}$ (b) Fe $2p_{3/2,}$ (c) Mo $3d_{5/2\text{-}3/2}$ and (d) O 1s regions (take-off angle: 90°).

The Mo 3d spectra were fitted with three 5/2-3/2 spin-orbit doublets (see e.g. Figure IV-5, Table IV-1) [22][27][31][33][36][45][48]. One (Mo1/Mo1') corresponds to metallic Mo^0 in the substrate and the other two, (Mo2/Mo2') and (Mo3/Mo3'), to Mo^{IV} and Mo^{VI} in the surface oxide layers, respectively. The Mo^{VI} to Mo^{IV} intensity ratio is 6.4 in the native oxide film, indicating that Mo(VI) species are mostly present. After treatment at U_{OCP} (Figure IV-6, Table IV-1), the Mo^{IV+VI} to Mo^0 intensity ratio slightly increases in agreement with the Mo enrichment in the oxide outer layer observed by ToF-SIMS. It further increases after treatment at U_{Pass} (Figure IV-7, Table IV-1). The Mo^{VI} to Mo^{IV} ratio also increases after treatment at U_{OCP} (7.1) and further after treatment at U_{Pass} (7.4), indicating further enrichment in Mo(VI) species after electrochemical treatment. An additional peak S1, assigned to the S 2s core level, was necessary for reconstruction of the Mo 3d spectra measured after the electrochemical treatments (Figure IV-6, Figure IV-7, Table IV-1). The presence of sulfur originating from the sulfuric acid electrolyte was confirmed by the presence of a S 2p doublet

assigned to sulfate species (Table IV-1), most likely adsorbed at the surface of the oxide films (Table IV-1).

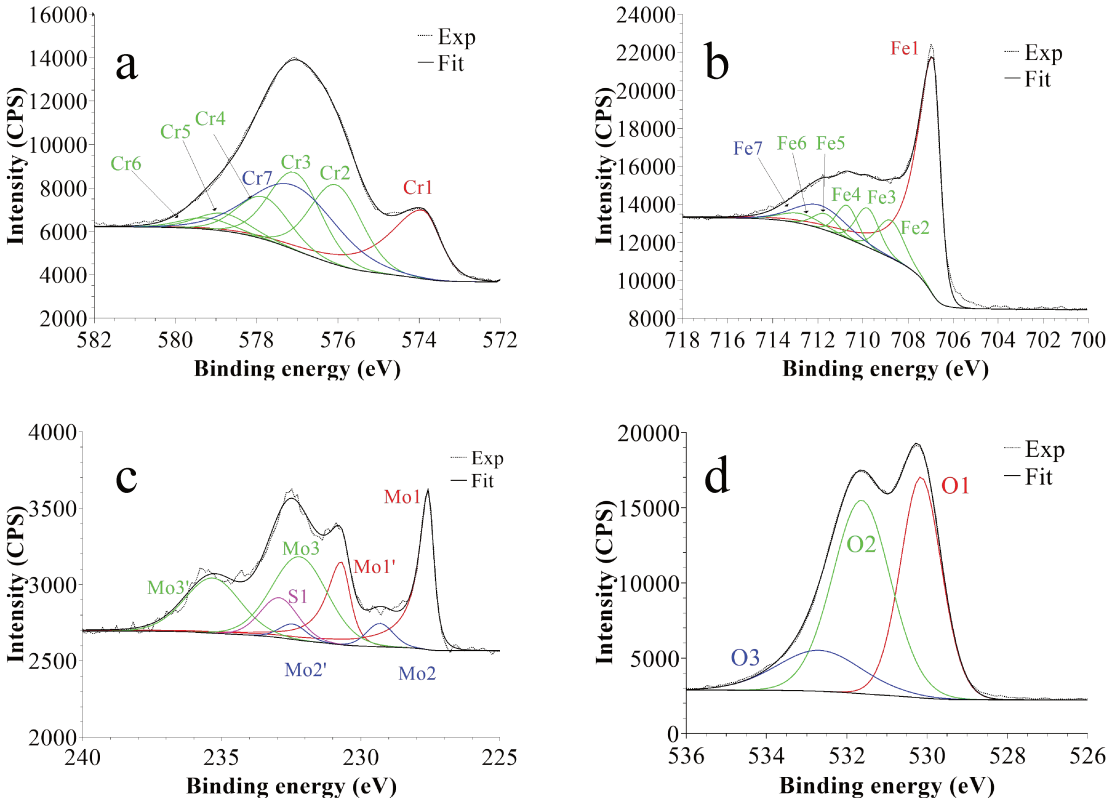

Figure IV-7 XPS core level spectra and their reconstruction for 316L SS passivated in 0.05 M H2SO4 at UPASS = 0.5 V/SCE for 30 min : (a) Cr 2p3/2, (b) Fe 2p3/2, (c) Mo 3d5/2-3/2 and (d) O 1s regions (take-off angle: 90°).

The Ni $2p_{3/2}$ spectra were fitted using a single peak corresponding to metallic Ni^0 in the substrate (Table IV-1) [13][27][45], evidencing that the Ni oxide species measured by ToF-SIMS were at trace level below the detection limit of XPS in all three cases (< 0.5 at%).

The O 1s spectra were fitted with three components O1, O2 and O3 assigned to oxide (O^{2-}), hydroxide (OH^-) and water (H_2O) ligands in the surface oxide films, respectively (see e.g. Figure IV-5, Table IV-1) [11][27][34][45][48]. The OH^-/O^{2-} intensity ratio increases from 0.58 for the native oxide film to 1.72 after treatment at U_{OCP} and then decreases to 1.24 after treatment at U_{Pass}. Similarly, the H_2O/O^{2-} intensity ratio increases from 0.12 to 0.68 and then decreases to 0.39. Clearly, these variations reflect the markedly increased hydroxylation of the initial air-formed oxide film after immersion in the aqueous solution at OCP, showing that the oxide film not only decreases in thickness and gets enriched in Cr and Mo due to preferential iron oxide dissolution but also incorporates much more hydroxyl and water ligands. Anodic

passivation causes competitive re-oxidation of the metallic elements leading to the oxide film growth in thickness, with the preferential formation of oxide ligands since the fractions of hydroxyl and water ligands decrease.

Based on the ToF-SIMS results, the 2-layer model, previously proposed to calculate the thickness and composition of the outer and inner layers of the oxide films as well as the composition of the modified alloy underneath the oxide films (see Chapter III), was used to process the XPS intensity data. This model assumes a mixed iron-chromium hydroxide outer layer and a mixed iron-chromium oxide inner layer. Molybdenum oxide is included in the outer layer and neglected in the inner layer. Assignment of the intensities of the different components was as follows: Cr2-Cr6 and Fe2-Fe4 components to the oxide film inner layer, Cr7, Fe5-Fe7 and Mo2-Mo3 components to the oxide film outer layer and Cr1, Fe1, Mo1 and Ni1 components to the modified alloy region underneath the oxide film. The results are presented in Table IV-2. The overall compositions of the oxide films were obtained by weighting the cation concentration value of each element by the fractional thickness of the inner and outer layers.

Let us first discuss the initial native oxide film. The total thickness is found to be 2.2 nm with outer and inner layers of 0.7 and 1.5 nm thickness, respectively. This total value is very close to that (2 nm) found following the same procedure on the same as-prepared surface of polycrystalline 316L samples (see Chapter III). The overall composition of the film shows that chromium is already enriched in the air-formed native oxide film with Cr^{III} ions representing 41% of the metal cations in the film. Consistently, Cr^{0} is found depleted (17 at% instead of 20 at% in the bulk alloy) in the modified alloy underneath the oxide film. Nickel, not in measurable amount in the oxide film, is found enriched in the alloy underneath the oxide film (26 at% instead of 12 at% in the bulk alloy) in agreement with the ToF-SIMS profile. Concerning molybdenum, the calculated composition shows that it is enriched in the native oxide film (4 at% globally and 13 at% in the oxide outer layer instead of 1.6 at% in the bulk alloy). It is also found enriched in the alloy underneath the oxide film (4 at% instead of 1.6 at% in the bulk alloy). Compared to the more hydroxylated native oxide film formed on the same as-prepared surface of polycrystalline 316L samples (OH^{-}/O^{2-} intensity ratio of 0.93 instead of 0.58 in the present case) (see Chapter III), the present data show lower Cr^{III} (41 vs 55% of the metal cations) and $Mo^{IV/VI}$ (4 vs 6%) enrichments in the oxide film. This might be due to an aging effect, some studies having reported a decreasing Cr/Fe balance in the native oxide with aging in air [2][12][20].

Table IV-2. Thickness and composition of the air-formed native oxide film on polycrystalline 316L SS and variations after immersion for 30 min at OCP in 0.05 M H_2SO_4, and after passivation for 30 min at 0.5 V/SCE in 0.05 M H_2SO_4 as calculated from the XPS data.

		Global film	**Outer layer**	**Inner layer**	**Modified alloy**
Native oxide film	d (nm)	2.2	0.7	1.5	/
	[Fe] (at%)	54.7	82.0	42.0	54.0
	[Cr] (at%)	41.1	5.0	58.0	17.0
	[Ni] (at%)	/	/	/	26.0
	[Mo](at%)	4.1	13.0	/	4.0
	Ratio Cr/Fe	0.8	0.1	1.4	/
OCP oxide film	d (nm)	1.8 (1.7)	0.8 (0.5)	1.0 (1.2)	/
	[Fe] (at%)	24.1 (23.9)	18.0 (26.0)	29.0 (23.0)	52.0 (52.0)
	[Cr] (at%)	68.3 (68.5)	65.0 (48.0)	71.0 (77.0)	20.0 (20.0)
	[Ni] (at%)	/	/	/	24.0 (24.0)
	[Mo](at%)	7.6 (7.6)	17.0 (26.0)	/	4.0 (4.0)
	Ratio Cr/Fe	2.8 (2.9)	3.6 (1.8)	2.4 (3.3)	/
Passive oxide film	d (nm)	2.2	0.8	1.4	/
	[Fe] (at%)	26.1	28.0	25.0	52.0
	[Cr] (at%)	67.7	55.0	75.0	18.0
	[Ni] (at%)	/	/	/	26.0
	[Mo](at%)	6.5	18.0	/	3.0
	Ratio Cr/Fe	2.6	2.0	3.0	/

After treatment in sulfuric acid at U_{OCP}, the results reported in Table IV-2 confirm the overall thickness decrease of the oxide film observed by ToF-SIMS. However, this decrease affects the inner layer only, in contrast with the ToF-SIMS data. The overall composition of the film shows the loss of Fe and the related increases of the Cr and Mo enrichments suggested by ToF-SIMS but the hierarchy of the Cr/Fe ratio between outer and inner layers is not respected. These discrepancies originate from the assignment of the Cr7 component, markedly increased in intensity. Since immersion at OCP causes iron oxide dissolution and pronounced hydroxylation of the film, it can be reasonably assumed that not only the outer layer but also the inner layer is hydroxylated, and thus that a fraction of the intensity of the Cr7 component can be assigned to the inner layer. The values reported in brackets in Table IV-2 have been calculated assigning 50% of the Cr7 intensity to the oxide inner layer. The hierarchy of the Cr/Fe ratio between outer and inner layers is now reproduced as well as the decrease in thickness of both the outer and inner layers. Based on these assumptions, the composition in the outer and inner layers are calculated as $26Fe^{III}$-$48Cr^{III}$-$26Mo^{IV/VI}$ and $23Fe^{III}$-$77Cr^{III}$,

respectively, versus $82Fe^{III}$-$5Cr^{III}$-$13Mo^{IV/VI}$ and $42Fe^{III}$-$58Cr^{III}$ for the native oxide. The overall composition of the film also reflects the compositional changes, independently of the balance in the assignment of the Cr7 peak. The Cr^{III} and $Mo^{IV/VI}$ concentrations increase up to 68.5 % and 7.6 % in the oxide film, respectively, after treatment at U_{OCP}, as a result of the preferential loss of iron oxide by dissolution. In the modified alloy underneath the oxide film, the calculated values suggest no preferential consumption of one of the alloying elements if one considers a ±1 at% accuracy.

Clearly, these data show that the loss of oxide is caused by the preferential dissolution of iron oxide at open circuit potential. It is also shown that oxide growth is too slow to compensate the loss of oxide due to dissolution and, if occurring, does not preferentially consumes one of the alloying elements. To our knowledge, this is observed for the first time on an oxide pre-covered SS surface thanks to the transfer from liquid to UHV environments avoiding the contact with ambient air. Such a procedure was previously applied to ferritic Fe-17Cr samples but starting from an oxide-free surface, not an oxide pre-covered surface, and showed the preferential growth of Cr(III) oxide at anodic potential [16]. The present data highlight that the alterations of the surface oxide film caused by immersion at open circuit potential results from the preferential dissolution of iron oxide.

After passivation at U_{Pass} and compared to the treatment at U_{OCP}, the overall thickness of the oxide film increases with both partitions growing (Table IV-2), which confirms the ToF-SIMS observation. The steady state thickness of the passive film increases due to faster growth of the surface oxide film. There are no significant variations of the overall composition of the oxide film and of the composition of the modified alloy region if one considers a ±1 at% accuracy of the calculated values, indicating that all alloying element are consumed but with iron oxide preferentially dissolving in order to maintain the Cr enrichment. Cr remains enriched in both layers of the passive film and more predominantly in the inner layer. In the hydroxide outer layer, Mo would be less enriched than before re-growth of the oxide film under anodic polarization.

Compared to the native oxide film, there is no significant thickness variation after passivation at U_{PASS}. However, the composition of the oxide film is markedly modified with further Cr(III) enrichment in both layers and Mo(IV-VI) enrichment in the outer layer, in agreement with the previous studies on the same polycrystalline 316L surface (Chapter III) and on a single-crystalline model Fe-Cr-Ni-Mo surface [27]. Thanks to the transfer procedure adopted here and avoiding the contact with ambient air, it is shown here that the preferential dissolution of

Fe(III) is at the origin of these enrichments and essentially takes place at open circuit potential in the absence of any applied anodic polarization. Anodic passivation causes competitive re-growth of the oxide film and dehydroxylation of Fe(III), Cr(III) and Mo(IV-VI) oxide species It increases the steady state thickness of the passive film despite dissolution still occurring and counteracting the formation of the oxide species. The preferential dissolution of Fe(III) oxide species persists to maintain the Cr and Mo enrichments.

IV. 4. Conclusion

Starting from the air-formed native oxide-covered surface, ToF-SIMS and XPS were combined to study the mechanisms of Cr and Mo enrichments leading to passivation of 316L austenitic stainless steel.

The native oxide film formed in ambient air on the 316L surface prepared by mechanical polishing was found to have a thickness of 2.2 nm. It is a mixed Cr(III)-Fe(III) hydroxylated oxide with a bi-layered structure highly enriched in Cr(III) oxide in the inner layer. Iron is concentrated as Fe(III) hydroxide in the outer layer together with molybdenum, mostly present as Mo(VI). Nickel is below the XPS detection limit. Immersion at open circuit potential in aqueous acid solution causes hydroxylation and preferential dissolution of Fe(III) from both layers of the film, decreasing the thickness and promoting the enrichments in Cr and Mo. In the absence of an anodizing electric field, oxide growth and thickness increase do not happen. Upon anodic polarization in the passive domain, dehydroxylation is promoted in the inner layer and oxidation of iron, chromium and molybdenum takes place, leading to re-growth of the oxide film and increase of the steady-state thickness without affecting the overall Cr enrichment but slightly mitigating the Mo enrichment. Cr and Mo enrichments persist owing to preferential dissolution of Fe(III).

These results were obtained using an experimental approach preventing contact to ambient air of the samples during transfer from liquid environment for electrochemical treatment to UHV environment for surface analysis. They show that the treatment of the surface native oxide film in acid solution, in the absence of applied electric field, promotes the Cr and Mo enrichments known as beneficial to the resistance to passivity breakdown and initiation of localized corrosion.

Acknowledgements

This project has received funding from the European Research Council (ERC) under the European Union's Horizon 2020 research and innovation program (ERC Advanced Grant no. 741123). Région Île-de-France is acknowledged for partial funding of the ToF-SIMS equipment.

References

1. P. Schmuki, From Bacon to barriers: a review on the passivity of metals and alloys, J Solid State Electrochem. 6 (2002) 145–164. doi:10.1007/s100080100219.
2. V. Maurice, W.P. Yang, P. Marcus, XPS and STM Study of Passive Films Formed on Fe-22Cr(110) Single - Crystal Surfaces, J. Electrochem. Soc. 143 (1996) 1182 – 1200. doi:10.1149/1.1836616.
3. M. Seo, N. Sato, Differential composition profiles in depth of thin anodic oxide films on iron-chromium alloy, Surface Science. 86 (1979) 601 – 609. doi:10.1016/0039-6028(79)90440-0.
4. G. Hultquist, M. Seo, T. Leitner, C. Leygraf, N. Sato, The dissolution behaviour of iron, chromium, molybdenum and copper from pure metals and from ferritic stainless steels, Corrosion Science. 27 (1987) 937–946. doi:10.1016/0010-938X(87)90060-6.
5. D.F. Mitchell, M.J. Graham, Comparison of Auger and SIMS analysis of a thin passive oxide film on iron—25% chromium, Surface and Interface Analysis. 10 (1987) 259–261. doi:10.1002/sia.740100507.
6. S. Mischler, H.J. Mathieu, D. Landolt, Investigation of a passive film on an iron chromium alloy by AES and XPS, Surf. Interface Anal. 11 (1988) 182 – 188. doi:10.1002/sia.740110403.
7. P. Marcus, I. Olefjord, A Round Robin on combined electrochemical and AES/ESCA characterization of the passive films on Fe-Cr and Fe-Cr-Mo alloys, Corrosion Science. 28 (1988) 589–602. doi:10.1016/0010-938X(88)90026-1.
8. C. Calinski, H.-H. Strehblow, ISS Depth Profiles of the Passive Layer on Fe/Cr Alloys, J. Electrochem. Soc. 136 (1989) 1328–1331. doi:10.1149/1.2096915.

9. R. Kirchheim, B. Heine, H. Fischmeister, S. Hofmann, H. Knote, U. Stolz, The passivity of iron-chromium alloys, Corrosion Science. 29 (1989) 899 – 917. doi:10.1016/0010-938X(89)90060-7.

10. J.E. Castle, J.H. Qiu, A co-ordinated study of the passivation of alloy steels by plasma source mass spectrometry and x-ray photoelectron spectroscopy — 1. characterization of the passive film, Corrosion Science. 29 (1989) 591 – 603. doi:10.1016/0010-938X(89)90010-3.

11. J.E. Castle, J.H. Qiu, A co-ordinated study of the passivation of alloy steels by plasma source mass spectrometry and x-ray photoelectron spectroscopy — II. growth kinetics of the passive film, Corrosion Science. 29 (1989) 605 – 616. doi:10.1016/0010-938X(89)90011-5.

12. W.P. Yang, D. Costa, P. Marcus, Resistance to Pitting and Chemical Composition of Passive Films of a Fe-17%Cr Alloy in Chloride-Containing Acid Solution, J. Electrochem. Soc. 141 (1994) 2669–2676. doi:10.1149/1.2059166.

13. S. Haupt, H.-H. Strehblow, A combined surface analytical and electrochemical study of the formation of passive layers on FeCr alloys in 0.5 M H2SO4, Corrosion Science. 37 (1995) 43–54. doi:10.1016/0010-938X(94)00104-E.

14. L.J. Oblonsky, M.P. Ryan, H.S. Isaacs, In Situ Determination of the Composition of Surface Films Formed on Fe-Cr Alloys, J. Electrochem. Soc. 145 (1998) 1922 – 1932. doi:10.1149/1.1838577.

15. D. Hamm, K. Ogle, C.-O.A. Olsson, S. Weber, D. Landolt, Passivation of Fe–Cr alloys studied with ICP-AES and EQCM, Corrosion Science. 44 (2002) 1443 – 1456. doi:10.1016/S0010-938X(01)00147-0.

16. P. Keller, H.-H. Strehblow, XPS investigations of electrochemically formed passive layers on Fe/Cr-alloys in 0.5 M H2SO4, Corrosion Science. 46 (2004) 1939 – 1952. doi:10.1016/j.corsci.2004.01.007.

17. S. Mischler, A. Vogel, H.J. Mathieu, D. Landolt, The chemical composition of the passive film on Fe-24Cr and Fe-24Cr-11Mo studied by AES, XPS and SIMS, Corrosion Science. 32 (1991) 925–944. doi:10.1016/0010-938X(91)90013-F.

18. K. Hashimoto, K. Asami, K. Teramoto, An X-ray photo-electron spectroscopic study on the role of molybdenum in increasing the corrosion resistance of ferritic stainless steels in HC1, Corrosion Science. 19 (1979) 3–14. doi:10.1016/0010-938X(79)90003-9.

19. M.-W. Tan, E. Akiyama, A. Kawashima, K. Asami, K. Hashimoto, The effect of air exposure on the corrosion behavior of amorphous Fe-8Cr-Mo-13P-7C alloys in 1 M HCl, Corrosion Science. 37 (1995) 1289–1301. doi:10.1016/0010-938X(95)00035-I.

20. V. Maurice, W.P. Yang, P. Marcus, X-Ray Photoelectron Spectroscopy and Scanning Tunneling Microscopy Study of Passive Films Formed on (100) Fe-18Cr-13Ni Single-Crystal Surfaces, J. Electrochem. Soc. 145 (1998) 909–920. doi:10.1149/1.1838366.

21. I. Olefjord, B.-O. Elfstrom, The Composition of the Surface during Passivation of Stainless Steels, CORROSION. 38 (1982) 46–52. doi:10.5006/1.3577318.

22. E. De Vito, P. Marcus, XPS study of passive films formed on molybdenum-implanted austenitic stainless steels, Surf. Interface Anal. 19 (1992) 403 – 408. doi:10.1002/sia.740190175.

23. E. McCafferty, M.K. Bernett, J.S. Murday, An XPS study of passive film formation on iron in chromate solutions, Corrosion Science. 28 (1988) 559 – 576. doi:10.1016/0010-938X(88)90024-8.

24. P. Marcus, J.M. Grimal, The anodic dissolution and passivation of NiCrFe alloys studied by ESCA, Corrosion Science. 33 (1992) 805–814. doi:10.1016/0010-938X(92)90113-H.

25. M. Bojinov, G. Fabricius, T. Laitinen, K. Mäkelä, T. Saario, G. Sundholm, Influence of molybdenum on the conduction mechanism in passive films on iron–chromium alloys in sulphuric acid solution, Electrochimica Acta. 46 (2001) 1339–1358. doi:10.1016/S0013-4686(00)00713-1.

26. T. Yamamoto, K. Fushimi, M. Seo, S. Tsuri, T. Adachi, H. Habazaki, Depassivation–repassivation behavior of type-312L stainless steel in NaCl solution investigated by the micro-indentation, Corrosion Science. 51 (2009) 1545 – 1553. doi:10.1016/j.corsci.2008.11.020.

27. V. Maurice, H. Peng, L.H. Klein, A. Seyeux, S. Zanna, P. Marcus, Effects of molybdenum on the composition and nanoscale morphology of passivated austenitic stainless steel surfaces, Faraday Discuss. 180 (2015) 151–170. doi:10.1039/C4FD00231H.

28. K. Sugimoto, Y. Sawada, The role of molybdenum additions to austenitic stainless steels in the inhibition of pitting in acid chloride solutions, Corrosion Science. 17 (1977) 425–445. doi:10.1016/0010-938X(77)90032-4.

29. H. Ogawa, H. Omata, I. Itoh, H. Okada, Auger Electron Spectroscopic and Electrochemical Analysis of the Effect of Alloying Elements on the Passivation Behavior of Stainless Steels, CORROSION. 34 (1978) 52–60. doi:10.5006/0010-9312-34.2.52.

30. I. Olefjord, The passive state of stainless steels, Materials Science and Engineering. 42 (1980) 161–171. doi:10.1016/0025-5416(80)90025-7.

31. W. Yang, R.-C. Ni, H.-Z. Hua, A. Pourbaix, The behavior of chromium and molybdenum in the propagation process of localized corrosion of steels, Corrosion Science. 24 (1984) 691–707. doi:10.1016/0010-938X(84)90059-3.

32. I. Olefjord, B. Brox, U. Jelvestam, Surface Composition of Stainless Steels during Anodic Dissolution and Passivation Studied by ESCA, J. Electrochem. Soc. 132 (1985) 2854–2861. doi:10.1149/1.2113683.

33. A.R. Brooks, C.R. Clayton, K. Doss, Y.C. Lu, On the Role of Cr in the Passivity of Stainless Steel, J. Electrochem. Soc. 133 (1986) 2459–2464. doi:10.1149/1.2108450.

34. C.R. Clayton, Y.C. Lu, A Bipolar Model of the Passivity of Stainless Steel: The Role of Mo Addition, J. Electrochem. Soc. 133 (1986) 2465–2473. doi:10.1149/1.2108451.

35. Y.C. Lu, C.R. Clayton, A.R. Brooks, A bipolar model of the passivity of stainless steels—II. The influence of aqueous molybdate, Corrosion Science. 29 (1989) 863 – 880. doi:10.1016/0010-938X(89)90058-9.

36. C.R. Clayton, Y.C. Lu, A bipolar model of the passivity of stainless steels — III. The mechanism of MoO_4^{2-} formation and incorporation, Corrosion Science. 29 (1989) 881–898. doi:10.1016/0010-938X(89)90059-0.

37. I. Olefjord, L. Wegrelius, Surface analysis of passive state, Corrosion Science. 31 (1990) 89–98. doi:10.1016/0010-938X(90)90095-M.

38. H. Habazaki, A. Kawashima, K. Asami, K. Hashimoto, The corrosion behavior of amorphous Fe-Cr-Mo-P-C and Fe-Cr-W-P-C alloys in 6 M HCl solution, Corrosion Science. 33 (1992) 225–236. doi:10.1016/0010-938X(92)90147-U.

39. D.D. Macdonald, The Point Defect Model for the Passive State, J. Electrochem. Soc. 139 (1992) 3434–3449. doi:10.1149/1.2069096.

40. A. Elbiache, P. Marcus, The role of molybdenum in the dissolution and the passivation of stainless steels with adsorbed sulphur, Corrosion Science. 33 (1992) 261 – 269. doi:10.1016/0010-938X(92)90150-2.

41. T. Massoud, V. Maurice, L.H. Klein, A. Seyeux, P. Marcus, Nanostructure and local properties of oxide layers grown on stainless steel in simulated pressurized water reactor environment, Corrosion Science. 84 (2014) 198–203. doi:10.1016/j.corsci.2014.03.030.

42. V. Maurice, P. Marcus, Current developments of nanoscale insight into corrosion protection by passive oxide films, Current Opinion in Solid State and Materials Science. 22 (2018) 156–167. doi:10.1016/j.cossms.2018.05.004.

43. L. Ma, F. Wiame, V. Maurice, P. Marcus, New insight on early oxidation stages of austenitic stainless steel from in situ XPS analysis on single-crystalline Fe−18Cr−13Ni, Corrosion Science. 140 (2018) 205–216. doi:10.1016/j.corsci.2018.06.001.

44. Z. Wang, F. Di-Franco, A. Seyeux, S. Zanna, V. Maurice, P. Marcus, Passivation-Induced Physicochemical Alterations of the Native Surface Oxide Film on 316L Austenitic Stainless Steel, J. Electrochem. Soc. 166 (2019) C3376 – C3388. doi:10.1149/2.0321911jes.

45. Ma L, Wiame F, Maurice V, Marcus P. Origin of nanoscale heterogeneity in the surface oxide film protecting stainless steel against corrosion. npj Materials Degradation, in press.

46. P. Marcus, J. Oudar, I. Olefjord, Studies of the influence of sulphur on the passivation of nickel by Auger electron spectroscopy and electron spectroscopy for chemical analysis, Materials Science and Engineering. 42 (1980) 191 – 197. doi:10.1016/0025-5416(80)90028-2.

47. S. Haupt, U. Collisi, H.D. Speckmann, H.-H. Strehblow, Specimen transfer from the electrolyte to the UHV in a closed system and some examinations of the double layer on Cu, Journal of Electroanalytical Chemistry and Interfacial Electrochemistry. 194 (1985) 179–190. doi:10.1016/0022-0728(85)85002-6.

48. M.C. Biesinger, B.P. Payne, A.P. Grosvenor, L.W.M. Lau, A.R. Gerson, R.St.C. Smart, Resolving surface chemical states in XPS analysis of first row transition metals, oxides

and hydroxides: Cr, Mn, Fe, Co and Ni, Applied Surface Science. 257 (2011) 2717–2730. doi:10.1016/j.apsusc.2010.10.051.

49. T. Yamashita, P. Hayes, Analysis of XPS spectra of Fe2+ and Fe3+ ions in oxide materials, Applied Surface Science. 254 (2008) 2441 – 2449. doi:10.1016/j.apsusc.2007.09.063.

50. B.P. Payne, M.C. Biesinger, N.S. McIntyre, X-ray photoelectron spectroscopy studies of reactions on chromium metal and chromium oxide surfaces, Journal of Electron Spectroscopy and Related Phenomena. 184 (2011) 29 – 37. doi:10.1016/j.elspec.2010.12.001.

Chapter V

Chloride-induced alterations of the passive film on 316L stainless steel and blocking effect of pre-passivation

This chapter reproduces the final preprint of an original article published in Electrochimica Acta:
Z. Wang, A. Seyeux, S. Zanna, V. Maurice, P. Marcus, Chloride-induced alterations of the passive film on 316L stainless steel and blocking effect of pre-passivation, Electrochimica Acta. (2019) 135159. https://doi.org/10.1016/j.electacta.2019.135159.

Abstract

Electrochemical polarization measurements were combined with surface analysis by Time of Flight Secondary Ion Mass Spectroscopy (ToF-SIMS), X-Ray Photoelectron Spectroscopy (XPS) and Atomic Force Microscopy (AFM) to study the alterations of the passive film on 316L austenitic stainless steel induced by the presence of chlorides in sulfuric acid electrolyte. The work was performed at a stage of initiation of localized corrosion preceding metastable pitting at the micrometer scale as verified by current transient analysis and AFM. The results show that Cl^- ions enter the bilayer structure of the surface oxide already formed in the native oxide-covered initial surface state at concentrations below the detection limit of XPS (< 0.5 at%), mostly in the hydroxide outer layer where Fe(III) and Mo(IV,VI) species are concentrated but barely in the oxide inner layer enriched in Cr(III). Their main effect is to produce a less resistive passive state by poisoning dehydroxylation and further Cr(III) and Mo(IV,VI) enrichments obtained in the absence of chlorides. This detrimental effect can be suppressed by pre-passivation in a Cl-free electrolyte, which blocks the entry of chlorides in the passive film, including in the outer exchange layer, and enables the beneficial aging-induced variations of the composition to take place despite the presence of chlorides in the environment.

Ⅴ.1. Introduction

Passive films consisting of ultrathin oxide/hydroxide layers formed at the surface make stainless steels (SS) highly resistant against corrosion, even in harsh environmental conditions. On ferritic Fe-Cr(-Mo) [1]-[19] and austenitic Fe-Cr-Ni(-Mo) [20]-[40] SS substrates, the surface oxide/hydroxide layer is only a few nanometers thick but markedly enriched in Cr(III), which is the key for efficient passivity because of the higher stability of Cr(III) compared to Fe(II-III) oxide species. For austenitic SS, only very little Ni(II) is present when detected in

the passive film and the metallic alloy region underneath the oxide is enriched with Ni(0) [20]-[22][27]-[30].

With the addition of Mo in the alloy, e.g. in austenitic AISI 316L, an increased corrosion resistance is obtained in chloride-containing environments, where passive film breakdown can be followed by the initiation of localized corrosion by pitting. The passive films are similarly ultrathin but the composition include Mo(IV) and Mo(VI) oxide species at a few at% level [10][21][22][30][32][35][37]. It has been proposed, and it is still debated, that the beneficial role of molybdenum would be to mitigate passive film breakdown [10][19][28][30][36][39][40]-[45] or to promote passive film repair [18][30][32][33][41][43]-[45].

As suggested by recent nanometer scale studies [27][48], the Cr(III) enrichment may not be homogeneous in the passive film, and the Cr enrichment heterogeneities may cause the local failure of the passivity and the initiation of localized corrosion followed by pit growth where the passive film fails to self-repair [49]. The better understanding of the mechanisms governing the Cr (and Mo) enrichment requires to thoroughly investigate the initial stages of oxidation leading to pre-passivation of the SS surface [50][51][52] as well as the alterations brought by electrochemical passivation of the native oxide-covered SS surface [46][47].

On AISI 316L, recent surface analytical studies performed by Time-of-Flight Secondary Ion Mass Spectroscopy (ToF-SIMS) and X-ray Photoelectron Spectroscopy (XPS) [27][46][47]confirmed the bilayer structure of the passive film previously reported [21][22][27][30][32]. The native oxide film formed in air was found to already develop this bilayer structure with both the hydroxide outer and oxide inner layers enriched in Cr(III) and with Fe(III) more concentrated in the outer layer together with Mo(IV,VI). Electrochemical passivation in chloride-free sulfuric acid solution did not alter the bilayer structure and thickness of the surface oxide but promoted its Cr and Mo enrichments, owing to the lower stability and preferential dissolution of Fe(III) as previously proposed [4][16][53], and thereby increased the corrosion resistance of the passive state.

In the present work, we address the alterations of the surface oxide films brought by electrochemical passivation in Cl-containing sulfuric acid solutions. Potentiodynamic and potentiostatic polarization measurements were used to define the electrochemical conditions best suited to alter the passive state without initiating localized corrosion (i.e metastable pitting) at the micrometer scale. ToF-SIMS and XPS were applied to characterize the bilayer structure, thickness and composition of the passive film and the entry of chlorides. Surface

morphology was studied by Atomic Force Microscopy (AFM). The results provide new insight on the effect of pre-passivation on the entry of chlorides in the passive film and increased resistance to metastable pitting at the nanometer scale.

V. 2. Experimental

The same polycrystalline AISI 316L austenitic SS samples as in previous work were used (Chapters III and IV). The bulk composition in the main alloying elements was Fe–19Cr–13Ni–2.7Mo wt% (Fe–20Cr–12Ni–1.6Mo at%). The surface was prepared by mechanical polishing first with emery paper of successive 1200 and 2400 grades and then with diamond suspensions of successive 6, 3, 1 and 0.25 μm grades. Cleaning and rinsing were performed after each polishing step in successive ultrasonicated baths of acetone, ethanol and Millipore® water (resistivity > 18 MΩ cm). Filtered compressed air was used for drying.

A 3-electrode electrochemical cell controlled by a Gamry 600 potentiostat was used for the electrochemical measurements. It included a Pt grid as counter electrode and a saturated calomel electrode as reference electrode. The area of the working electrode was 0.5 cm^2 delimited by a Viton O-ring. The electrolyte was a 0.05 M H_2SO_4 aqueous solution in which NaCl was added at varying concentration. It was prepared from ultrapure chemicals (VWR®) and Millipore® water and bubbled with argon for 30 minutes prior to and continuously during the measurements. All experiments were performed at room temperature.

Passivation in the Cl-containing electrolyte was performed starting from two different surface states previously analyzed in details (see Chapter III): the native oxide-covered surface state and the pre-passivated surface state. The native oxide-covered sample was obtained after a short time (5-10 min) exposure in ambient air after surface preparation. The pre-passivated sample was produced by potentiostatic anodic polarization in the passive domain in the Cl-free 0.05 M H_2SO_4 electrolyte: after resting for 0.5 hour at open circuit value (U_{OC} = -0.23 V/SCE), the potential was stepped to U_{Pass} = 0.3 V/SCE and maintained at this value for 1 hour. The U_{Pass} value was selected from potentiodynamic polarization as described below. No cathodic pre-treatment was performed in order to avoid any reduction-induced alteration of the initial native oxide film prior to passivation. These exact same conditions as in our previous study were adopted so as to enable the comparative analysis of the effects brought by the presence of chlorides in the electrolyte.

In the Cl-containing electrolyte, two different passivated samples were prepared in order to study the alterations of the passive films brought by passivation in the presence of chloride and the modifications induced by pre-passivation of the surface. One sample was passivated directly from the initial native oxide-covered surface state using the same treatment conditions as for pre-passivation but in a 0.05 M H_2SO_4 + 0.05 M NaCl electrolyte. This concentration was selected from potentiostatic polarization curves as discussed below. The other sample was passivated in the same conditions but starting from the pre-passive surface state obtained in the Cl-free electrolyte.

Depth profile elemental analysis of the oxide-covered surfaces was performed using a ToF-SIMS 5 spectrometer (Ion ToF – Munster, Germany) operated at about 10^{-9} mbar. Topmost surface analysis in static SIMS conditions using a pulsed 25 keV Bi^+ primary ion source delivering 1.2 pA current over a 100 × 100 μm^2 area was interlaced with sputtering using a 1 keV Cs^+ ion beam giving a 32 nA target current over a 300 × 300 μm^2 area. Analysis was centered inside the eroded crater to avoid edge effects. The profiles were recorded with negative secondary ions that have higher yield for oxide matrices than for metallic matrices. The Ion-Spec software was used for data acquisition and processing.

Surface chemical analysis was performed by XPS with a Thermo Electron ESCALAB 250 spectrometer operating at about 10^{-9} mbar. The X-ray source was an AlK_α monochromatized radiation (hν = 1486.6 eV). Survey spectra were recorded with the pass energy of 100 eV at a step size of 1 eV. High resolution spectra of the Fe 2p, Cr 2p, Ni 2p, Mo 3d, O 1s, S 2p, Cl 2p and C 1s core level regions were recorded with a pass energy of 20 eV at a step size of 0.1 eV. The take-off angle of the analyzed photoelectrons was 90°. The binding energies (BE) were calibrated by setting the C 1s signal corresponding to olefinic bonds (–CH_2–CH_2–) at 285.0 eV. Data processing (curve fitting) was performed with CasaXPS, using a Shirley type background and Lorentzian/Gaussian (70%/30%) peak shapes. Asymmetry was taken into account for the metallic components (Cr^0, Fe^0, Mo^0, Ni^0) and a broader envelope was used to account for the multiplet splitting of the oxide components (Cr^{III}, Fe^{III}, Mo^{IV}, Mo^{VI}).

AFM analysis was performed with a Nano-Observer microscope (CSI instruments) operated in oscillating (Tapping®) mode. A “Model FORT” silicon probe from AppNano company was used. The resonant frequency f of the cantilever was 50-70 kHz and the stiffness factor k 1-5 N/m. Nominal tip radius was inferior to 10 nm. The AFM images were acquired in the topographic mode and analyzed with the Gwyddion software. The local measurements were

performed on three different zones on each sample.

V. 3. Results and discussion

V. 3. 1. Electrochemical conditions for Cl-induced alteration of the passive film

Several parameters such as electrolyte, pH, chloride concentration, temperature, time, polarization potential, material composition and microstructure, surface composition and microstructure, and surface roughness can influence the initiation of localized corrosion and pit growth on stainless steel [54]-[57]. In this work, only the polarization potential and the chloride concentration were varied in order to find the appropriate conditions to alter the passive state, however without initiating localized corrosion at least at the micrometer scale. All other parameters were kept unchanged by careful reproduction of the experimental conditions.

Figure V-1a shows the polarization curve recorded in the Cl-free electrolyte in the range -0.8 V < U < 1.5 V/SCE. In the anodic region starting at -0.34 V/SCE, a narrow “active” domain is observed before passivation at -0.30 V/SCE. At the active-passive transition, the current density is quite low (1.3×10^{-5} A cm^{-2}) owing to the presence of the native oxide initially protecting the surface and already impeding dissolution before anodic passivation. The passive domain extends from -0.30 V/SCE to about 0.80 V/SCE, beyond which transpassivity is observed before the onset of oxygen evolution. In the passive domain, the lowest current density, of about 5×10^{-6} A cm^{-2}, is reached in the 0.3-0.5 V/SCE range. Since corresponding to the most stable surface state reached in these non-steady state conditions, the lower limit at 0.3 V/SCE of this potential range was selected as passivation potential value for producing the steady state passive films to be studied.

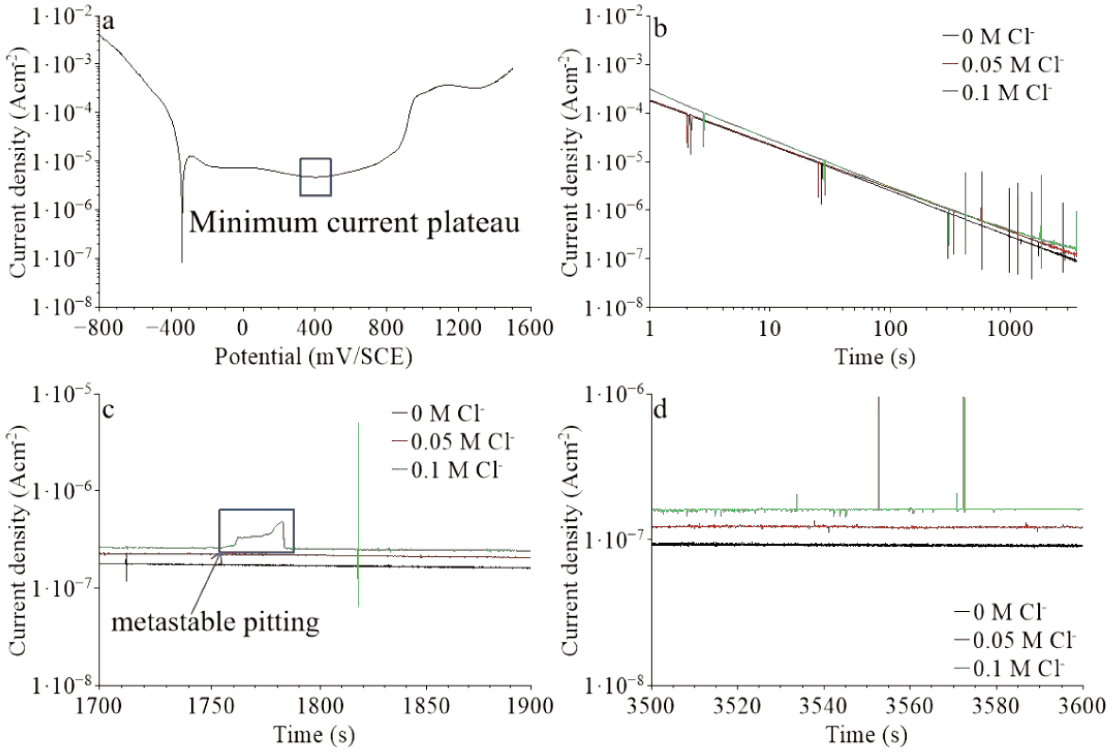

Figure V-1 Electrochemical polarization of the native oxide-covered 316L SS sample in 0.05 M H_2SO_4: a) Potentiodynamic polarization curve in the Cl-free electrolyte (scan rate 1 mV/s), b) Potentiostatic polarisation curves at 0.3 V/SCE at increasing chloride concentration, c) Zoom of (b) in the 1700-1800 s time range, d) Zoom of (b) in the 3500-3600 s time range.

Figure V-1b shows the passivation current transients obtained at U_{Pass} = 0.3 V/SCE and NaCl concentrations of 0 M, 0.05 M and 0.1 M. Due to the high noise while the potential is applied to the surface during the first second, all these curves are started at 1s. The log-log plot shows that in all cases the current density continuously decreases, by about 3 orders of magnitude in the time frame of the experiments. This means that the passive films become increasingly protective with time however without reaching stable steady state after 1 hour. Previous studies with ultra-low current measurement setups and micrometer size electrodes have shown that a stable steady state is beyond reasonable time reach on austenitic stainless steels [58][59]. Current spikes, both positive and negative appeared during the current range changes at 10^{-4}, 10^{-5}, and 10^{-6} A cm^{-2} with respect to the passive current, are observed independently of the Cl^- concentration. They correspond to instabilities generated by the electronic noise of the setup and captured by the measurement sampling (50 points per second). In 0.1 M NaCl, the passive current is systematically higher than in 0 M NaCl. In 0.05 M NaCl, the passive current is

almost identical (1.8×10^{-4} A cm^{-2}) to that in 0 M NaCl after 1 s of passivation, suggesting nearly no effect on early passivation. However, it becomes slightly higher in the later stages of passivation (1.2×10^{-7} vs 0.9×10^{-7} A cm^{-2} after 3600 s of passivation), showing a slightly delayed and milder poisoning effect than in 0.1 M NaCl.

Figure V-1c shows a blowup in semi-log scale of the current transients in the 1700-1800 s time range. In 0.1 M NaCl, one observes, in addition to the spike already seen in Figure V-1b, a transient typical for metastable pitting. The slow increase of current represents the anodic dissolution during the initial growth of the pit, and the sudden shut down the repassivation of the pit [58]-[60]. No such transient are observed in 0.05 M NaCl and in 0 M NaCl. The passive currents are increasingly higher with increased chloride concentration and appear stable in this semi-log scale although they are not (Figure V-1b). Figure V-1d presents another blowup of the current transients corresponding to the 3500-3600 s time range. No transients associated to metastable pitting are observed in 0.05 M NaCl and in 0 M NaCl. The positive current spikes observed in 0.1 M NaCl possibly correspond to metastable events occurring too fast to be resolved by the measurement sampling. The differences in passive currents with increasing chloride concentration can be explained by two hypothesis, first is the increase of chloride concentration changes the charge state of the double layer and modified the passive current. Also it can be a characteristic of the poisoning of the passive state due to the present of chloride ions.

From the current transient of metastable pitting observed in Figure V-1c, one can estimate the dimension of the associated metastable pitting event. To do so we consider that only one pit has formed in a single event and that it has a hemispherical shape. As Fe is the most concentrate and the less noble metal in the metallic substrate so we have considered the most consumed metal is Fe in the pitting process. Based on the Pourbaix diagram, with out electrochemical condition 0.3V/SCE and 0.05M H2SO4 (pH near 1.2), the Fe2+ is the most stable ion in the solution. The principal reaction considered is the oxidative dissolution of the metal M(0) to M(II) with the transfer of 2 electrons. The diameter d of the pit is expressed as:

$$d = 2 * \sqrt[3]{\frac{2*3*Q*M_M}{4*2*e*N_A*\rho_M*\pi}} \qquad \text{eq. V-1}$$

where Q is the charge of the current transient (with the passive current eliminated), e the elementary charge (1.6×10^{-19} C), N_A the Avogadro number (6.02×10^{23} mol^{-1}), M the molar mass of the metal (56 g mol^{-1} for Fe) and ρ its density Fe (7.8 g cm^{-3} for Fe).

From the charge of 6.1 μC of the current transient measured in 0.1 M NaCl (Figure V-1c), one obtains a diameter of 9.5 μm. Also, the presence of the pits at micrometric scale has been confirmed by optic microscope. This means that not only metastable pitting has occurred, which we want to avoid, but also that the generated pit, or pits if several have formed simultaneously, has reached micrometer dimensions before repassivating, which is far beyond the early stage of passivity alteration preceding passivity breakdown that we want to study. In other words, the concentration of 0.1 M NaCl is too high for our study. In 0.05 M NaCl, no metastable pitting transient are detected and this concentration is thus more adapted for our investigation.

With a simple transformation, eq. V-1 can be reverted to express the charge Q associated with the formation a single hemispherical pit of diameter d. The expression is:

$$Q = (\frac{d}{2})^3 * \frac{4*2*e*N_A*\rho_M*\pi}{2*3*M_M} \qquad \text{eq. V-2}$$

For a pit of sub-micrometer diameter of 500 nm (which is the average value for nanometric pits), the estimated charge is 0.88 nC. Assuming a metastable pitting time of 1 s, the current amplitude of the associated transient would be 0.88 nA, which is below the background currents of 80 and 60 nA measured after 3600 s in the 0.1 and 0.05 M NaCl electrolytes. The dimensions of the working electrode could be reduced to micrometer size in order to reduce the background current and detect sub-micrometer and even nanometer metastable pitting events, like achieved in previous studies [58],[59]. However, this was not considered here for the sake of surface analysis that requires a measuring area of at least 1 mm^2. Hence, even though the 0.05 M NaCl electrolyte was selected for mild alteration of the passive state in the presence of chloride, it cannot be excluded that nanometer scale and even sub-micrometer scale metastable pits formed during the applied passivation treatment.

V. 3. 2. Passivation transients and surface topography

Figure V-2 shows the log-log plots of the passivation transients obtained in the 0.05 M H_2SO_4 + 0.05 M NaCl electrolyte starting from the native oxide-covered surface state and the pre-passivated surface state on the samples subsequently used for surface analysis.

The transient obtained in the Cl-free 0.05 M H_2SO_4 electrolyte starting from the native oxide-covered surface state, and corresponding to the pre-passivation treatment, is also shown for comparison. No current spikes are observed in these experiments performed in more stable

measuring conditions. Like in Figure V-1, the plots comparing the samples passivated and the native oxide-covered surface state with or without chlorides in the electrolyte show a continuous decrease in passive current, confirming that an increasingly protecting passive film is formed and that the stable steady state is not reached after 1 hour. The slightly higher current measured in the 0.05 M NaCl electrolyte confirms the alterations of the passive state at the later stage of passivation after 3600 s (1.2×10^{-7} vs 1.0×10^{-7} A cm^{-2}). A slightly higher current is also observed in the early passivation stages after 1 s (1.8×10^{-4} vs 1.4×10^{-4} A cm^{-2}), a difference more marked than in Figure V-1 possibly due to slight differences in the native oxide-covered surface state. The poisoning effect of chlorides is observed also during initial passivation in this experiment and it is continuous.

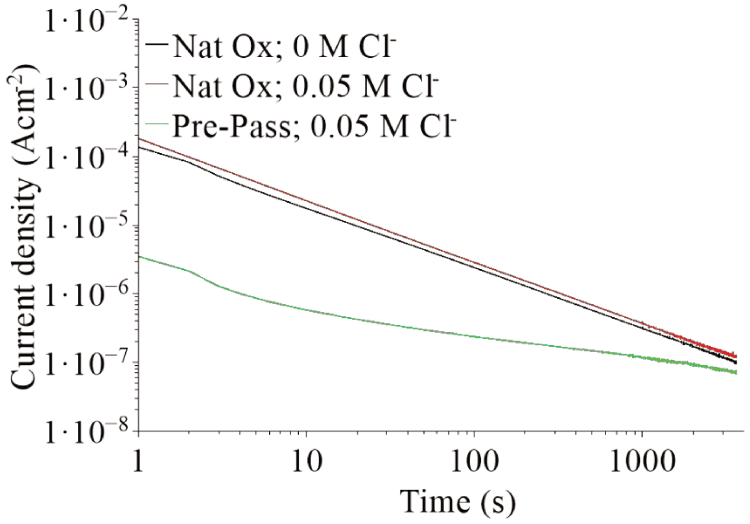

Figure V-2 Potentiostatic polarisation curves at 0.3 V/SCE for 316L SS in 0.05 M H_2SO_4 for the native oxide-covered sample in the Cl-free electrolyte (Nat Ox; 0 M Cl^-) and in the 0.05 M NaCl electrolyte (Nat Ox; 0.05 M Cl^-), and for the pre-passivated sample in the 0.05 M NaCl electrolyte (Pre-Pass; 0.05 M Cl^-)

Based on the relation between volume of consumed material and associated charge, it is possible to express the equivalent thickness h dissolved during the passivation process. Still considering that the metal M(0) oxidizes to M(II) with the transfer of 2 electrons, the expressions is:

$$h = \frac{Q * M_M}{2 * e * N_A * \rho_M * S} \qquad \text{eq. V-3}$$

where S is the electrode area (0.5 cm^2 in our case).

For the transient measured in the Cl-free 0.05 M H_2SO_4 electrolyte starting from the native oxide-covered surface state (black curve), the charge obtained by integrating the current curve from 1s to 3600 s is 1.9 mC corresponding to an equivalent thickness of 1.4 nm. From the *fcc* structure of stainless steel of parameter 0.359 nm, this corresponds to 7.8 atomic (100) planes of stainless steel being consumed by the transition from native-oxide surface state to passivated surface state. For the transient obtained in the Cl-containing 0.05 M H_2SO_4 electrolyte also starting from the native oxide-covered surface state (red curve), the charge is 2.3 mC corresponding to an equivalent thickness of 1.7 nm. This slightly higher (about 20%) value shows that the passivation process consumes more material in the presence of chlorides in the electrolyte, and thus confirms the poisoning effect of chlorides on passivation.

On the pre-passivated sample, the decrease in passive current is also continuous and a stable steady state is not reached after 3600 s. However, the current has much lower amplitude, starting from 3.5×10^{-6} A cm^{-2} after 1 s, nearly two orders of magnitude lower, and ending at 7.0×10^{-8} A cm^{-2} after 3600 s, also lower than in the absence of pre-passivation. This shows that the pre-passivation treatment increases the stability of the surface state, including in the presence of chlorides in the electrolyte, and suggests that it reduces the Cl-induced alterations of the passive state. The charge measured during this treatment is 0.4 mC corresponding to an equivalent thickness of 0.3 nm. This value, markedly lower than the value of 1.4 nm, confirms the beneficial effect of pre-passivation on the surface residual reactivity in the presence of chlorides.

Figure V-3 presents the AFM topographic data for the initial native oxide-covered surface and the surface passivated in the Cl-containing electrolyte.
In both cases, the grooves produced by the mechanical polishing treatment are clearly seen. Protruding micro particles are also present, likely originating from dust deposited from the ambient atmosphere. The two histograms present the distribution of the pixels along the surface normal (Z position). Each distribution is referred to a zero value corresponding to the median topographic level of the image. For the native oxide-covered surface (Figure V-3a), the Z axis shows the deepest value of -15.9 nm, which is confirmed in the histogram (Figure V-3c). The number of pixels at a depth in the range from -12 to -16 nm does not exceed 100 counts. They correspond to the deepest points located in the polishing grooves. For the passivated surface (Figure V-3b), the deepest point with respect to the median topographic level is lower, -24 nm. From the histogram (Figure V-3d), the number of pixels in the range from -12 to -16 nm now exceeds 100 counts and there are more than 60 pixels in the depth

range from -16 to -24 nm. Identification of the location of these pixels shows that they correspond to two metastable pits of nanometer dimensions (400 nm), circled in the image and initiated at polishing grooves.

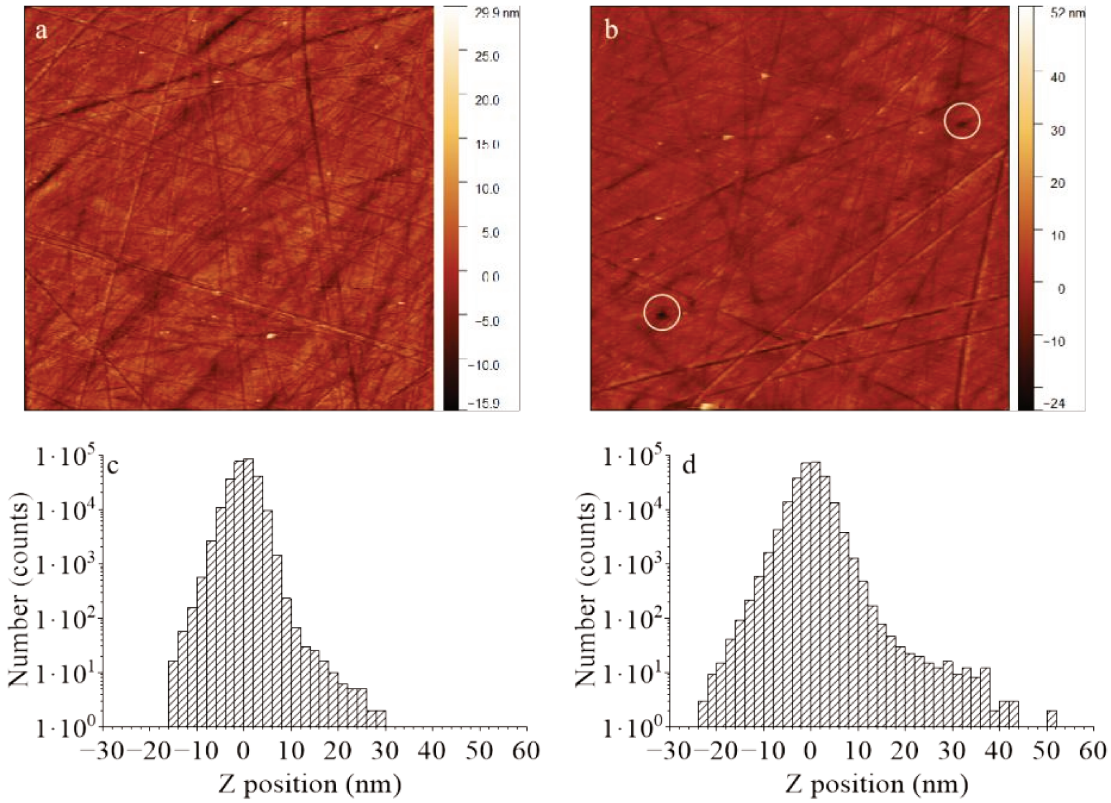

Figure V-3 AFM analysis for the native oxide-covered sample before (a,c) and after (b,d) passivation at 0.3 V/SCE in the 0.05 M H_2SO_4 + 0.05 M NaCl electrolyte: (a,b) AFM images (10 × 10 μm^2), (c,d) Z position histograms.

Taking into account this time a disk pit shape of height h, the expression of charge Q becomes:

$$Q = \frac{\pi * (\frac{d}{2})^2 * h * 2 * e * N_A * \rho_M}{3 * M_M} \qquad \text{eq. V-4}$$

The charge associated to the observed metastable pits is 0.03 nC, which, considering a current transient of 0.02 s, amounts to a current of 1.5 nA and confirms that the metastable pits observed by AFM were undetectable in the current transients because masked by the background passive current.

The polishing grooves remain clearly seen independently of the passivation treatment. For the sample pre-passivated in the Cl-free electrolyte (Figure V-4a,c), the deepest point reaches -15.7 nm and the number of pixels in the range -12 to -16 nm does not exceed 100 counts, like

for the native oxide-covered surface, showing no significant effect of the passivation treatment on the surface topology. The deepest pixels are also located in the polishing grooves. After passivation in the Cl-containing electrolyte (Figure V-4b,d), the deepest pixel is at -10.8 nm, less deep than prior to passivation possibly due to a slight loss in resolution caused by tip blunting. The deepest pixels are in the range -10 to -12 nm (38 counts) and located in the polishing groove. No local pit of nanometer dimensions can be detected like observed in the absence of pre-passivation. These observations, repeated in three distinct local areas of the samples, confirm that the pre-passivation in the absence of chlorides increases the resistance to passivity breakdown and the initiation of localized corrosion as reported previously from macroscopic measurement [10][11]. They show that, in the conditions tested here, metastable pitting can be blocked at the micrometer scale and at least mitigated at the nanometer scale.

Figure V-4 presents the AFM topographic data for the surface pre-passivated in the Cl-free electrolyte and further passivated in the Cl-containing electrolyte.

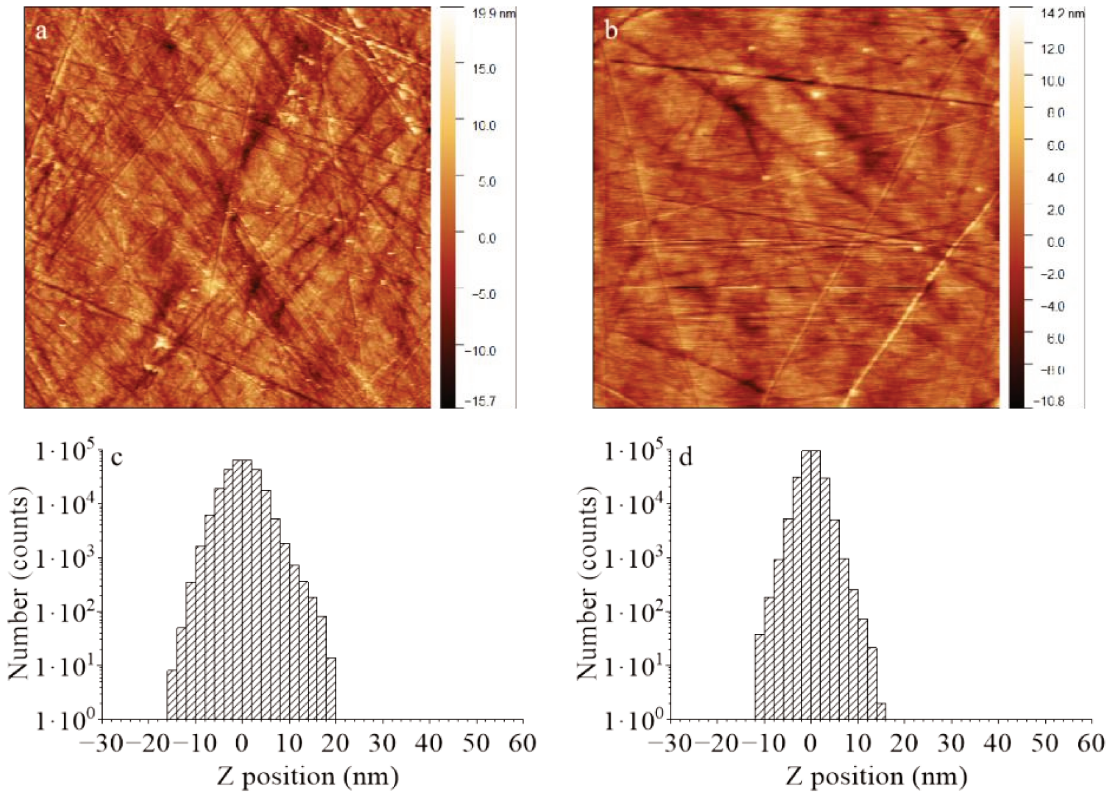

Figure V-4 AFM analysis for the pre-passivated sample before (a,c) and after (b,d) passivation at 0.3 V/SCE in the 0.05 M H_2SO_4 + 0.05 M NaCl electrolyte: (a,b) AFM images (10 × 10 μm^2), (c,d) Z position histograms.

V. 3. 3. Surface analysis of the Cl-induced alterations of the passive state

Surface analysis by ToF-SIMS and XPS was applied to the samples passivated in the presence of chlorides. The ToF-SIMS and XPS data for the native oxide-covered surface state and the pre-passivated surface state have been reported in Chapter III. Figure V-5 shows the ToF-SIMS analysis of the elemental in-depth distribution for the native oxide-covered surface state after passivation in the 0.05 M Cl-containing electrolyte.

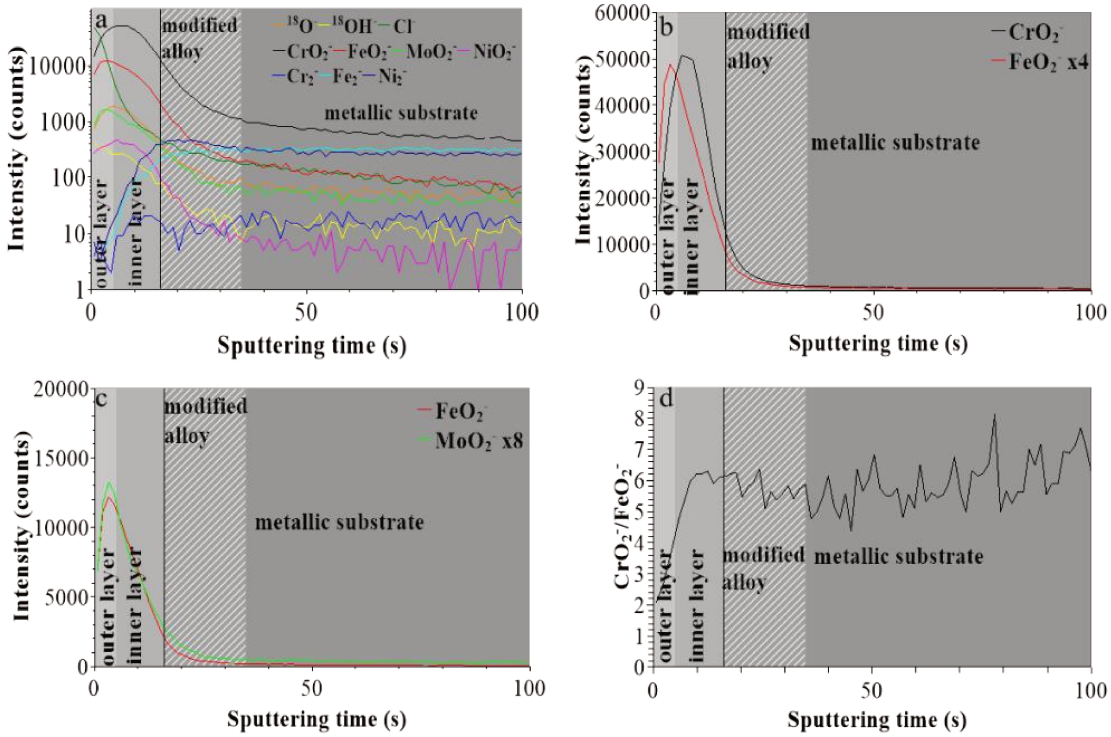

Figure V-5 ToF-SIMS negative ions depth profiles for 316L SS passivated at 0.3 V/SCE in 0.05 M H_2SO_4 + 0.05 M NaCl starting from the native oxide-covered surface state: (a) $^{18}O^-$, $^{18}OH^-$, Cl^-, CrO_2^-, FeO_2^-, NiO_2^-, MoO_2^-, Cr_2^-, Fe_2^- and Ni_2^- secondary ions, (b) CrO_2^- and FeO_2^- secondary ions, (c) FeO_2^- and MoO_2^- secondary ions, (d) CrO_2^-/ FeO_2^- intensity ratio.

In Figure V-5a, the intensities of selected secondary ions characteristic of the oxide film ($^{18}O^-$, $^{18}OH^-$, Cl^-, CrO_2^-, FeO_2^-, NiO_2^- and MoO_2^-) and substrate (Cr_2^-, Fe_2^- and Ni_2^-) are plotted in logarithmic scale versus sputtering time. Between the oxide film and metallic bulk substrate regions, there is the "modified alloy" region where Ni is enriched in agreement with previous studies on austenitic stainless steels [20]-[22][27]-[30][46][47]. The region was placed between 16 and 35 s of sputtering time, meaning that the oxide film region extends from 0 to 16 s and the metallic substrate region after 35 s. In the surface oxide region, the most predominant profiles of the oxidized metals are those of the CrO_2^-, FeO_2^- and to a lesser extent MoO_2^- ions while that of the NiO_2^- ions has much lower intensity, like previously found for passivation in the Cl-free electrolyte in Chapters III and IV.

Figure V-5b compares the CrO_2^- and FeO_2^- ions profiles. The profiles do not peak at the same position, which is in agreement with the bilayer structure having iron and chromium oxides more concentrated in the outer and inner layers, respectively, like reported for passivation in the absence of chlorides [7][17][27][46][47]. The interface between outer and inner layers was positioned at 5 s which is the median sputtering position between the two intensity maxima. Figure V-5c shows that the MoO_2^- ions profile peaks concomitantly with the FeO_2^- profile, meaning that Fe and Mo oxides are both concentrated in the outer layer, again like observed for passivation of 316L SS in the absence of chlorides [27][46][47]. Figure V-5d shows that, starting from the extreme surface, the CrO_2^-/FeO_2^- intensity ratio continuously increases in the outer and inner parts of the oxide film before reaching saturation in the inner layer, with values similar to that for the passive film formed in the Cl-free electrolyte (see Chapter III and IV).

Figure V-5a also shows the depth distribution of anions. The Cl^- ions profile is maximum at the topmost surface and continuously decreases in the surface oxide region, whereas the $^{18}O^-$ ions profile peaks at about 5 s of sputtering time where we position the interface between outer and inner layers. The $^{18}OH^-$ ions profile is also more intense in the outer layer than in the inner layer of the surface oxide.

In Figure V-6, the Cl^- ions profile is superimposed to that recorded for the native oxide covered sample prior to passivation using a linear plot. This plot shows that chlorides are present at trace level in the native oxide film, most likely due to trace contaminants present in the products used for degreasing and cleaning after polishing and/or in ambient atmosphere. This trace contamination is accumulated in the outer part of the surface oxide. After passivation in the Cl-free electrolyte, there is no increase of the trace chloride contamination. However, after passivation in the Cl-containing electrolyte, more chlorides enter the passive film but mostly in the outer layer. This is consistent with most of the alterations occurring in the outer exchange layer of the surface oxide in direct contact with the Cl-containing electrolyte. The inner barrier layer of the surface oxide film appears barely affected by the penetration of chlorides.

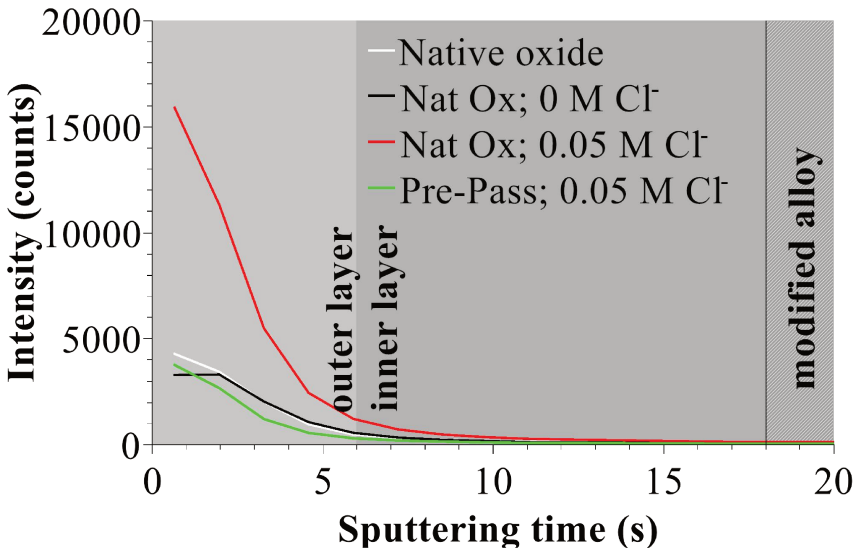

Figure V-6 ToF-SIMS Cl^- ions depth profiles for the native oxide-covered sample passivated at 0.3 V/SCE in the Cl-free 0.05 M H_2SO_4 electrolyte (Nat Ox; 0 M Cl^-) and in the 0.05 M NaCl + 0.05 M H_2SO_4 electrolyte (Nat Ox; 0.05 M Cl^-), and for the pre-passivated sample passivated at 0.3 V/SCE in the 0.05 M NaCl + 0.05 M H_2SO_4 electrolyte (Pre-Pass; 0.05 M Cl^-).

Figure V-7 shows the XPS core level spectra and their reconstruction for the native oxide-covered surface state after passivation in the 0.05 M Cl-containing electrolyte. The BE values, Full Widths at Half-Maximum (FWHM) values and relative intensities of the peak components obtained by curve fitting are compiled in Table. 1. The exact same fitting procedure as for the native oxide-covered surface before and after passivation in the Cl-free electrolyte was applied (see Chapter III and IV). Seven peaks were used to fit the Cr $2p_{3/2}$ experimental curve (Figure V-7a) as proposed previously [61]. The first one (Cr1) is associated to metallic Cr^0 in the substrate. The next five peaks (Cr2-Cr6) form a well-defined series with fixed BE intervals, FWHMs and relative intensities and correspond to Cr^{III} oxide in the inner part of the oxide film. The additional peak (Cr7) is associated to Cr^{III} hydroxide in the outer part of the oxide film. No Cr^{VI} expected at a BE of ~579.5 eV [61] was needed for curve fitting.

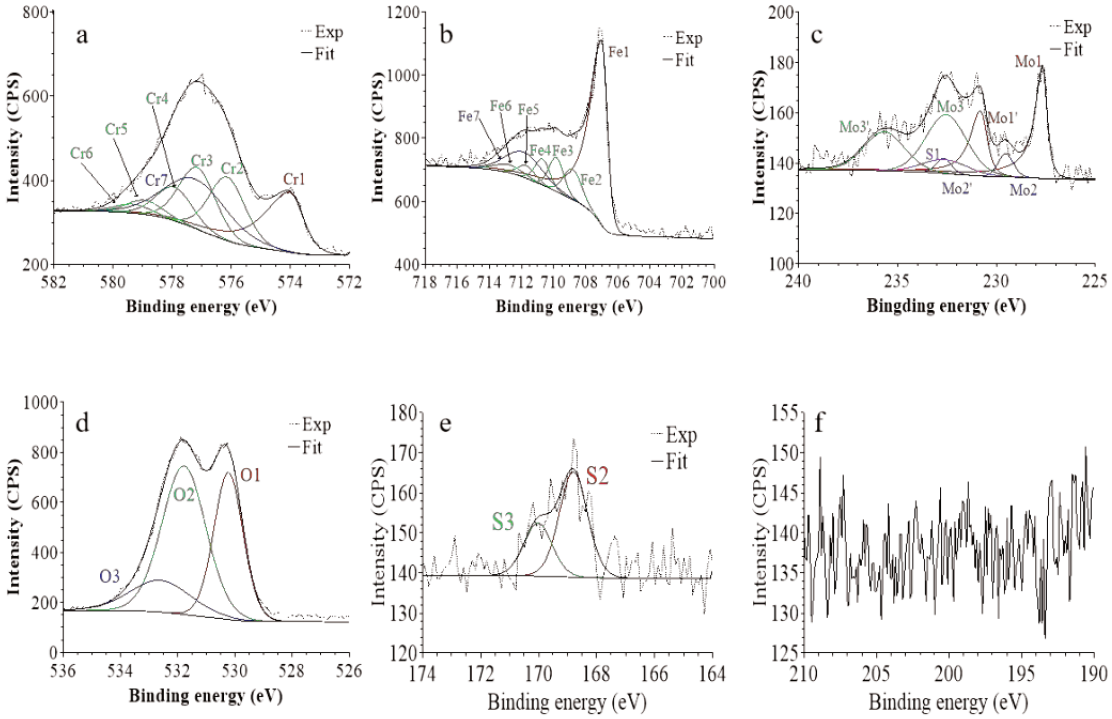

Figure V-7 XPS core level spectra and their reconstruction for 316L SS passivated at 0.3 V/SCE in 0.05 M H_2SO_4 + 0.05 M NaCl starting from the native oxide-covered surface state: (a) Cr $2p_{3/2,}$ (b) Fe $2p_{3/2,}$ (c) Mo $3d_{5/2-3/2}$ (d) O 1s (e) S 2p and (f) Cl 2p regions.

Seven peaks were also used for fitting the Fe $2p_{3/2}$ spectrum [61][62] (Figure V-7b). The first peak (Fe1) corresponds to metallic Fe^0 in the substrate, the next five peaks (Fe2-Fe6), also forming a well-defined series, correspond to Fe^{III} oxide in the surface oxide layers, and the additional peak (Fe7), needed at higher BE to optimize the fit, corresponds to Fe^{III} hydroxide also in the oxide film.

The Mo 3d spectrum was fitted with three 5/2-3/2 spin-orbit doublets (Figure V-7c): one (Mo1/Mo1') corresponding to metallic Mo^0 in the substrate and the other two, (Mo2/Mo2') and (Mo3/Mo3'), to Mo^{IV} and Mo^{VI} in the surface oxide film, respectively [21][22][27][31][33][36][46][47][61].

The presence of an S 2s peak (S1 component) can be observed in Figure V-7c (Table V-1). It originates from the sulfate counter ions of the solution. The S 2p components measured at 168.8 and 170.0 eV (Figure V-7e, Table V-1) confirm the presence of SO_4^{2-} species at the surface of the passive film.

The Ni 2p3/2 spectrum was fitted using a single peak (Table V-1) corresponding to metallic Ni^0 in the substrate [27][46][47]. No Ni(II) oxide species were observed, like for the native oxide film and after passivation in the Cl-free electrolyte [46][47], evidencing that the Ni oxide species measured by ToF-SIMS were at trace level below the detection limit of XPS

(~0.5 at%).

Figure V-7d shows the O 1s spectrum fitted with three components, O1, O2 and O3, assigned to the oxide (O^{2-}), hydroxide (OH^-) and water (H_2O) ligands in the surface oxide films, respectively [27][46][47][61]. The OH^-/O^{2-} intensity ratio is 1.5, higher than for the native oxide (0.9) but also higher than after passivation in the Cl-free electrolyte (1.2) [46], meaning that the presence of chlorides in the outer layer of the passive film is associated with an increased hydroxylation as suggested by the ToF-SIMS depth profile.

Figure V-7f shows the Cl 2p core level region spectrum. No peaks are observed, meaning that the quantity of chlorides measured by ToF-SIMS was below the detection limit of XPS (~0.5 at%).

The bi-layer model previously used to calculate the thickness and composition of the outer and inner layers of the oxide films as well as the composition of the modified alloy underneath the oxide films (Chapter III) was applied to process the XPS intensity data. This model assumes a mixed iron-chromium hydroxide outer layer and a mixed iron-chromium oxide inner layer. Molybdenum oxide is included in the outer layer and neglected in the inner layer. Assignment of the intensities of the different components was as follows: Cr2-Cr6 and Fe2-Fe4 components to the oxide film inner layer, Cr7, Fe5-Fe7 and Mo2-Mo3 components to the oxide film outer layer and Cr1, Fe1, Mo1 and Ni1 components to the modified alloy region underneath the oxide film. The results are presented in Table V-2, together with a reminder of the results for the native oxide-covered surface and the surface passivated in the Cl-free solution corresponding to the pre-passivation treatment. The overall compositions of the oxide films were obtained by weighting the cation concentration value of each element by the fractional thickness of the inner and outer layers.

Table V-1 BE, FWHM and relative intensity values of the peak components measured by XPS on 316L SS for the native oxide-covered sample passivated in the 0.05 M NaCl + 0.05M H_2SO_4 electrolyte and for the pre-passivated sample passivated in the 0.05 M NaCl + 0.05M H_2SO_4 electrolyte.

			Native oxide-covered surface passivated in 0.05 M [Cl^-]			**Pre-passivated surface passivated in 0.05 M [Cl^-]**		
Core level	Peak	Assignment	BE (±0.1 eV)	FWHM (±0.1 eV)	Intensity (%)	BE (±0.1 eV)	FWHM (±0.1 eV)	Intensity (%)
Fe 2p3/2	Fe1	Fe^0 (met)	707.0	0.8	57.9	707.0	0.8	63.3
	Fe2	Fe^{III} (ox)	708.8	1.3	8.3	708.8	1.2	8.1
	Fe3	Fe^{III} (ox)	709.8	1.1	7.5	709.8	1.1	7.3
	Fe4	Fe^{III} (ox)	710.7	1.1	5.8	710.7	1.1	5.7
	Fe5	Fe^{III} (ox)	711.7	1.3	3.3	711.7	1.2	3.2
	Fe6	Fe^{III} (ox)	712.8	2.0	3.3	712.8	2.0	3.2
	Fe7	Fe^{III} (hyd)	711.9	2.7	13.9	711.9	2.7	9.2
Cr 2p3/2	Cr1	Cr^0 (met)	574.0	1.1	22.3	574.0	1.0	20.7
	Cr2	Cr^{III} (ox)	576.1	1.4	18.5	576.2	1.5	21.8
	Cr3	Cr^{III} (ox)	577.2	1.4	17.9	577.2	1.5	21.1
	Cr4	Cr^{III} (ox)	577.9	1.4	9.8	578.0	1.5	11.5
	Cr5	Cr^{III} (ox)	578.9	1.4	4.1	579.0	1.5	4.8
	Cr6	Cr^{III} (ox)	579.3	1.4	2.6	579.4	1.5	3.1
	Cr7	Cr^{III} (hyd)	577.2	2.5	24.8	577.2	2.5	17.1
Ni 2p3/2	Ni1	Ni^0 (met)	852.9	0.9	100	852.9	0.9	100
Mo 3d5/2	Mo1	Mo^0 (met)	227.7	0.5	27.2	277.7	0.5	26.7
	Mo2	Mo^{IV} (ox)	229.5	0.9	4.3	229.4	0.9	4.2
	Mo3	Mo^{VI} (ox)	232.5	2.4	28.8	232.5	2.5	29.4
Mo 3d3/2	Mo1’	Mo^0 (met)	230.8	0.8	17.9	230.8	0.8	17.6
	Mo2’	Mo^{IV} (ox)	232.7	0.9	2.8	232.6	0.9	2.7
	Mo3’	Mo^{VI} (ox)	235.7	2.4	19.0	235.6	2.5	19.4
O 1s	O1	O^{2-}	530.2	1.2	33.8	530.2	1.2	37.2
	O2	OH^-	531.7	1.8	51.1	531.7	1.7	43.2
	O3	H_2O	532.6	2.5	15.1	532.6	2.5	19.6
S 2s	S1	SO_4^{2-}	232.9	1.7	100	232.9	1.7	100
S 2p3/2	S2	SO_4^{2-}	168.8	1.1	66.5	168.7	1.1	61.6
S 2p1/2	S3	SO_4^{2-}	170.0	1.1	35.5	169.9	1.1	38.4

Comparing the present data for passivation in the Cl-containing electrolyte with the native oxide-covered surface, one notices no significant difference in thickness of the inner layer taking into account an uncertainty of ±0.1 nm, like after passivation in the Cl-free electrolyte. The outer layer is possibly slightly thicker owing to the incorporation of chlorides and increased hydroxylation. The further enrichment of the inner layer in Cr(III) obtained by passivation in the Cl-free solution appears to be blocked after passivation in the Cl-containing

electrolyte. The further enrichment in Cr(III) in the outer layer is also attenuated in the presence of chlorides. This is also observed for the enrichment in Mo(IV,VI) of the outer layer. No marked variation of the composition of the modified alloy underneath the surface oxide are observed. Thus it appears that the incorporation of chlorides in trace amounts (< 0.5 at%) and the increased hydroxylation of the outer layer of the surface oxide is detrimental to the passive state since mitigating the increase of the beneficial Cr and Mo enrichments brought by passivation, including in the inner layer where chlorides do not enter.

Table V-2 Thickness and composition of the surface oxide for the 316L SS native oxide-covered sample before (from Chapter III) and after passivation in the 0.05 M NaCl + 0.05M H_2SO_4 electrolyte, and for the pre-passivated sample before (from Chapter III) and after passivation in the 0.05 M NaCl + 0.05M H_2SO_4 electrolyte.

		Global film	Outer layer	Inner layer	Modified alloy
Native oxide-covered surface (Chapter III)	d (nm)	2.0	0.8	1.2	/
	[Fe] (at%)	39	41	36	52
	[Cr] (at%)	55	44	64	18
	[Ni] (at%)	/	/	/	28
	[Mo](at%)	6	15	/	3
	Ratio Cr/Fe	1.4	1.1	1.8	/
Native oxide-covered surface passivated in 0.05 M H_2SO_4 + 0.05M [Cl^-]	d (nm)	2.0	0.9	1.1	/
	[Fe] (at%)	36	36	36	52
	[Cr] (at%)	57	48	64	18
	[Ni] (at%)	/	/	/	26
	[Mo](at%)	7	16	/	4
	Ratio Cr/Fe	1.6	1.3	1.8	/
Pre-passivated surface (Chapter III)	d (nm)	1.9	0.7	1.2	/
	[Fe] (at%)	26	26	26	51
	[Cr] (at%)	67	56	74	20
	[Ni] (at%)	/	/	/	26
	[Mo](at%)	7	18	/	4
	Ratio Cr/Fe	2.6	2.2	2.8	/
Pre-passivated surface passivated in 0.05 M H_2SO_4 + 0.05M [Cl^-]	d (nm)	1.9	0.6	1.3	/
	[Fe] (at%)	26	34	22	51
	[Cr] (at%)	68	45	78	17
	[Ni] (at%)	/	/	/	29
	[Mo](at%)	6	21	/	3
	Ratio Cr/Fe	2.6	1.3	3.5	/

V. 3. 4. Surface analysis of the effect of pre-passivation

Similarly to Figure V-5, Figure V-8 presents the ToF-SIMS data for the sample pre-passivated in Cl-free conditions and further treated in the Cl-containing electrolyte. The “modified alloy” region was positioned between 18 s to 37 s (Figure V-8a). The bilayer structure of the oxide film is still observed with the interface between outer and inner layers placed at 6 s (Figure V-

8b). Cr oxide remains concentrated in the inner layer and Fe oxide in the outer layer with Mo oxide (Figure V-8c). The variation of the intensity ratio of CrO_2^- to FeO_2^- ions, shown in Figure V-8d, shows also a similar trend, confirming the higher chromium enrichment in the inner layer. A higher value is reached in the inner layer, suggesting increased enrichment in Cr oxide.

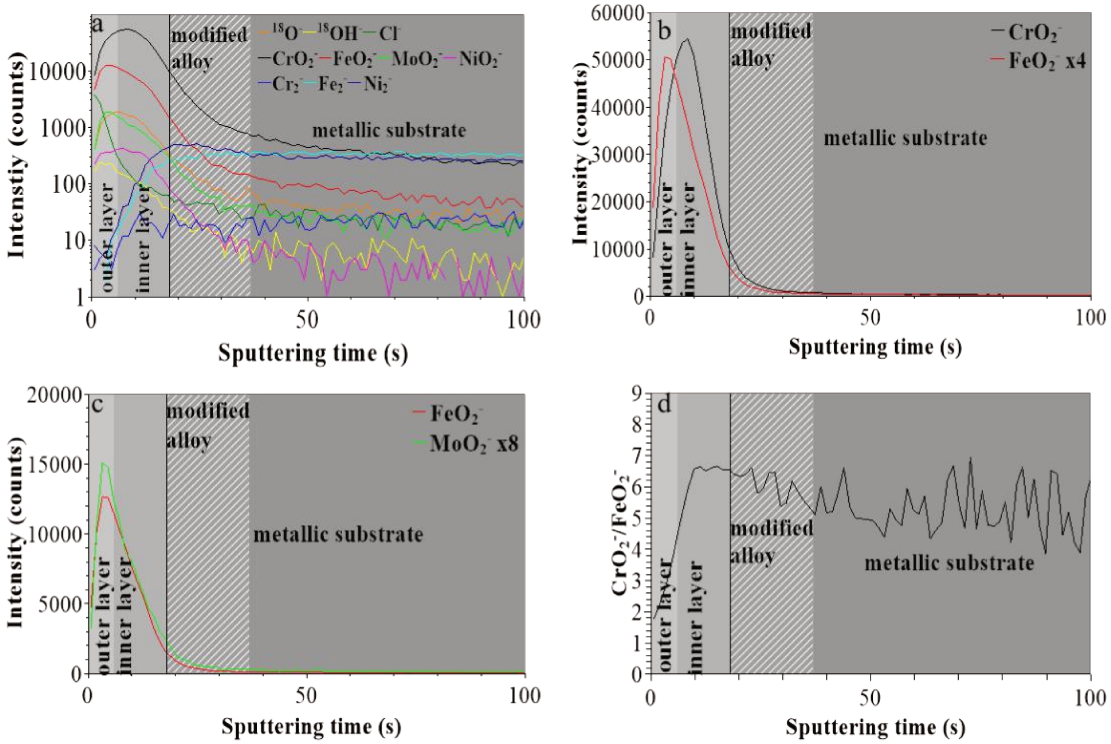

Figure V-8 ToF-SIMS negative ions depth profiles for 316L SS passivated at 0.3 V/SCE in 0.05 M H_2SO_4 + 0.05 M NaCl starting from the pre-passivated surface state: (a) $^{18}O^-$, $^{18}OH^-$, Cl^-, CrO_2^-, FeO_2^-, NiO_2^-, MoO_2^-, Cr_2^-, Fe_2^- and Ni_2^- secondary ions, (b) CrO_2^- and FeO_2^- secondary ions, (c) FeO_2^- and MoO_2^- secondary ions, (d) CrO_2^-/ FeO_2^- intensity ratio.

Figure V-8a also shows that the depth profiles for the Cl^-, $^{18}O^-$ and $^{18}OH^-$ ions are similar to those for the non-pretreated sample (Figure V-5a), however with different intensities. The Cl^- ion profile has much lower intensity. It is at a level similar to those measured in the samples not exposed to chlorides as shown in Figure V-6, indicating that the pre-passivation treatment would block the entry of the chlorides in the passive film. The $^{18}OH^-$ ions profile has also a lower intensity owing to the pre-passivation treatment in the absence of chlorides [46][47].

Similarly to Figure V-7, Figure V-9 presents the XPS core level spectra recorded for the sample pre-passivated in Cl-free conditions and further treated in the Cl-containing electrolyte.

The spectra could be reconstructed using the same components with no significant differences of the BE and FWHM values within the accuracy of ±0.1 eV (Table V-1). Only slight variations of the relative intensities were observed. In the O 1s core level region, the OH^-/O^{2-} intensity ratio is 1.2, the same as for the film after pre-treatment in the Cl-free electrolyte (1.2) [46], but lower than on the sample post-treated in the Cl-containing electrolyte (1.5) thereby confirming the poisoning effect of chlorides on the dehydroxylation of the passive film. In the Cl 2p core level region (Figure V-9f), no signal is detected meaning that the residual trace quantity of chlorides measured by ToF-SIMS and already observed before treatment in the Cl-containing electrolyte was below the detection limit of XPS (~0.5 at%).

The results for the calculated thickness and composition are compiled in Table V-2. Compared with the data for the surface after the pre-passivation treatment, one observes no significant variations of thickness of the outer and inner layers. The inner layer is slightly more enriched in Cr(III) whereas the outer layer is less enriched in Cr(III) but more in Mo(IV,VI), which are the variations also observed to be induced by aging under anodic polarization in the absence of chlorides [46]. Thus, it is suggested that, thanks to the blocking effect of the pre-passivation treatment on the entry of chlorides in the outer layer of the passive film, the aging-induced variations of the composition could take place despite the presence of chlorides in the environment.

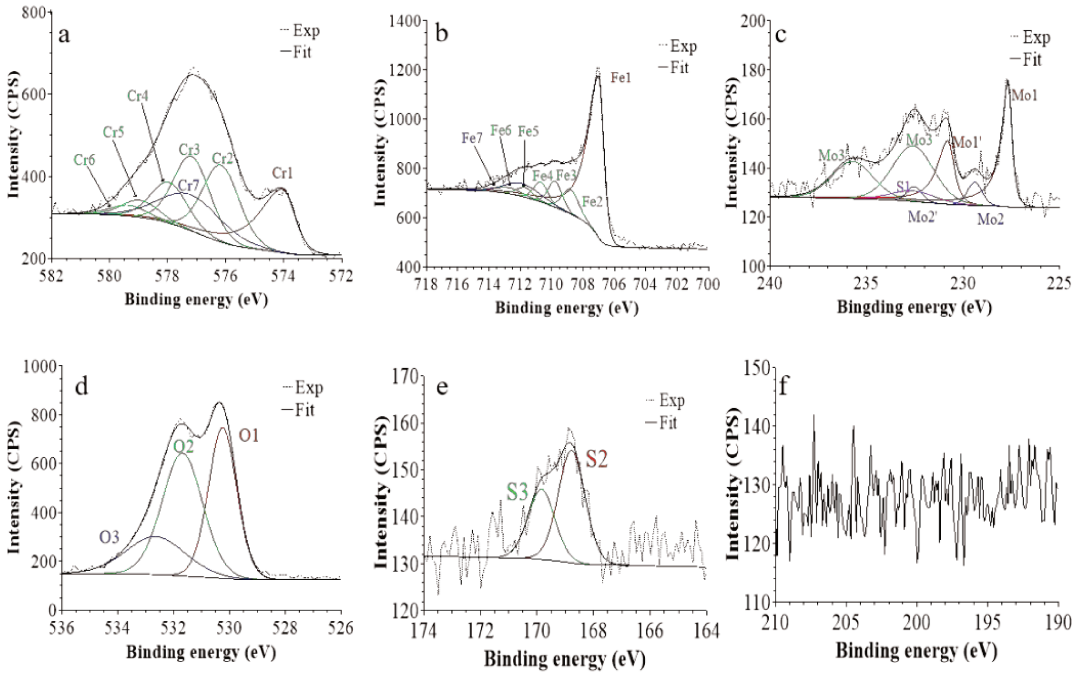

Figure V-9 XPS core level spectra and their reconstruction for 316L SS passivated at 0.3 V/SCE in 0.05 M H_2SO_4 + 0.05 M NaCl starting from the pre-passivated surface state: (a) Cr $2p_{3/2,}$ (b) Fe $2p_{3/2,}$ (c) Mo $3d_{5/2-3/2}$ and (d) O 1s (e) S 2p and (f) Cl 2p regions.

These results show that pre-passivation by anodic polarization in the Cl-free electrolyte increases the stability of the passive state obtained in the Cl-containing electrolyte and blocks the entry of the chlorides in the passive film, including in the outer exchange layer. Comparison of the data in Table V-2 for the native oxide and pre-passivated films shows that pre-passivation in chloride-free environment does not significantly change the thickness of the passive film but that the composition of the passive film is changed, including in the outer layer further enriched in Cr and Mo by the pre-passivation process. It is suggested that this change of composition, possibly modifying the n-type electronic properties [63,64] and thus the driving force for chloride entry under anodic polarization, is at the origin of the blocking effect of pre-passivation on the chloride entry. Curing structural effects on the local sites for entry of chloride ions cannot be excluded.

V. 4. Conclusion

Surface analysis by ToF-SIMS, XPS and AFM were combined to electrochemical measurements in order to study the alterations of the passive state of 316L austenitic stainless steel brought by the presence of chlorides in sulfuric acid passivating electrolyte and the effect of pre-passivation in the absence of chlorides. The passivation conditions (potential, time and Cl concentration) were selected so as to enable Cl-induced alterations of the passive film, however without generating stable pit growth and limiting metastable pitting to the nanometer scale as confirmed by current transients and AFM measurements.

Passivation by anodic polarization in the Cl-containing electrolyte causes Cl^- ions to enter the bilayer structure of the surface oxide already formed in the native oxide-covered surface state, mostly in the hydroxide outer layer where Fe(III) and Mo(IV,VI) species are concentrated but barely in the oxide inner layer enriched in Cr(III). Their concentration is below the detection limit of XPS (< 0.5 at%). The passivation mechanisms leading to dehydroxylation of the oxide film and to further Cr(III) enrichment in the outer exchange layer and inner barrier layer and to Mo(IV,VI) enrichment in the outer layer are negatively impacted, resulting in a less protective passive state poisoned by the interactions with chlorides. These alterations suggest that the preferential dissolution of iron oxide, leading to Cr and Mo enrichment, is slow down by the interactions with the Cl^- ions at the surface of the passive film.

Pre-passivation by anodic polarization in the Cl-free electrolyte increases the stability of the passive state obtained in the Cl-containing electrolyte. It blocks the entry of the chlorides in the passive film, including in the outer exchange layer, which enables the aging-induced

variations of the composition to take place despite the presence of chlorides in the environment.

Acknowledgements

This project has received funding from the European Research Council (ERC) under the European Union's Horizon 2020 research and innovation program (ERC Advanced Grant no. 741123). Région Île-de-France is acknowledged for partial funding of the ToF-SIMS equipment.

References

1. P. Schmuki, From Bacon to barriers: a review on the passivity of metals and alloys, J Solid State Electrochem. 6 (2002) 145–164. doi:10.1007/s100080100219.
2. V. Maurice, W.P. Yang, P. Marcus, XPS and STM Study of Passive Films Formed on Fe-22Cr(110) Single-Crystal Surfaces, J. Electrochem. Soc. 143 (1996) 1182–1200. doi:10.1149/1.1836616.
3. M. Seo, N. Sato, Differential composition profiles in depth of thin anodic oxide films on iron-chromium alloy, Surface Science. 86 (1979) 601–609. doi:10.1016/0039-6028(79)90440-0.
4. G. Hultquist, M. Seo, T. Leitner, C. Leygraf, N. Sato, The dissolution behaviour of iron, chromium, molybdenum and copper from pure metals and from ferritic stainless steels, Corrosion Science. 27 (1987) 937–946. doi:10.1016/0010-938X(87)90060-6.
5. D.F. Mitchell, M.J. Graham, Comparison of Auger and SIMS analysis of a thin passive oxide film on iron—25% chromium, Surface and Interface Analysis. 10 (1987) 259–261. doi:10.1002/sia.740100507.
6. S. Mischler, H.J. Mathieu, D. Landolt, Investigation of a passive film on an iron chromium alloy by AES and XPS, Surf. Interface Anal. 11 (1988) 182–188. doi:10.1002/sia.740110403.

7. P. Marcus, I. Olefjord, A Round Robin on combined electrochemical and AES/ESCA characterization of the passive films on Fe-Cr and Fe-Cr-Mo alloys, Corrosion Science. 28 (1988) 589–602. doi:10.1016/0010-938X(88)90026-1.

8. C. Calinski, H.-H. Strehblow, ISS Depth Profiles of the Passive Layer on Fe/Cr Alloys, J. Electrochem. Soc. 136 (1989) 1328–1331. doi:10.1149/1.2096915.

9. R. Kirchheim, B. Heine, H. Fischmeister, S. Hofmann, H. Knote, U. Stolz, The passivity of iron-chromium alloys, Corrosion Science. 29 (1989) 899–917. doi:10.1016/0010-938X(89)90060-7.

10. J.E. Castle, J.H. Qiu, A co-ordinated study of the passivation of alloy steels by plasma source mass spectrometry and x-ray photoelectron spectroscopy—1. characterization of the passive film, Corrosion Science. 29 (1989) 591–603. doi:10.1016/0010-938X(89)90010-3.

11. J.E. Castle, J.H. Qiu, A co-ordinated study of the passivation of alloy steels by plasma source mass spectrometry and x-ray photoelectron spectroscopy—II. growth kinetics of the passive film, Corrosion Science. 29 (1989) 605–616. doi:10.1016/0010-938X(89)90011-5.

12. W.P. Yang, D. Costa, P. Marcus, Resistance to Pitting and Chemical Composition of Passive Films of a Fe-17%Cr Alloy in Chloride-Containing Acid Solution, J. Electrochem. Soc. 141 (1994) 2669–2676. doi:10.1149/1.2059166.

13. S. Haupt, H.-H. Strehblow, A combined surface analytical and electrochemical study of the formation of passive layers on FeCr alloys in 0.5 M H2SO4, Corrosion Science. 37 (1995) 43–54. doi:10.1016/0010-938X(94)00104-E.

14. L.J. Oblonsky, M.P. Ryan, H.S. Isaacs, In Situ Determination of the Composition of Surface Films Formed on Fe-Cr Alloys, J. Electrochem. Soc. 145 (1998) 1922–1932. doi:10.1149/1.1838577.

15. D. Hamm, K. Ogle, C.-O.A. Olsson, S. Weber, D. Landolt, Passivation of Fe–Cr alloys studied with ICP-AES and EQCM, Corrosion Science. 44 (2002) 1443–1456. doi:10.1016/S0010-938X(01)00147-0.

16. P. Keller, H.-H. Strehblow, XPS investigations of electrochemically formed passive layers on Fe/Cr-alloys in 0.5 M H2SO4, Corrosion Science. 46 (2004) 1939–1952. doi:10.1016/j.corsci.2004.01.007.

17. S. Mischler, A. Vogel, H.J. Mathieu, D. Landolt, The chemical composition of the passive film on Fe-24Cr and Fe-24Cr-11Mo studied by AES, XPS and SIMS, Corrosion Science. 32 (1991) 925–944. doi:10.1016/0010-938X(91)90013-F.

18. K. Hashimoto, K. Asami, K. Teramoto, An X-ray photo-electron spectroscopic study on the role of molybdenum in increasing the corrosion resistance of ferritic stainless steels in HC1, Corrosion Science. 19 (1979) 3–14. doi:10.1016/0010-938X(79)90003-9.

19. M.-W. Tan, E. Akiyama, A. Kawashima, K. Asami, K. Hashimoto, The effect of air exposure on the corrosion behavior of amorphous Fe-8Cr-Mo-13P-7C alloys in 1 M HCl, Corrosion Science. 37 (1995) 1289–1301. doi:10.1016/0010-938X(95)00035-I.

20. V. Maurice, W.P. Yang, P. Marcus, X-Ray Photoelectron Spectroscopy and Scanning Tunneling Microscopy Study of Passive Films Formed on (100) Fe-18Cr-13Ni Single-Crystal Surfaces, J. Electrochem. Soc. 145 (1998) 909–920. doi:10.1149/1.1838366.

21. I. Olefjord, B.-O. Elfstrom, The Composition of the Surface during Passivation of Stainless Steels, CORROSION. 38 (1982) 46–52. doi:10.5006/1.3577318.

22. E. De Vito, P. Marcus, XPS study of passive films formed on molybdenum-implanted austenitic stainless steels, Surf. Interface Anal. 19 (1992) 403–408. doi:10.1002/sia.740190175.

23. E. McCafferty, M.K. Bernett, J.S. Murday, An XPS study of passive film formation on iron in chromate solutions, Corrosion Science. 28 (1988) 559–576. doi:10.1016/0010-938X(88)90024-8.

24. P. Marcus, J.M. Grimal, The anodic dissolution and passivation of NiCrFe alloys studied by ESCA, Corrosion Science. 33 (1992) 805–814. doi:10.1016/0010-938X(92)90113-H.

25. M. Bojinov, G. Fabricius, T. Laitinen, K. Mäkelä, T. Saario, G. Sundholm, Influence of molybdenum on the conduction mechanism in passive films on iron–chromium alloys in

sulphuric acid solution, Electrochimica Acta. 46 (2001) 1339–1358. doi:10.1016/S0013-4686(00)00713-1.

26. T. Yamamoto, K. Fushimi, M. Seo, S. Tsuri, T. Adachi, H. Habazaki, Depassivation–repassivation behavior of type-312L stainless steel in NaCl solution investigated by the micro-indentation, Corrosion Science. 51 (2009) 1545–1553. doi:10.1016/j.corsci.2008.11.020.

27. V. Maurice, H. Peng, L.H. Klein, A. Seyeux, S. Zanna, P. Marcus, Effects of molybdenum on the composition and nanoscale morphology of passivated austenitic stainless steel surfaces, Faraday Discuss. 180 (2015) 151–170. doi:10.1039/C4FD00231H.

28. K. Sugimoto, Y. Sawada, The role of molybdenum additions to austenitic stainless steels in the inhibition of pitting in acid chloride solutions, Corrosion Science. 17 (1977) 425–445. doi:10.1016/0010-938X(77)90032-4.

29. H. Ogawa, H. Omata, I. Itoh, H. Okada, Auger Electron Spectroscopic and Electrochemical Analysis of the Effect of Alloying Elements on the Passivation Behavior of Stainless Steels, CORROSION. 34 (1978) 52–60. doi:10.5006/0010-9312-34.2.52.

30. I. Olefjord, The passive state of stainless steels, Materials Science and Engineering. 42 (1980) 161–171. doi:10.1016/0025-5416(80)90025-7.

31. W. Yang, R.-C. Ni, H.-Z. Hua, A. Pourbaix, The behavior of chromium and molybdenum in the propagation process of localized corrosion of steels, Corrosion Science. 24 (1984) 691–707. doi:10.1016/0010-938X(84)90059-3.

32. I. Olefjord, B. Brox, U. Jelvestam, Surface Composition of Stainless Steels during Anodic Dissolution and Passivation Studied by ESCA, J. Electrochem. Soc. 132 (1985) 2854–2861. doi:10.1149/1.2113683.

33. A.R. Brooks, C.R. Clayton, K. Doss, Y.C. Lu, On the Role of Cr in the Passivity of Stainless Steel, J. Electrochem. Soc. 133 (1986) 2459–2464. doi:10.1149/1.2108450.

34. C.R. Clayton, Y.C. Lu, A Bipolar Model of the Passivity of Stainless Steel: The Role of Mo Addition, J. Electrochem. Soc. 133 (1986) 2465–2473. doi:10.1149/1.2108451.

35. Y.C. Lu, C.R. Clayton, A.R. Brooks, A bipolar model of the passivity of stainless steels—II. The influence of aqueous molybdate, Corrosion Science. 29 (1989) 863–880. doi:10.1016/0010-938X(89)90058-9.

36. C.R. Clayton, Y.C. Lu, A bipolar model of the passivity of stainless steels—III. The mechanism of MoO42− formation and incorporation, Corrosion Science. 29 (1989) 881–898. doi:10.1016/0010-938X(89)90059-0.

37. I. Olefjord, L. Wegrelius, Surface analysis of passive state, Corrosion Science. 31 (1990) 89–98. doi:10.1016/0010-938X(90)90095-M.

38. H. Habazaki, A. Kawashima, K. Asami, K. Hashimoto, The corrosion behavior of amorphous Fe-Cr-Mo-P-C and Fe-Cr-W-P-C alloys in 6 M HCl solution, Corrosion Science. 33 (1992) 225–236. doi:10.1016/0010-938X(92)90147-U.

39. D.D. Macdonald, The Point Defect Model for the Passive State, J. Electrochem. Soc. 139 (1992) 3434–3449. doi:10.1149/1.2069096.

40. A. Elbiache, P. Marcus, The role of molybdenum in the dissolution and the passivation of stainless steels with adsorbed sulphur, Corrosion Science. 33 (1992) 261 – 269. doi:10.1016/0010-938X(92)90150-2.

41. R. f. a Jargelius-Pettersson, Electrochemical investigation of the influence of nitrogen alloying on pitting corrosion of austenitic stainless steels, Corrosion Science. 41 (1999) 1639 – 1664. doi:10.1016/S0010-938X(99)00013-X.

42. L. Wegrelius, F. Falkenberg, I. Olefjord, Passivation of Stainless Steels in Hydrochloric Acid, J. Electrochem. Soc. 146 (1999) 1397 – 1406. doi:10.1149/1.1391777.

43. A. Pardo, M.C. Merino, A.E. Coy, F. Viejo, R. Arrabal, E. Matykina, Effect of Mo and Mn additions on the corrosion behaviour of AISI 304 and 316 stainless steels in H2SO4, Corrosion Science. 50 (2008) 780 – 794. doi:10.1016/j.corsci.2007.11.004.

44. A. Pardo, M.C. Merino, A.E. Coy, F. Viejo, R. Arrabal, E. Matykina, Pitting corrosion behaviour of austenitic stainless steels – combining effects of Mn and Mo additions, Corrosion Science. 50 (2008) 1796 – 1806. doi:10.1016/j.corsci.2008.04.005.

45. G.O. Ilevbare, G.T. Burstein, The role of alloyed molybdenum in the inhibition of pitting corrosion in stainless steels, Corrosion Science. 43 (2001) 485 – 513. doi:10.1016/S0010-938X(00)00086-X.

46. Z. Wang, F. Di-Franco, A. Seyeux, S. Zanna, V. Maurice, P. Marcus, Passivation-Induced Physicochemical Alterations of the Native Surface Oxide Film on 316L Austenitic Stainless Steel, J. Electrochem. Soc. 166 (2019) C3376 – C3388. doi:10.1149/2.0321911jes.

47. Z. Wang, E.-M. Paschalidou, A. Seyeux, S. Zanna, V. Maurice, P. Marcus, Mechanisms of Cr and Mo enrichments in the passive oxide film on 316L austenitic stainless steel, Front. Mater. 6 (2019). doi:10.3389/fmats.2019.00232.

48. T. Massoud, V. Maurice, L.H. Klein, A. Seyeux, P. Marcus, Nanostructure and local properties of oxide layers grown on stainless steel in simulated pressurized water reactor environment, Corrosion Science. 84 (2014) 198–203. doi:10.1016/j.corsci.2014.03.030.

49. V. Maurice, P. Marcus, Current developments of nanoscale insight into corrosion protection by passive oxide films, Current Opinion in Solid State and Materials Science. 22 (2018) 156–167. doi:10.1016/j.cossms.2018.05.004.

50. L. Ma, F. Wiame, V. Maurice, P. Marcus, Stainless Steel Surface Structure and Initial Oxidation at Nanometric and Atomic Scales, Applied Surface Science, in press, doi: 10.1016/j.apsusc.2019.07.166

51. L. Ma, F. Wiame, V. Maurice, P. Marcus, New insight on early oxidation stages of austenitic stainless steel from in situ XPS analysis on single-crystalline Fe–18Cr–13Ni, Corrosion Science. 140 (2018) 205–216. doi:10.1016/j.corsci.2018.06.001.

52. L. Ma, F. Wiame, V. Maurice, P. Marcus. Origin of nanoscale heterogeneity in the surface oxide film protecting stainless steel against corrosion. npj Materials Degradation, in press.

53. C. Leygraf, G. Hultquist, I. Olefjord, B.-O. Elfström, V.M. Knyazheva, A.V. Plaskeyev, Ya.M. Kolotyrkin, Selective dissolution and surface enrichment of alloy components of passivated Fe18Cr and Fe18Cr3Mo single crystals, Corrosion Science. 19 (1979) 343–357. doi:10.1016/0010-938X(79)90026-X.

54. M.H. Moayed, N.J. Laycock, R.C. Newman, Dependence of the Critical Pitting Temperature on surface roughness, Corrosion Science. 45 (2003) 1203 – 1216. doi:10.1016/S0010-938X(02)00215-9.

55. T. Hong, M. Nagumo, Effect of surface roughness on early stages of pitting corrosion of Type 301 stainless steel, Corrosion Science. 39 (1997) 1665–1672. doi:10.1016/S0010-938X(97)00072-3.

56. Z.H. Jin, H.H. Ge, W.W. Lin, Y.W. Zong, S.J. Liu, J.M. Shi, Corrosion behaviour of 316L stainless steel and anti-corrosion materials in a high acidified chloride solution, Applied Surface Science. 322 (2014) 47–56. doi:10.1016/j.apsusc.2014.09.205.

57. N.J. Laycock, M.H. Moayed, R.C. Newman, Metastable Pitting and the Critical Pitting Temperature, J. Electrochem. Soc. 145 (1998) 2622–2628. doi:10.1149/1.1838691.

58. G.T. Burstein, P.C. Pistorius, S.P. Mattin, The nucleation and growth of corrosion pits on stainless steel, Corrosion Science. 35 (1993) 57 – 62. doi:10.1016/0010-938X(93)90133-2.

59. P.C. Pistorius, G.T. Burstein, Aspects of the effects of electrolyte composition on the occurrence of metastable pitting on stainless steel, Corrosion Science. 36 (1994) 525–538. doi:10.1016/0010-938X(94)90041-8.

60. W. Tian, N. Du, S. Li, S. Chen, Q. Wu, Metastable pitting corrosion of 304 stainless steel in 3.5% NaCl solution, Corrosion Science. 85 (2014) 372 – 379. doi:10.1016/j.corsci.2014.04.033.

61. M.C. Biesinger, B.P. Payne, A.P. Grosvenor, L.W.M. Lau, A.R. Gerson, R.St.C. Smart, Resolving surface chemical states in XPS analysis of first row transition metals, oxides and hydroxides: Cr, Mn, Fe, Co and Ni, Applied Surface Science. 257 (2011) 2717–2730. doi:10.1016/j.apsusc.2010.10.051.

62. T. Yamashita, P. Hayes, Analysis of XPS spectra of Fe2+ and Fe3+ ions in oxide materials, Applied Surface Science. 254 (2008) 2441–2449. doi:10.1016/j.apsusc.2007.09.063.

63. F. Di Franco, M. Santamaria, G. Massaro, F. Di Quarto, Photoelectrochemical monitoring of rouging and de-rouging on AISI 316L, Corrosion Science. 116 (2017) 74–87. https://doi.org/10.1016/j.corsci.2016.12.016.

64. G. Tranchida, M. Clesi, F. Di Franco, F. Di Quarto, M. Santamaria, Electronic properties and corrosion resistance of passive films on austenitic and duplex stainless steels,

Electrochimica Acta. 273 (2018) 412–423. https://doi.org/10.1016/j.electacta.2018.04.058.

Conclusions and perspectives

The first objective of this work was to study in details the transition from native oxide-covered surface state to passive surface state on 316L stainless steel, and in particular the mechanisms of Cr and Mo enrichments that are key aspects of the passivity of Mo-bearing austenitic stainless steels.

The native oxide film formed on a mechanically polished polycrystalline 316L SS surface has been characterized in details. Surface analysis by XPS and ToF-SIMS showed that the oxide film has a bilayer structure with a total thickness of ~2 nm. The outer layer is 0.8 nm thick and consists of 44%Cr(III)-41%Fe(III)-15%Mo(VI). The inner layer is 1.2 nm thick with a composition of 64%Cr(III)-36%Fe(III). Nickel is below the XPS detection limit in the oxide film but enriched in the modified alloy region underneath the oxide film (18%Cr-52%Fe-28%Ni-3%Mo). Photocurrent spectroscopy performed in a borate buffer solution at and near open circuit potential confirmed the bilayer structure. The band gaps of the inner and outer layers are 3.0 eV and 2.6-2.7 eV, respectively, in agreement with the variation of the chromium enrichment. According to the PCS data, the oxide film would behave as an insulator with an inversion potential of ~ - 0.4 V vs. Ag/AgCl at pH ~ 9.5.

Electrochemical passivation (at 0.3 V/SCE) in sulfuric acid (0.05 M) for 1 hour does not destroy the bilayer structure of the native oxide but modifies its composition. The total thickness is ~1.9 nm. The outer layer is 0.7 nm thick with a composition of 56%Cr(III)-26%Fe(III)-18%Mo(VI). The inner layer is 1.2 nm thick with a composition of 74%Cr(III)-26%Fe(III). Compared to the air formed native oxide film, the thickness barely changes but Mo is further enriched in the outer layer and Cr in both layers after electrochemical passivation. The increase of the corrosion resistance brought by the Cr and Mo enrichments is evidenced by the anodic shift of the corrosion potential and the increase of the polarization resistance observed on the pre-passivated surface by linear sweep voltammetry and impedance spectroscopy.

In order to further study the mechanisms of the Cr and Mo enrichments brought by immersion in acid solution, the samples were treated in sulfuric acid (0.05 M) at OCP for 30 min and

analyzed by ToF-SIMS and XPS with a transfer procedure avoiding contact to ambient air. The total thickness of the film decreases slightly to 1.7 nm. The bilayer structure of the air formed native oxide film persists but the composition is altered. The outer layer becomes 0.5 nm thick with a composition of 48%Cr(III)-26%Fe(III)-26%Mo(VI). The inner layer is 1.2 thick and consists of 77%Cr(III)-23%Fe(III). Compared to air formed native oxide, the outer layer becomes thinner and increasingly enriched in Mo(VI), the inner layer thickness is unchanged but enriched in Cr(III). All these results show that the preferential dissolution of the Fe(III) oxide species, less stable in sulfuric acid, is at the origin of the Cr and Mo enrichments that are beneficial to the corrosion resistance. Upon anodic polarization in the passive domain (at 0.3 V/SCE), dehydroxylation is promoted in the inner layer and oxidation of iron, chromium and molybdenum takes place, leading to re-growth of the oxide film and increase of the steady-state thickness without affecting the overall Cr enrichment but slightly mitigating the Mo enrichment. Cr and Mo enrichments persist owing to preferential dissolution of Fe(III).

The second objective was to study the influence of chlorides on the electrochemical passivation process of 316L stainless steel in acid solution.

After passivation (at 0.3V/SCE) in sulfuric acid (0.05 M) in the presence of chlorides (0.05 M), the outer layer is 0.9 nm thick with a composition of 48%Cr(III)-36%Fe(III)-16%Mo(VI) and the inner layer composition 64%Cr(III)-36%Fe(III). The composition is similar to that of the air formed native oxide but the passive film contains less Cr(III) than when produced by the same procedure in the absence of chlorides. ToF-SIMS depth profiling shows that Cl^- ions enter the bilayer structure of the native surface oxide, mostly in the hydroxide outer layer where Fe(III) and Mo(IV,VI) species are concentrated but barely in the oxide inner layer enriched in Cr(III). Their concentration is below the detection limit of XPS (< 0.5 at%). The passivation mechanisms leading to dehydroxylation of the oxide film and to further Cr(III) enrichment in the outer exchange layer and inner barrier layer and to Mo(IV,VI) enrichment in the outer layer are negatively impacted, resulting in a less protective passive state poisoned by the interactions with chlorides. These results suggest that the preferential dissolution of iron oxide, leading to Cr and Mo enrichment, is slowed down by the interactions with the Cl^- ions at the surface of the passive film. Metastable pitting at the nanometer scale was detected by AFM.

However, if the sample is pre-passivated (at 0.3V/SCE) in Cl-free sulfuric acid (0.05M) and

further treated by passivation in the presence of chlorides, the outer layer of the passive film is 0.6 nm thick with a composition of 45%Cr(III)-34%Fe(III)-21%Mo(VI) and the inner layer 1.3 nm thick with a composition of 78%Cr(III)-22%Fe(III). Composition and structure are very similar to those before exposure to chlorides. Moreover ToF-SIMS shows no entry of chloride ions in the passive film and AFM does not reveal any metastable pitting at the nanometer scale. These results show that the stability of the oxide film is increased by pre-passivation in the absence of chlorides. Pre-passivation blocks the entry of chlorides in the passive film, including in the outer exchange layer, which enables the aging-induced variations of the composition to take place despite the presence of chlorides in the environment.

Several perspectives for further work can be proposed based on the present research work.

It would be interesting to apply the methodology and passivation conditions used in the present work to a single crystal 316L stainless steel in order to seek information at the nanoscale making advantage of a better controlled surface topography. Using EC-STM (Electrochemical Scanning Tunneling Microscopy), one should be able to apply the passivation and treatment conditions studied in the present work and to characterize their effects on the surface morphology at a local scale. The topographic and crystallographic modifications induced by passivation could be observed and analyzed. Moreover, in the presence of chlorides, it could be possible to determine the initiation sites of metastable pitting and to relate their distribution to the presence of chemical defects in the passive film impacting the local resistance to localized corrosion. This may result in a new vision of the mechanisms of passivity breakdown and the initiation of localized corrosion by pitting.

Another perspective is related to the better understanding of the role of molybdenum on the corrosion resistance. The present work shows that passivation in the presence of chloride causes their entry in the passive film but only in the outer layer of the passive film, where the Mo(IV,VI) species are concentrated. Applying our methodology to a 304 stainless steel and comparing the results of the entry of chlorides in the passive film with those on 316L stainless steel may help to understand how Mo improves the resistance of stainless steel to localized corrosion.

Annexe :
Résumé étendu en français des travaux présentés dans la thèse

Cette thèse contient 5 chapitres. Le Chapitre I présente une synthèse bibliographique de l'état d'art et les objectifs de l'étude. Le Chapitre II présente les différentes techniques électrochimiques et d'analyse de surface utilisées pour réaliser le travail de recherche expérimentale. Le Chapitre III porte sur l'étude de l'influence de la passivation sur le film d'oxyde formé à l'air (film natif) sur acier inoxydable austénitique 316L (alliage Fe-Cr-Ni-Mo). Dans ce chapitre, le film oxyde formé à l'air et les films passifs formés à 0,3 V (SCE) pendant 1 h et 20 h en milieu acide sulfurique 0,05 M ont été étudiés en détail. Le chapitre IV se concentre sur les mécanismes d'enrichissement en oxydes de Cr et Mo induits par l'immersion en milieu acide sulfurique 0,05 M et par la passivation électrochimique au moyen d'une procédure expérimentale préservant les échantillons d'une exposition à l'air ambiant entre milieu électrochimique et analyse de surface ex situ. Le Chapitre V porte sur l'effet des ions chlorures sur les mécanismes de passivation à l'échelle nanométrique.

Chapitre I

Les aciers inoxydables sont des alliages à base de fer qui présentent une teneur massique minimale en chrome de 10,5 % et une teneur massique maximale en carbone de 1,2 %. Leur histoire commence en 1821 lorsque le minéralogiste et géologue français Pierre Berthier fit la découverte des premiers aciers inoxydables en montrant que l'alliage fer chrome était d'autant plus résistant à certains acides que sa teneur en chrome était plus élevée. Entre 1904 à 1911, les aciers inoxydables ont été classifiés selon leur structure cristallographique, ce qui a permis de définir trois familles : ferritique, austénitique et martensitique. Les aciers inoxydables ferritiques ont une structure cristallographique cubique centrée (α) et sont ferromagnétiques. Les aciers inoxydables austénitiques ont une structure cristallographique cubique à faces centrées (γ) et sont paramagnétiques. Les aciers inoxydables martensitiques contiennent la phase martensite qui est une structure cristallographique tétragonale centrée métastable due à la présence d'atomes de carbone dans les sites interstitiels de la maille.

La forte résistance à la corrosion des aciers inoxydables est due à la passivité induite par la formation d'un film d'oxyde de surface tel que décrit initialement par l'allemand Philipp Monnartz en 1908. Le mécanisme de formation de ce film d'oxyde protecteur est décrit en 5 étapes : (a) Adsorption de molécules d'eau sur la surface métallique, (b) déprotonation de la surface et migration d'un cation métallique, (c) déprotonation et pontage entre sites voisins, (d) adsorption de molécules d'eau sur la monocouche d'oxyde formée, (e) déprotonation et migration d'un cation métallique pour créer une nouvelle couche d'oxyde.

De nombreuses études ont été réalisées sur la passivation et la caractérisation du film passif formé sur acier inoxydable. Pour les alliages Fe-Cr, les études électrochimiques montrent que la quantité de chrome joue un rôle très important sur la stabilité du film passif. L'augmentation de la quantité de chrome dans l'alliage diminue le potentiel de passivation, la densité de courant critique de passivation (maximum dans la région active des courbes de polarisation) et la densité de courant passif. L'analyse de surface nous montre que l'épaisseur du film est entre 1 et 3 nm. Le film est composé principalement du Cr(III) et Fe(III) sous forme oxyde et hydroxyde. La présence de Cr(VI) est observée quand le potentiel atteint le domaine transpassif. Sur ces alliage Fe-Cr, les films passifs ont une structure bicouche avec une couche externe qui contient plus d'hydroxyde et une couche interne plus d'oxyde.

Pour les alliages Fe-Cr-Mo, les études électrochimiques montrent que l'addition de molybdène améliore la résistance à la corrosion. Plus la quantité de Mo dans l'alliage augmente, plus sa résistance à la corrosion localisée est meilleure. Les analyses de surface montrent que le structure bicouche et l'épaisseur du film passif restent inchangées. La plupart des études ont montré que le Mo se présente souvent sous forme Mo(IV) et Mo(VI). D'autres degrés d'oxydation comme Mo(II), Mo(III) et Mo(V) ont été rapportés par certains auteurs.

L'ajout de Ni dans l'alliage Fe-Cr modifie le structure cristallographique de ferritique (cc) à austénitique (cfc) pour les alliages Fe-Cr-Ni, un exemple typique étant l'acier inoxydable 304. Les mesures électrochimiques montrent que l'ajout de Ni dans l'alliage améliore la résistance à la corrosion de façon significative. Cependant la quantité de Ni présent dans le film passif reste très faible voire indétectable ce qui montre que le Ni n'influence ni la composition ni la structure bicouche du film passif.

Puisque Ni et Mo améliorent tous deux la résistance à la corrosion de l'acier inoxydable, il est raisonnable d'ajouter les deux éléments en même temps. L'analyse électrochimique montre que les alliages Fe-Cr-Ni-Mo ont la meilleure résistance à la corrosion localisée. Les analyses

de surface montre que le film passif sur alliage Fe-Cr-Ni-Mo contient du Fe,Cr et Mo sous forme oxyde/hydroxyde. Le structure du film est aussi un structure bi couche.

Les films passifs formés sur aciers inoxydables sont généralement compacts et protecteurs, mais sous certaines conditions, le film peut être endommagé de façon physique ou chimique et perdre son caractère de barrière protectrice, ce qui induit le phénomène de corrosion localisée. La corrosion désigne l'ensemble des interactions entre un métal et son environnement qui aboutissent à la dégradation des matériaux métalliques par une succession de réactions chimiques et/ou électrochimiques.

La corrosion se manifeste selon plusieurs types. La corrosion généralisée se traduit par une dissolution uniforme de la surface, à l'échelle macroscopique, par une perte d'épaisseur au cours du temps, correspondant à la vitesse de corrosion. La corrosion galvanique intervient lorsque deux métaux de nature différente sont en contact électrique dans un électrolyte et forment une pile électrochimique. La corrosion sous contrainte est liée à l'action conjuguée d'un environnement corrosif et de contraintes mécaniques. La corrosion caverneuse survient dans des zones confinées due à la teneur en oxygène dissous qui diminue au cours du temps, ce qui entraîne une aération différentielle entre caverne (anode) et reste de la surface exposé au milieu milieu extérieur (cathode). La corrosion intergranulaire des aciers inoxydables est le plus souvent liée à la précipitation de carbures de chrome au niveau des joints de grains ou de phases secondaires. La corrosion par piqûres est une forme de corrosion localisée qui survient généralement en présence d'ions agressif, par exemple les ions chlorures, suite à la rupture du film passif et l'absence de re-passivation de la surface.

Dans la première partie de ce chapitre, les propriétés des films passifs formés sur les aciers inoxydables ont été présentées. Les aciers inoxydables sont généralement recouverts d'un film d'oxyde natif formé le plus souvent à l'air. L'interaction de ce film avec un environnement corrosif, surtout dans des milieu acides, peut modifier ses caractéristiques physicochimiques. Ainsi le premier objectif de cette thèse est d'étudier en détails la transition entre film d'oxyde formé à l'air et film passif formé en milieux acide sur acier inoxydable 316L (alliage Fe-Cr-Ni-Mo). Nous nous intéressons plus particulièrement aux mécanismes d'enrichissement des deux éléments importants pour la passivité des aciers inoxydable austénitiques contenant du molybdène, Cr et Mo.

Dans une deuxième partie, les différents types de corrosion des aciers inoxydables ont été présentés. Cette thèse a pour deuxième objectif d'étudier l'influence de la présence d'ions

chlorures dans l'environnement sur la transition entre film natif et film passif produit par polarisation anodique et sur l'effet de la pré-passivation en l'absence d'ions chlorures sur les modifications engendrées par la présence de chlorures.

Chapitre II

Les techniques électrochimiques utilisées pour l'étude de la résistance à la corrosion et du processus de passivation sont la polarisation potentiodynamique et la polarisation potentiostatique.

La polarisation potentiodynamique est une technique de mesure du courant en fonction du potentiel appliqué. Cette méthode permet d'observer la variation du courant généré par un balayage du potentiel à une vitesse constante. La polarisation potentiostatique est une technique de mesure de courant pour un potentiel appliqué à une valeur constante. Cette méthode permet d'observer la variation du courant en fonction du temps.

Le système électrochimique utilisé est constitué d'une cellule classique à trois électrodes. L'électrode de référence est une électrode au calomel saturé (SCE). La contre-électrode est une spirale de fil en or. L'électrode de travail est l'échantillon avec une surface de travail de 0,44 cm^2 délimitée par un joint Viton. L'électrolyte est une solution aqueuse d'acide sulfurique de concentration 0,05 M, préalablement désaérée par un bullage d'argon.

Les techniques de caractérisation de surface mises en œuvre sont la spectroscopie de photoélectrons induits par rayons X (XPS), la spectrométrie de masse d'ions secondaires à temps de vol (ToF-SIMS), la microscope à force atomique (AFM) et la spectroscopie de photo curent (PCS).

L'analyse XPS permet d'obtenir un spectre représentant le nombre de photoélectrons détectés (en coups par seconde) en fonction de l'énergie de liaison (en eV) des niveaux de cœur des éléments présents en surface. Le principe de l'XPS repose sur l'émission de photoélectrons suite à l'interaction rayonnement-matière. Cette technique permet l'identification qualitative des principaux éléments présents à la surface de l'échantillon et de leur environnement chimique.

La décomposition des spectres XPS permet d'obtenir des informations quantitatives, composition de la surface, épaisseur de la couche d'oxyde, à partir des intensités spectrales mesurées. Dans notre cas le logiciel utilisé pour la décomposition spectrale est CasaXPS. La

ligne de base est fixée et soustraite sous forme Shirley. Les paramètres des pics représentant les métaux, dans notre cas Fe, Cr, Ni et Mo, comme l'énergie de liaison, la largeur à mi-hauteur et les facteurs de forme sont déterminés sur des surfaces métalliques préparées sous UHV en utilisant le bombardement ionique pour éliminer le film d'oxyde et la contamination.

La spectrométrie de masse d'ions secondaires avec détection à temps de vol (ToF-SIMS) permet l'analyse élémentaire et moléculaire surfacique avec une très haute sensibilité. Dans une analyse de SIMS, la surface de l'échantillon est bombardée par un faisceau pulsé d'ions primaires ayant une énergie de plusieurs keV. La dissipation de l'énergie des ions primaires résulte en une cascade de collisions sur les 2 ou 3 premières monocouches atomiques, avec rupture des liaisons chimiques et émission de particules secondaires. Les ions secondaires sont post-accélérés pour être analysés en temps de vol et ainsi triés en masse.

Plusieurs types d'analyse sont utilisables. Dans notre étude, nous avons réalisé des profils de concentration permettant de déterminer la distribution en profondeur des différents éléments présents dans les films passifs et à l'interface avec le substrat. Un canon ionique (Cs^+) est opéré en courant continu permettant l'érosion ionique (qui enlève quelques couches de matériaux), et un second canon ionique (Bi^+) est opéré en mode pulsé pour l'analyse de la surface.

La microscopie à force atomique (AFM) est basée sur la mesure des forces attractives ou répulsives entre deux atomes. Son principe consiste à cartographier, par balayage, la force d'interaction mesurée localement entre un agrégat atomique (la pointe) et la surface en regard pour reconstituer un profil topographique de la surface.

Trois modes peuvent être utilisés en AFM, qui dépendent de la distance pointe-échantillon et des interactions mesurées. Le mode contact où la pointe et la surface de l'échantillon sont en contact et des interactions répulsives sont mesurées. Le mode non-contact dans lequel la pointe oscille à une fréquence proche de sa fréquence de résonance sans entrer en contact avec la surface de l'échantillon. Le mode contact intermittent où la pointe oscille à une fréquence proche de sa fréquence de résonance et entre ponctuellement en contact avec la surface de l'échantillon. Dans nos travaux, le mode choisi est le mode contact intermittent.

La spectroscopie de photo courant est une technique permettant de caractériser *insitu* les propriétés électroniques des matériaux, semi-conducteurs et isolants. Elle renseigne sur les niveaux d'énergie caractéristiques des jonctions film d'oxyde/électrolyte, telles que la valeur

de la bande interdite (E_g), le potentiel de bande plate (U_{fb}) et le type de conductivité. Ces données sur les propriétés électroniques permettent de faire le lien avec la composition et la structure stratifiée des films passifs ultra minces. Le principe de cette technique est le passage d'électrons, similaire à l'émission de photoélectrons lors de l'interaction rayonnement-matière utilisée en spectroscopie photoélectronique. Ici les électrons sont mesurés sous forme de photocourant sous un champ électrique fourni par un potentiostat.

Nous avons choisi pour cette étude de produire un état de surface initial qui est un poli mécanique. L'échantillon polycristallin d'acier inoxydable austéntique 316L a été poli sur papier abrasif de numéro 1200 puis 2400, puis avec des pâtes diamantées de tailles successives 6 µm, 3 µm, 1 µm et 0,25 µm. La taille de grain finale utilisée est 0,25 µm. En fin de polissage, les échantillons sont rincés successivement dans des bains de nettoyage avec agitation ultrasonique d'acétone (VWR Chemicals, pureté 99%), d'éthanol (VWR Chemicals, pureté 99,5%) et d'eau ultra-pure (résistivité supérieur à 18,2 MΩcm).

Chapitre III

Dans ce chapitre, le film d'oxyde natif formé à l'air et les films passifs formés par polarisation anodique à 0,3 V (SCE) dans H_2SO_4 0,05 M ont été étudiés.

Pour la surface à l'état natif obtenu après polissage, les profils élémentaires en profondeur obtenus par ToF-SIMS (Figure Annexe-1) montrent que le film superficiel d'oxyde a une structure bicouche avec une couche externe contenant majoritairement du Fe et du Mo oxydés et une couche interne contenant majoritairement du Cr oxydé. Une région métallique riche en Ni a été observée entre le film d'oxyde et le substrat métallique. Cette région est nommée "couche d'alliage modifié" (modified alloy en Anglais). Le rapport CrOx/FeOx, caractéristique de l'enrichissement en Cr dans l'oxyde, augmente depuis la surface jusqu'à la couche interne du film oxyde atteignant une valeur d'environ 3.

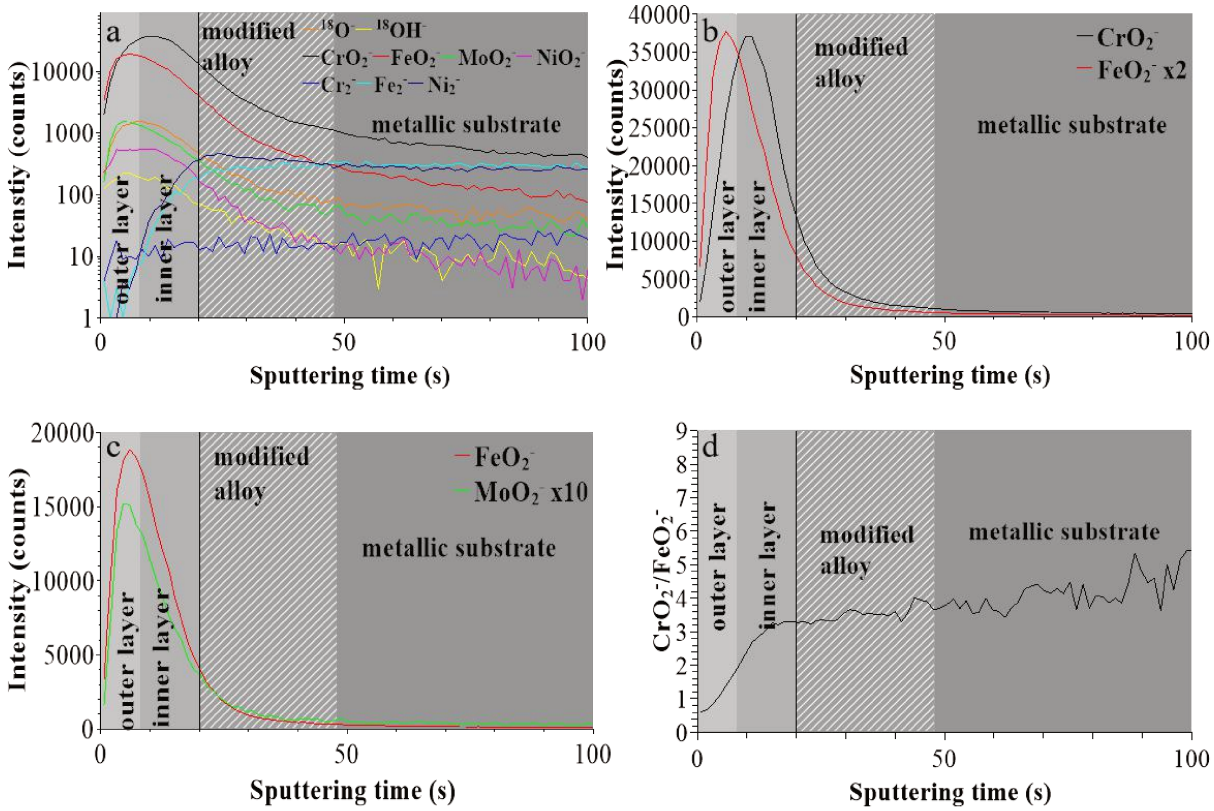

Figure Annexe-1 :Profils en profondeur ToF-SIMS pour le film d'oxyde natif sur acier inoxydable 316L : (a) ions secondaires $^{18}O^-$, $^{18}OH^-$, CrO_2^-, FeO_2^-, NiO_2^-, MoO_2^-, Cr_2^-, Fe_2^- et Ni_2^-, (b) ions secondaires CrO_2^- et FeO_2^- , (c) ions secondaires FeO_2^- et MoO_2^- , (d) rapport d'intensité CrO_2^-/FeO_2^-

Les analyses XPS angulaires réalisées à 40 et 90 degrés montrent que le film est majoritairement constitué de ligands hydroxydes en partie externe et oxydes en partie interne. Le ratio hydroxyde/oxyde est de 0,9. La décomposition des spectres à haute résolution montre que dans le film le Cr est présent sous forme de Cr(III) ox/hyd, le Fe sous forme de Fe(III) ox/hyd et le Mo sous forme de Mo(IV) et, très majoritairement, Mo(VI). Les traces d'oxyde de nickel observées par ToF-SIMS ne sont pas détectables pas XPS (< 1 at%). La Figure Annexe-2 présente les spectres des niveaux de cœur XPS et leur reconstruction pour la surface couverte par le film d'oxyde natif.

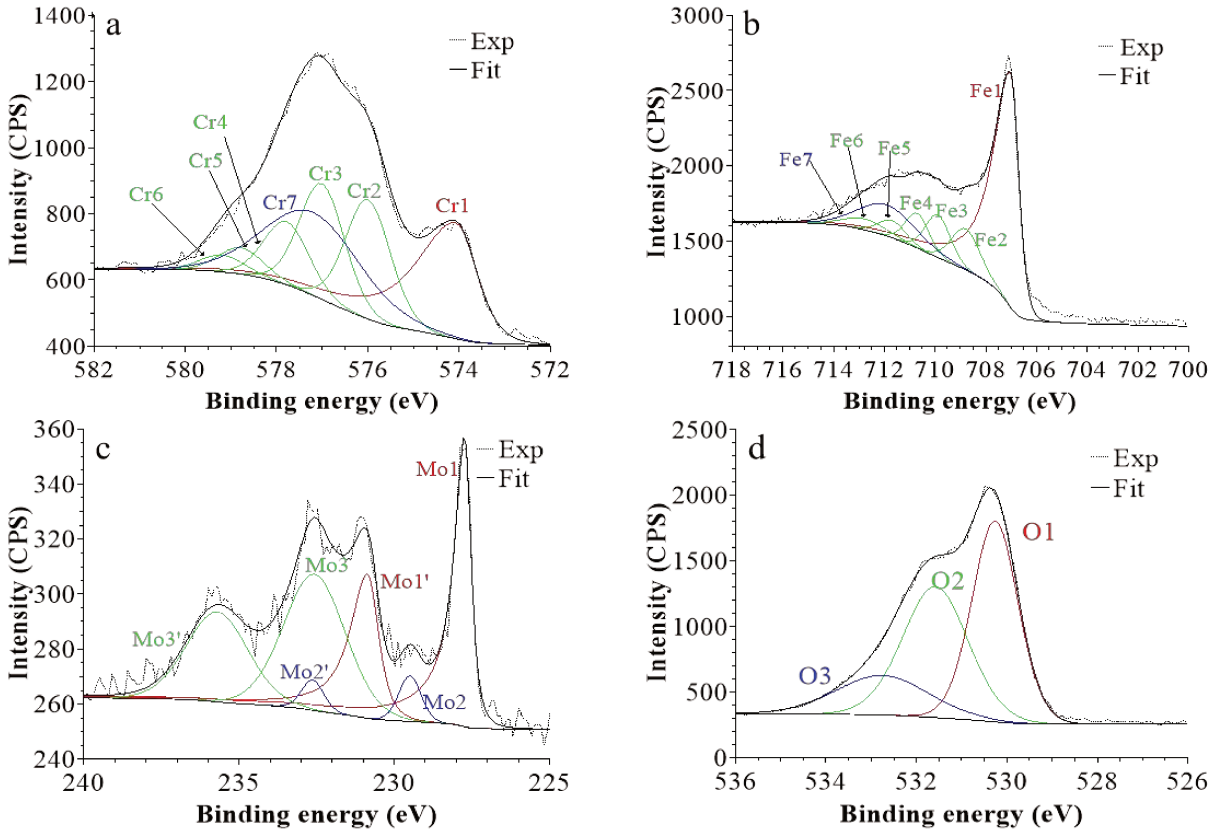

Figure Annexe-2 : Spectres XPS des niveaux de cœur et reconstruction pour la surface d'acier inoxydable 316 couverte par le film d'oxyde natif sur: (a) Cr $2p_{3/2,}$ (b) Fe $2p_{3/2,}$ (c) Mo $3d_{5/2-3/2}$ et (d) O 1s

Sur la base des données ToF-SIMS et XPS, un modèle bicouche a été construit pour calculer composition et épaisseur surfaciques. Les résultats indiquent que la couche externe du film d'oxyde a une épaisseur de 0,8 nm et une composition de 41Fe-44Cr-15Mo (at%), et la couche interne une épaisseur de 1,2 nm et une composition de 36%Fe-64%Cr (at%). Globalement, le film a une épaisseur de 2 nm et une composition de 39Fe-55Cr-6Mo (at%). Le film d'oxyde formé à l'air est donc riche en oxyde de Cr. Sous le film d'oxyde, la couche d'alliage modifié a une composition 52Fe-18Cr-28Ni-3Mo (at%). Comparé à la composition de l'alliage métallique Fe–20Cr–12Ni–1.6Mo (at%), l'enrichissement en Ni de l'alliage modifié est confirmé.

Pour les films formés par polarisation potentiostatique en milieu acide sulfurique 0,05 M pendant 1 h et 20 h, les analyses ToF-SIMS montrent la même structure bicouche que pour le film natif. Les profils élémentaires présentent les mêmes tendances que pour le film natif. Cependant le profil du rapport CrOx/FeOx augmente jusqu'à une valeur de 6-7 dans la partie interne, indiquant un plus fort enrichissement en chrome.

La décomposition des spectres XPS à haute résolution montre que les éléments ont les même degrés d'oxydation que pour le film natif. Le Cr(VI) n'est pas détecté après polarisation électrochimique dans le domaine passif. Dans le spectre d'O 1s, le ratio hydroxyde/oxyde devient 1,2 au lieu de 0,9, montrant que le film passif contient plus d'hydroxyde que le film natif. Pour le film passivé 1 h, la couche externe du film d'oxyde a une épaisseur de 0,7 nm et une composition de 26Fe-56Cr-18Mo (at%), et la couche interne une épaisseur de 1,2 nm et une composition de 26Fe-74Cr (at%). Globalement, l'épaisseur est de 2 nm et la composition 26Fe-67Cr-7Mo (at%). Pour le film passivé 20 h, la couche externe du film d'oxyde a une épaisseur de 0,6 nm et une composition de 32Fe-49Cr-19Mo (at%), et la couche interne une épaisseur de 1,3 nm et une composition de 23Fe-77Cr (at%). Globalement, l'épaisseur est de 2 nm et la composition 26Fe-68Cr-6Mo (at%). Comparés au film natif, le Cr est fortement enrichi dans les deux couches des films passifs et le Mo est légèrement enrichi dans la couche externe.

Les analyses PCS réalisées à 0 V(Ag/AgCl) en milieu borate (Figure Annexe-3) montrent que le film natif a une structure bicouche également observée in situ en solution aqueuse. Deux valeurs de largeur de bande interdite sont mesurées : 2,7 eV pour la couche externe et 3,0 eV pour la couche interne. Ces valeurs sont compatibles avec un enrichissement en chrome plus important en couche interne. Le spectre d'efficacité photonique mesuré à longueur d'onde fixe en fonction du potentiel appliqué montre que le film d'oxyde se comporte comme une isolant avec une potentiel d'inversion de -0,4 V(Ag/AgCl). La modélisation basée sur la composition calculée à partir des données XPS et ToF-SIMS donne des valeurs de bande interdite de 2,7 ± 0,3 eV et 2,8 ± 0,3 eV, ce qui est proche des valeurs mesurées par PCS.

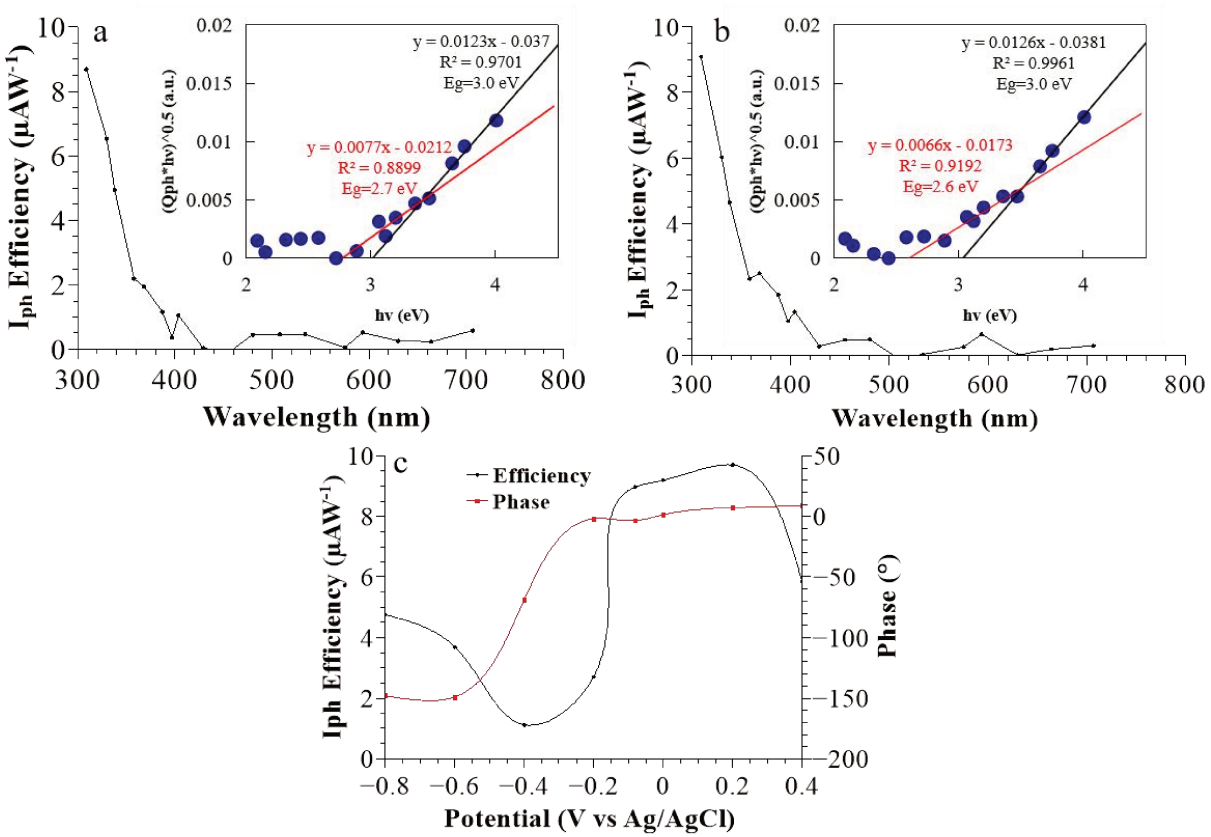

Figure Annexe-3 : Analyse PCS, dans 0,1 M $Na_2B_4O_7$, du film d'oxyde natif sur acier inoxydable 316L: (a, b) spectres de photo courant et $(Q_{ph}h\nu)^{0,5}$ vs $h\nu$ (en incrustation) (a) U_{OCP} = - 0,07 V vs Ag/AgCl et (b) U_E = 0,2 V vs Ag/AgCl; (c) photo courant et phase vs potentiel appliqué pour λ= 309 nm

Pour les films passifs, la forte diminution de l'efficacité photonique, compatible avec l'augmentation de l'enrichissement en chrome, ne permet pas d'analyser les spectres de photo courant et d'extraire des valeurs de bande interdite fiables.

Les mesures électrochimiques confirment que l'enrichissement supplémentaire en chrome de la couche d'oxyde apporté par la passivation électrochimique confère une meilleure résistance à la corrosion. Les courbes de polarisation potentiodynamique montrent que le film passif a un potentiel de corrosion de -0,19 V, plus élevé que celui du film natif (-0,37 V). Les mesures de spectroscopie d'impédance indiquent que le film passif a une résistance de polarisation de $8{,}3\cdot10^5$ ($\Omega\cdot cm^2$) quatre fois plus élevée que celle du film natif $1{,}8\cdot10^5$($\Omega\cdot cm^2$).

Dans ce chapitre, les caractéristiques physicochimiques du film natif formé à l'air sur l'acier inoxydable 316 L et celles de films passifs formés par passivation électrochimique ont été analysées en détails et comparées. Aussi bien à l'état natif que passif, les films d'oxydes de surface ont une structure bicouche avec une couche externe où il y a majoritairement Fe(III) et

Mo(IV/VI) et une couche interne où il y a majoritairement Cr(III). Cependant le film passif est plus enrichi en Cr(III) et Mo(IV/VI) que le film natif. Les analyses de spectroscopie de photo courant confirment la structure bicouche du film natif et sa stratification. L'enrichissement de Cr(III) et Mo(IV/VI) par passivation électrochimique à 0,3 V(SCE) en milieu acide sulfurique 0,05 M confère une meilleure résistance à la corrosion.

Chapitre IV

Le Chapitre IV porte sur les mécanismes d'enrichissement du film d'oxyde en Cr et Mo générés par la passivation électrochimique en milieu acide sulfurique 0,05 M.

Pour pouvoir étudier ces mécanismes, trois états de surface ont été étudiés : état natif, état passif obtenu par polarisation anodique et état passif obtenu à potentiel de circuit ouvert (OCP) en l'absence de polarisation anodique. Pour chacun des deux états passivés, les transferts entre milieu électrochimique et chambre UHV pour analyse de surface ont été réalisés sous argon à l'abri de l'air ambiant dans le but de ne pas altérer l'état produit électrochimiquement. L'état natif est celui obtenu après polissage mécanique de la surface. Les états passifs sont générés en milieu acide sulfurique 0,05 M, l'un par 30 minutes d'immersion à OCP, l'autre par 30 minutes de polarisation potentiostatique à 0,5 V(SCE) après 30 minutes d'immersion à OCP.

Les analyses ToF-SIMS montrent que sur les 3 échantillons, les film d'oxydes ont une structure bicouche constituée majoritairement de Fe(III) et Mo(IV/VI) en partie externe et majoritairement de Cr(III) en partie interne. Les deux films passifs ont un ratio CrOx/FeOx plus élevé que le film natif. Ces observations sont cohérentes avec les résultats du chapitre III. Toutefois le film passif produit à OCP est moins épais que les deux autres films et contient moins de Fe oxydé en partie externe.

Les analyses XPS montrent que dans les films d'oxyde le Cr est présent sous forme Cr(III) ox/hyd, le Fe sous forme Fe(III) ox/hyd, et le Mo sous forme de Mo(IV et VI). La quantité d'oxyde de Ni est sous la limite de détection de l'XPS dans tous les cas. Ces résultats sont en accord avec les résultats du chapitre III.

Le traitement quantitatif des données XPS montre que, comparé au film d'oxyde natif, le film passif formé à OCP possède des épaisseurs de couches externe et interne plus faibles. Pour la couche externe, l'épaisseur varie de 0,7 nm à 0,5 nm et pour la couche de 1,5 nm à 1,2 nm. Cela confirme l'observation ToF-SIMS de diminution d'épaisseur de la couche d'oxyde. De

plus l'augmentation marquée de la teneur en Cr(III) de la couche (de 5% à 48% en couche externe et de 58% à 77% en couche interne) et en Mo(IV,VI) (de 13% à 26% en couche externe) montre que l'enrichissement en Cr et Mo se produit déjà à OCP, c.-à-d. en l'absence de polarisation anodique appliquée . Puisqu'il y a diminution de la quantité de Fe(III) et diminution de l'épaisseur du film d'oxyde, on peut conclure que l'enrichissement combiné en Cr et Mo résulte de la dissolution préférentielle de l'oxyde de fer dans le milieu acide passivant.

La différence de composition entre film passif formé à OCP et film passif formé par polarisation anodique dans le domaine passif est moins marquée. On observe que le film passif polarisé a une épaisseur plus importante (0,8 nm pour la couche externe et 1,4 nm pour la couche interne), ce qui montre que la passivation sous potentiel appliqué reforme l'oxyde et créé une compétition entre dissolution et reformation du film d'oxyde générant un état stationnaire passif plus épais.

Pour conclure, l'enrichissement de la couche d'oxyde en Cr et Mo généré par passivation en milieu acide se produit dès l'immersion à OCP du fait de la dissolution préférentielle de l'oxyde de fer. L'application d'une polarisation anodique reforme l'oxyde partiellement dissous sans toutefois amoindrir de façon marqué les enrichissements en Cr et Mo obtenus à OCP.

Chapitre V

Dans ce chapitre la passivation électrochimique à 0,3 V(SCE) en milieu acide sulfurique 0,05 M a été étudiée en présence d'ions chlorures dans l'électrolyte dans le but de comprendre l'effet des ions chlorures sur les mécanismes de passivation.

Une étude préliminaire combinant mesures électrochimiques et analyse AFM a consisté à identifier la concentration de chlorures requise pour générer un état passif altéré sans toutefois initier de piqûration à l'échelle sous micrométrique. Cette étude montre que la concentration des ions chlorures correspondant à nos besoins est 0,05 M dans l'électrolyte H_2SO_4 0,05 M. Ensuite l'état passif obtenu par passivation à 0,3 V(SCE) dans H_2SO_4 0,05 M + NaCl 0,05 M à partir de la surface à l'état natif a été analysé par XPS, ToF-SIMS et AFM. Les images et histogrammes AFM sont présentés dans la Figure Annexe-4.

Les données AFM montrent clairement la présence de piqûres à l'échelle nanométrique et les

histogrammes de hauteur montrent que la surface devient plus rugueuse après passivation. dans la solution contenant des chlorures.

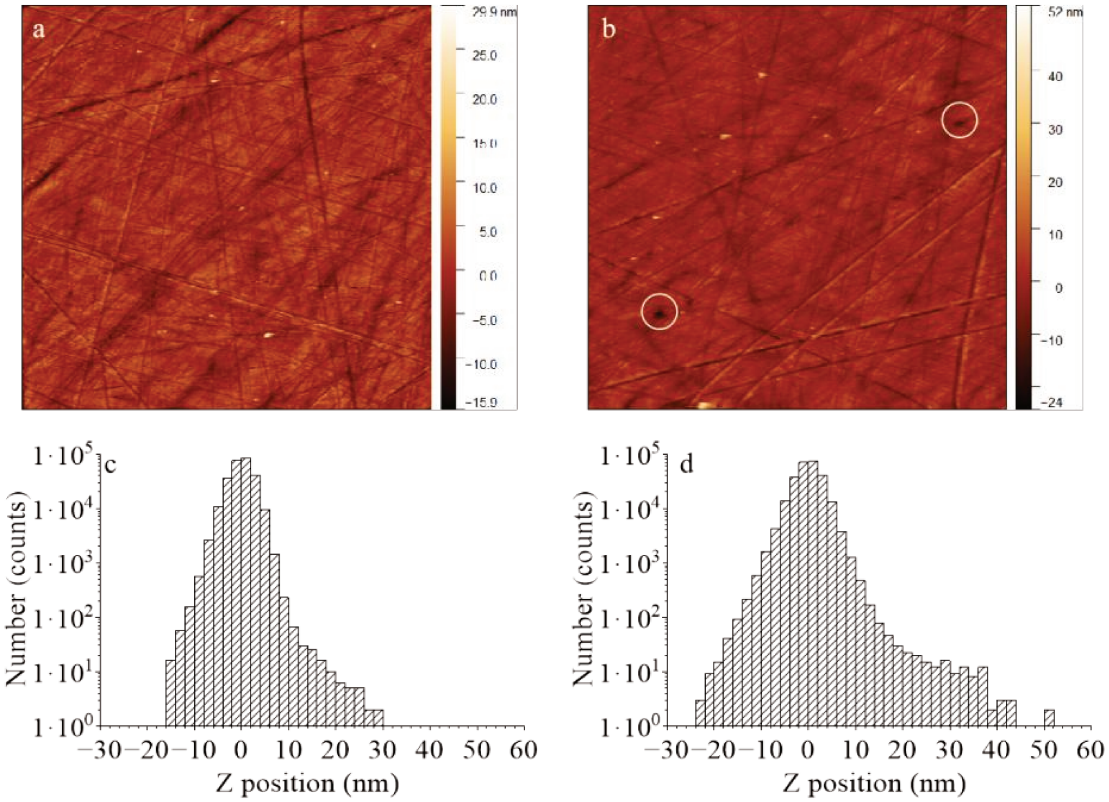

Figure Annexe-4 : Analyse AFM pour l'échantillon recouvert d'oxyde natif avant (a, c) et après (b, d) passivation à 0,3 V / SCE dans l'électrolyte 0,05 M H_2SO_4 + 0,05 M NaCl: (a, b) images AFM (10 × 10 μm^2), (c, d) histogrammes de position Z.

L'analyse ToF-SIMS montre que le film passif généré dans l'électrolyte 0,05 M H_2SO_4 + 0,05 M NaCl a une structure bicouche comme avant passivation. La comparaison des profils élémentaires en profondeur montre que les ions chlorures pénètrent la couche externe du film, mais pas la partie interne de façon significative. L'analyse XPS indique une quantité de chlorures inférieure au seuil de détection. Le film est moins enrichi en Cr et légèrement moins en Mo que lorsqu'il est produit en l'absence de chlorures (48% de Cr(III) et 16% de Mo(IV,VI) en couche externe contre 56% de Cr(III) et 18% de Mo(IV,VI) et 64% de Cr(III) en couche interne contre 74%). Ainsi, la présence de chlorures semblent partiellement bloquer les mécanismes d'enrichissement à l'origine de l'enrichissement du film en chrome. Des piqûres métastables sont créées à l'échelle nanométrique.

L'influence de la pré-passivation en l'absence de chlorures sur les altérations de l'état passif générées par la présence de chlorures a également été étudiée. L'état passif a été généré dans

H_2SO_4 0,05 M sans chlorure comme au Chapitre III puis exposé dans H_2SO_4 0,05 M + NaCl 0,05 M au même potentiel anodique. Cette fois aucune piqûre n'est observée après passivation en présence de chlorures.

Les analyses ToF-SIMS montrent que la structure bicouche et l'épaisseur de chaque couche varient très peu après la passivation. L'intensité du signal correspondant aux chlorures est identique à celle mesurée pour le film natif, indiquant le blocage de l'entrée des chlorures par le traitement de pré-passivation. Les compositions calculées à partir des données XPS montre une différence très faible avant et après la passivation. Ces résultats indiquent que la pré-passivation par polarisation anodique dans l'électrolyte sans Cl^- augmente la stabilité de l'état passif obtenu dans l'électrolyte contenant du Cl^-. Il bloque l'entrée des chlorures dans le film passif, y compris dans la couche d'échange externe, ce qui permet aux variations de la composition induites par le vieillissement de se produire malgré la présence de chlorures dans l'environnement.

RÉSUMÉ

La clé de la haute résistance à la corrosion des aciers inoxydables est la formation en surface d'un film ultra mince mais protecteur appelé film passif. Ce film contient des espèces Fe(III) et Cr(III) et est stable dans la plupart des environnements. Cependant en conditions plus sévères telles qu'en environnement acide ou en présence d'ions agressifs comme les chlorures, le film passif peut être rompu, conduisant à l'initiation de phénomènes de corrosion localisée. Dans ce travail, des techniques électrochimiques (voltamètrie à balayage linéaire, polarisation potentiostatique, spectroscopie de photocourant, spectroscopie d'impédance électrochimique) ont été combinées à des techniques d'analyse de surface spectroscopiques (spectroscopie de photoélectrons, spectrométrie d'ions secondaires à temps de vol) et microscopiques (microscopie à force atomique) afin d'étudier en détails les altérations du film d'oxyde de surface résultant du processus de passivation sur acier inoxydable polycristallin 316L. Le film d'oxyde natif formé à l'air a été analysé et comparé aux films passifs formés dans l'acide sulfurique (0,05 M) dans différentes conditions (potentiel de polarisation, temps de polarisation, présence de chlorures). Les résultats montrent que la passivation en acide sulfurique enrichit le film d'oxyde en espèces Cr(III) et Mo(IV, VI) du fait de la dissolution préférentielle des espèces Fe(III) sulfurique. La présence de chlorure produit un état passif moins résistant en limitant sa déshydroxylation et les enrichissements en Cr(III) et Mo(IV, VI), mais une pré-passivation dans un électrolyte sans Cl^- bloque l'entrée de chlorures dans le film passif et permet aux enrichissements supplémentaires induits par le vieillissement d'avoir lieu malgré la présence de chlorures dans l'électrolyte.

MOTS CLÉS

acier inoxydable, film d'oxyde, passivité, analyse de surface, électrochimie

ABSTRACT

The key of the high corrosion resistance of stainless steels is the formation of an ultra-thin but protective surface oxide film called passive film. This film contains Fe(III) and Cr(III) and is stable in most common environment. However in severe conditions such as in acid environments or in the presence of aggressive ions like chlorides, the passive film can breakdown leading to the initiation of localized corrosion phenomena. In this work, electrochemical techniques (Linear Scan Voltammetry, potentiostatic polarisation, Photo-Current Spectroscopy, Electrochemical Impedance Spectroscopy) were combined with surface spectroscopic techniques (X-ray Photoelectron Spectroscopy, Time-of-Flight Secondary Ion Mass Spectrometry) and microscopic techniques (Atomic Force Microscopy) in order to study the alterations brought by anodic passivation to the surface oxide film on polycrystalline 316L stainless steel. The air-formed native oxide film was analyzed and compared with the passive films formed in sulfuric acid (0.05 M) in different conditions (polarization potential, polarization time, presence of chloride). The results show that passivation in sulfuric acid enriches Cr(III) and Mo(IV,VI) species in the passive film owing to the preferential dissolution of Fe in sulfuric acid. The presence of chloride produces a less resistive passive state by poisoning dehydroxylation and further Cr(III) and Mo(IV,VI) enrichments, but pre-passivation in a Cl-free electrolyte, that blocks the entry of chlorides in the passive film, enables the beneficial aging-induced variations of the composition to take place despite the presence of chlorides in the environment.

KEYWORDS

Stainless steel, oxide film, passivity, surface analysis, electrochemisty